The Use of Metasurfaces for Magnetic Resonance Imaging Applications

Ismail Masoud Issa

Department of Electronic and Electrical Engineering

University of Sheffield

This dissertation is submitted for the degree of

Doctor of Philosophy

June 2018

Dedicated to:

To the soul of my father **Masoud**, may Allah have a mercy on him.

To my mother**Hailma**.

To my small wonderful family, my wife **Boshra** and my kids.

To my brothers and sisters.

Acknowledgements

It would not have been possible to write this thesis without the help and support of the people around me, it is with immense gratitude that I thank Dr.Kenneth Lee Ford for his tremendous support throughout my PhD study, his encouragement and endless enlightening ideas were very helpful to the success of my work.

Special thanks go to Professor James Wild and Dr.Madhweash Rao. Their detailed feedback and responses to my work helped save me valuable time in the my thesis development, and for that I am very grateful.

I would like also grateful to the Ministry of Higher Education in Libya for their financial support.

I am also indebted to many of my colleagues in the Antenna design group for their support; I would like to thank my wife and the members of my family in Libya.

Publication

Journal articles

I. Issa, K. L. Ford, M. Rao, and J. Wild, "Enhancement of radio frequency magnetic field for a 1.5T magnetic resonance system using a high impedance surface," IET Microwaves, Antennas Propagation, vol. 10, no. 13, pp. 1378–1383, 2016.(Chapter 3)

I. Issa, K. L. Ford, M. Rao, and J. Wild, "A Magnetic Resonance Imaging Surface Coil Transceiver Employing a Metasurface for 1.5T Applications," IEEE Transaction of Biomedical Engineering, submitted, 2018. (Chapter 6)

Conference proceedings papers

[1] **I. Issa**, L. K. Ford, J. M. Wild, and M. Rao, "A high impedance surface for improving the radio frequency magnetic field for a 1.5T magnetic resonance system," in Antennas and Propagation Conference (LAPC), 2015 Loughborough, pp. 1–4, IEEE, 2015.(Chapter 3)

I. Issa, K. L. Ford, M. Rao, and J. Wild, "Evaluation of high impedance surfaces for MRI RF coil applications-simulations of RF field and specific absorption rate," in Antennas and Propagation (EuCAP), 2016 10th European Conference on. IEEE, 2016, pp. 1–3.(Chapter 3)

I. Issa, K. L. Ford, M. Rao, and J. M. Wild, "A reflective capacitive impedance surface for 1.5T magnetic resonance imaging applications," in 2016 Loughborough Antennas Propagation Conference (LAPC), pp. 1–5, Nov 2016.(Chapter 4)

I. Issa, K. L. Ford, M. Rao, and J. M. Wild, "A Reconfigurable Capacitive Impedance Surface for 1.5T Magnetic Resonance Imaging Applications," in 2017 Loughborough Antennas Propagation Conference (LAPC),Nov 2017. (Appendix A)

[1] This paper has been accepted with 40/40 review and awarded the 3th prize of the best student paper

Abstract

The development of metasurface structures has provided new methods of designing electromagnetic devices and materials with unique features. This thesis reports new approaches of metasurface structure, which have been designed to improve the local performance of a radio frequency (RF) magnetic field and SNR of MRI images acquired on a 1.5T MRI scanner. In this context, comprehensive investigations of different metasurafce structures combined with RF coils, have been evaluated and compared against the standard coil performance. In order to determine the best options which are able to improve the RF magnetic field and SNR in terms of their strength and more penetration depth inside the dielectric phantom, different metasurface approaches have been investigated. This framework was applied in different metasurafce structures, which include a high impedance surface (HIS) and capacitive impedance surface (CIS), which has been applied as a reflective or a transmission surface. A novel design of a HIS is miniaturized using distributed interdigital capacitors. The HIS with an electrically small unit cell $\lambda/92$ was positioned between a RF transmit-receive (TR) coil and an RF shield. The magnitude of the magnetic flux density from an RF coil when coupled to a dielectric phantom load (mimicking a biological sample) was estimated using numerical simulation and corroborated with SNR measurements on a MRI scanner. The results show that, the RF magnetic flux profile can be increased by using the miniaturised HIS, however, the measured SNR showed a limited improvement. For this reason, a new structure has been developed, which is a reflective capacitive impedance surface (RCIS)combined with a radio frequency loop coil. The proposed RCIS structure is based on a miniaturized surface unit cell using an interdigital capacitance approach. Full field simulations employing an interdigital frequency selective surface show a high improvement in magnetic flux density inside a homogeneous dielectric phantom as compared to a loop coil alone. This improvement has been for the first 20 mm inside the phantom. Since MRI applications require more penetration depth, a new method of using the CIS is developed as a transmission capacitive impedance surface combined with a radio frequency loop coil. Full field simulations employing an interdigital frequency selective surface show a significant improvement of 160% and 210% in normalised

receive magnetic flux density $\frac{|B_1^-|}{\sqrt{P_L}}$ and transmit magnetic flux density $|B_1^+|$ respectively inside homogeneous dielectric phantom in the first 50 mm of the penetration depth as compared to a loop coil alone at the coil centre, where P_L is the power absorbed in the system. The concept has been demonstrated through bench measurements and experimentally demonstrated within the MRI scanner. By using an odd number of the miniaturised unit cells of the TCIS structure new results have been achieved. These results show there is a significant improvement of the SNR at the coil centre and edge for the first 50 mm of the penetration inside the phantom. The results have illustrated that there is maximum improvements of 216% and 133% of the transmission efficiency and receiver sensitivity respectively.

Abbreviations

AEC	Artificial electromagnetic materials
AMC	Artificial magnetic conductor
BALUN	Balance to unbalance circuit
CDF	Cumlative density function
CLR	Capacitively loaded ring
DNG	Double negative material
EBG	Electromagnetic band gap
FID	Free induction decay
FOV	Field of view
FSS	Frequency selective surface
HDC	High dielectric constant
HIS	High impedance surface
IEC	International Electrotechnical Commission
LHM	Lift hand material
MI	Magneto inductive
MRI	Magnetic resonance image
NMR	Nuclear magnetic resonance
PBG	Photonic band gap
PEC	Perfect electrical conductor
PMC	Perfect magnetic conductor
RAM	Radar absorbing material
RCIS	Reflector capacitive impedance surface
RF	Radio frequency
RCS	Radar cross section
SAR	Specific absorption rate
SIBC	Surface impedance boundary condition
SNR	Signal to Noise ratio
ROI	Region of interest
TCIS	Transmission capacitive impedance surface

Symbols

ϕ	Magnetic momentum
$\wp$	Angular momentum
γ	Gyromagnetic ratio [MHz/T]
$^1(H)$	Hydrogen nucleus
H_0	Static magnetic field
B_0	Static magnetic flux density
M	Magnetisation
M_0	Net magnetisation
ω	Angular frequency
ω_0	Larmor angular frequency
h	Plank's constant=6.626×10^{-34} Js
I_c	Spin quantum number
n_i	Nuclear magnetic quantum number
$\mathscr{E}$	Nuclear interaction energy
$\mathscr{E}^+$	Nuclear higher energy level
$\mathscr{E}^-$	Nuclear lower energy level
$\mathbf{T}$	Temperature in Kelvin
U	Number of nuclei
τ	Time constant
$\mathbf{k}$	Boltzmann constant =1.38×10^{-23} J/k
ρ	Proton,density
H_1	Radio frequency magnetic field
B_1	Radio frequency magnetic flux density
B_1^-	Radio frequency magnetic flux density negatively rotated
B_1^+	Radio frequency magnetic flux density positively rotated
α	Flip angle
αg	global Flip angle

T_1	Spin- lattice relaxation time
T_2	Spin-spin relaxation time
T_s	Slice thickness
T_R	Pulse repetition time (ms)
T_E	Echo,time (ms)
G	Gradient function amplitude
G_{ss}	Gradient amplitude of slice selection function
G_P	Gradient amplitude of phase encoding
G_f	Gradient amplitude of frequency encoding
μ	Magnetic of medium
μ_0	Freespace medium permeability $= 4\pi \times 10^{-7}$ H/m
ε	Electrical of medium
ε_0	Freespace permittivity $= 8.85 \times 10^{-12}$ F/m
φ	Magnetic flux
I	Electrical current
E	Electrical field
S_1	Rectangular coil width
S_2	Rectangular coil length
c	Rectangular strip bar width
b	Rectangular strip bar thickness
L	Coil inductance
D_c	Circular coil diameter
C_T	Radio frequency coil total capacitor
Q	Quality factor
ζ	MRI received signal
V	Sample volume
j	Complex number $=\sqrt{-1}$
V_n	Thermal noise
F	Noise figure
P_L	Dissipated power

$S(r)$	Image signal intensity
σ_{stdv}	Image background noise intensity
c_0	Freespace light speed
λ	Freespace wavelength
n	refractive index
D	Digit length
W_d	Digit width
g_d	Gap width between digits
N	Number of digits
J_c	Conductive current density
J_d	Displacement current density
Y_0	Freespace admittance
σ	Electrical conductivity
$tan\,\delta$	Tangent dielectric losses
ε_{eff}	Effective medium permittivity
$K(k)$	Complete elliptic integral
ρ	Reflection phase of high impedance surface
P	Unit cell periodicity
N_P	Number of unit cells
P_{coil}	Dissipated power in the coil
P_{acc}	Accepted power in the system
$P_{Phantom}$	Dissipated power in the dielectric phantom
β	Freespace propagation constant
P_{RCIS}	Dissipated power in the reflector capacitive impedance surface
P_{TCIS}	Dissipated power in the Transmission capacitive impedance surface
X_{HIS}	Cross sectional of the high impedance surface
ρ_m	Mass density of the tissue in Kg
$H^-_{1,normalised}$	Normalised negatively rotated magnetic field
$B^-_{1,normalised}$	Normalised negatively rotated magnetic flux density
η	The percentage improvement in transmission efficiency of RF surface coil
Ψ	The percentage improvement in receiver sensitivity of RF surface coil
$S11$	Forward reflection coefficient
$S21$	Forward transmission coefficient

Table of contents

List of figures

List of tables

Chapter 1

Introduction and Background

1.1 Introduction

Magnetic resonance imaging which is named as (MRI), is an analyze imaging strategy utilized primarily in medical applications to create an image of the interior of the human body. Images are produced using nuclear magnetic resonance (NMR) which excites, without non-ionising radiation effects, the organic molecules found in living tissue. The increasing interest in the use of MRI as a real time imaging technique useful for disease detection, diagnosis and monitoring of treatment progress, along with other applications, has led to an increased effort toward improving image quality in order that MRI can be even more effectively used by the medical community. The primary method for improving this quality is to improve the MR image signal to noise ratio (SNR), the exploration of which forms the basis of this present research. Thus, this introduction seeks to provide an overview of the scientific principles behind MRI signal detection and SNR improvement before stating the research problem. From this, the aims and objectives of this thesis are stated. MRI systems use a combination of three types of magnetic field of differing strengths on the subject being imaged. The first is the static magnetic flux density, which is known as B_0. This field is measured in Tesla and is used to align the nuclei inside the subject. This field strength of clinical MRI scanner is 0.5T, 1.0T and 3T, however, 75% of the clinic MRI scanners use 1.5T [1]. The second is a magnetic gradients field which are used for spatial encoding of the resonance frequency and phase of the signal along the x, y, and z-axis. Its strength is measured in $milli-Tesla/meter$. Finally, radiofrequency magnetic field pulses are used to create the nuclear magnetic resonance (NMR) signal with its strength being measured in micro-Tesla. The MRI signals are generated from protons inside the body, consisting mainly of water. The patient is placed inside a very strong magnet, which produces a static magnetic

field [2] and each proton inside the body can be considered as a small charged particle, which acts as a magnetic field. These protons populate into two energy levels, high and low energy states and starting to precess around the centre of the static magnetic field. The frequency of precession is proportional to the strength of the static magnetic field. The sum of all protons precessing is detected as an induced voltage using an RF detector, this signal is spatially encoded and therefore, a Fourier transform is performed to convert this spatial information to MRI image. The efficacy of the MRI scans in any application is limited by the image quality the scanner can generate. In general, three keys issues need to be addressed in order to improve the image quality of the MRI scanner : spatial resoluton, image contrast and signal to noise ratio SNR [3].

Since the SNR is considered to be the key parameter for efficient MRI scanner, numerous investigate researches have focused on improving the SNR of an RF coil by enhancing the RF magnetic fields. Many approaches have been developed to improve the SNR in low frequency MRI scanners. The focus of the research presented throughout this thesis is to investigate new ways of enhancing the radio frequency magnetic field in low frequency MRI systems.

1.1.1 Problem definition

It is well known that the strength of a magnetic resonance imaging (MRI) signal depends on the static magnetic field of the imaging system,where the majority of clinical scanners operate at 1.5T or 3T. Recent developments in high-field MRI operating at 7T and above have shown improvements in image quality, due to an increase in (SNR) and image resolution [2]. An associated problem for high static magnetic field MRI systems is the increase in human tissue temperature due to high RF field specific absorption rate (SAR), whilst this problem is negligible at low magnetic field system such as 1.5T [4]. It is partly for these reasons that research is being carried out for alternative methods of improving image quality without the need to increase the static magnetic field and RF frequency. In this thesis, metasurfaces are proposed as a method of increasing the RF coil intensity for a 1.5 Tesla MRI scanner. The challenge is how to implement a metasurface at lower frequencies, typical of the resonance frequency of (^1H)at clinical field frequency (60-130 MHz) and the designing of miniaturised unit cell dimensions.

1.1.2 Thesis aim and objectives

In this thesis, the primary aim is to improve (SNR) of a 1.5 T MRI system which operates at 63.8MHz. This is achieved by improving the strength of the RF magnetic field by including

metasurfaces. The specific objectives to achieve the main aim are set:
1. **The first** main objective focuses on the application of a High Impedance Surface (HIS) to enhance the RF magnetic field for an MRI system. The proposed structure is based on a miniaturized HIS using an interdigital capacitance approach. The surface utilizes a HIS between the RF transmit/receiver (transceiver) coil and the MRI scanner RF shield.
2. **The second** main objective presents a new approach which combines a capacitive impedance surface (CIS) as a reflector with the RF transceiver coil to improving the RF magnetic field, which leads to improve the SNR of the MRI system.
3. **The third** main objective focus on the possibility of using the CIS as a transmission layer instead of using it as a reflector layer to improve the RF magnetic field for MRI system.

1.1.3 Areas of Novelty and Originality

This thesis proposes a novel design of different miniaturised metasurfaces to enhance the the magnetic flux density and the SNR of 1.5T MRI systems. The areas of novelty in this thesis are summarised as follows
1. Proposing a new design of miniaturised HIS structure for surface coils for MRI systems by using an interdigital capacitance approach. The magnitude of the magnetic flux density from an RF coil when coupled to a HIS structure was investigated using numerical simulation (finite integral methods) and corroborated with vector network analyser measurements.
2. Testing the designed HIS within the MRI scanner. In order to quantify the improvement in SNR under a real MRI environment and results compared with the case where only the RF coil was used.
3. The development of a novel method of using a reflector capacitive impedance surface (RCIS) to further improve the magnetic flux density and SNR. The SNR was measured with and without the RCIS within the MRI scanner and good improvements have been obtained.
4. A new method for improving the magnetic flux and SNR has been proposed. This method uses a capacitive impedance surface as a transmission surface (TCIS) between the RF transceiver coil and water phantom. Similarly, this method was validated by full wave simulation and a real system MRI measurements.

1.1.4 Thesis Structure

This thesis consists of seven chapters. Following this introductory chapter, the rest of the thesis is organised as follows:
Chapter 2 gives a historical background of 3D periodic metamaterials and its main appli-

cations. A literature review of the relevant research is provided which includes the various approaches used to enhance the SNR of MRI systems. These approaches are categorised into three main methods: the first method uses metamaterial devices which include flux guide such as a Swiss roll, lens, wired medium devices and high impedance surface. The HIS miniaturised methods have been explained. The second method utilises a metasurface approach and finally the dielectric pads approach is described. This chapter emphasises the necessity of the research carried out in this thesis.

Chapter 3 presents the designs and characterisation of miniaturised high impedance surfaces coupled to RF coil in order to enhance the magnetic field flux density of MRI systems. RF coil design for 63.8MHz is explained and it is demonstrated how the SNR of the MRI scanner is enhanced by including the HIS instead of using the normal RF shielded, which is a perfect electrical conductor (PEC).

Chapter 4 illustrates reflective capacitive impedance surface (RCIS) as a new approach to improve the RF magnetic field for the MRI system. Simulated RF magnetic field, electric field, specific absorption rate and measured transmission coefficient $S21$ and real system measurements of SNR of the homogeneous dielectric phantom are presented.

Chapter 5 modified the RCIS described in chapter 4 into transmission model (TCIS) by considering the periodicity of the capacitive layer. The capacitive layer periodicity is assumed to be an even number (4×4), the magnetic field and SNR localisation can be performed when the even periodicity of the TCIS is utilized compared to only coil. This is demonstrated through numerical simulations, vector network analyser measurements and within the the MRI scanner.

Chapter 6 develops the transmission model presented in chapter 5 into an odd periodicity of the capacitive layer in order to focus the improvement of the SNR at the RF coil centre instead of localising the RF magnetic field. The TCIS is assumed to be 3×3 and the simulated metric of magnetic field, electric field, SAR, and measured SNR within the MRI scanner are reported . The full maps of flip angle, transmission efficiency and receiver sensitivity are calculated in this chapter.

Chapter 7, a summary of the work covered in this thesis is presented and the main conclusions are provided. Moreover, suggestions and areas of potential future research are given.

1.2 MRI Background

This section gives the MRI background foundation knowledge required for the reader to acquire a good understanding of the work carried out in this dissertation. The overview of the MRI principles has been provided in this section. Also, the background section provides the principles information of the MRI RF coil's design and characterisation. Following this, the MRI image quality parameters are presented which include spatial resolution, image contrast and signal to noise ratio. Improving of MRI image SNR is the main aim of this thesis.

1.2.1 Nuclear magnetic resonance

MRI is a medical imaging method which yields biological tissue images based on a nuclear magnetic resonance phenomenon (NMR), discovered by Bloch [5] and Purcell in 1946 in bulk materials[6]. The simple principles of NMR are based on the interaction between hydrogen or protons nucleus, which are excited primarily as water in tissue, and an applied magnetic field. This interaction can be described in terms of nuclear magnetism and quantum mechanics, both of which are described in this section.

Magnetic moments and nuclei spins

Atomic nuclei comprises of three fundamental particles, proton, which has a positive charge, electron with a negative charge and neutron which has no charge. All nuclei with an odd atomic number and an odd atomic weight have a fundamental quantum mechanical feature termed "spin" [2]. The hydrogen nucleus $^1(H)$ is more important in imaging by magnetic resonance because it gives the strongest magnetic resonance signal due to positive spinning and least complex nucleus, with only one proton and no neutrons. The spin property can be described as a proton spinning around an internal axis of rotating, which gives it a certain value of angular momentum, which is denoted by $\wp$. Because the nuclei is a charged particle, this rotating gives it a magnetic moment which is termed as ϕ. This magnetic moment generates an associated magnetic field called H_1. Fig. 1.1(a) shows the single proton spin of the hydrogen nucleus, taking into account, an arbitrary tissue volume which contain hydrogen atoms (protons), all protons have a spin vector of equal magnitude. In the absence of a static magnetic field, all of the proton spin vectors are randomly orientated and their effects cancel each other which lead to no net magnetization, which is termed as M_0, is generated in the volume tissue as shown in Fig. 1.1(b) [7]. In this state, the magnitude of $\wp$ is quantised, which means it can take one certain discrete value and this discrete value is determined by

proton fundamental property as given by 1.1 [3].

$$|\wp| = \frac{h}{2\pi}\sqrt{I_c(I_c+1)} \tag{1.1}$$

where the value of I_c is a spin quantum number and **h** is Plank's constant ($6.63 \times 10^{-34} Js$). The value of I_c depends on the number of neutrons and protons in the nucleus and I_c is nonzero value of nuclei having an odd number of neutrons , an odd number of atomic number, or both of them [3]. The value of I_c is equal 0.5 in the case of protons, applying this in 1.1, resulting the magnitude of $\wp$ in protons is given by 1.2.

$$|\wp| = \frac{h}{2\pi}\frac{\sqrt{3}}{2} \tag{1.2}$$

The magnetic moment magnitude $|\phi|$ which is produced of $\wp$ of the proton is given by 1.3

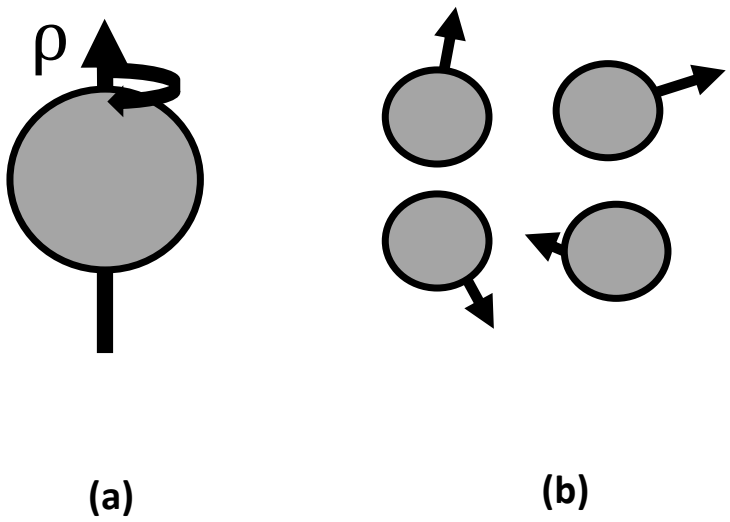

Fig. 1.1 Nuclear spin . (a) The spin of a single proton produces a magnetic moment. (b) In the absence of an external magnetic field, the proton spin orientation moment is random.

[2]

$$|\phi| = \gamma|\wp| \tag{1.3}$$

where γ is the nucleus' gyromagnetic ratio in (MHz/T) and it has a certain value for different nuclei such as carbon, protons, or phosphorus. Table 1.1 shows the I_c and γ properties of nuclei which are found in high abundant in the human body, gives an MRI signal [3].

Table 1.1 Features of nuclei found at high abundance in the human body

Nucleus	Atomic number	Atomic mass	I_c	$\gamma/2\pi$ (MHz/T)
Proton	1	1	0.5	42.58
Phosphorus	15	31	0.5	17.24
Carbon	6	12	0	-
Oxgen	8	16	0	-
Sodium	11	23	1.5	11.26

The value of $|\phi|$ is quantised and is given by 1.4 by substituting 1.3 in1.1.

$$|\phi| = \gamma|\wp| = \frac{\gamma h}{2\pi}\sqrt{I_c(I_c+1)} \tag{1.4}$$

Therefore, the magnitude of the proton ϕ is given by 1.5

$$|\phi| = \frac{\gamma h}{4\pi}\sqrt{3} \tag{1.5}$$

The magnetic moment, being a vector, contains components in x-axis, y-axis, and z-axis which include (ϕ_x, ϕ_y, and ϕ_z), corresponding. Equation 1.5 shows that each component can have any certain value, however, in the presence of a static magnetic flux density, B_0, only ϕ_z can have a value, given by 1.6 [8]as illustrated in Fig. 1.2a.

$$|\phi| = \frac{\gamma h}{2\pi}n_i \tag{1.6}$$

where n_i is the nuclear magnetic quantum number, and it can have a certain number between I_c, $I_c - 1$,.....,-I_c. In the case of a proton, the value of n_i takes two values , +0.5, and -0.5; resulting values of ϕ_z are $\gamma h/4\pi$ and $-\gamma h/4\pi$. In the presence of a B_0, the ϕ is oriented in two directions antiparallel and parallel to the main static magnetic field, as shown in Fig. 1.2b. The associated number of protons in each configuration can be determined by calculating the interaction energy, denoted by,$\mathscr{E}$, of the ϕ in the presence of the B_0. The B_0 only interacts with the z-axis component of the ϕ and $\mathscr{E}$ can be calculated by 1.7 [3].

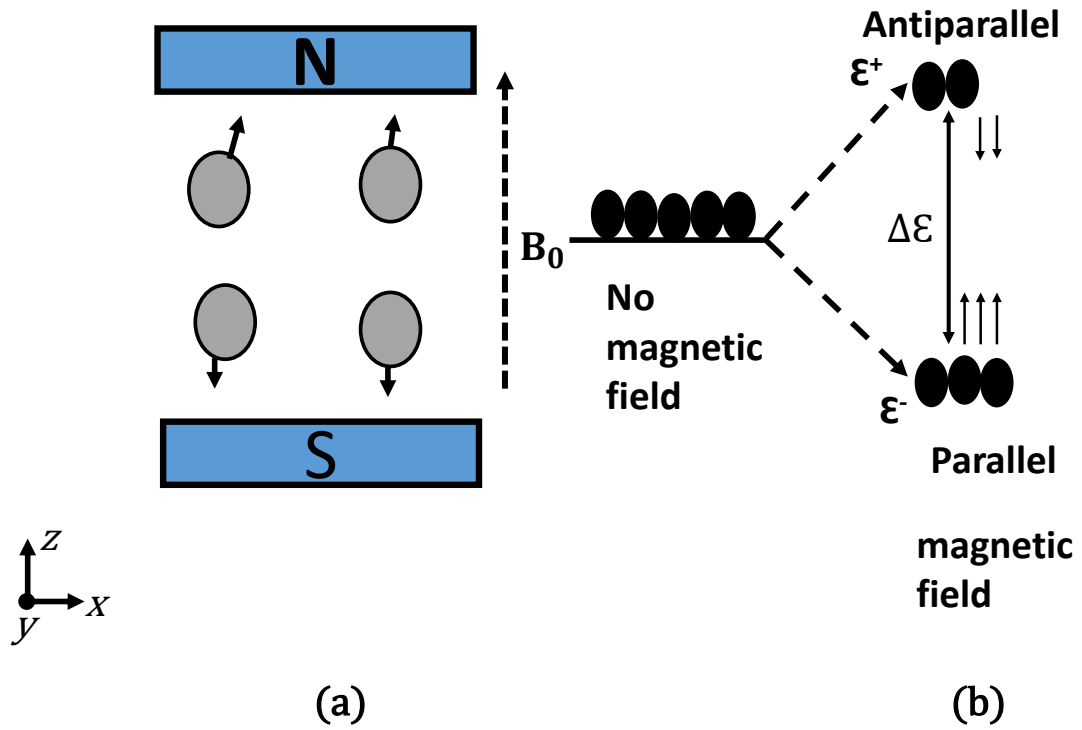

Fig. 1.2 Nuclear spin. (a) Applying an external magnetic field B_0. (b) Zeeman diagram. In the absence of external magnetic field, there is only one energy level. In the presence of B_0, the nuclei can fall one of two energy levels

$$\mathscr{E} = -\phi_z B_0 \tag{1.7}$$

By applying 1.6 in 1.7, the $\mathscr{E}$ is given by 1.8

$$\mathscr{E} = \pm \frac{\gamma h B_0}{4\pi} \tag{1.8}$$

These two types of spin (up, and down) orientation depends on the hydrogen's energy including higher energy $\mathscr{E}^+$ (antiparallel configuration), and lower energy $\mathscr{E}^-$ (parallel configuration). The difference of the energy $\Delta\mathscr{E}$ shown in Fig. 1.2b between high state and low state is given by 1.9 [2, 9].

$$\Delta\mathscr{E} = \frac{\gamma h B_0}{2\pi} \tag{1.9}$$

The relative number of nuclei in each energy configuration can be calculated by using the Boltzmann equation as given by 1.10

$$\frac{U_{antiparallel}}{U_{parallel}} = exp\big(-\frac{\Delta\mathscr{E}}{KT}\big) = exp\big(-\frac{\gamma hB_0}{2\pi KT}\big) \tag{1.10}$$

where T is the temperature in kelvin, K is the Boltzmann constant with value 1.38×10^{-23} J/k, U is a nuclei number. In order to simplify equation 1.10, a first order approximation is made as given in 1.11. The MRI signal is a function of the difference in number of relative nuclei in the energy in each case. This difference can be estimated using equation 1.12, when $U_{parallel}$ is assumed to be half of the total number of protons in the body.

$$\frac{U_{antiparallel}}{U_{parallel}} = 1 - \big(\frac{\gamma hB_0}{2\pi KT}\big) \tag{1.11}$$

$$U_{parallel} - U_{antiparallel} = \big(U_T \frac{\gamma hB_0}{4\pi KT}\big) \tag{1.12}$$

where U_T is a total number of proton in the body.

1.2.2 Radiofrequency pulses and rotation frame of magnetisation

In order to acquire an MRI signal, transitions have to be induced between the protons in the antiparallel and parallel energy levels. The energy needed to induce this transition is provided by an oscillating electromagnetic field. Due to a certain energy gap in equation 1.9 between the high energy and low energy states, the electromagnetic field has to be applied at a certain frequency. This frequency is named the resonance frequency or " Larmor frequency", can be determined by 1.13. Equation 1.14 gives the Larmor frequency in Hz, or radians per second ω_0 [3].

$$\Delta\mathscr{E} = hf_0 = \frac{\gamma hB_0}{2\pi} \tag{1.13}$$

where f_0 is the Larmor frequency.

$$f_0 = \frac{\gamma B_0}{2\pi}, \omega_0 = \gamma B_0 \tag{1.14}$$

In order to consider all the protons in the body, the term of net magnetisation is needed. The net magnetisation of the sample to be imaged was defined as M_0 and is given by equation

1.15 [2, 3].

$$M_0 = \sum_{n=1}^{U_T} \phi_z, n = \frac{\gamma h}{4\pi}(U_{parallel} - U_{antiparallel}) = \frac{\gamma^2 h^2 B_0 U_T}{16\pi^2 KT} \tag{1.15}$$

When the sample is placed within the B_0, the M_0 can be considered as a net of all single spin magnetic moments. These individual ϕ precess around the B_0 as shown in Fig 1.3a. Fig 1.3b shows the M_0, where the M_0 has only a z component value parallel to z- axis $M_z = M_0$, given a result that the components of $M_x = M_y = 0$. The MRI received signal can be produced only

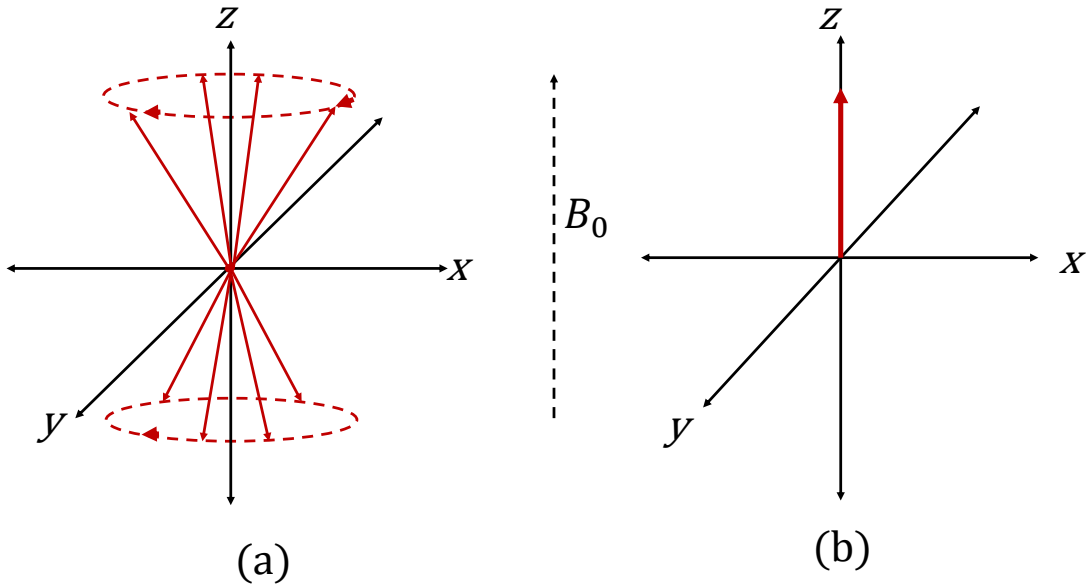

Fig. 1.3 Spin precession and net magnetization in the presence of B_0. (a) The protons precess around z axis. (b) The net magnetisation parallel to static field B_0

by the transceiver components M_x, and M_y and not by the parallel M_z component. In order to generate M_x, and M_y, M_0 has to transfer from the longitudinal axis to transverte plane. This can be achieved by applying a second magnetic field at a 90 degree angle to the z-axis, creating a second torque, which rotates the M_0 toward the xy-plane. This second magnetic flux density, termed B_1, oscillates at the Larmor frequency as pulses [2]. These pulses are known as excitation pulses which produces a magnetic flux density B_1 perpendicular to a static magnetic field. This locations difference provides a coupling between the applied RF pulse and the magnetisation vector, therefore the energy can be transferred to the proton. Thus, the applied RF magnetic field can rotate the M_0 vector from the longitudinal plane (z-plane) to the transceiver-plane by a certain angle value. This angle is named the 'flip

angle' or 'tip angle' and is termed as α, which is defined as the angle through which the M_0 is rotated by the action of the B_1. This angle is a function of the magnitude of applying RF magnetic flux density, B_1, and its pulse time τ_{B_1} duration and is given by 1.16 [1, 2].

$$\alpha = \gamma B_1 \tau_{B_1} \tag{1.16}$$

where τ_{B_1} is the RF pulse duration and B_1 is RF magnetic flux density created by the RF

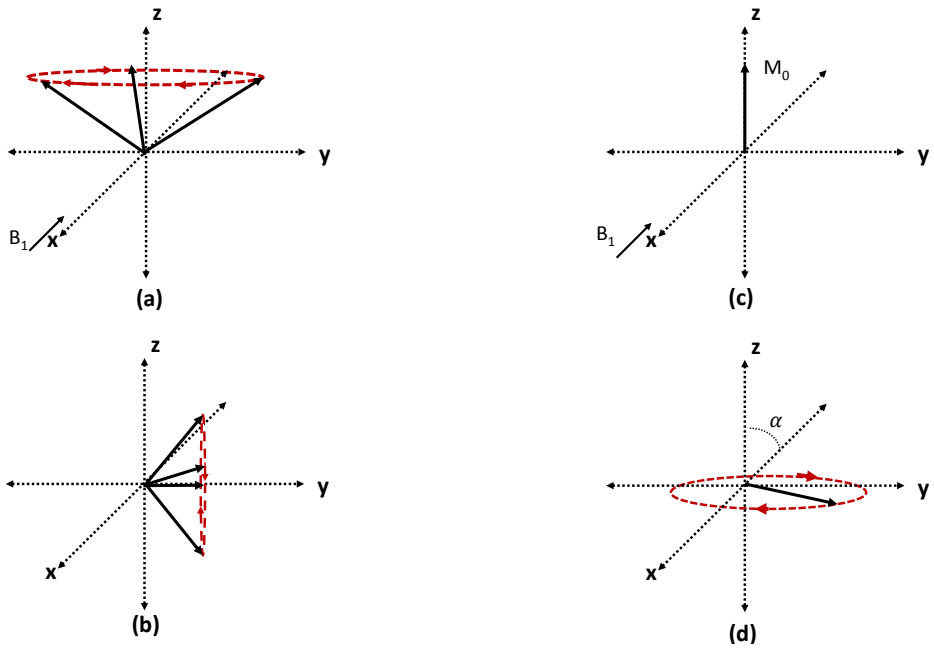

Fig. 1.4 Magnetisation vector moves from z- axis to xy -plane. (a) Applying the RF pulse B_1 along x-axis to the individual proton magnetic moments spin around B_0 toward xy-plane. (b) The individual parallel proton magnetic moments rotates around y-axis in xy-plane. (c) The net magnetisation vector $M_z = M_0$, before applying B_1. (d). The net magnetisation vector after applying B_1.

coil. If the RF transmitter has enough amplitude and it is left on long enough, the absorbed energy causes the magnetisation to rotate entirely from z-plane to xy-plane, the resultant pulse is called a 90^o pulse. The time-varying magnetic field generated by presession of the bulk magnetsation vectors in xy-plane results in a voltage being induced in the RF coil. The simplest form of the RF coil is a single loop of wire, which is polarised in-plane to xy-plane. This voltage, which follows the Faraday's law [10], is known as a free induction decay (FID)

which is the MR signal. The FID is proportional to the rate of time-varying magnetic flux, which generated by precession of bulk magnetisation, is characterised by equation 1.17.

$$FID \propto \frac{-d\varphi}{dt} \tag{1.17}$$

where φ the magnetic flux through the RF coil.

Spin-lattice and spin-spin relaxation

The relaxation process can be defined the procedure after the cessation of the B_1 RF oscillator pulse, the spin configuration system will return back to the original thermal equilibrium state. The relaxation procedure can be divided into two separated states when observing transverse and longitudinal magnetisation as separate entities. While the transverse magnetisation components M_x, M_y are decaying, the longitudinal magnetisation component M_z is recovering. The longitudinal magnetisation recovery rate is governed by the spin-lattice relaxation time,which is termed by T_1 . This configuration of returning the magnetisation towards the thermal equilibrium pulse is given by Bloch equation in longitudinal relaxation1.18 [3].

$$\frac{dM_z(t)}{dt} = \frac{M_0 - M_z(t)}{T_1} \tag{1.18}$$

By solving the differential equation 1.18 as shown in 1.19 to 1.22 using $\frac{d}{dt}f(t) = af(t)$ its integration is $f(t) = f(0)e^{at}$ and when RF=0, the B has no effect on longitudinal component which leads to $M_z(0) = 0$.

$$\frac{d}{dt}\big(M_z(t) - M_0\big) = -\frac{1}{T_1}M_z(t) + \frac{M_0}{T_1} \tag{1.19}$$

$$\frac{dM_z(t)}{dt} = -\frac{1}{T_1}M_z(t) + \frac{M_0}{T_1} \tag{1.20}$$

$$M_z(t) - M_0 = \frac{1}{T_1}\big(M_z(0) - M_0\big)e^{\frac{-t}{T_1}} \tag{1.21}$$

$$M_z(t) = M_0\big(1 - e^{\frac{-t}{T_1}}\big) + M_z(0)e^{\frac{-t}{T_1}} \tag{1.22}$$

After 90^o pulse the equation 1.18 becomes equation 1.23 which represented the recovery of the $M_z(t)$ component, Fig. 1.5(a) shows this recovery configuration with a scan time (t). The basic physical concept of this process involves the protons losing their energy to

the surrounding lattice characterised by spin-lattice and the lattice means to the physical surrounding the nucleus [11].

$$M_z(t) = M_0\left(1 - e^{-t/T_1}\right) \tag{1.23}$$

The transverse components of magnetisation return to their initial thermal equilibrium value

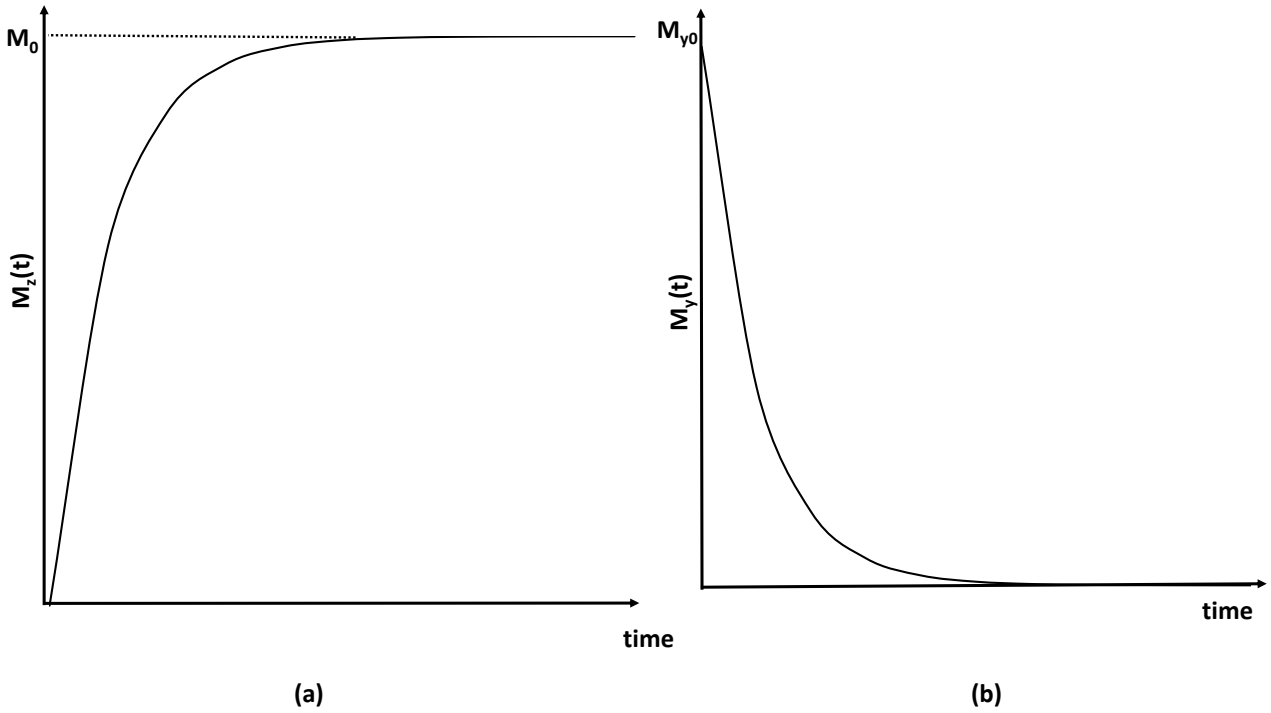

Fig. 1.5 Nucleus spin in volume. (a) A recovery of the parallel component. (b) A decay of the transverse components

which is to equal zero after a constant time termed the 'spin-spin time', T_2. Fig. 1.5(b) shows this relaxation of the M_y components toward the value of zero. The decay of the transverse components can be governed by 1.24 [2].

$$M_{xy}(t) = M_{xy}(0)\left(e^{-t/T_2}\right) \tag{1.24}$$

where $M_{xy}(0)$ is the initial value of the transverse components immediately after B_1 pulse. For simplification of equation 1.24, if a B_1 pulse of arbitrary flip angle is applied along the x-axis, then there are no M_x components. Following this assumption the $M_{xy}(0) = M_0 sin\alpha$ as shown in Fig. 1.4(d), and the equation 1.24 can be described by 1.25 [3, 12].

$$M_y(t) = M_0 sin\alpha\left(e^{-t/T_2}\right) \tag{1.25}$$

1.2.3 MRI Magnetic fields

As mentioned above, the MRI scanner contains three different magnetic fields types which include a homogeneous fixed magnetic flux density B_0, a radio frequency magnetic flux density B_1, a spatial magnetic field (gradient field) the MRI settings and image parameters. This section describes these three magnetic fields categories as shown in Fig. 1.6 [8].

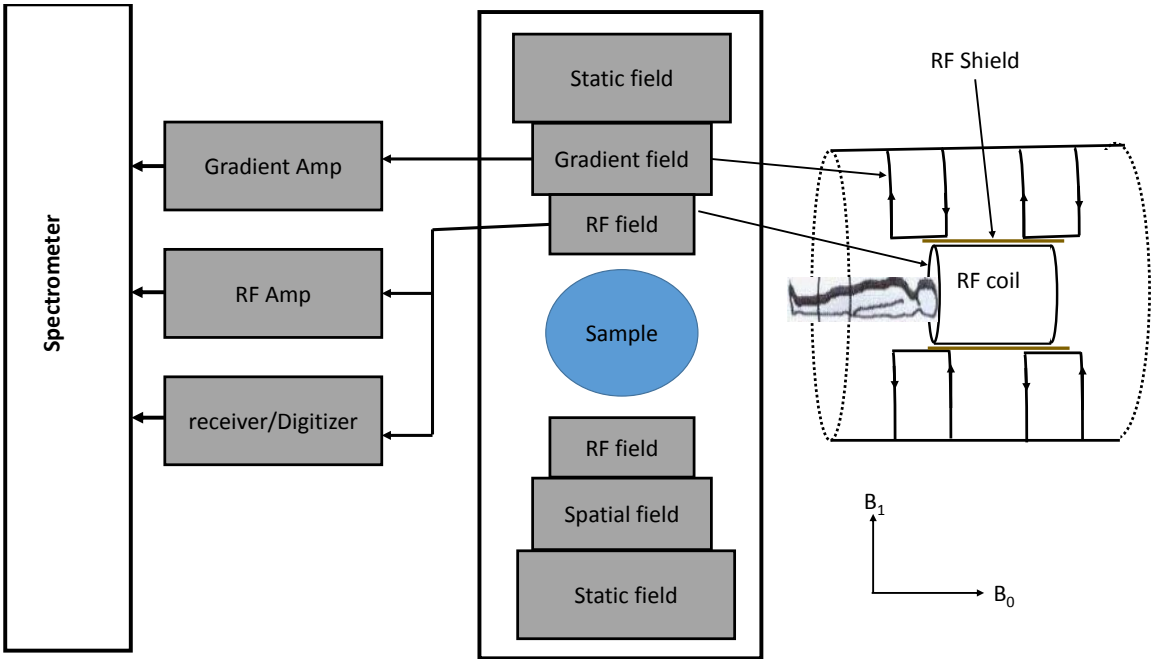

Fig. 1.6 Schematic diagram of MRI system

The MRI static magnetic field

The purpose of a static magnet field is to generate a strong ,homogeneous, and stable magnetic field [13]. A strong magnetic field increases the magnetisation as described by equation 1.15 which leads to increase in strength of the MRI signal as shown in equation 1.17. A homogeneous magnetic field reduces the phase coherent phenomenon, and stability is needed to avoid artifacts into MRI images [3]. In MRI systems there are three kind of magnet, which include permanent, resistive, and superconducting [2]. A permanent magnet is constructed from ferromagnetic materials and this magnet has advantages of relatively low cost because there is no additional requirement needed; such as electrical energy, or cooling devices. It has a sufficient image quality for many examinations. However, it has disadvantages, for example, its weight and sensitivity to temperature; a field homogeneity requires high

temperature stability, limited field strength which leads to limited SNR. Also, the system cannot be switched on or off.

In a resistive magnet, the magnetic field is produced by the passage of a constant current through a conductor, for example copper. The strength of this field is proportional to the value of the current. The high current can produce high field, however, the amount of power dissipated in the wires is increased because it is directly proportional to the wire's resistance and the square of the current. Because the power is dissipated as heat, the need for cooling the conductors is the main disadvantage. This limits the field strength which results in limited value of SNR. However, this system can be switched off which is an advantage in terms of safety. The solution to the heating problem is to minimise the conductor's resistance by using the method of superconductivity. The superconductive means the resistance of many conductors becomes very low (up to zero) at low temperature for example conductors made from niobium-titanium. The basic superconducting magnets implementation includes a double cooling system using liquids such as Helium and Nitrogen. The critical value of the system temperature between 4 to 10K or -263^o and -269^o. Since the conductor resistance is very small under this conduction a high current can pass through the coil, and an extremely magnetic field can be generated. Table1.2 describes a summary of advantages and disadvantages of these three types of MRI magnetic system [4, 14, 15].

Table 1.2 Advantages and disadvantages of MRI magnetic types

Magnetic type	**Maximum field strength**	**Advantages**	**Disadvantages**
Permanent	0.4T	No additional requirement; Relatively low cost sufficient image quality for many examinations.	Large weight 5-30 tones Sensitive to temperature System cannot be switched off Limited field strength limited SNR
Resistive	0.5T	Easy installation System can be switched off	Limited field strength Limited SNR High electric power consumption
Superconducting	1.5T, or higher	High field strength High SNR Relatively homogeneous field	High cost Special sites necessary System cannot be switched off

Spatial magnetic field (Gradient coils)

Typically, an MRI system needs a method that spatially differentiates MR signals because in medical imaging, specialists would like to take images of the body at specific positions [8]. In order to create a spatial variation in the MRI image, three spatial fields are required. A gradient is a change in magnetic field in a specific direction and for most modern imaging schemes it can be generated in any of three dimensions by three gradient coils. The gradient coils are denoted G_x, G_y, G_z present inside the B_0 to produce changes in the main magnetic field in the x, y, and z directions of the magnetic fields [12]. In an MRI system only z-components interact with the proton's magnetic moments. Due to this, only the spatial variation in the z component is required because B_z components vary linearly with position. The spatial variation of z components in the x, y, and z directions can be characterised by 1.26,and 1.27. By controlling the amount of current passing through the coils, the strength of the gradient fields can be changed [12].

$$\frac{dB_z}{dz} = G_z \quad \frac{dB_z}{dy} = G_y \quad \frac{dB_z}{dx} = G_x \tag{1.26}$$

$$G = G_x\hat{X} + G_y\hat{Y} + G_z\hat{Z} \tag{1.27}$$

where G is the gradient amplitude and has a unit mT/m. The MRI gradient coils are designed such that there is no change of the magnetic field at the isocentre ($x = y = z = 0$) of the magnetic. This means that the magnetic flux density at this point is equal to B_0. Fig. 1.7 and equation 1.28 describe the spatial position changing with respect to the r, where r is the three dimension vector of $r = x\hat{X} + y\hat{Y} + z\hat{Z}$ and $\hat{X}, \hat{Y}$ and $\hat{Z}$ are unit vectors in directions of the x, y and z axes, respectively. The $B(r) = B_0$ at the position of $r = 0$, however, at all other positions $r < 0$ the value of $B(r) < B_0$, while at $r > 0$, the value of $B(r) > B_0$ [2].

$$B(r) = (B_0 + r.G_r) \tag{1.28}$$

The corresponding frame precessing frequency ω_r of the protons becomes a function of their position in r and given by 1.29 [3].

$$\omega_0(r) = \gamma(B_0 + r.G_r) \tag{1.29}$$

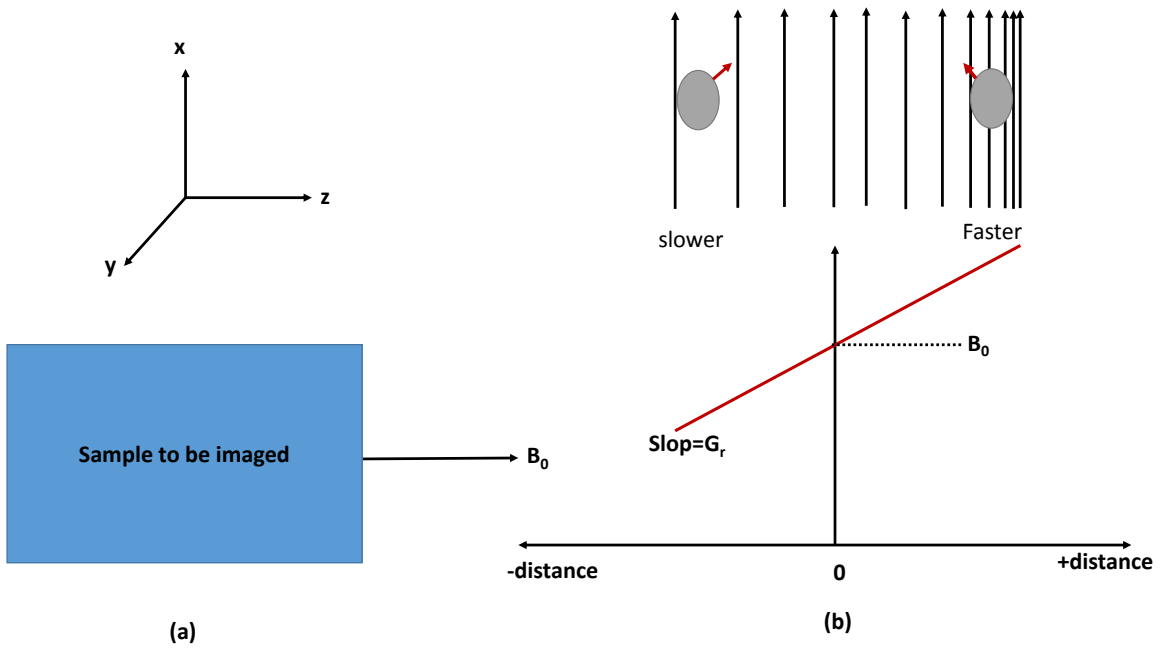

Fig. 1.7 (a). MRI coordinate system. (b). A linear magnetic field gradient applied in the r direction, the new precession frequency $B_0 + G_r$ depends upon position

In the precessing reference proton frame, which rotates in the z-axis, the precessional frequency is given by 1.30 [3].

$$\omega_0(z) = \gamma(B_0 + z.G_z) \tag{1.30}$$

The image process formulation can be divided into three components slice selection, phase encoding and frequency encoding, which are covered in the following section.

1.2.4 Slice selection, phase encoding, a frequency encoding and k-Space formalism

Slice selection

Slice selection can be achieved by using spatially selective RF pulse'. This pulse is applied at the same time with one gradient magnetic field and it is denoted by G_{ss}. The slice selection, including coronal, axial and sagittal slices can be accomplished by selecting the x, z, or y direction, respectively, as shown in Fig. 1.8 [2]. The frequency selective pulse is applied at frequency ω_s, within the RF existent bandwidth $\pm\Delta\omega_s$, [12]. The protons precessing at frequencies inside the bandwidth are rotated into the xy-plane. The slice thickness, denoted

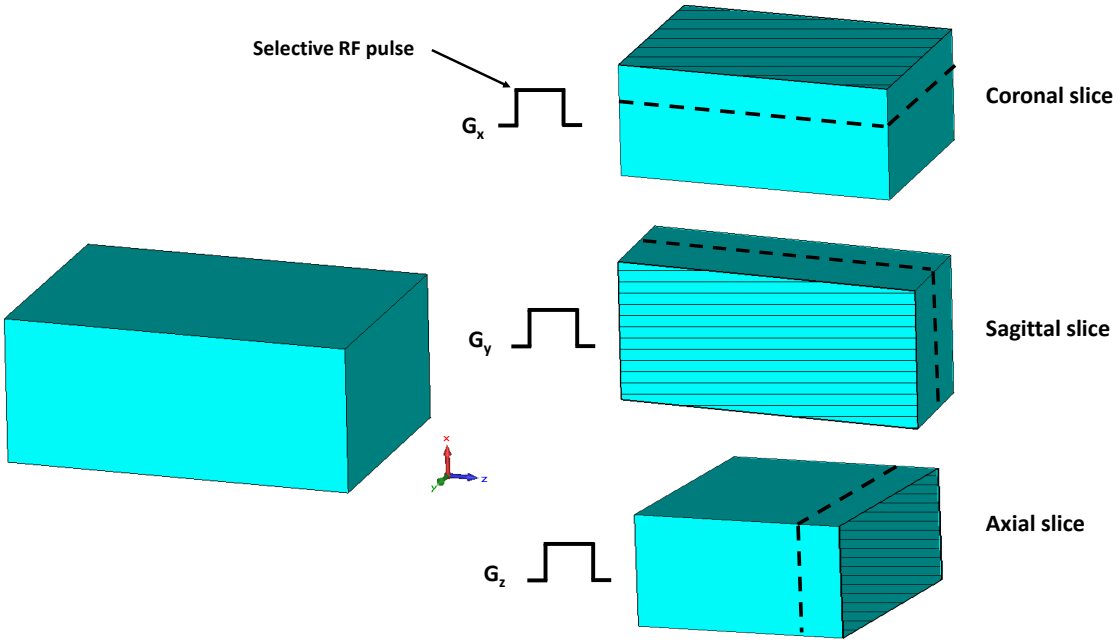

Fig. 1.8 Schematic diagram of MRI slice selection using a frequency selective pulse in x,z, and y gradient, a coronal, axial and sagittal can be selected

by T_s is characterised by 1.31 [12]. Fig. 1.9 shows the relationship between the strength of the G_{ss} and the frequency bandwidth of the selection pulse. It can be seen that T_s can be increased by decreasing the strength of G_{ss} or increasing the frequency bandwidth of the applied RF pulse[3].

$$T_s = \frac{2\Delta\omega_s}{\gamma G_{ss}} \tag{1.31}$$

Phase Encoding

The above section has described the method which is used to select the slices. After the slice is selected, the other two dimensions have to be encoded to generate a two dimensional image. There are two more ways to encode the signal : phase encode, and frequency encode. One direction of the signal, from the precessing protons, is encoded by applying a spatially dependent phase. This can be achieved by applying a gradient G_P for a period of time τ_P which is switched off before data acquisition starts [12]. Fig . 1.10(a) illustrates the basic image sequence of the image phase and frequency encoded gradient. A slice selection is applied simultaneously to the 90^o excitation pulse. If phase encoded is applied at the y-direction of data, the protons precess at a frequency $\omega_y = \gamma(B_0 + yG_y)$, then the phase

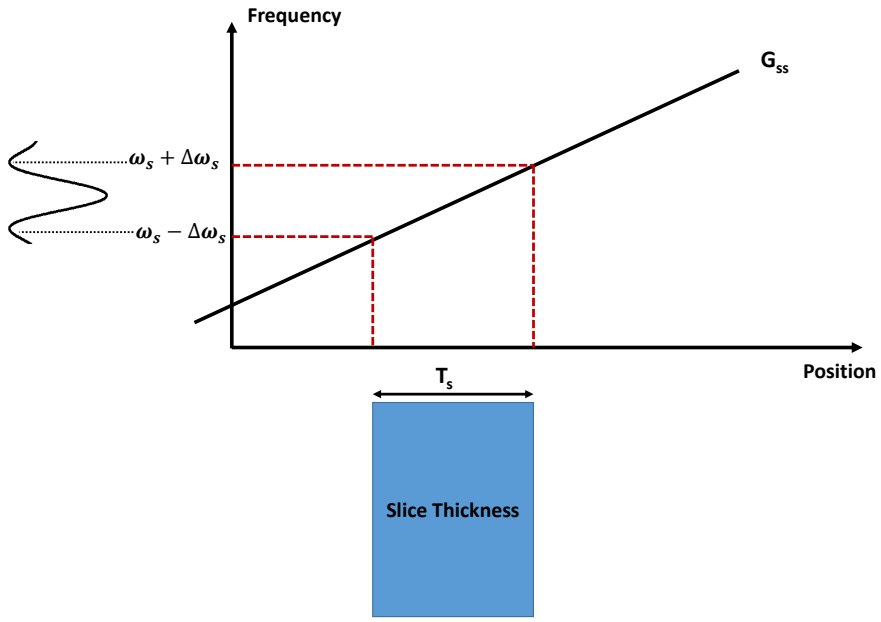

Fig. 1.9 The relationship between G_{ss} and slice thickness of the image

encoded produces a spatially depended phase, denoted by $\phi_p(G_y, \tau_P)$ into acquired signal, with value is given by 1.32 [3].

$$\phi_p(G_y, \tau_P) = \gamma(B_0 + y.G_y)\tau_P \tag{1.32}$$

The total signal after applying the phase encoded of the MRI signal, from exited slice, is denoted by $S(G_y, \tau_P)$ and given by 1.33 [3].

$$S(G_y, \tau_P) = \int \rho(y) e^{-j\gamma(B_0 + y.G_y)\tau_P} dy \tag{1.33}$$

where $\rho(y)$ is the proton density, (i.e) the number of protons at a position (y).

Frequency Encoding

Frequency encoding is created by applying a spatially gradient dependent frequency in another direction aligned to the phase and slice encode gradients, during the data acquisition [12]. If the direction of the frequency gradient, donated by G_f, in the x-direction, and only frequency encoded is assumed to be considered, the signal is given by 1.34 [3].

$$S(G_x, t) \propto \int \int \rho(x, y) e^{-j\omega_x t} dx dy \tag{1.34}$$

The combined signal after frequency and phase encoding, therefore is given by 1.35

$$S(G_x,t,G_y,\tau_P) \propto \int\int \rho(x,y)e^{-j\omega_x t}e^{-j(y.G_y)\tau_P}dxdy \tag{1.35}$$

k-space

After phase and frequency encoded are applied, a raw data matrix is filled of reciprocal image data, which is denoted k-space. The k-space is created by two variables, k_x and k_y, both of which represent the number of data points in k-space as shown in Fig. 1.10(b), where y and x are the phase and frequency encoding directions respectively. k_x and k_y can be characterised by 1.36 [3].

$$k_x = \frac{\gamma}{2\pi}G_x t \quad k_y = \frac{\gamma}{2\pi}G_y \tau_P \tag{1.36}$$

When the G_f is switched on, the first line of k-space is filled. The second line in k-space corresponds to the next value of the G_P. This process is repeated for different values of G_P as shown in Fig. 1.10(a) (dashed lines) and so on until all k-space lines are completed. The spaces between data points in the k-space are dictated by the required field of view, (FOV) of the image. The FOV is given by 1.37 in the x and y directions [12]. Fig 1.11 shows the final step to create the MRI image from the acquired k-space data by applying a Fourier transform.

$$FOV_x = \frac{1}{\Delta k_x} \quad FOV_y = \frac{1}{\Delta k_y} \tag{1.37}$$

1.2.5 MRI radio frequency (RF) coils

Radio frequency coils are used to produce a magnetic flux density B_1, which flips the net magnetisation vector from longitudinal direction to transverse direction by a flip angle. The B_1 must be applied antiparrallel and perpendicular to the main magnetic field at the Larmor frequency as shown in Fig 1.4(a). B_1 can be decomposed into three components including the parallel component B_{1z} at the longitudinal and two transverse components at xy-plane. For a transmit side it is referred as B_1^+ and for the recievier side, it is denoted by B_1^-. The terms of B_1^+ and B_1^- are defined in 1.38 and 1.39 assuming $B_0$is aligned along the z-axis.

$$B_1^+ = \left(\frac{B_x + jB_y}{2}\right) \tag{1.38}$$

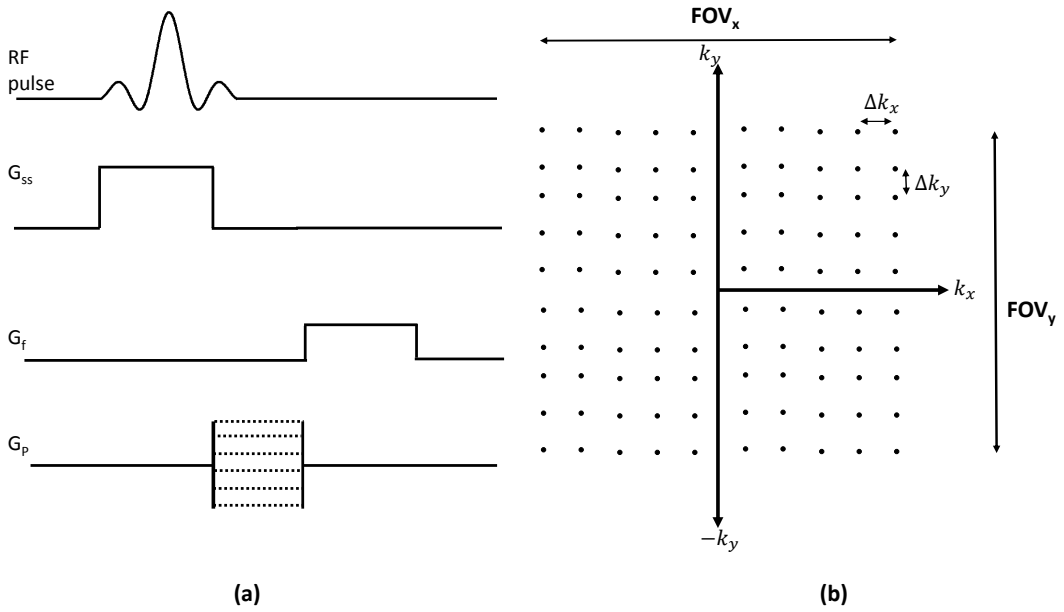

Fig. 1.10 (a). The basic principles of the image phase and frequency encoded gradient. (b). The k-space formalisation of the image

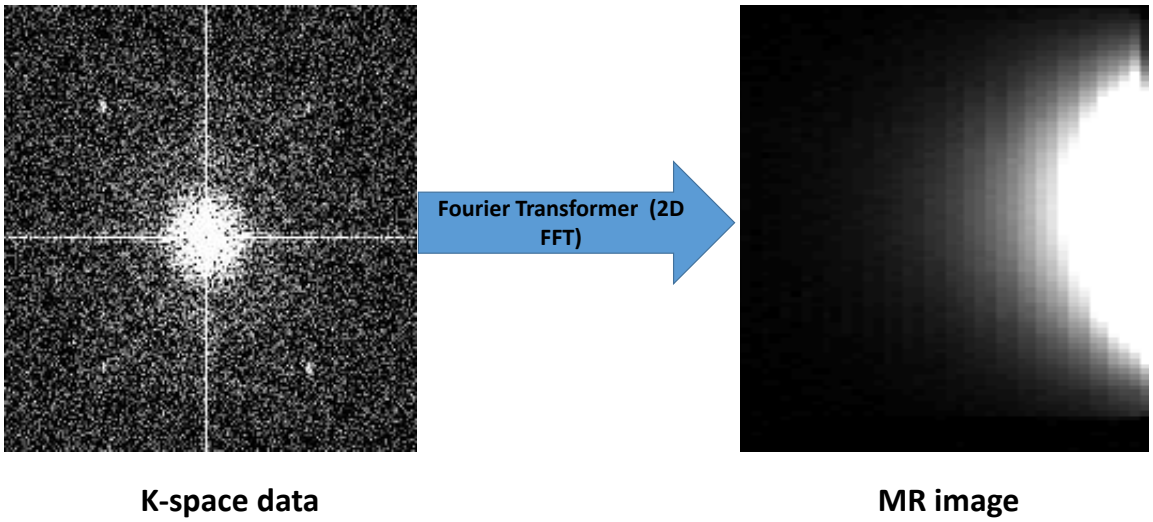

Fig. 1.11 The acquired k-space data is transformed by a 2D Fourier transform to create the final MRI image

$$B_1^- = \left(\frac{B_x - jB_y}{2}\right)^* \tag{1.39}$$

The RF coils can be constructed in different shapes and types for imaging different parts of a sample [1]. Examples of RF coils types for imaging different body parts are shown in Fig. 1.12. The volume coil, shown in (a),termed 'birdcage', is designed to generate a spatially uniform magnetic field over the entire sample to be imaged. Typically it is used for abdominal, brain, and knee investigation studies [16]. The second type of the RF coil is a surface coil, shown in (b) designed to image parts at the surface of the body with high sensitivity [12]. The third type is the phased array, shown in (c) consisting of a series of surface coils. The phased array has advantage of the high sensitivity of a small coil; by using a number of surface coils the FOV can be extended. However, phase of array coils need a more complex system than the other type requiring multiple receiver channels, one for each surface coil.

In this thesis the basic surface coil is used. The next section will describe this coil in more details.

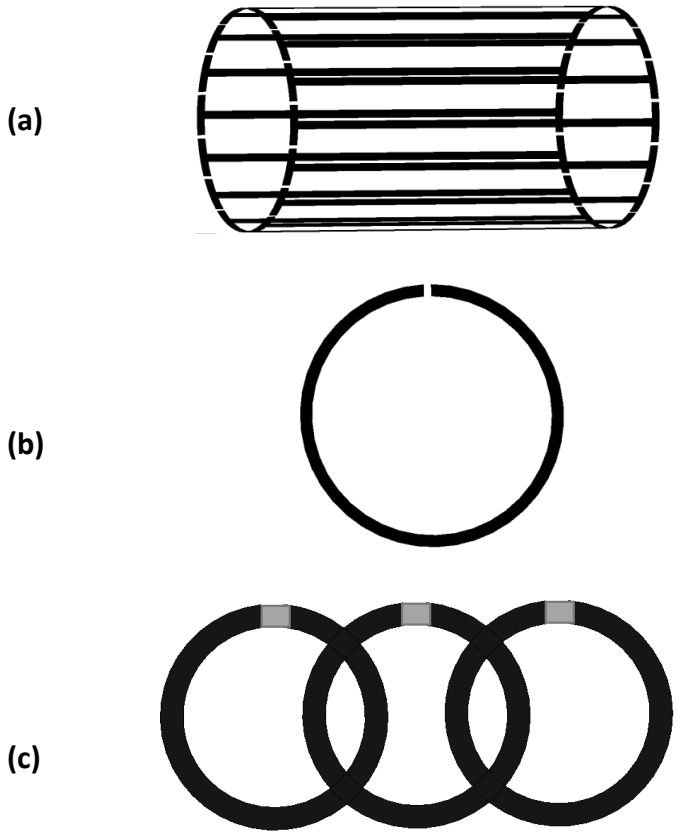

Fig. 1.12 Three RF coils used for MRI (a). Volume coil (birdcage) coil. (b). Surface coil. (c) Phased array coil.

RF surface coils design and specification

There are many shape geometries which can be used as surface coils. A selection of the most common, which include rectangular and circular loop coils shape types, are illustrated in Fig. 1.13. The RF coils have to be large enough to give acceptable RF magnetic field strength inside the (ROI) and achieve the desired penetration depth, denoted by (P_d), however if the RF coils are larger than the optimum size, they are more sensitive to thermal noise from the large part of the sample to be imaged causing to a reduction in SNR [17]. If the direction of

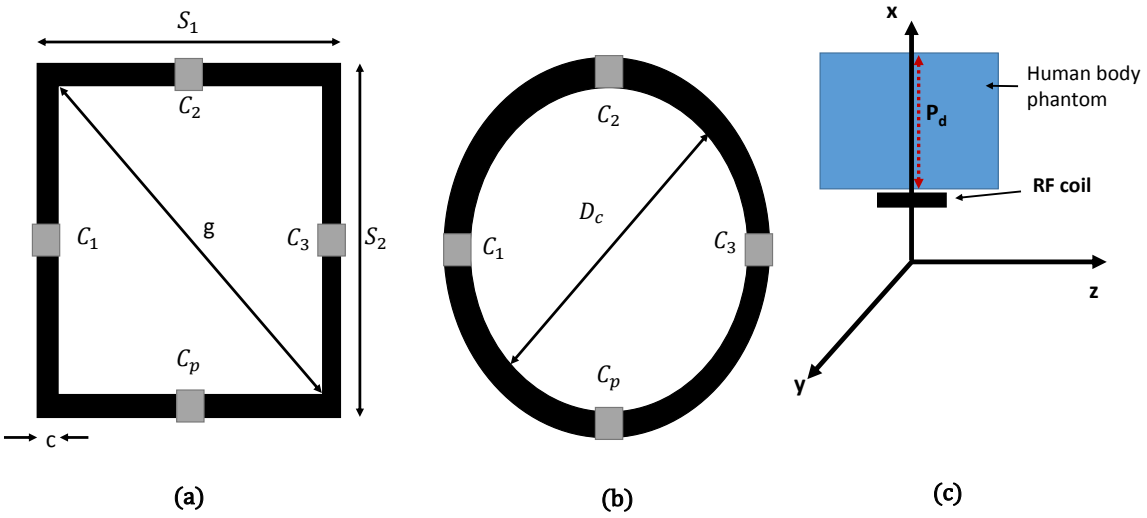

Fig. 1.13 Block diagram of the RF coil. (a). Rectangular loop coil. (b) Circular coil. (c). The relationship between magnetic field, generated by RF coil and the penetration depth inside the body phantom P_d at the coil centre

the RF coil is assumed to be coaxial to the x-axis, as shown on 1.13(c), the magnetic flux density of a circular loop coil and rectangular loop coil geometry can be characterised by 1.40 and 1.41, respectively[18].

$$B_x = \frac{(0.5D_c)^2 I\mu_0}{\sqrt{((0.5D_c)^2 + P_d^2)^3}} \tag{1.40}$$

where D_c is the circular coil diameter, I is an electric current passing the coil, μ_0 is the magnetic permeability of the freespace and P_d is the penetration depth along the x-axis.

$$B_x = \frac{2S_1S_2I\mu_0}{\sqrt{(S_1^2+S_2^2+4P_d^2)}} \times \left(\frac{1}{S_1^2+4P_d^2}+\frac{1}{S_2^2+4P_d^2}\right) \tag{1.41}$$

where S_1, and S_2 are the rectangle coil sides.

In the RF loop coil design, the inductance and capacitance are calculated to determine the RF loop coil resonance frequency (Larmor frequency). In order to determine the capacitance values necessary to resonate the RF coil at the Larmor frequency, the first step is to calculate the inductance of the RF loop coil based on Equation 1.42 for a rectangular coil [19] and the resulting inductance (L) is in nH when all dimensions in the equation 1.42 are in mm.

$$L = \begin{array}{l} 0.921\left[(S_1+S_2)\log\left(\frac{2S_1S_2}{b+c}\right)-S_1\log(S_1+g)-S_2\log(S_2+g)\right] \\ +0.4\left[2g-\frac{S_1+S_2}{2}+0.447(b+c)\right] \end{array} \tag{1.42}$$

where g is the diagonal, b the strip bar thickness and c the rectangular strip bar width.

The RF coil capacitor can be achieved by Equation 1.43. Capacitors distributed in Figure 1.13(a and b) $(C_1, C_2, C_3, and C_p)$ are used to reduce radiation loss in the coil. Another reason for using several capacitors in series in RF coil design is in order to reduce each segment length of the coil segments. Based on the literature review the segment length should have a length less than $\frac{\lambda}{10}$ at Larmor frequency to ensure that phase shift along the conductive element of the coil is kept to a minimum [20, 21], and C_p used for the matching purpose.

$$\frac{1}{C_T} = \Sigma\frac{1}{C_{si}} \tag{1.43}$$

where C_T is a total capacitor, C_S a sectional capacitor and $i = 1, 2, ..n$. The loop coil inductance and the required capacitance are calculated by equations 1.42, and 1.43, respectively. The resonance frequency of the RF coil can be calculated by 1.44:

$$\omega_0 = \frac{1}{LC_T} \tag{1.44}$$

More information about RF coil engineering such as Q-factor and BALUNs circuit are described in the Appendix B2.

1.2.6 Parameters of MR image quality

Magnetic Resonance image quality depends on a number of parameters, for instance spatial resolution, contrast resolution, signal to noise and scan time. The imaging spatial resolution is the feature visualisation in the MR systems. The spatial resolution performance metrics include field of view, slice thickness, and k-space matrix size or bandwidth per pixels. Another key factor which affects the MR image quality is a signal to noise, which provides a ratio of MR signal received from the tissue of the patient being imaged to the background noise. The third factor is a contrast resolution which looks at differences in adjacent areas in signal intensities from tissues being imaged. These parameters will discussed in this section.

MRI spatial resolution

In an MR image the spatial resolution depends on a specific imaging sequence used to produce the imaging data. The spatial resolution is generally different in three spatial dimensions. In a phase and a frequency encoded dimension, three factors affect the spatial resolution: data truncation, a relaxation time meaning relaxation during the data acquired and digital resolution. Assuming all other parameters are constant, raising number of phase or number of frequency encode samples leads to enhancing the spatial resolution [22], however, increasing the frequency and phase encoding points leads to increasing the k-space matrix size, which may need extra data storage memory. In slice selection dimension, the spatial resolution is a function to the frequency response of the RF pulse of the slice selection. Also,according to equation (1.32) SNR decreases as a voxel size decrease, this can affect the system performance. [22, 23].

The MRI image contrast

MR signal is proportional to the amount of protons in the body, and the image signal created is mainly a map of the signal intensity of the water. Since the water concentration varies from one part to another part and depends on the tissue type, the image contrast is altered in the intensity regions of an image, where any signal having bright pixels means high signal intensity and dark signal means low signal intensity. For example, the signal intensity varies from the brain, which is high in water concentration, to the bone which is low in water concentration. Basic image contrast is affected by the amplitude and timing of the RF pulses used to excite the spin system. For a more in-depth description of the spatial resolution and the image contrast, the reader is referred to standard MRI textbooks [1, 2, 10, 24].

The signal to noise ratio (SNR)of MRI surface coils

SNR is an important metric used to present the performance of an image created by magnetic resonance systems and determined by the sensitivity of an RF coil to the biological sample. The SNR is proportional to the ratio of the induced FID signal to the root mean square of the thermal noise voltage at the coil terminal and the sample [25, 26]. In [27], the authors investigated an analytical solution of the SNR for RF surface coils used in MRI applications. They assumed a B_1 generated by the RF coil carrying a current I for the sample to be imaged of volume V. Thus, the the signal strength at the xy-plane can be calculated by equation 1.45 [28].

$$\zeta = \frac{-j2\omega_0 M_0 sin(\alpha) B_1^+}{I|B_1^+|} \left(B_1^-\right)^* \tag{1.45}$$

where $\omega_0 = 2\pi f_0$, f_0 is a Larmor frequency, asterisk denotes the complex conjugate and $\alpha = \gamma \tau_{B_1^+} |B_1^+|$. Noise in magnetic resonance signal arises from thermal fluctuations in the electronic noise in the RF coil and preamplifiers[29]. The amount of noise present is given by equation 1.46

$$V_n = \sqrt{4FKTR\Delta f} \tag{1.46}$$

where F is a noise figure of the preamplifiers, R is a resistance of RF coil and the sample to be imaged as given by $R = R_{coil} + R_{sample}$, Δf is the receiver bandwidth in (Hz) and T is the probe temperature. The general form of SNR in the MRI can be calculated via Equation 1.47 by applying the Equations 1.45 and 1.46 .

$$SNR = \frac{-j2\omega_0 M_0 sin(\alpha) B_1^+}{I|B_1^+|\sqrt{8FKTR\Delta f}} \left(B_1^-\right)^* \tag{1.47}$$

By substituting the $\alpha = 90^\circ$ in Equation 1.47 the signal-to-noise-ratio (SNR) of the MRI only receiver can be estimated by 1.48, [30].

$$SNR = \frac{\zeta}{\sqrt{2V_n}} = \frac{-j2\omega_0 M_0 \frac{B_1^+}{|B_1^+|} \left(B_1^-\right)^*}{I\sqrt{8FKTR\Delta f}} \Rightarrow |SNR| = \frac{\omega_0 M_0 |\left(B_1^-\right)^*|}{I\sqrt{2FKTR\Delta f}} \tag{1.48}$$

The SNR can be estimated as a function of system dissipated power by substituting equation (1.49) in (1.48) and the final formula is given by 1.50[31]

$$P_L = I^2 R \tag{1.49}$$

where P_L is the dissipated power through the system resistance R.

$$|SNR| = \frac{\omega_0 M_0 |\left(B_1^-\right)^*|}{\sqrt{2FkTP_L\Delta f}} \tag{1.50}$$

In such a way that increasing the B_1-flux density can increase SNR if other factors are constant, which is the focus of this thesis. In experimental methods, several approaches have been published to measure the SNR of the image generated by the MRI system such as the difference method [30], and the two regions method. The most common method is the two regions method, the basic concept of this approach is analysis of the signal statistics in two different locations (ROI) from the image intensity signal: one in the high intensity region which represents the tissue and another region in the image background to determine the noise intensity signal. SNR can be calculated by Equation 1.51. [32, 33].

$$SNR = \frac{S(r)}{\sqrt{2}\sigma_{stdv}} \tag{1.51}$$

where $S(r)$ is an image intensity and σ_{stdv} is the standard deviation of the image background.

Chapter 2

Literature Review

2.1 Introduction

The literature review presents a broad review of the research carried out in the field of RF surface coil sensitivity enhancement via increased the radio frequency magnetic flux density (B_1) which leads to improving the MRI image quality. As mentioned in the previous chapter, the MRI image quality depends on the spatial resolution, image contrast and SNR. The SNR is a widely accepted parameter to measure an RF coil performance and it is a function of an induced MR signal intensity and a magnetic flux density B_1 created by the RF coil [2]. The approaches which can be used to enhance the SNR of the RF coil for the MRI are shown in Fig. 2.1 and these can be summarised as follows;

• Increasing the static magnetic flux density B_0, such as 3T, 7T, and 9.4T.
• Improving the quality factor by electronic circuit design.
• Improving the radio frequency magnetic flux density (B_1).

Although the strength of the MR signal is proportional to the static magnetic field and the nuclear net magnetisation of the MR system [2], increasing the static magnetic field can enhance the sytem SNR [1], which can improve the image intensity. However, a high static magnetic field needs a high Larmor frequency of the applied RF pulse in order to achieve the transverse configuration. A high resonance frequency of the nuclei leads to further challenges in the factors of an image quality; for instance, it can lead to inhomogeneities of the RF magnetic flux density, B_1 [4]. Another challenge of increasing the Larmor frequency is a rise in human tissue temperature due to high RF field specific absorption rate, while these challenges are negligible at low magnetic field system such as 1.5T [1, 4]. These are some reasons which motivated many researches to be carried out for different approaches of improving image quality without the need to increase the static magnetic field. Many

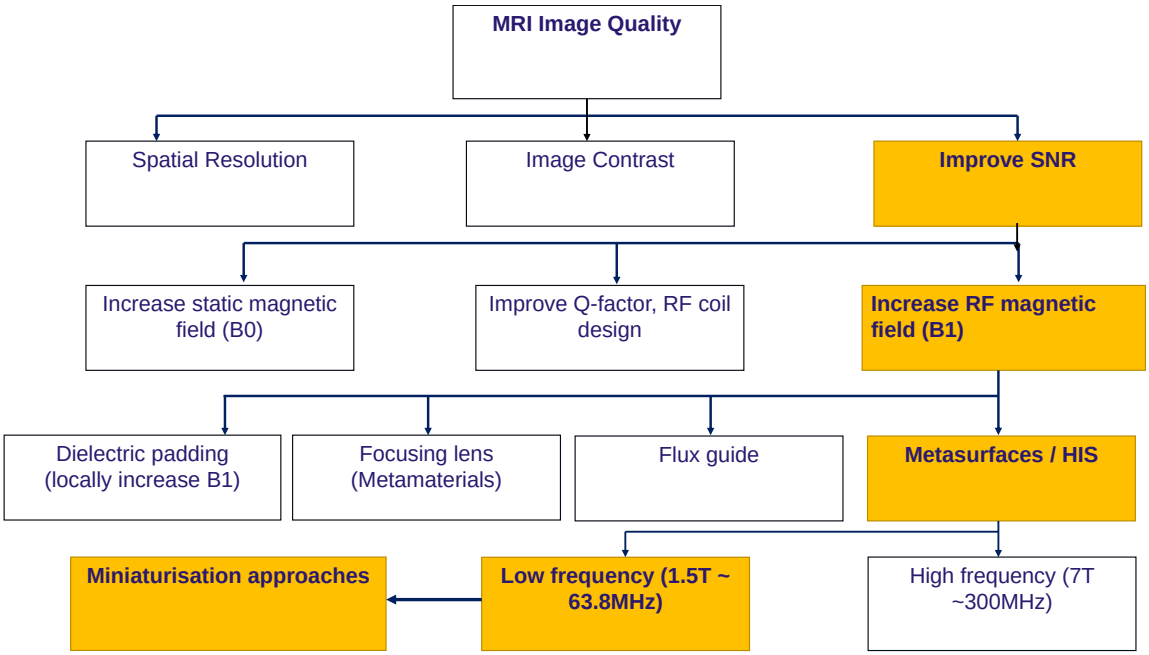

Fig. 2.1 Overview of MRI research topics

different approaches based on metamaterial structures have been published in order to improve MRI system performance for low B_0. In recent research the approaches used to improve the RF magnetic field are categorised as follows; a metamaterial method: many studies have illustrated proof of implementation of this method in MRI applications using focusing lens such as capacitively loaded metallic rings (CLRs) [34]; a Swiss roll [35]; a wired medium [36]; magnatoindictive flux guide [34] and a high impedance surface [37]. Since the majority of MRI scanners operate over a frequency band 40-400MHz, the main challenge of successfully applying a metamaterial in a real application, such as an MRI environment, is the physical size of the unit cell which lies in the tens of centimetre range. This is obvious because the majority of these structures are based on three dimensional devices which aim to reduce the physical dimensions of these structure. Another different approach is high dielectric constant materials which have proved useful for locally improving the signal to noise ratio and reducing the specific absorption rate for many MRI applications. However, due to the physical size the utilisation of such devices in real applications is limited. A potential solution to this problem is to design flexible, a thin metasurface which can be implemented with an MRI scanner. Our objective in this research, is to design thin, flexible metasurfaces to improve the B_1 at frequencies of (60-130) MHz, representative of clinical MRI system.

2.1.1 Background of metamaterial and metasurface

The term 'metamaterial' is used to represent composite materials with unique properties and useful features. One of the most improtant features of metamaterial is a negative refraction index ($n = -1$) [38], which could result in many numbers of application such as a perfect lens [39]. The perfect lens is a medium with both negative permeability ($\mu < 0$) and permittivity ($\varepsilon < 0$) in the same specific frequency range, that would possess certain features, not observed in natural materials such as focusing the magnetic field at specific region.

In the literature review, it is noticed that based on the metamaterial definition, cannot be referred to as a metasurface if the structure periodicity is not smaller than their freespace wavelength, or if the structure elements are designed in lattice with small gaps between the elements, but the total structure thickness is large. Such as structure array are named a metamaterial [40].

The metasurface can be considered as kind of two dimensional (2-D) textured structure which are built as metal protrusions printed on a dielectric substrate. For simple non-resonant metasurface as patch arrays which acts as a capacitive or aperture elements which acts as inductive are shown in Fig. 2.2 [41]. The capacitive and inductive values can be calculated by averaging the currents flowing on the periodic surface. The derived metasurface impedance is angle dependent and it has different experssions for the TM and the TE polarisation. In the case of a capacitive array, the metasurface impedance can be calculated by equations (2.1) to (2.3) while the impedance of an inductive mesh grids can be calculated by equations (2.4) to (2.6).

$$Z_{patch}^{TM/TE} = \frac{1}{j\omega C_p} \tag{2.1}$$

$$C_p^{TE} = \frac{P\varepsilon_0(\varepsilon_{r1}+\varepsilon_{r2})}{\pi} ln\left(\frac{1}{sin(\frac{\pi w}{2P})}\right)\left(1-\frac{k_0^2 sin^2(\theta)}{2k_{eff}^2}\right) \tag{2.2}$$

$$C_p^{TM} = \frac{P\varepsilon_0(\varepsilon_{r1}+\varepsilon_{r2})}{\pi} ln\left(\frac{1}{sin(\frac{\pi w}{2P})}\right) \tag{2.3}$$

$$Z_{grid}^{TM/TE} = j\omega L_g \tag{2.4}$$

$$L_g^{TM} = \frac{P\mu_0}{\pi} ln\left(\frac{1}{sin(\frac{\pi w}{2P})}\right)\left(1-\frac{k_0^2 sin^2(\theta)}{2k_{eff}^2}\right) \tag{2.5}$$

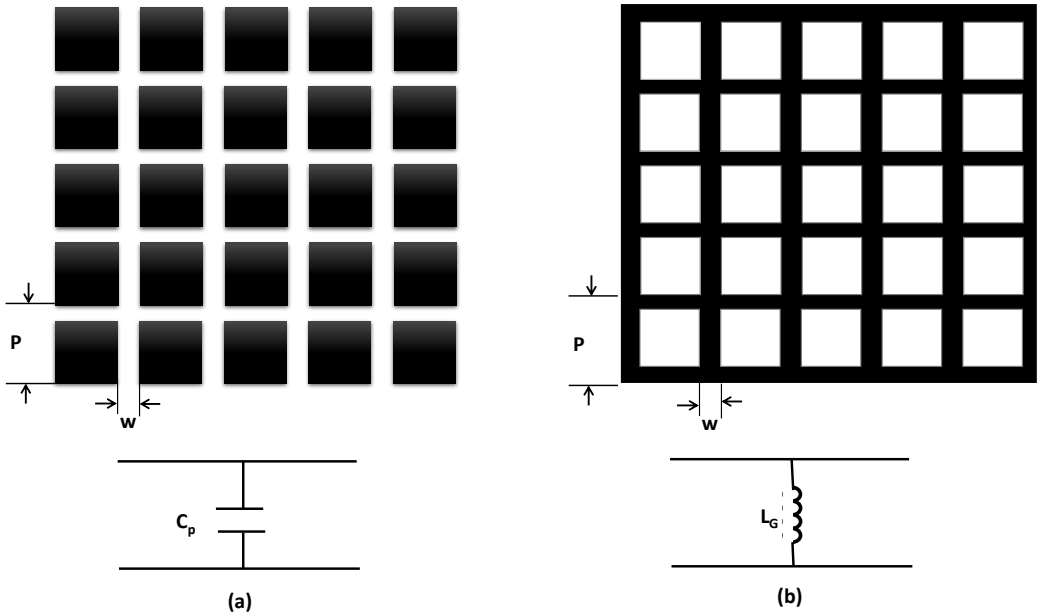

Fig. 2.2 FSS patch and aperture geometries (a) capactive patch array, (b) inductive mesh array

$$L_g^{TE} = \frac{P\mu_0}{\pi} ln\left(\frac{1}{sin(\frac{\pi w}{2P})}\right) \tag{2.6}$$

where P is the surface periodicity, w is the gap between square patches, k_0 is the wave number in the freespace, k_{eff} is the wave number of the incident wave vector in the effective medium, which can be calculated as $k_{eff} = k_0\sqrt{(\varepsilon_{r1}+\varepsilon_{r2})/2}$, θ is the incident wave angle. ε_{r1} and ε_{r2} are the dielectric relative permittivity of the dielectric slabs surround the metasurface [42, 43].

In particular, the 2-D metasurface structure such as frequency selective surface (FSS) has been investigated over the years for different applications in the communication area such as microwave, radar systems and antenna systems. One application of the FSS in a radar system is to reduce the radar cross section (RCS). The FSS was designed in stealth technology for reducing the RCS of antennas at the out-of-band frequencies. The metamaterial surfaces in Radar systems are also used in a circuit analogue absorbed in the radar absorbing material (RAM) for the Stealth technology to provide wider bandwidth and better absorption compared with the traditional RAMs. Filters design, [41], is an important area of the FSS applications. The FSS was used to secure buildings, and was designed to prevent the penetration of external signals inside them by using a metasurface time-varying transmission phase to

impair the external signal [44, 45]. More recently, the FSS structures were used in wireless communication systems, for example to improve the operation of emergency services by preventing the use of mobile phones in public places such as some hospital departments and libraries, by printing the FSS on the wall and the windows of buildings and allowing the emergency calls [46]. Recently, the authors of, [47, 48], have investigated the application of the metasurface for medical application, they studied the effects of using an external metasurface with an implanted microstrip patch antenna.

2.2 Surface coil sensitivity improvement methods using metamaterial

In recent years, there has been a great deal of attention devoted to improve the MRI SNR of surface coils using metamaterial structures. In this section, the methods which have been used to improve the magnetic flux density B_1 and SNR in MRI applications are presented. Improving the B_1 can improve the Signal to Noise ratio (SNR) of the receiving and transmitting of the RF coil, resulting in improved image quality of the MRI techniques without increasing the main magnetic field and Larmor frequency. The metamaterial approaches which have been used to improve the magnetic flux density in MRI application are categorised into three methods in this literature review section: (i) flux guide methods, which include a Swiss roll capacitor and a wire medium, (ii) an RF metamaterial lens, such as split ring lens, and capacitively loaded metallic rings and (iii) a high impedance surface.

2.2.1 Metamaterial as a Radio frequency flux guide

The magnetic resonance imaging techniques use RF coils, either singly or as array coils, to transmit and receive the RF magnetic flux density from regions of interest (ROI). RF flux guides offer possibilities for MRI experiments, to guide the magnetic flux from the regions of interest (ROI) to a surface transmit/receive coil [49]. Parts in the samples that are otherwise hard to access can be reached by inserting flux guide metamaterial devices. These devices are self resonant through their pure inductive and capacitive properties, and one example of such a material is a Swiss roll capacitor, which is described by [35]. The Swiss roll device works as a magnetic field guide [39] based on the existence of a negative permeability which in turns focuses the magnetic evanescent modes [50]. The Swiss Roll capacitor is fabricated by turning a metallic sheet around dielectric cylinder as shown in Fig. 2.3a. The self capacitance can be determined by the permittivity and thickness of dielectric, while the

self inductance is controlled by the number of conductor layers [50]. In [35], the authors derived the capacitance between the first and last turns of the Swiss roll device for ideal material as given in equation (2.7), and the Swiss roll resonance frequency can be calculated by equation (2.8)[50].

$$C = \frac{\varepsilon_0}{d_s(N_s - 1)} = \frac{1}{\mu_0 d_s c_0^2 (N_s - 1)} \tag{2.7}$$

$$\omega_0 = \sqrt{\frac{d_s}{2\pi^2 \varepsilon r_s^3 (N_s - 1)}} \tag{2.8}$$

where C, is the Swiss roll capacitance in (pF), d_s is the insulator thickness between conducting sheets, c_0 is the light speed, N_s is number of turns with radius of r_s and μ_0 is the free space permeability. In the first demonstration of the Swiss roll acting as a flux guide [49], a metamaterial was designed of 19 turns in hexagonal close packed array of 2cm conductor rolls length. This device was formed to operate at 21MHz, which is the operation Larmor frequency of 0.5T MRI scanner. The coupling effects were measured using $S21$ between two short probes, connected by a part of the Swiss roll, as a function of their separation distance. The results have shown that the coupling with the Swiss roll was higher than without it. This result proved that the Swiss roll can act as a flux guiding medium. However, the device tuning was a problem. To overcome it, tuning was carried out by adding a capacitively coupled sleeve that extended beyond the roll, resulting that 1% tuning could be achieved [51]. The metamaterial device is formed by stacking many of these cylinders together and it is placed between the RF coil and the dielectric sample as shown in Fig. 2.3b described by [49]. Reported in[49, 52] , they demonstrated this work within the MRI environment using hand of patient(as an example). The results have shown that by using bundle of Swiss rolls, the image signal intensity can be increased in receiving detector, however without the Swiss rolls no patient hand image can be seen.

Further analysis of the Swiss roll metamaterial devices has shown proof of the theoretical principle by demonstrating a mathematical model of impedance matrix of the Swiss roll device including the loss [53]. Since the MRI applications need more higher frequencies, another type of metamaterial device has been proposed, a wire medium. The wire medium can be designed for higher Larmor frequencies, which was demonstrated at a 3T MRI scanner which operates at 127.6 MHz [36]. The wire medium is made of an array of parallel lattice low-loss wire grids [54]. Fig. 2.4 shows the block diagram of the placing the wire medium between transmitter/receiver RF surface coil applications. The main concept behind the wire medium is to utlize a wire collimator designed of an array of parallel wire, which worked as

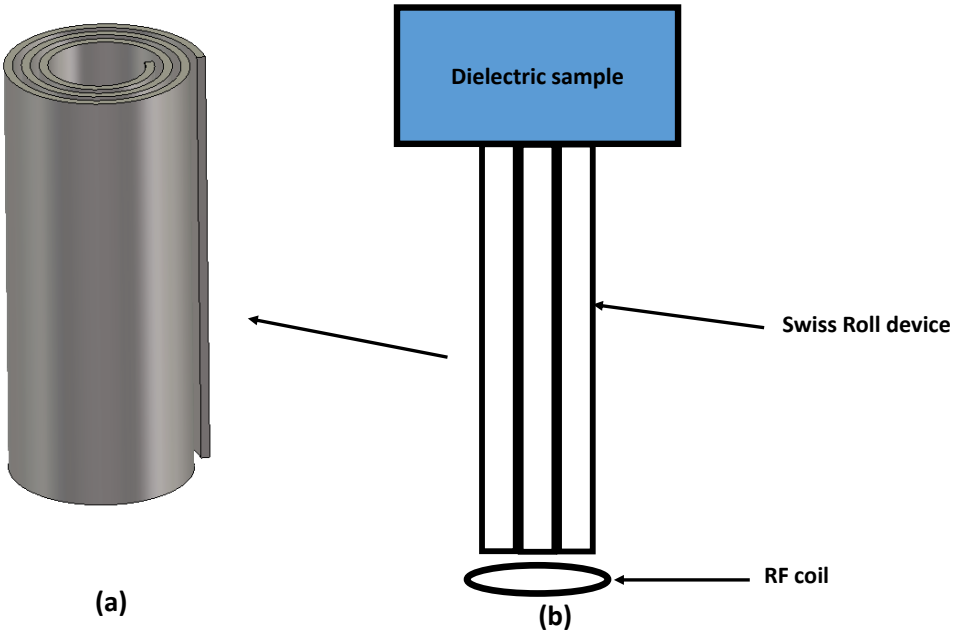

Fig. 2.3 (a). 3D sketch view of the Swiss Roll. (b). Schematic showing configuration Swiss Roll as a flux guide system

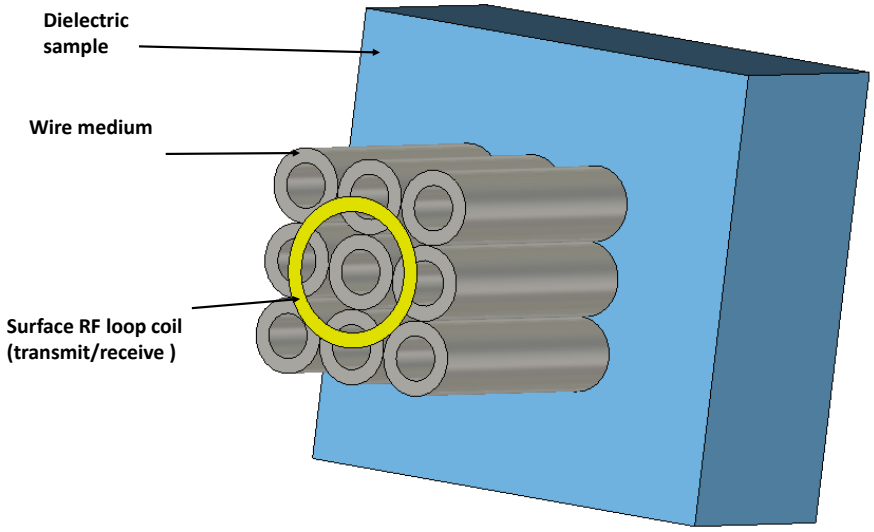

Fig. 2.4 The wire medium system

a resonator. This resonator can transport evanescent waves into propagation waves inside the medium. These wire grids are capable of transmitting the transverse magnetic component (TM) of the source spectum [55], consequently, the normal components of electric field which are along the wire grids, generated by the source on the other side of the medium, can be totally restored [56]. In [36]the authors demonstrated experimentally the ability of a straight wire medium to enhance MR images. A new type of wired medium device has been proposed by [57] and denoted by an endoscope. The endoscope consists of a 20 by 20 array of cylindrical wires with length of 250 mm, the structure periodicity of 10 mm and wire radius of 1 mm. The results from this work experimentally determined that the image was improved when compared to not using the endoscope. However, the implementation of such devices in a real MR system is limited, due to physical size and space in the scanner bore.

2.2.2 Metamaterial Radio frequency lens

Among these methods, which are used at radio frequency received magnetic fields, are metamaterial lenses. The metamaterial lenses were applied to increase signal intensity in RF surface coils for MRI applications. An example of these RF lenses is a split ring lens which was fabricated of a relative small open three-dimension loop of copper which was loaded with non-magnetic capacitor element as shown in Fig. 2.5a, Fig. 2.5b shows the cross section of the lens, which has 5×2 unit cells and Fig. 2.5c shows the lens placed between an RF surface coil and a dielectric phantom. This example of lens was proposed in [58] with dimensions of $27 \times 27 \times 3cm^3$ of the height, width and the thickness respectively, using a three dimensional array of $18 \times 18 \times 2$ cubic cells, the unit cell periodicity was 15 mm. The results of this study have shown better image intensity by using the lens when compared with no lens. The authors of [59], overcame the limitation of the previous work [58], by modeling of the metamaterial lens as a bulk material with an effective permeability extracted from the work reported by [60] and the effects of finite structure has not been considered. This study [59] solved this problem by simulating a full system model which is shown in Fig. 2.5c using a full wave numerical software, and supported by measurements. These measurements were achieved by measuring the transmission coefficient $S21$ between a matched RF coil and a small probe located inside the dielectric phantom at various spaces inside the phantom using network analyzer. The result of the $S21$ was proved by transmission line theory, that the $S21$ is proportional to magnetic flux density B_1 [61]. The fabricated system in this work [59] was demonstrated within the 1.5 T MRI system and the results show that by using such as lenses the SNR of the 1.5T MRI system can be improved. The results have also illustrated that the

best size of the split ring lens to achieve a better enhancement of the SNR of the RF coil was slightly smaller that the RF coil size and these results agreed with the measured SNR by the real MR scanner.

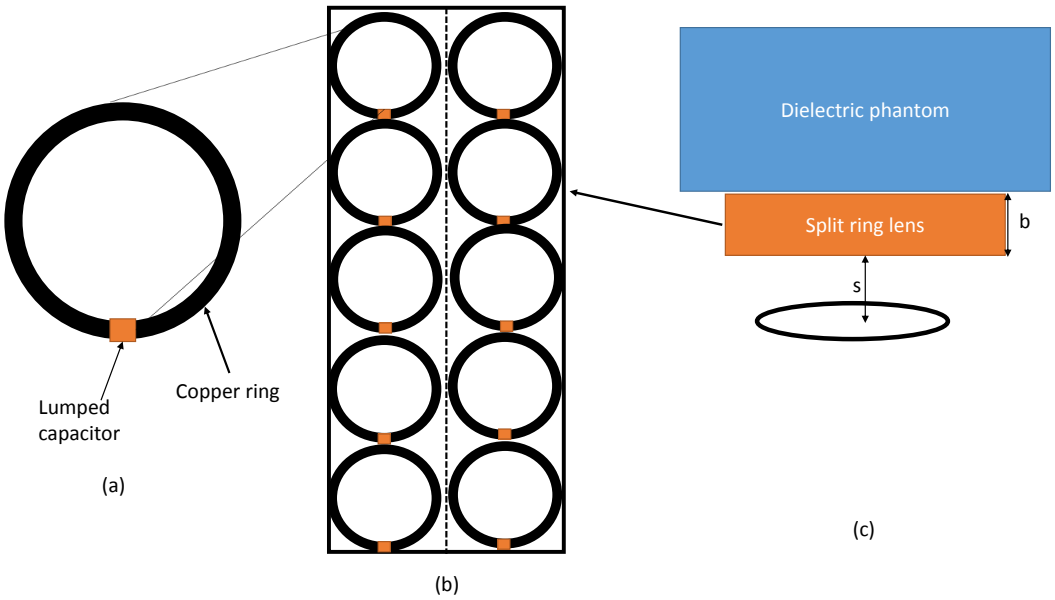

Fig. 2.5 (a). The unit split ring .(b). The side cross sectional of the split ring metamaterial lens. (c). Sketch of the configuration where a RF coil is placed at the *s* distance from the split-ring lens of thickness *b*

Another example of metamaterial lenses is a capacitively loaded metallic rings (CLRs), which was proposed by [34]. This lens has also received much attention because of its ability to create the 3D isotropy arrays when CLRs are designed in a cubic lattice. This is an important feature in providing the 3D image source which is an advantage over other metamaterial devices. The CLR lens can be placed between the surface RF coil and the sample to be imaged. The lens improves the surface coil sensitivity by focusing the magnetic field of the RF coil inside the phantom. In the near field region, the RF magnetic field generated by the RF coil can be decomposed by summation of the Fourier harmonics, these spatial harmonics are evanescent in the region of the far field . The main focusing concept with a metamaterial lens is amplification of these evanescent harmonics inside the lens, which means the far field harmonics can be transferred to the other side of the lens, resulting in focusing the RF magnetic field at a certain location out of the lens inside the phantom. The authors of [62] have investigated the CLR lens in more details in ideal and realistic cases. They reported that the CLR lens slab shows a permeability depending on the frequency and

when an RF coil is located near by the CLR lens, the lens generated an extra impedance in RF coil. In ideal case, the RF coil impedance was not changed, however, in real lens, the RF real impedance (resistance part) was minimised and there was no change in the imaginary part. Based on this fact, the authors of [34] developed an approach of mathematical analysis for the designed metamaterial CLR lens. Therefore, the lens parameters are set to achieve null in the reactance and minimum in the resistance parts at desired frequency. In [34] optimal design for a metamaterial CLR lens was established which minmise the losses produced by the lens, this metamaterial lens was termed as magneto inductive lens (MI lens) , which was simpler than the earlier one that investigated in MHz range [63] and in sub-wavelength imaging [58] which was 2D array of CLRs. The authors in [64] have studied, both experimentally and mathematically, the possibility of using MI lens to improve the SNR of RF surface coil at different Larmor frequencies, which included 0.5T, 1.5T, and 3T. The plot diagram of the configuration under investigation was a MI lens including of two parallel arrays of 6×6 rings as shown in Fig. 2.6 with dimension of $L = 12cm$ of the RF coil separated, $d = 7mm$ distance from the phantom and the two arrays are separated by a distance of h = 11 mm using Rohacell form between them. The experiments and numerical results have shown that, at 0.5T MI lens provided a slightly improvement of the SNR for approxmiatly 11mm depth inside the phantom, however, the SNR was degraded for long penetration depth. At 1.5T and 3T, there was a maximum improvement of 100% and 200% at the top face of the phantom near by the MI lens respectively. These SNR enhancement were observed for 35mm and 40mm of penetration depth of 1.5T and 3T respectively.

2.2.3 The High impedance surface (HIS) approach

In recent years, there has been increasing interest in artificial electromagnetic materials (AEM), such as double negative materials (DNG)[65, 66], Photonic Crystal[67, 68], photonic band gap (PBG) [68], electromagnetic band gap (EBG) and artificial materials conductor (AMC). The Artificial Magnetic Conductor (AMC) has the perfect conductor properties in specific frequencies range, this surface structure was investigated by Sievenpiper in [69]. The AMC has a high impedance at resonance frequency, which can be useful for many applications. It is clearly known that, for a generally incident plane wave, the properties of the perfect magnetic conductor (PMC) does not find in nature, has a reflection phase of 0°, while, the perfect electric conductor (PEC) has a 180° reflection phase which reflects the incident wave out of phase [70]. Furthermore, a HIS is designed by a frequency selective surface (FSS) grounded by PEC as shown in Fig. 2.7. The HIS structure which is shown in

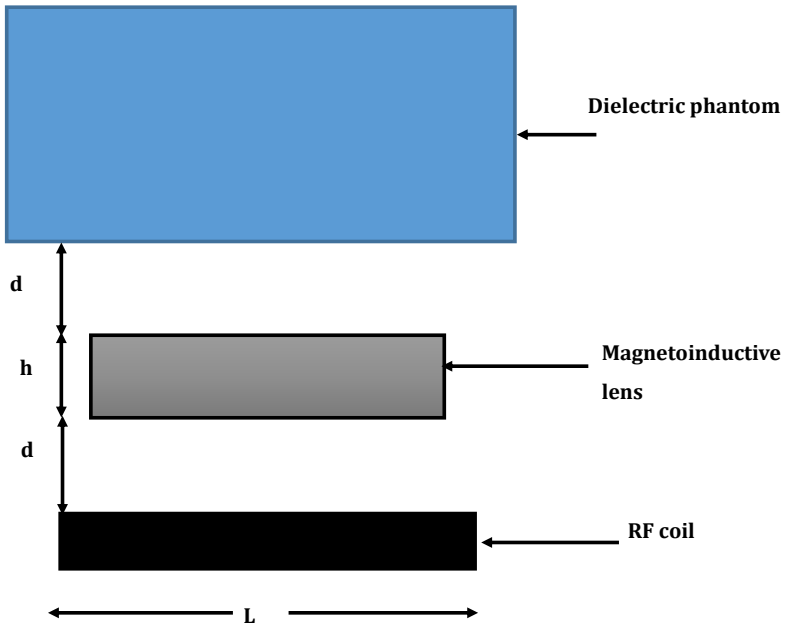

Fig. 2.6 Scheme of the configuration of metamaterial MI lens

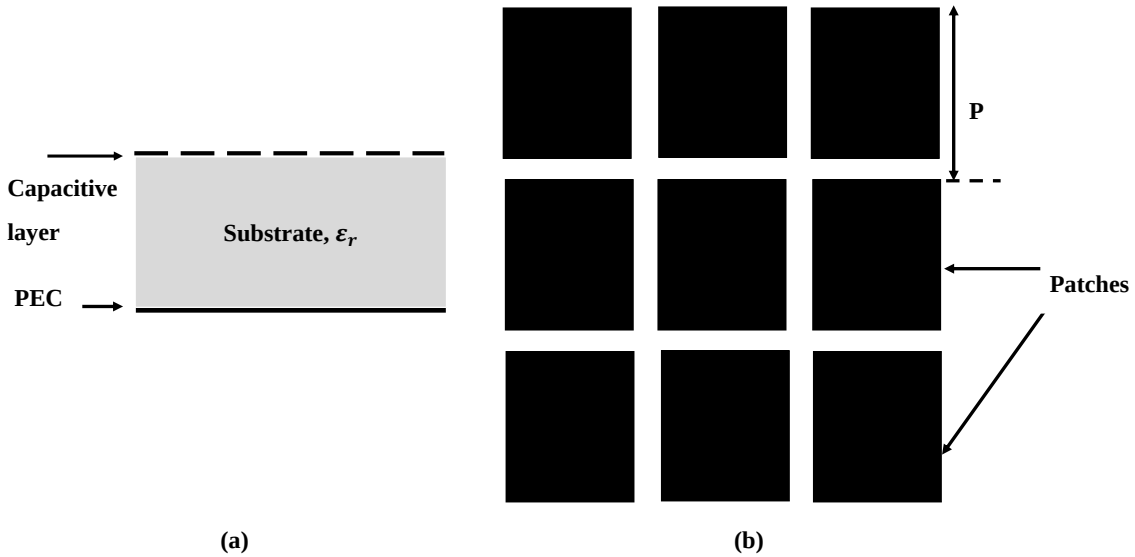

Fig. 2.7 (a). Cross section of the HIS. (b).Top view of the HIS with the a unit cell periodicity of P .

Fig. 2.8 is introduced as an artificial ground plane that solves the image current destructive interference[70]. The main function of the HIS is to improve the reflection phase of the incident wave, in other words, to reflect the incident wave in-phase instead of out-of-phase as shown in Fig. 2.8(b). Thus, a constructive interference takes place and a poor radiation pattern can be enhanced without requirement of the quarter-wavelength gap distance condition. The reflection phase features of the HIS can be used to improve the field over the surface [37, 71], which is an important property used in chapter 3 in this research.

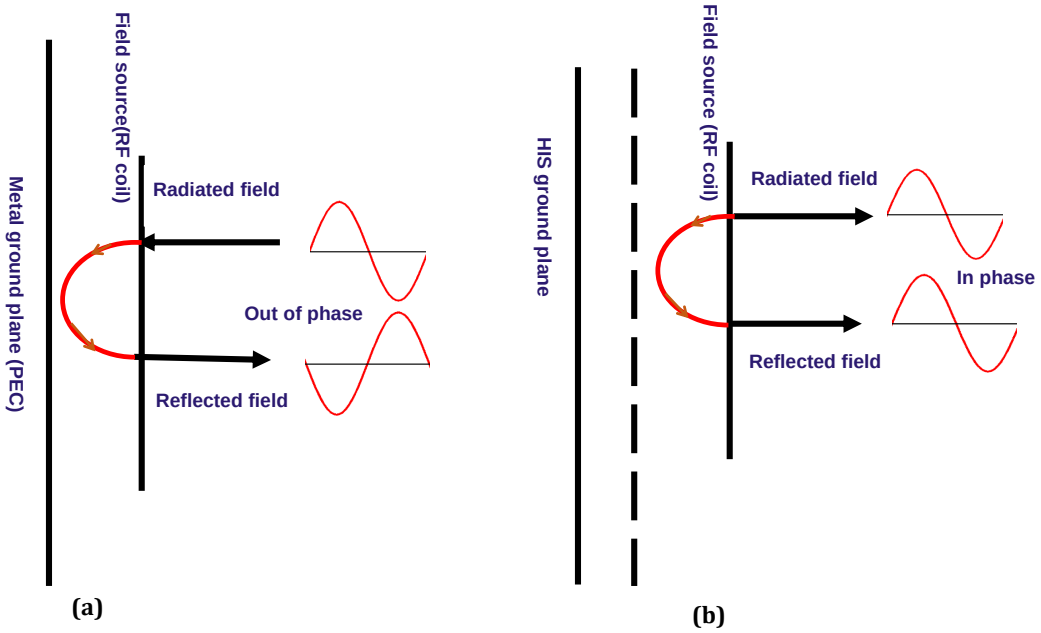

Fig. 2.8 (a). Field source printed over metal ground plane, out-phase reflected field. (b) Field source printed over the HIS plane, in-phase reflected field.

The properties of a PMC can be produced using a HIS at resonance frequency, based on the HIS dimension described in section (3.2), it is clearly seen that zero degree phase can be achieved at the resonance frequency of 63.8MHz as shown in Fig. 2.9. In [71], the authors analysed the properties of HIS for use in a 7T MRI system operating at 300MHz which used electrically small HIS unit cells, and their ability to increase SNR of the MRI RF coil. The authors in the study reported in [72], the results of this study demonstrated using RF bench measurements that the HIS can improve the RF magnetic field intensity by 26% when a dipole antenna was placed 5 mm away from a HIS, this dipole antenna was used instead of using an RF loop coil at 7T MRI system. The study [37], developed the method described by [72] and they applied a HIS approach, which simulated using a surface impedance boundary condition (SIBC), for 7T MRI systems, their result has shown that there was an increasing

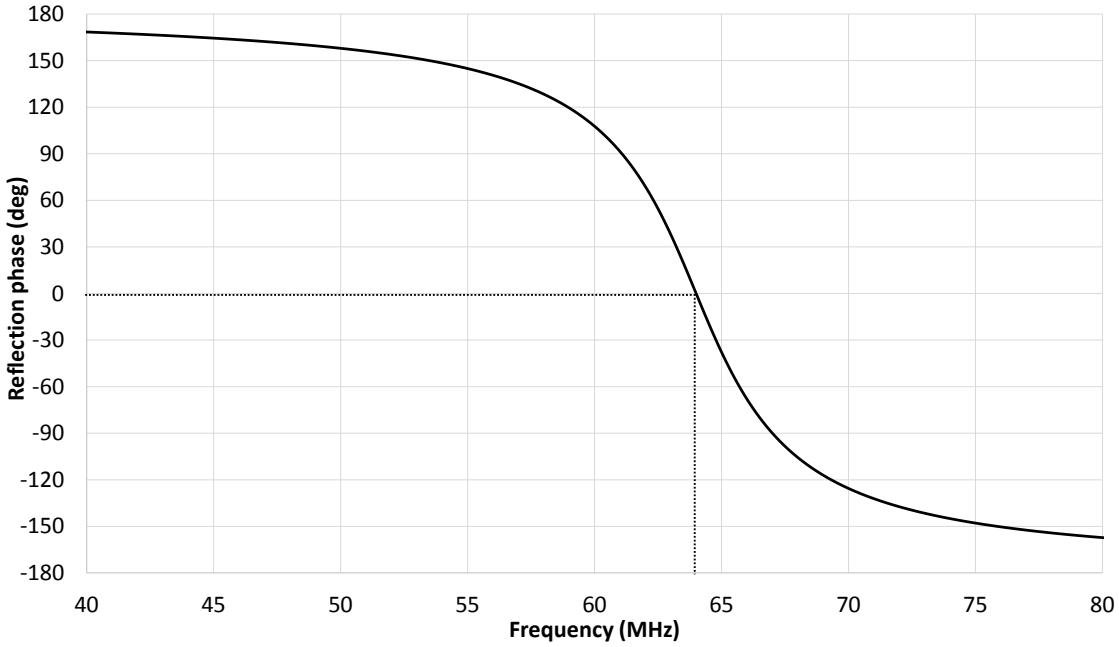

Fig. 2.9 The numerical reflection phase of the HIS.

of the magnetic flux density by 7%. The challenge for a utilization a HIS method at low resonance frequencies of the order 60 to 130 MHz, which are the Larmor frequencies of the typical MRI systems is the miniaturisation of the unit cell physical size of the metasurace. Approaches used to reduce the cell size physical dimensions of the metasurface have been presented in details in the next section, including multilayer structures, lumped elements and interdigital capacitance.

2.2.4 Miniaturization of metamaterial surfaces.

As previously mentioned the main challenge of an HIS design for use as an RF coil reflector in the MRI system which operates at 63.8MHz is a unit cell size, due to, this reason miniaturization methods are needed in this study in order to achieve suitable cell size for a low frequency MRI system. The miniaturisation of the AMC structure can be obtained by using different approaches which include changing the symmetry of the HIS to change the polarization, using extra components to design the HIS, and adding multilayer structures to reduce the patch size [73]. In previous studies, the authors have investigated the miniaturisation methods based on the compact a AMC design, including Hilbert curves [74, 75] and space filling curves such as a Peano shape [76, 77]. In addition, a considerable amount of literature has been published on miniaturisation techniques based on a FSS loaded with lumped ele-

ments and lumped reactive components in order to reduce a cell size of the surface [78–80], where research has been carried out to insert lumped elements in to the FSS in with resonant geometry effects to miniaturized the unite cell size up to 0.02 of the free space wavelength in a single band system FSS application. However, these miniaturisation approaches were not able to be used underneath the MRI system because the lumped elements could increase the losses. Authors of [81, 82], ascertained that by using double stacked and alternated FSS structures and setting the distance between the layers as thin as possible effects to achieve a miniaturisation of the FSS patch width in range of (0.5 to 0.9) of total cell size. Due to the physical MRI dimensions, state available bore size 60-70 cm maximum, the double layer miniaturisation approach may not be used. For these reasons, the interdigital capacitors are used as a miniaturisation approach in this study because high order miniaturised surface can be achieved by using this method as explained in the literature below.

In recent years, there has been increasing interest in interdigital capacitors as an effective miniaturisation technique, which is a multi-digit periodic structure as shown in Fig. 2.10. The methodology of the interdigital capacitors approach is used in the capacitance that occurs between digits' metallic gaps and the capacitance increases by increasing number of digits or by using thin high dielectric material layer, however, it will increase the loss. The analysis

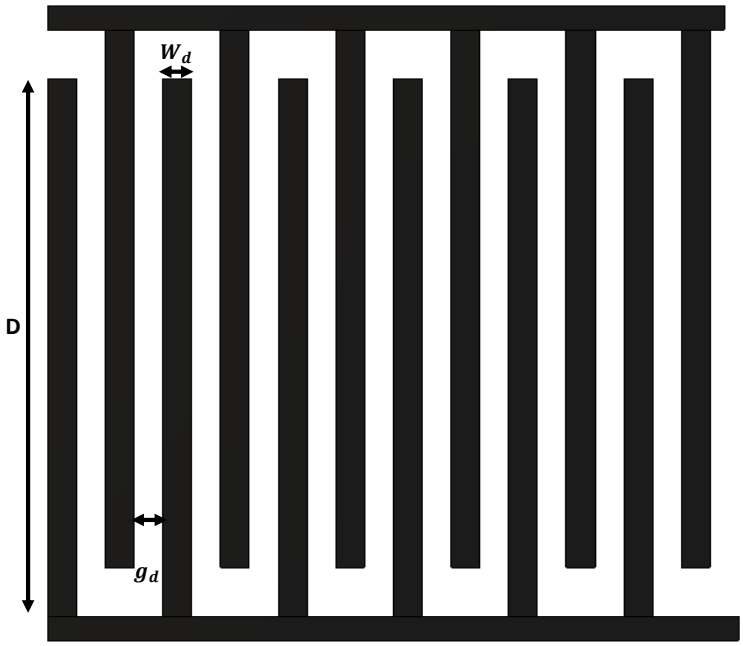

Fig. 2.10 Top view of the interdigital structure with N=12.

and characterisation of interdigital capacitor to be used in microwave integrated circuit, and microstrip antenna has been reported in the literature [83, 84]. More recent studies using

this approach was performed in[85, 86] and they investigated using interdigital capacitor technique in dual band HIS at frequency range (480MHz-930MHz). As a result of this study, by using this approach the HIS unit cell size could be reduced to 0.0625 of free space wavelength.

2.3 The metasurface approach

Over the last several years, metamaterials have moved from being simple theoretical principles to complex 3D devices such as lens and flux guides which are described in previous sections. These three-dimensional devices can be transferred by arranging electrically small holes or scatter such as metallic rings, or patches into two dimensional pattern at a surface. These such types of planar metamaterial structures are termed a metasurface. Metasurfaces have advantage of being smaller in physical size than the 3D metamaterials devices; consequently, metasurfaces provide alternative devices which may less lossy [87]. For many applications, metasurfaces have been used instead of three dimensional metamaterial devices to overcome the physical size problem. Metasurfaces have abroad range of potential applications in electromagnetic field for example, a bandstop frequency selective surface, a bandpass frequency selective surface, a narrowband perfect absorber, focusing transmitarray, and focusing reflectarray as shown in Fig. 2.11, respectively. Conventional frequency selective surfaces (FSSs) usually have element dimensions and resonance periodicity, however, in some certain cases FSSs with a periodicity $P << \lambda$ have been implemented [41]. The bandstop and bandpass features can be achieved only by a specific unit cell shape making it resonate. These structure arrays were defined self resonant grid structures as shown in Fig. 2.11 (a, and b). Metasurfaces can perform as an absorber as shown in Fig. 2.11(c). A thin structured of metasurface with a special design capable of absorbing almost all incident power are required in many applications in the microwave range such as the applications which were described in section (2.1.1). Another function of metasurfaces is shaping of the RF magnetic field waves, such that, the waves beam can be reflected or refracted, focused or defocused in such structure is a metamaterial lens. This concept was demonstrated such as focusing reflect array, or transmit array as shown in Fig. 2.11 (d, and e) respectively. Reflect array was defined as a structure that completely reflects an incident wave, alternating the shape of the wave front. The reflect array was demonstrated with a microstrip patch antenna [88] or dipole antenna [89]. The transmit array was described as a structure, which can change the transmitted wave pattern without reflection in the ideal case, this structure was proved by [90] using constrained lenses. More recent applications of metasurfaces have

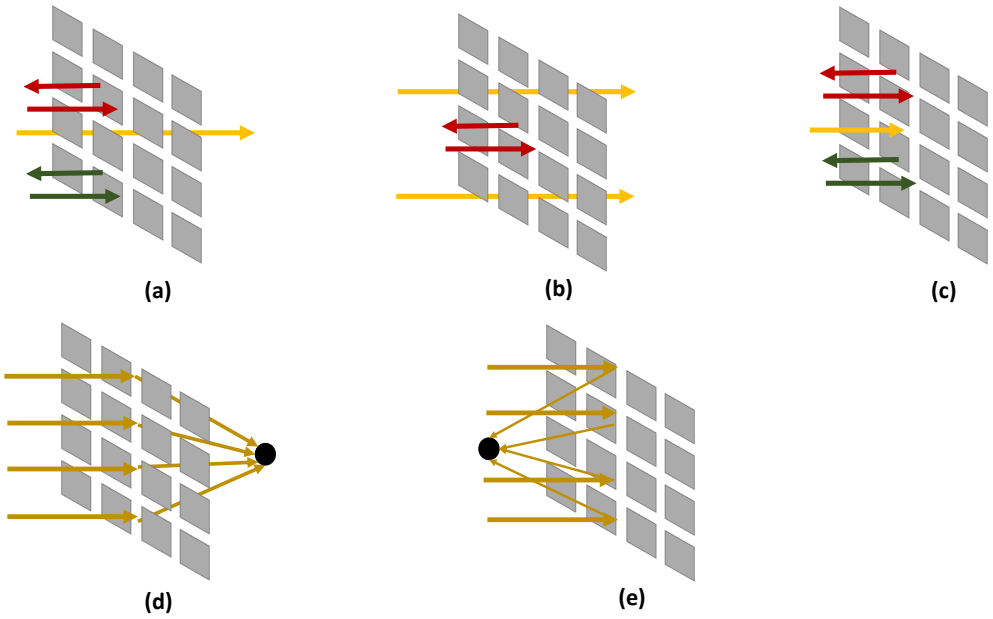

Fig. 2.11 Examples of metasurfaces application; (a) bandpass frequency selective surface; (b) bandstop frequency selective surface; (c) narrowband perfect absorber; (d) focusing transmitarray; (e)focusing reflectarray

been used for MRI imaging applications to improve the SNR of an RF coil at a 1.5T MRI system. This application has been demonstrated by [91], the array of nonmagnetic conductor wires, which operate as a resonance structure at 63.8MHz. The results have shown that, the SNR of the RF surface coil can be enhanced by 2.7 times when compared to the metasurface was not employed. Placing a metasurface inside the MRI scanner increases the coupling between a sample and a receiving coil by redistributing and enhancing B_1 in the region of interest. However, the use of this structure is limited in a real MRI environment because of the physical dimensions size which was tens of centimeters in each side and it may not be able to place it in near proximity of the body due to metallic wires.

2.4 High constant dielectric material (dielectric pads)

The RF field distribution inside the sample to be imaged depends on many factors such as electrical properties, a relative position, and geometry of the dielectric sample when compared to the RF coil. Fig. 2.12 shows the configuration of pads with RF surface coil and the dielectric phantom, which is mimicking the body part. Recent experimental studies have shown that the dielectric constant of the sample tissues can play an important role in the

behavior of the RF magnetic field distributions inside biological tissues [92]. High dielectric constant materials have also proved useful for locally improving the signal to noise ratio and reducing the specific absorption rate for neck and head image applications [93, 94]. In this context, dielectric shimming and focusing of the RF magnetic field have been widely used for improving image homogeneity at 3T, 4T, and 7T, MRI systems. In [95, 96], the authors proposed using high dielectric pads to improve the magnetic flux and signal to noise ratio of human head imaging at 3T. By placing high dielectric pads at 3T MRI around the human head the RF power excitation pulse can be reduced by approximately 50%, and the measured SNR can be improved up to 40%, and the SAR was reduced by 27%. More recent work in terms of decreasing SAR and improving the magnetic field flux is [97] which showed that by using 15 mm high dielectric sleeve at 3T MRI the magnitude of the electric field can be reduced by 13%, this can lead to reducing the SAR by 14% average the entire ROI. The dielectric pads were made of a mixture of distilled water with Barium Titanate powder with relative permittivity equal ($\varepsilon_r = 300$). Due to the depth limitation of this approach at 3T, the study [76] proposed the dielectric pads could be useful in applications of short penetration depth for example, internal ear and neck. By inserting the the barium titanate pads surrounding the volume RF coil the magnetic flux density B_1^+ inside the internal ear can be improved by 29% when compared without the pads. At higher magnetic field of 300MHz for 7T MRI application, dielectric pads can produce an enhancement in the B_1 strength. These studies showed that by placement of high dielectric pads the magnetic field can locally enhance SNR in a small region of interest (ROI) near to the dielectric pads[98]. Results in improving the SNR and decreasing the amount of SAR, however, using high dielectric permittivity pads can lead to image artifacts due to the electromagnetic wavelength in biological tissue of the sample being imaged becoming shorter when compared to the relevant dimensions of the whole body dimensions. This leads to degradation of the homogeneity of the excitation field at high frequency than at lower frequency. In order to overcome this problem, the study [99] investigated how wavelength effects at 7T can be reduced by using pads with holes and different permittivities with a mix of barium titanate and Calcium titanate with permittivities 300 and 100. The results showed that the B_1 magnetic flux density generated by the RF coil with pads which include holes can be improved by 20% when compared to full pads, and 60% when compared to no pads.

The theory behind magnetic field focusing using dielectric pads is the displacement current works as a second source of the magnetic field. For a human tissues, which is an example of a conductive dielectric materials, the RF magnetic field inside the these material is function of conductive (Jc) and displacement (Jd) currents according to Maxwell's equation

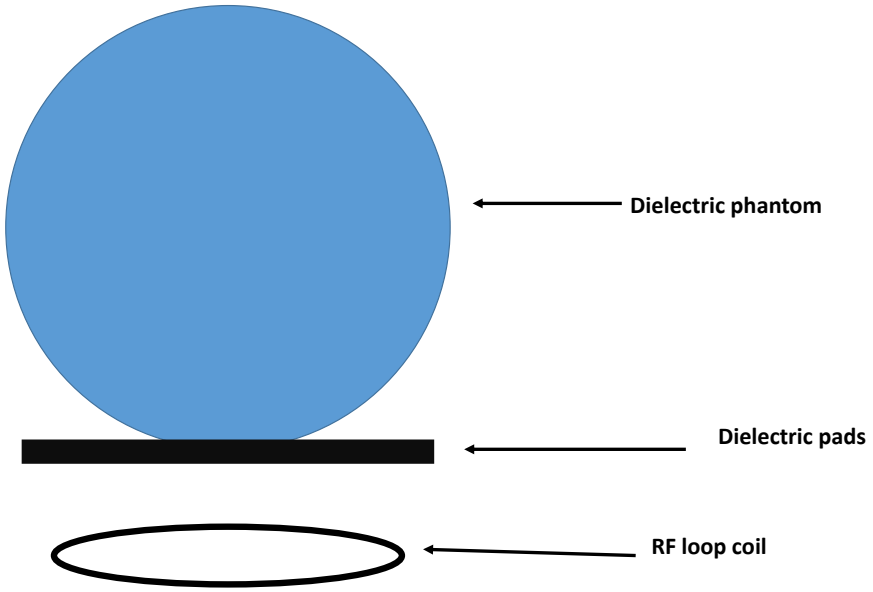

Fig. 2.12 The configuration of dielectric pads and the dielectric phantom with surface loop coil

(2.9)

$$\nabla \times B = \mu(Jc + Jd) = \mu(\sigma E + i\varepsilon_r \varepsilon_0 \omega E) \tag{2.9}$$

where E is the electric field, B is magnetic flux density, ω is the angular frequency, ε_r is the relative electric permittivity (dielectric constant), ε_0 is electric permittivity in vacuum, σ is electrical conductivity of the sample, μ is magnetic permeability, i is the complex unit that introduce antiphase shift between the displacement and conductive currents. The conductive current induced by the RF field (eddy current) can attenuate the RF magnetic field in the sample to be imaged as a function of the penetration depth, while the displacement current works as a secondary RF field source which helps RF waves propagate through the sample. The authors in [99, 100], demonstrated experimentally that high dielectric pads can alter displacement current distribution. The high dielectric constant also reduces the length of the wavelength of the RF field wave when compared to the physical dimension of the body size sample [101]. Consequently, the pattern phase distribution of the RF magnetic field inside the patent body becomes spatially dependent on the sample tissues [102], thus, the high permittivity dielectric pads can control the RF field wave behaviour in the body sample [97]. More recent study in this area was proposed by the authors' of [103], they applied a new version of the HDC, which was donated as a ultra-HDC (uHDC) in a vivo system of 7T MRI applications. The uHDC is a ceramic material with a relative permittivity of 1200, has

dimensions of $10 \times 8 \times 2cm^3$ of the high, width and thickness respectively. The experimental results have demonstrated that the four rectangular uHDC materials significantly improve RF magnetic transmit flux density (B_1^+) and reception flux density (B_1^-). Consequently, the uHDC technique having an appropriate permittivity value with a RF coil can significantly improves the receiver sensitivity and reduces RF transmission power for applications at ultrahigh field.

A more recent work using a combination of resonance metasurface and a high permittivity pad to locally improve the SNR at 1.5T and 7 T MRI applications from the concept of human trials. The proposal metasurface under the 1.5T investigation was quite thick of 57 cm and located at 25mm from the patient [104, 105]. The results show by using such hybrid dielectric pads with resonant metasurface in human brain, the SNR can be locally improved, the magnetic flux density is concentrated in the central region of the metasurface which behaives as a resonant metalenses [106].

2.5 Summary

This chapter provided a background literature review for the area of work of this thesis. Firstly, an overview of the historical periodic metamaterial background has been provided. Then, the three main techniques which have been used to improve the RF magnetic flux density are discussed. These techniques are metamaterial devices, metasurfaces, and dielectric pads. The metamaterial was categorised into flux guide, RF lens, and HIS and the state-of-the art in providing improvement of RF coil sensitivity, SNR, penetration depth, and SAR were discused.

Some key studies showed that metasurface and high impedance surface can improve the magnetic flux density and SNR generated by a RF loop coil, which leads to enhance MR image quality. The most recent studies have shown that RF magnetic flux density can be improved by 7% using high impedance surfaces at 7T [72], however, to the best of our knowledge this method has not been demonstrated with a RF coil on a MRI scanner. Also, recent research has investigated the use of the resonate metasurface inside a dielectric medium with a biological sample showing a 2.7 fold increase in SNR, however, use of such a structure in a real system is limited due to the physical size.

The literature review then took a close look at the use of dielectric pads to improve the SNR and B_1 magnetic flux density of the MRI systems. The gaps in this literature are highlighted as:

(1) While the high impedance surface has been used successfully at 300MHz for the 7T MRI

systems. The challenge for successful implementation of HIS at lower RF frequencies of the order 60 to 130MHz which are the operation frequencies of a typical clinical MR scanner has not been investigated.
(2). In this literature review, the main challenge of implementing such as these methods in real MRI systems has been highlighted which was the structure physical size. In order to overcome this problem, a small non resonate and thin metasurface is required, which can be implemented with anatomically useful RF coils on an MRI scanner at 1.5T or 3T.

Table 2.1 shows the summary of the literature review and compares the parameters that have been used in the different literature review studies. This table is updated after each chapter work of this thesis to compare our results with the state-of-the-art.

Table 2.1 Literature Review studies summary based on measured parameters ‡**- Volume coil** †**- Surface coil**

Metric	**Approaches**	**1.5T,** $f_0 = 64MHz$	**3T,** $f_0 = 128MHz$	**7T,** $f_0 = 300MHz$
$\|B_1\|$	HIS	-	-	7% ‡[37] 25%†[72]
	Metasurface	-	-	-
	RF lens	-	-	-
	Dielectric pads	-	50%‡[95]	100%‡[103]
SNR	HIS	-	-	-
	Metasurface	270%‡[91]	-	-
	RF lens	100% [64]	200% [64]	-
	Dielectric pads	-	20-40%‡[95]	53%‡[98], 200%‡[103]
Penetration depth	HIS	-	-	-
	Metasurface	-	-	-
	RF lens	35mm†[64]	40mm†[64]	-
	Dielectric pads	-	-	-
SAR	HIS	-	-	+48% †[71]
	Metasurface	-	-	-
	RF lens	-	-	-
	Dielectric pads	-	-50% ‡[95]	-33% ‡[98]

Chapter 3

Enhancement of RF magnetic field for a 1.5 T magnetic resonance system using a high impedance surface

3.1 Introduction

In MRI system deployment, the efficiency of radio frequency magnetic flux density (B_1) of transmit and receive RF coil vital for MRI system performance. Chapter 2 outlined the current progress in approaches to improve RF magnetic field and SNR of a surface and volume coils of MRI systems . This chapter develops of using a miniaturised high impedance surafce (HIS) as a reflector instead of the conventional RF shield, which is a PEC ground plane, and to present a design methodology for improving the strength of magnetic field H_1 and magnetic flux density B_1 inside the dielectric phantom, which can lead to improved SNR for 1.5T MRI systems. The challenge for successful implementation of HIS at frequency of the order 63.8MHz is the miniaturization of the HIS unit cells. The proposed system is based on a miniaturized surface unit cell of the HIS using an interdigital capacitance approach. The efficacy of the approach is demonstrated with simulations, RF bench and MRI measurements of the magnetic field within a dielectric phantom for various design parameters of the proposed HIS. Additionally, the Specific Absorption Rate (SAR) inside the phantom was simulated and verified against regulatory standards such as IEC60604-2-33/2010. This chapter is organized as follows: section 3.2 shows the tools and materials which have been used for measurements . MRI concept and HIS design are presented in section 3.3, RF coil design and characterisation is shown in section 3.4. Simulation results of the MRI system

performance which include magnetic field (H_1), magnetic flux density (B_1), electric field (E), specific absorption rate(SAR), signal to noise ratio SNR, and cumulative density function inside the phantom). In section 3.6 experimental validation of the proposed system in the RF laboratory is presented. The system is then demonstrated imaging experiments on a 1.5T MRI scanner in section 3.7. Finally, section 3.8 concludes the chapter.

3.2 MRI Concept and HIS Design

Fig.3.1a shows a schematic representation of a shielded (PEC) RF coil which is proximal to a dielectric phantom where the implementation is appropriate for a classic planar surface coil imaging approach. Fig. 3.1b shows the proposed system which includes a capacitive layer between the RF coil and the PEC shield. The cross-sectional area (X^2_{HIS}) of the capacitive layer and PEC shield are equal and it is assumed that the thickness of the capacitive and PEC layers are electrically small. The combination of the capacitive layer and the PEC shield forms a high impedance surface (HIS). The properties of the dielectric phantom were $\varepsilon_r = 65$ and $\sigma = 0.4\ S/m$, [107, 108], with dimensions x=14cm, y=33.5cm and z=23cm. The distance between the coil and phantom, s, was 5mm which is similar to used in practical MRI systems for safety reasons [109].

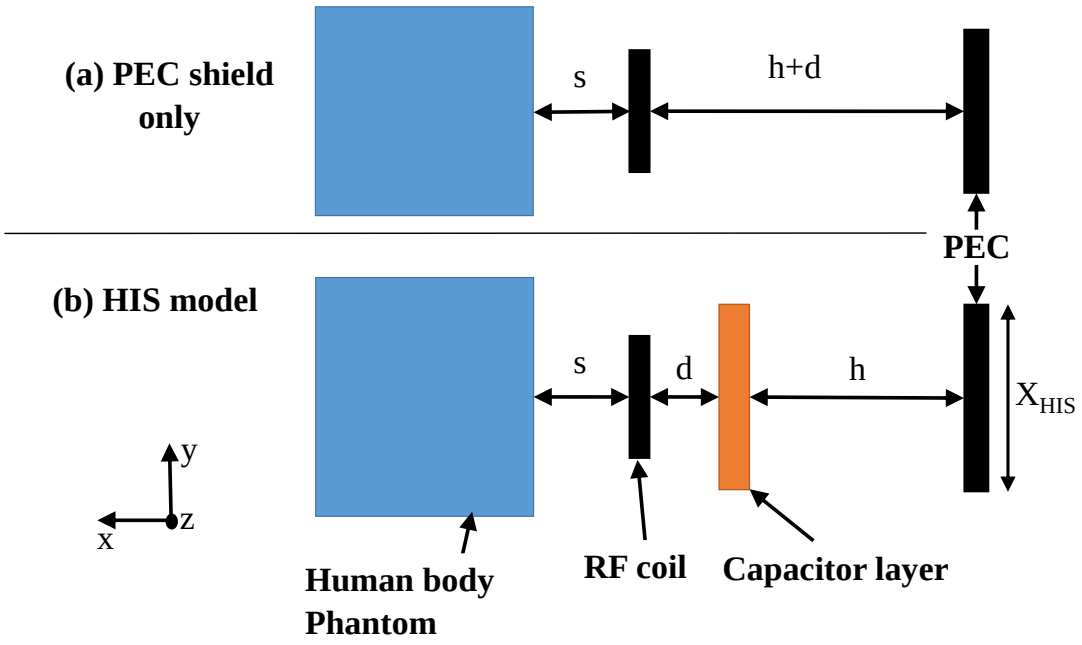

Fig. 3.1 (Cross-sectional view of the RF system (a) PEC shield only (b) HIS model.

Fig. 3.2 shows the cross section of the HIS (Y_0 denotes the admittance of freespace), Fig. 3.3 shows a unit cell of the proposed capacitive layer which comprises inter-digital metallic elements and Figure.3.4 the equivalent circuit of the HIS. The PEC layer, spaced a distance, h, away from the capacitive layer, has an equivalent admittance that is inductive ($Y_{PEC} = -jcot(\beta h)$) where β is the freespace propagation constant. The capacitive surface acts as a shunt admittance such that the total input admittance is given by $Y_{in} = Y_{PEC} + Y_C$.

The inter-digital capacitive surface was adopted in order to maximize the capacitance density, [86], and provide an electrically small unit cell design. It was assumed that the capacitive layer has a 0.8mm thick FR4 substrate ($\varepsilon_r = 4.3, tan\delta = 0.025$) and that it is placed 50mm away from the RF shield which acts as the ground plane for the HIS. This thickness is commensurate with the practical dimensions that might be found in MRI systems. In order to achieve a dual polarised HIS a second capacitive surface, labelled "back surface" in Fig. 3.2, is on the reverse of the FR4 substrate, however, the back surface is rotated through 90° and as such the unit cell is rotationally symmetric. An illustration of the orientations of the digits is shown in Fig. 3.3.

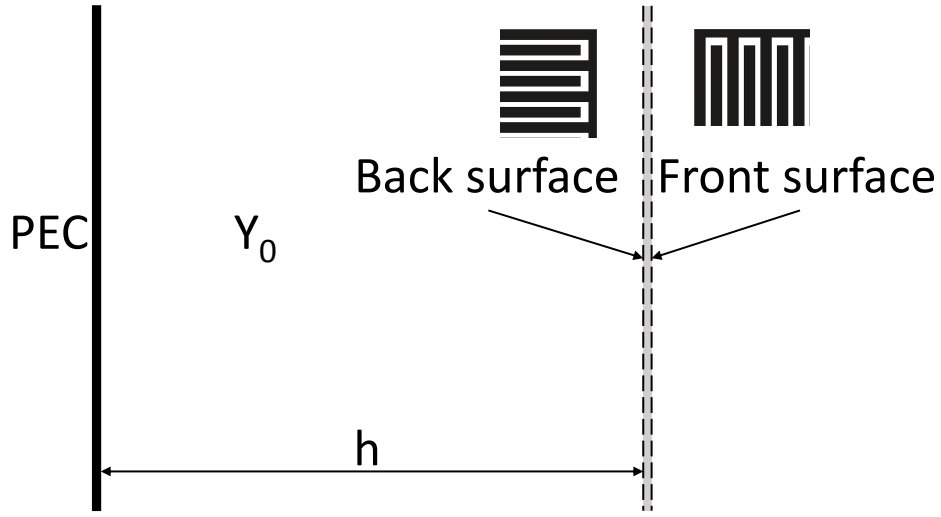

Fig. 3.2 Cross section of HIS

Initially the design of the HIS was carried out using approximations for interdigital capacitance, [110], using (3.1) where the units of capacitance are pF. When using the

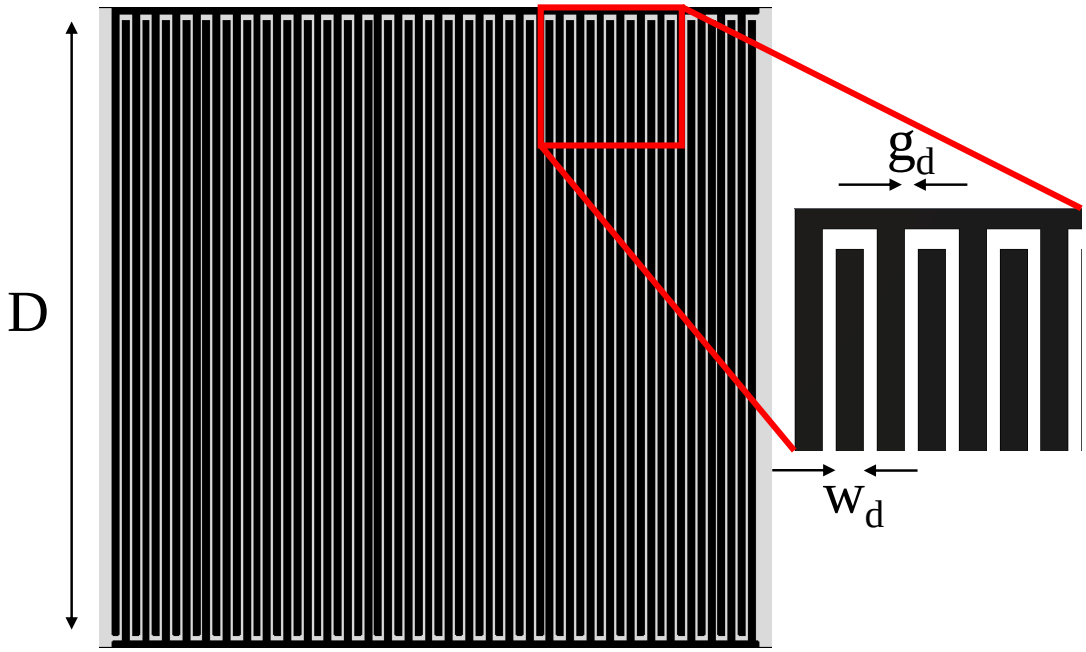

Fig. 3.3 Front layer of capacitive surface

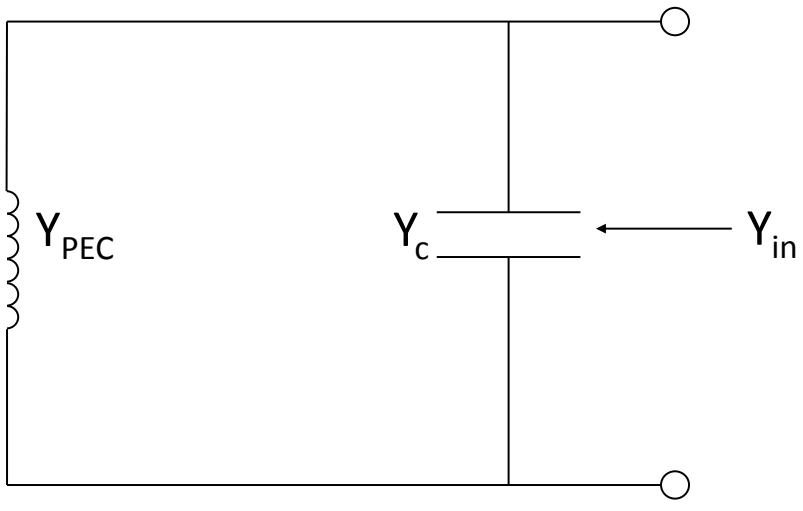

Fig. 3.4 Equivalent circuit of HIS

approximation equations it was assumed that the second capacitive layer on the back surface was transparent.

$$C = \frac{\varepsilon_{eff}(N-1)D}{18\pi}\frac{K(k)}{K'(k)} \tag{3.1}$$

where

$$\frac{K(k)}{K'(k)} = \begin{cases} \dfrac{1}{\pi} ln\left[\dfrac{2(1+\sqrt{k})}{1-\sqrt{k}}\right] & 0.707 \leq k \leq 1 \\ \dfrac{\pi}{ln\left[\dfrac{2(1+\sqrt{k'})}{1-\sqrt{k'}}\right]} & 0 \leq k \leq 0.707 \end{cases} \tag{3.2}$$

and

$$k = \tan^2\left(\frac{a\pi}{4b}\right), a = w_d/2, b = \frac{w_d + g_d}{2}, k' = \sqrt{1-k^2} \tag{3.3}$$

where $K(k)$ is the complete elliptic integral of the first kind and its complement is $K'(k)$, D is the digit length, N is the number of digits, $\varepsilon_{eff} = \frac{\varepsilon_r+1}{2}$, w_d is the width of the digits and g_d is the space between the digits. In the approximation the losses in the substrate are not included, however, this was included in later full field simulations. The reflection coefficient of the HIS can be calculated using (3.4). This approximation considerably simplifies the design process when compared to a full field analysis and optimization.

$$\rho = \frac{Y_0 - Y_{in}}{Y_0 + Y_{in}} \tag{3.4}$$

Fig. 3.5 shows the reflection phase for the proposed dual polarised HIS where D=48.5 mm, with a 0.5 mm gap between the end of the digits and the metallic horizontal strip. The number of digits, N=64, w_d= 0.5 mm, g_d= 0.25 mm, the unit cell inter element spacing is 1mm resulting in a unit cell periodicity of 50 mm which is $\lambda/94$ at 63.8MHz. For comparison CST Microwave Studio frequency domain simulations were carried out using periodic Floquet mode boundary conditions to approximate an infinite HIS and the CST simulations included the substrate and copper losses and both capacitive layers were incorporated into the simulation. It can be seen that there is good agreement between the approximate equivalent circuit model and the CST simulations. Fig. 3.6 shows a photograph of the manufactured HIS to be used in later measurements.

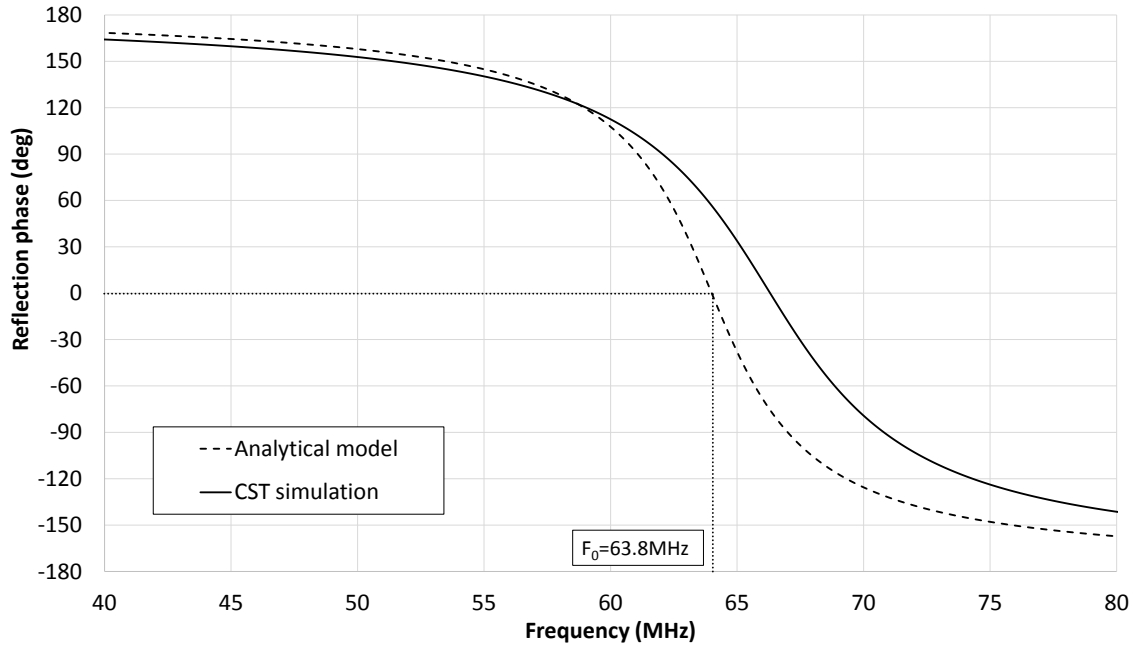

Fig. 3.5 Reflection phase of proposed dual polarised HIS

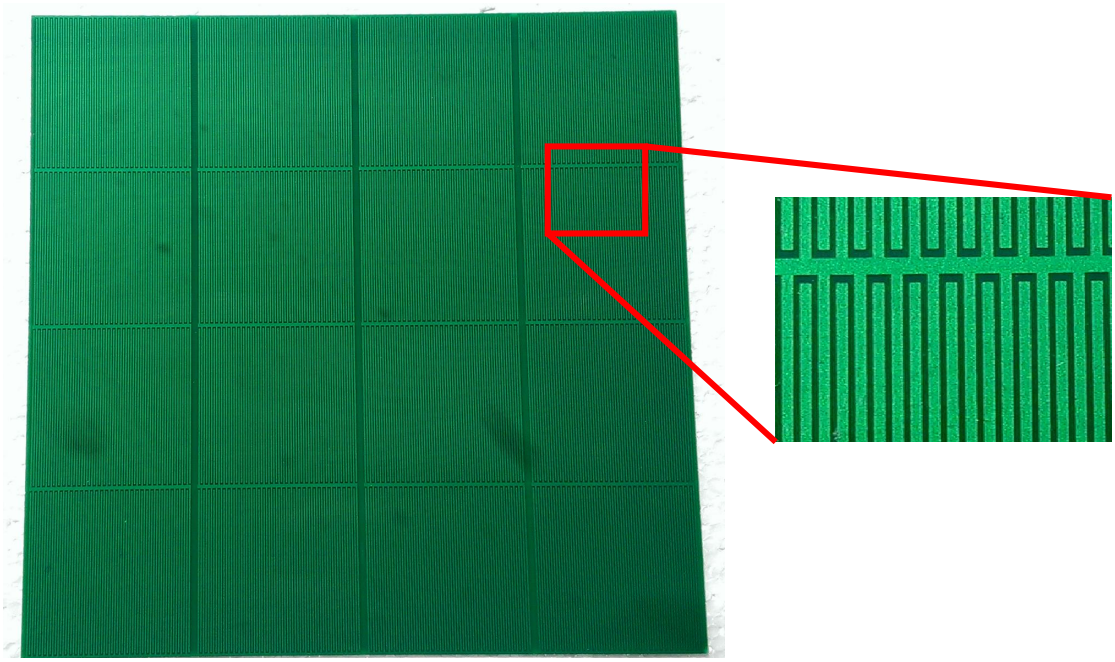

Fig. 3.6 Front layer of manufactured dual polarised capacitive surface.

3.3 RF Coil Design and Characterisation

Fig. 3.7 shows a schematic of a single loop RF transmit/receive surface coil which is realized with lumped capacitance to tune the resonance of the coil to the appropriate Larmor frequency, specifically 63.8MHz for a 1.5T MRI system. The coil has an equivalent circuit of a series inductance and capacitance where the inductance (nH) can be estimated using (1.42), [19] where the dimensions are in mm. The required capacitance to tune the resonant frequency to 63.8MHz can be calculated accordingly. Fig. 3.8 also shows the manufactured coil including lumped components and balun.

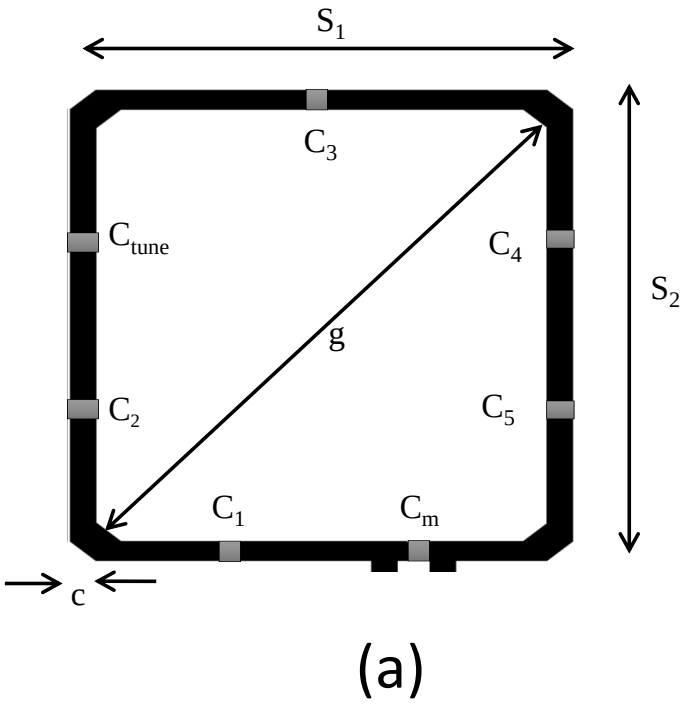

Fig. 3.7 Schematic of RF coil.

The dimensions of the coil are shown in Fig. 3.7 with a coil metal thickness, b. The designed coil has dimensions, S_1=120 mm, S_2=150 mm, b=32μm, g=192 mm and c=6 mm with a 1.6 mm thick FR4 substrate. The coil material was assumed to be copper with no surface roughness and a conductivity of 5.8 $\times 10^7$ S/m. The resulting equivalent inductance and total capacitance are (L=414 nH) and (C_t=15 pF) respectively. The coil was simulated using CST Microwave Studio incorporating seven capacitors (C_1 to C_5, C_m and C_{tune} as illustrated in Fig. 3.7). The fixed capacitors, C_1 to C_5, are 100 pF and C_m and C_{tune} are variable capacitors (7-100) pF. C_m is used to match the RF coil in the presence of the dielectric

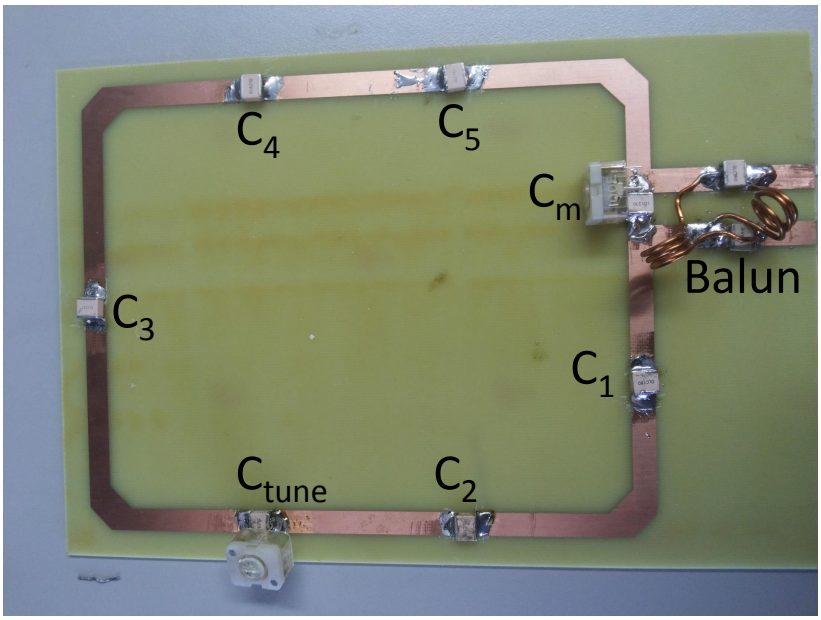

(b)

Fig. 3.8 manufacture RF coil.

phantom and HIS and C_{tune} is used to tune the resonant frequency of the RF coil. The RF power was fed to the coil through a balun circuit which is connected either side of C_m. Fig. 3.9 shows the simulated and measured input match (S11) when the coil is spaced 5 mm away from a dielectric phantom consisting of 5L distilled water and 200g Sodium Chloride which was placed inside a plastic container with the same dimensions as used in Fig. 3.1. In the experimental bench system the manufactured coil was connected to an Agilent E5071B Vector Network Analyser (VNA) and the resonant frequency was tuned to 63.8MHz using the variable capacitor, C_{tune}, in the presence of the HIS and dielectric phantom and the magnitude of S11 was controlled using C_m. Also presented is the S11 when the HIS is removed which has the effect of shifting the measured resonance from 63.8MHz to 64.6MHz. It was possible to tune the resonant frequency back to 63.8MHz with the use of C_{tune} for later field measurements. The difference between measurement and simulation is due to tolerances in the lumped capacitor values, the coil inductance approximation and material property assumptions.

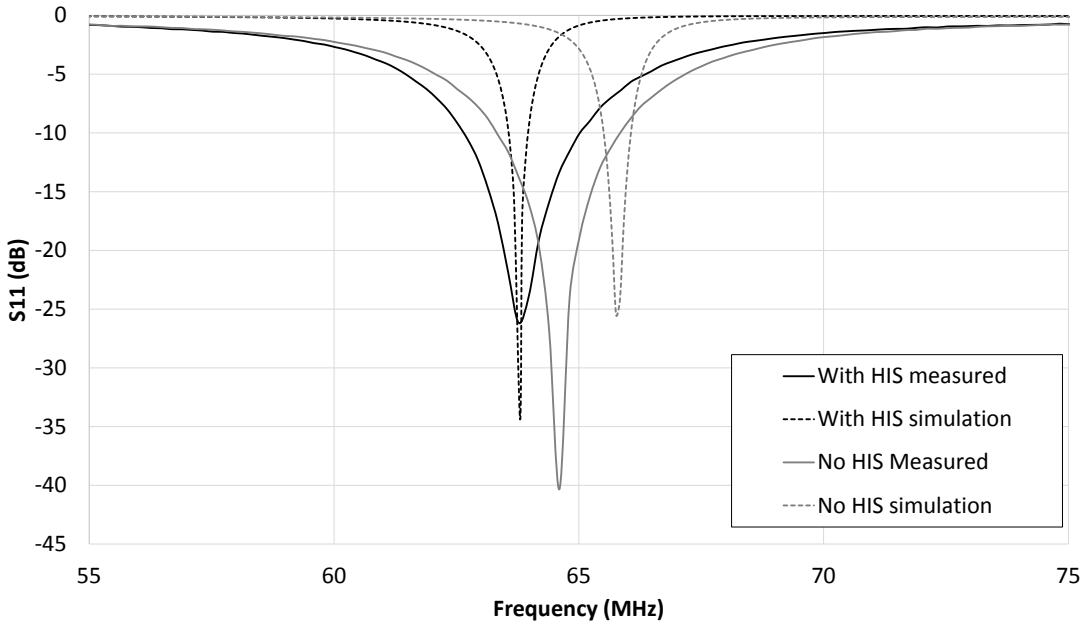

Fig. 3.9 Simulation and measurement of input match of RF coil.

3.4 Simulated results with a dielectric phantom

In this section the RF magnetic field, magnetic flux density, electric field and SAR were investigated based on Fig. 3.1. For a fair comparison the magnetic field H_1, and magnetic flux density B_1^- were normalised to the square root of the accepted RF power $\sqrt{P_{acc}}$. The normalised value of the H_1, and B_1^- are given by 3.5, and 3.6 respectively.

$$H_{1,normalised} = \frac{|H_1|}{\sqrt{P_{acc}}} \tag{3.5}$$

$$B^-_{1,normalised} = \frac{|B_1^-|}{\sqrt{P_{acc}}} \tag{3.6}$$

3.4.1 Magnetic field monitoring

In order to reduce simulation complexity for the scenario shown in Fig. 3.1 the capacitive layer was implemented as an effective surface impedance model which has been previously shown to be an effective approach [37, 111]. The surface impedance was determined using full field simulations of the dual polarised unit cell of the capacitive layer using CST. The impedance is complex and includes the losses due to the FR4 substrate and copper losses.

Fig. 3.10 shows the CST simulation geometry including the dielectric phantom, RF coil, capacitive layer and PEC shield.

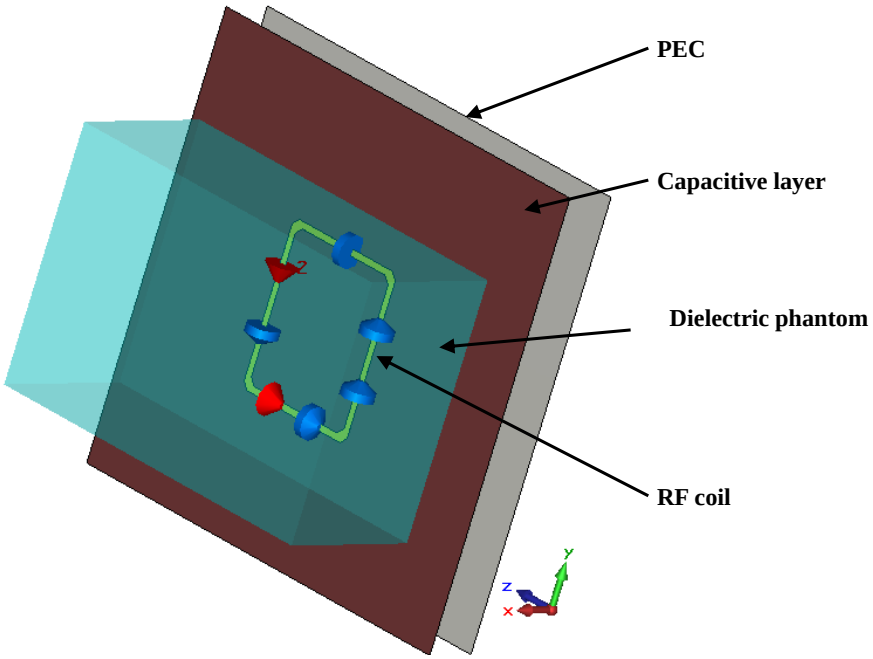

Fig. 3.10 CST simulation geometry.

CST simulations were carried out for both models in Fig. 3.1 where the magnitude of the magnetic field inside the dielectric phantom was monitored along the x-axis (y=z=0) and y-axis (x=140mm, z=0) assuming s=5mm and the RF coil was fed by a 1W, 50Ω source. The effect of variation of the separation distance, d, between the RF coil and the capacitive layer was investigated to provide the largest magnitude of the magnetic field inside the phantom, along the x-axis (z=70 mm)and HIS size was X_{HIS}=40 cm. Fig.3.11 shows that for an increased or decreased separation between the RF coil and the capacitor layer greater than or less than 5 mm, the strength of the magnetic field is reduced inside the phantom, whereas the highest value occurs for d=5 mm.

Of particular interest is the impact of the cross-sectional area of the HIS where in practice there would be a trade off between magnetic field enhancement and available space in an MRI system bore which typically have internal diameters of approximately 60-70 cm. Fig. 3.12 shows the normalised magnetic field when X_{HIS} =40cm and the PEC only case, along the x-axis. It can be seen that there is an improvement over the full range of the x-axis. A more in-depth analysis is shown in Fig. 3.13 showing the improvement in magnetic field when compared to a PEC shield of the same cross section. As X_{HIS} increases the improvement in

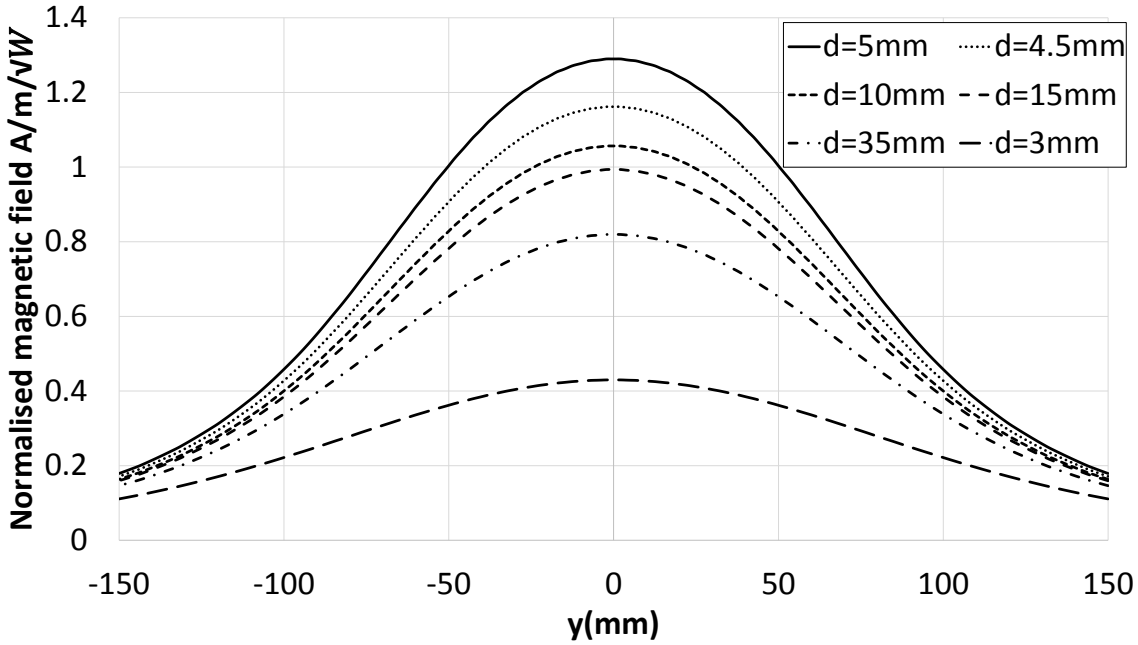

Fig. 3.11 Normalised magnitude of simulated magnetic field along y axis for varying ,d, the spacing between the HIS and RF coil.

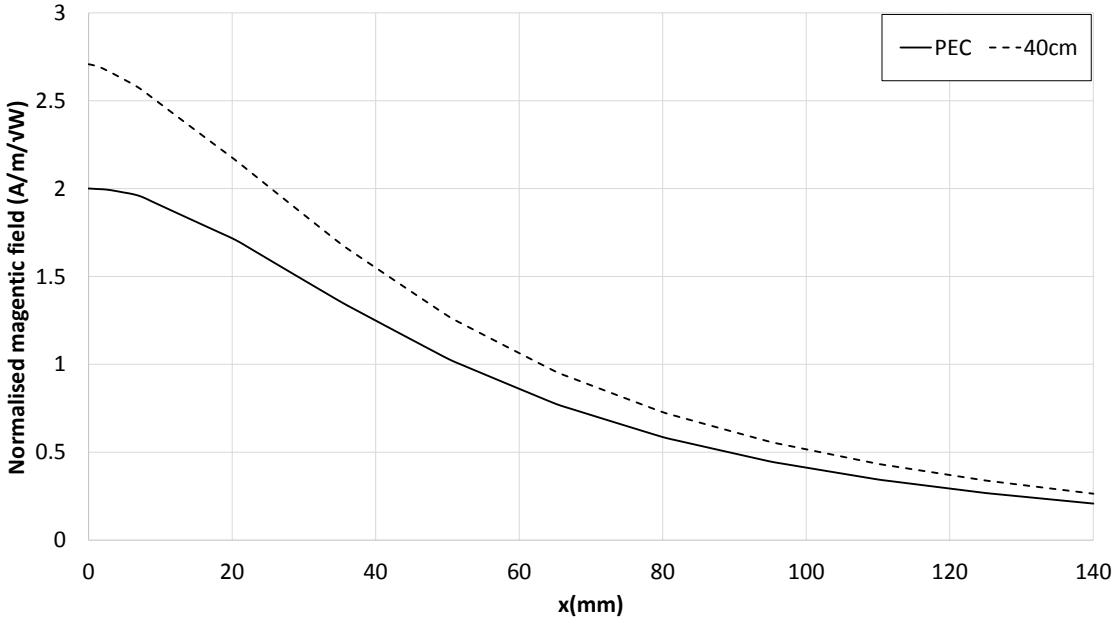

Fig. 3.12 Normalised magnitude of simulated magnetic field along x axis for the $X_{HIS} = 40cm$and a PEC case.

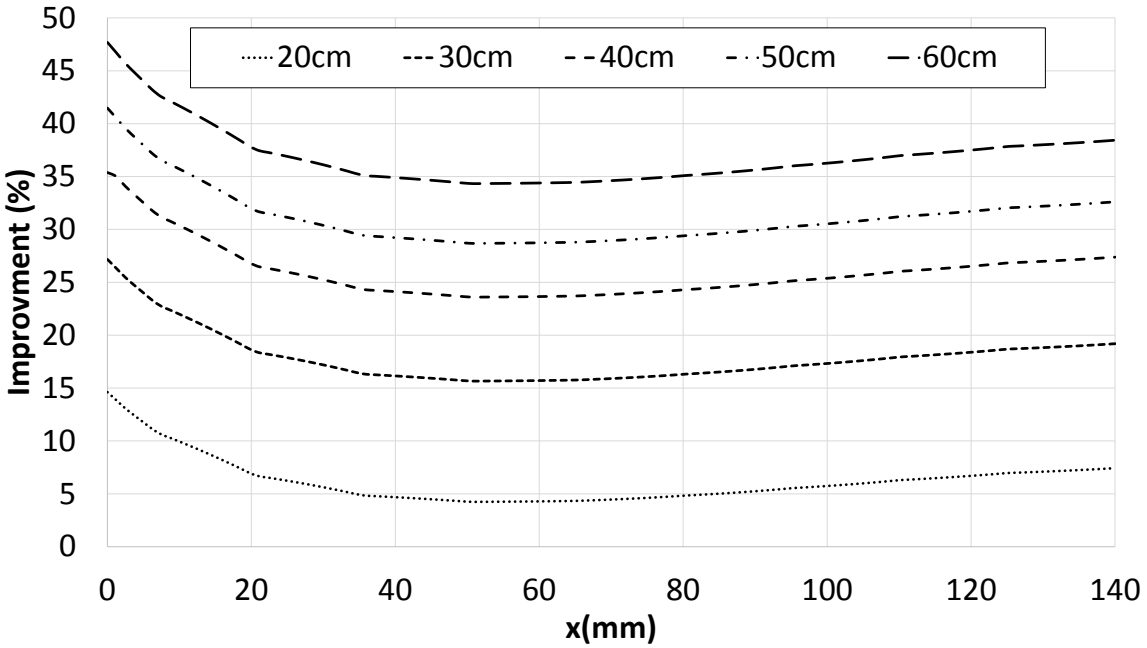

Fig. 3.13 Improvement in normalised magnetic field along x axis for varying HIS area.

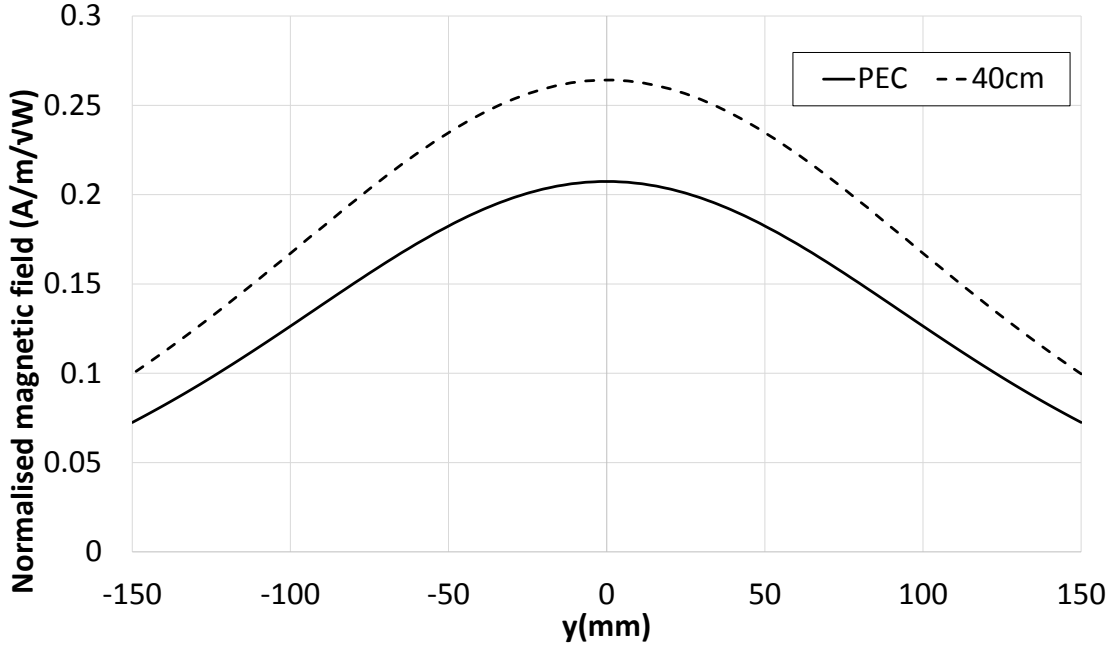

Fig. 3.14 Normalised magnitude of simulated magnetic field along y axis for varying HIS area.

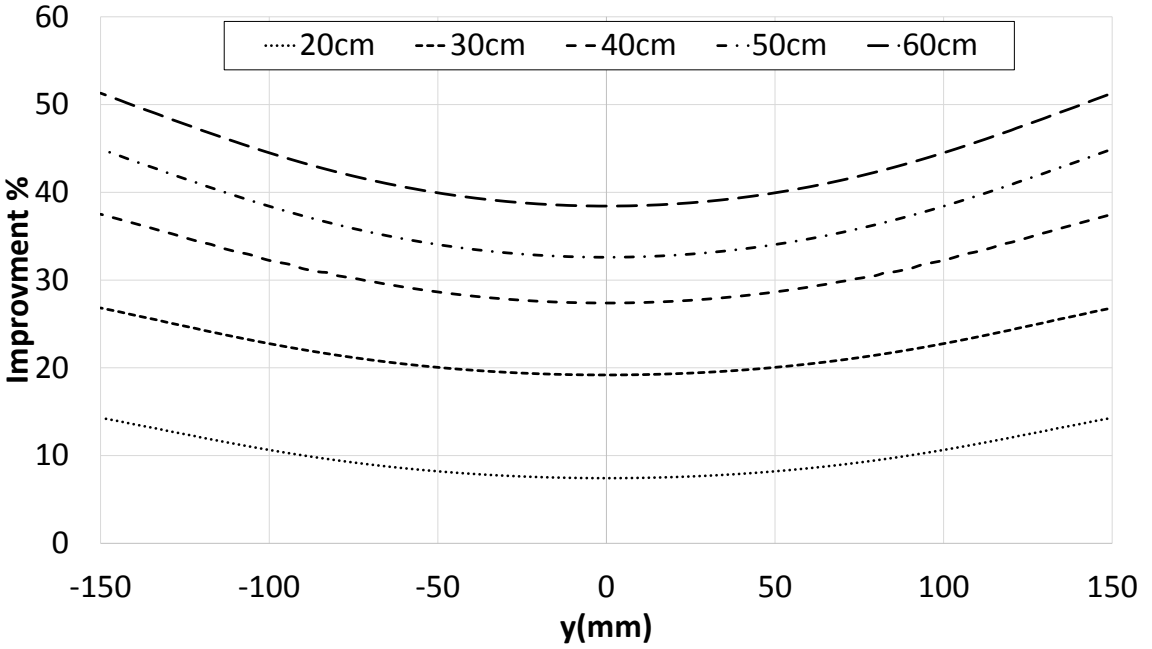

Fig. 3.15 Normalised magnitude of simulated magnetic field along y axis for varying HIS area.

magnetic field increases. Similar results are observed along the y-axis, shown in Fig. 3.14 and Fig. 3.15.

3.4.2 Cumulative density function (CDF) monitoring

Further analysis of the magnetic field throughout the volume of the dielectric phantom, in the form a cumulative density function of the magnetic field, is shown in Fig. 3.16 and the median improvement in magnetic field inside the dielectric phantom, when compared to the PEC only case, versus cross-sectional dimension is shown in Table 3.1 and it was calculated by equation (3.7).

$$Improvement_{median} = mean\left(\frac{HIS_{CDF} - PEC_{CDF}}{PEC_{CDF}}\right) \tag{3.7}$$

Fig.3.17 shows the magnitude of the magnetic field in the *xy* plane and further illustrates the

Table 3.1 Simulated median improvement in RF magnetic field (%) versus X_{HIS}

X_{HIS}	20cm	30cm	40cm	50cm	60cm
% improvement	18	22	24	31	32

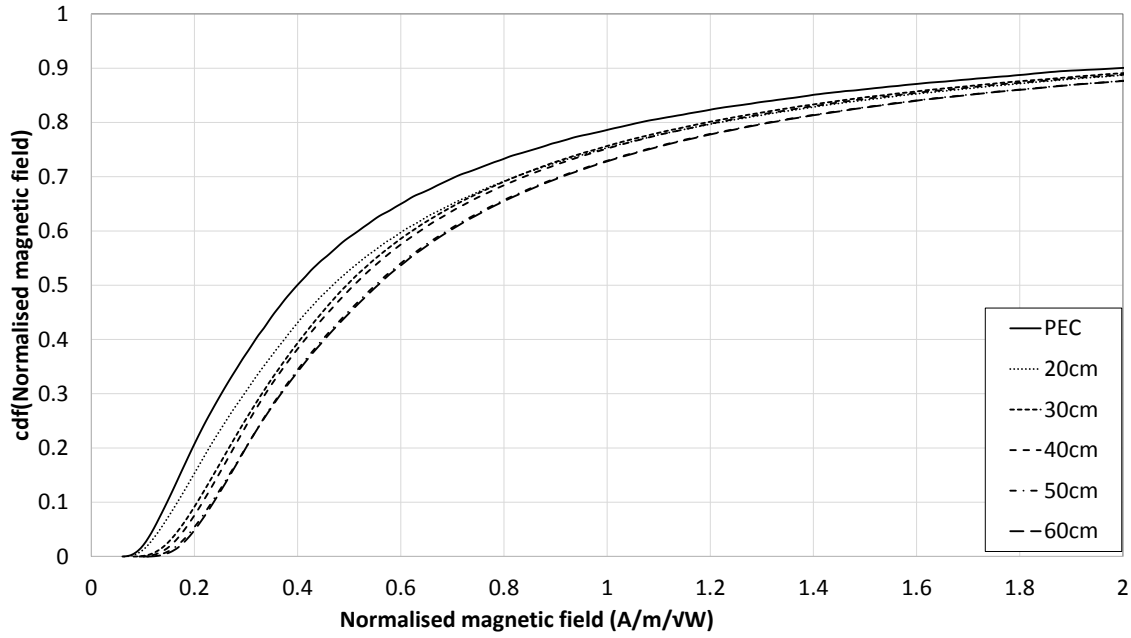

Fig. 3.16 Cumulative density function (CDF)of normalised magnetic field within the dielectric phantom.

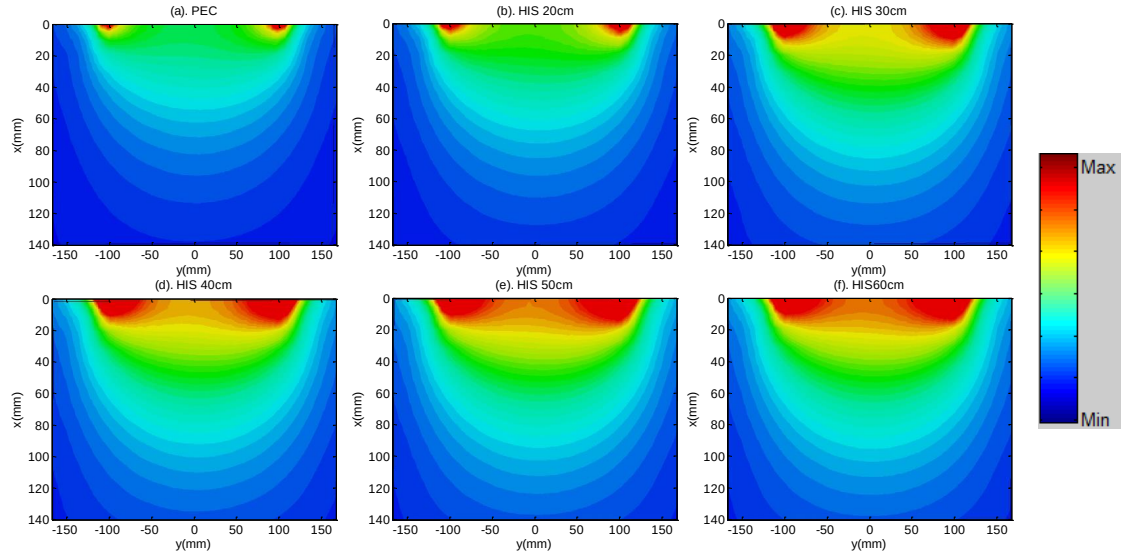

Fig. 3.17 Simulated magnitude of magnetic field inside dielectric phantom

improvement which can be achieved.

3.4.3 Magnetic flux density B_1 monitoring

In this section the enhancement on the magnitude of the magnetic flux density B_1 of the RF loop coil which was described in section 3.3 by using HIS is investigated based on the simulated model shown in Fig3.1. CST simulations were carried out for both models in Fig. 3.1 where the magnitude of the magnetic flux $|B_1^+|$ and the normalised magnitude of $|B_1^-|$ to the square root of the dissipated power P_L, $\frac{|B_1^-|}{\sqrt{P_L}}$ inside the dielectric phantom was monitored along the x-axis (y=z=0) assuming s=d=5 mm and the RF coil was fed by a 1 W, 50Ω source.

The context for these definations is to establish the important parameters for the designs presented in this thesis where SNR was given by equation (1.47) as $SNR \approx \frac{|sin\left(\gamma\tau|B_1^+|\left(B_1^-\right)^*|\right.}{\sqrt{P_L}}$. Figs. 3.18 and 3.19 show the magnitude of the magnetic flux density $|B_1^+|$ and normalised B_1^- respectively along x-axis (y=z=0, x=0 to x=140mm). The results illustrate that there is a maximum improvment of 34% and 27% at $x = y = z = 0$ for the B_1^+ and $\frac{B1^-}{\sqrt{P_L}}$ respectively.

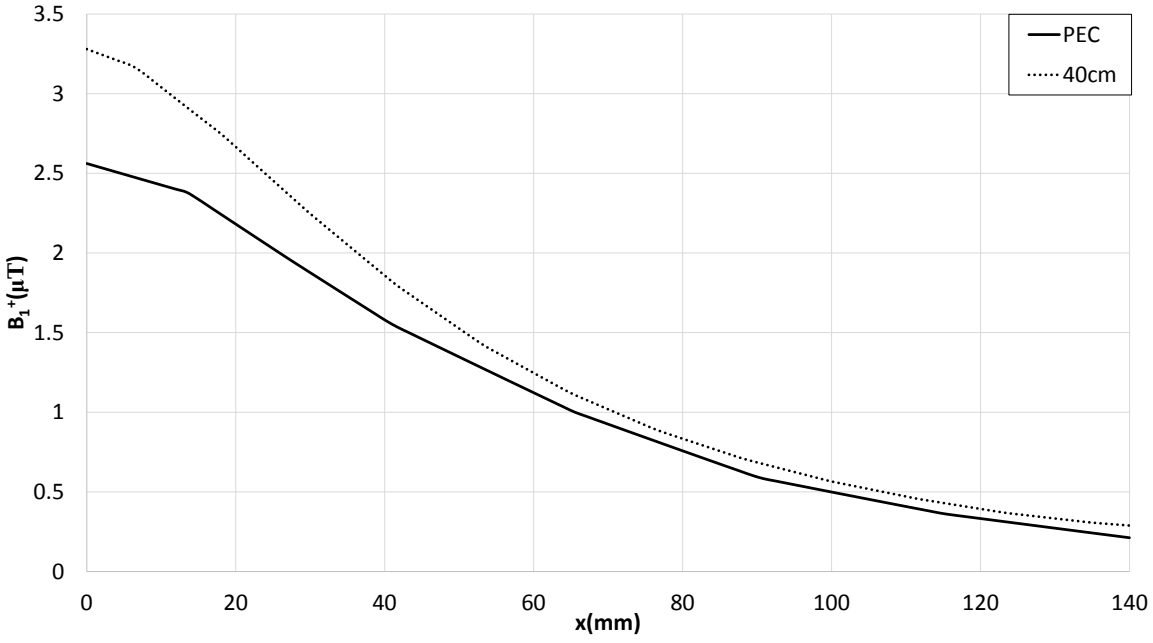

Fig. 3.18 Simulated magnitude of(B_1^+) inside dielectric phantom along x-axis, $y = z = 0$

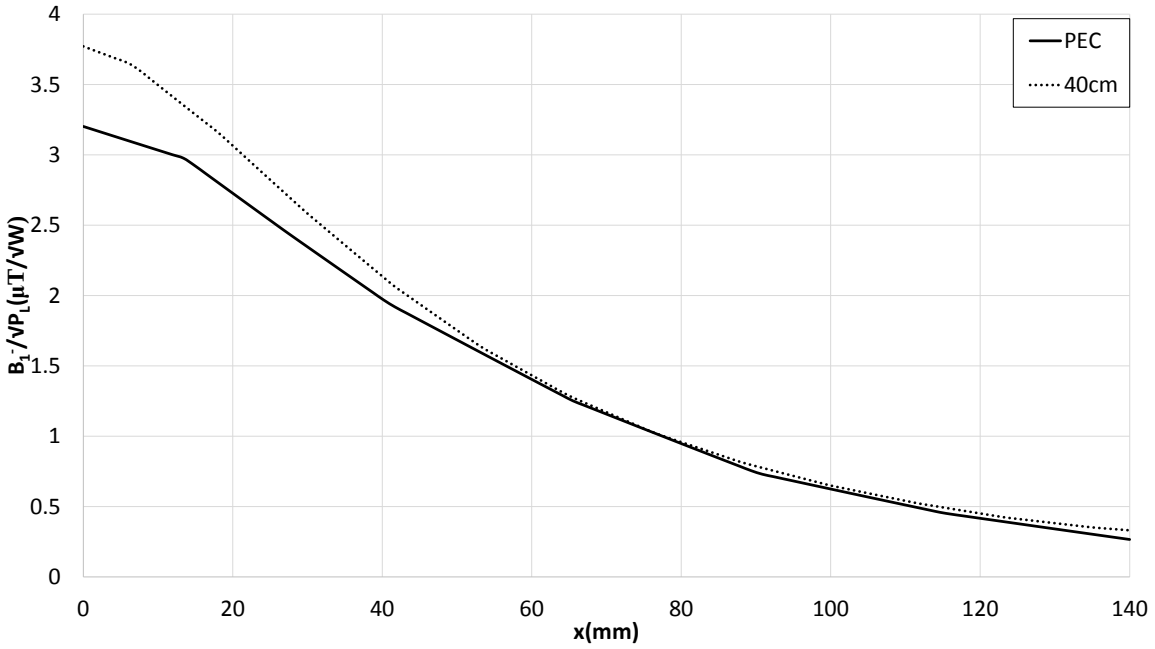

Fig. 3.19 Simulated magnitude of($\frac{B1^-}{\sqrt{P_L}}$) inside the dielectric phantom along x axis, $y = z = 0$

3.4.4 Electric field

Fig. 3.20 shows that the magnitude of the electric field is also increased when compared to the PEC case by approximately 14% at the maximum E-field position (y=100mm or y=200mm). It is observed from Fig. 3.20 that the minimum electric field is obtained at the centre of the phantom and the maximum values obtained at a position in the phantom corresponding to the distance between the centre of the coil and its edges. Due to this increase in E-field the effect on the SAR was then investigated further.

3.4.5 Specific Absorption Rate (SAR)

The SAR is a factor used to measure the electromagnetic energy absorbed by the biological tissue when exposed to a radio frequency magnetic field. The HIS can be used to improve the magnitude of the magnetic flux density, but when the $|B_1^+|$ distribution is changed the electric field and SAR distributions are also altered. In this section SAR levels inside the homogeneous dielectric phantom for the cases of with and without the capacitive layer are investigated and compared. The local SAR values can be evaluated within the biological tissue using (3.8)

$$SAR = \frac{1}{\rho_m}\frac{\partial P}{d\rho_m} = \sigma\frac{E^2}{2\rho_m} \tag{3.8}$$

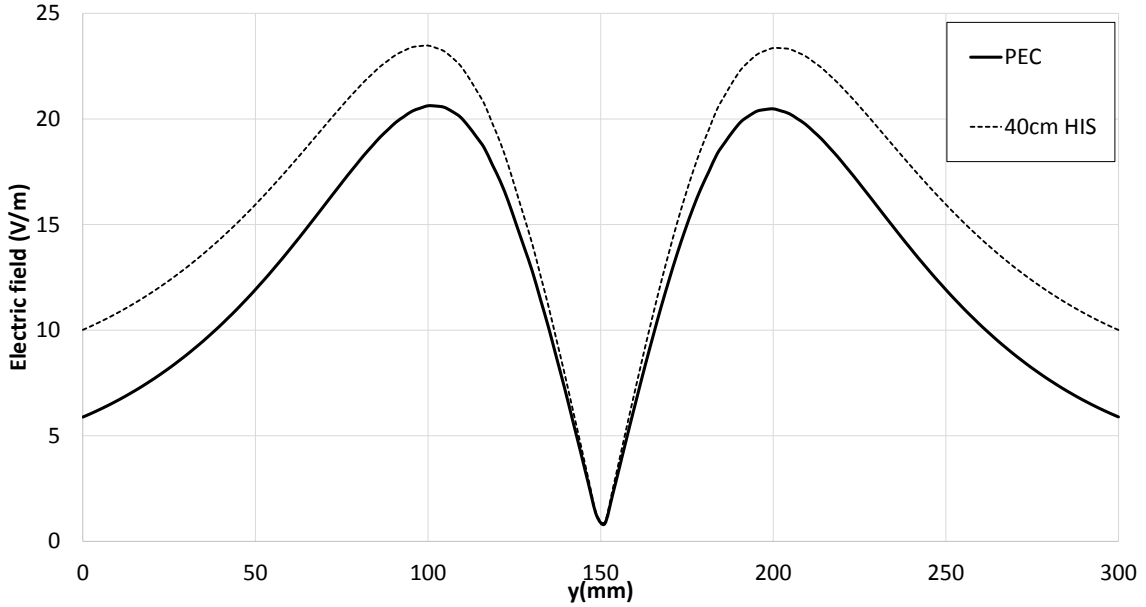

Fig. 3.20 Simulated magnitude of E-field at 45 mm above the RF coil at s=5 mm with and without the HIS.

where ρ_m is the tissue mass density in (Kg), E is the electric field produced in the body tissue, σ is the conductivity of the tissue in (S/m). In order to save the patients from rapid increase of the tissue temperature, which causes tissue harm during the MRI scan, the maximum SAR level in the RF health and safety guidelines such as IEC2010 standard [112], must not be exceeded. In these standards the SAR is averaged over a specific reference tissue mass from the body, often one gram (1 g), or 10 g or the whole body mass. In this section the SAR is investigated inside the homogeneous dielectric phantom for the cases of with and without the capacitive layer. All values of SAR have been normalized to a 1W transmission power. Following the full field simulations the values for the maximum 10g sample in the phantom and the whole body SAR were calculated using the in-built facility in CST. The simulated SAR values for the maximum 10g case were 5.6W/kg and 3.3W/kg for the capacitive layer and without capacitive layer respectively. The maximum value allowed by the IEC60604-2-33/2010 standard is 10W/kg. The whole body SAR was 0.26W/kg and 0.11W/kg for the capacitive layer and without capacitive layer respectively which can be compared to the IEC standard of 2W/kg [112].

3.5 Experimental Validation with a Dielectric Phantom

3.5.1 Measured transmission coefficient S21 on the RF bench

To demonstrate the concept a capacitive layer was manufactured for X_{HIS}=40cm using a chemically etched 32μm copper layer on a FR4 substrate comprising of four (20cm x 20cm) individual surfaces. Fig. 3.23 shows a photograph of the experimental set-up.

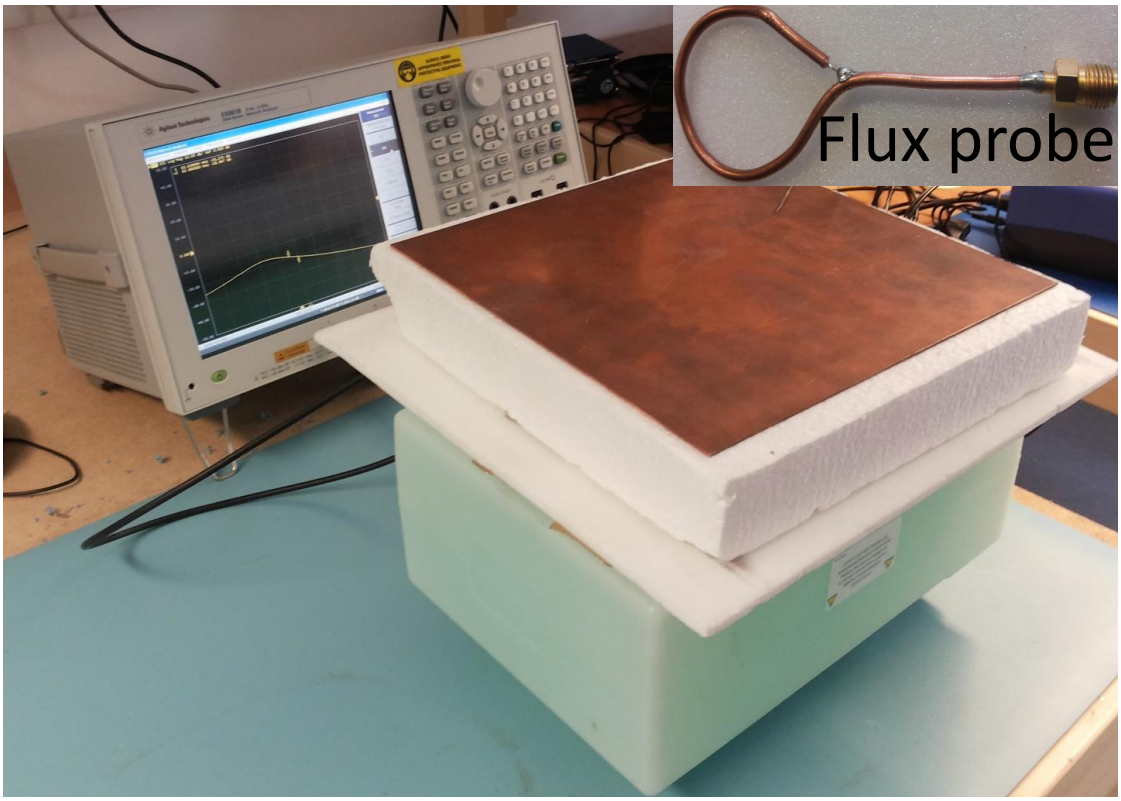

Fig. 3.21 Experimental set-up

A 5 cm diameter magnetic flux probe was built in-house using semi-rigid coaxial cable and the transmission coefficient (S21) between the RF coil and flux probe was measured such that comparisons between the models in Fig. 3.1 could be carried out. As the flux probe is an electrically small loop, where the resonant frequency of the loop was measured to be 2.2GHz, it was assumed that the probe will have negligible effect on the measurements and the comparisons against simulations is valid. Fig. 3.22 shows the normalised measured S21 along the x-axis ($y = z = 0$) and Fig. 3.23 shows the normalised S21 along the y-axis (x=140 mm, z=0). The S21 was normalised to the maximum of the PEC case for ease of comparison. The improvement in magnetic field measured at the bench (x=5 mm and x=140

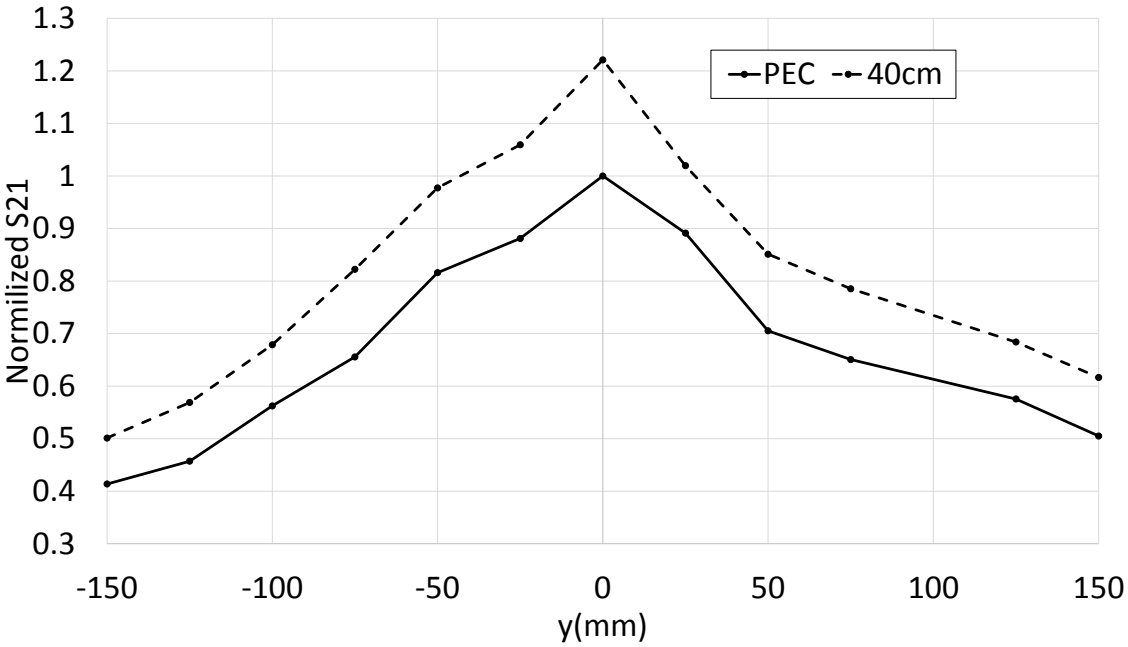

Fig. 3.22 Normalised magnitude of measured S21 along x axis

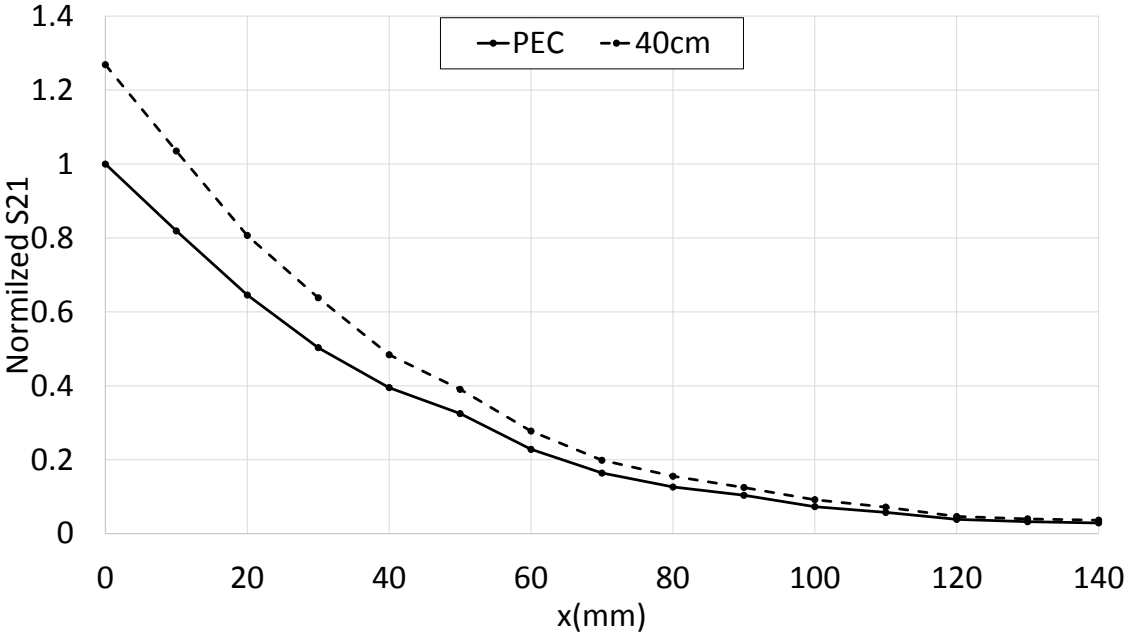

Fig. 3.23 Normalised magnitude of measured S21 along y axis

mm, y=z=0) 27% and 23% respectively, which is lower than the simulations due to tolerances in fabrication and uncertainties in material losses, however, the overall trends are similar.

3.5.2 Q-factor measurements

The Q-factor value was measured using two loop probe which measured the transmission coefficient $S21$. The cables of each coil (coil with HIS, and coil without HIS) were removed to prevent any RF interference with the probes. Q_{loaded} was first measured using a dielectric phantom to load the loop coil. The dielectric phantom was removed in order to measure the $Q_{unloaded}$. In order to insure fair comparison, the distance from the coil to the double probe was 2.5cm for the two cases. Table 3.2 shows the measured results of the Q-factor for both systems. The results show that the both of the coils with and without HIS can achieve more than 83 % of maximum SNR, as shown in appendix B, equation (B.2).

Table 3.2 The Q-factor measured results with and without the HIS

	Qunloaded	Qloaded	ratio
coil only	160	47.3	3.38
coil with HIS	70	21.7	3.2

3.6 Demonstrated HIS within a 1.5T MRI scanner

Fig. 3.24 shows the process of the proposed system as a transmit/receive RF coil within the 1.5T whole body MRI scanner. Homogeneous saline water phantom images were acquired on a 1.5T MRI machine (Hallamshire Hospital, The University of Sheffield). The images were acquired with identical imaging parameters with and without the HIS placed as shown in Fig.3.25, after the coil was matched and tuned to Larmor frequency 63.877MHz, The measurement parameters are listed in Table 3.3. The signal intensity at r, $S(r)$, was analysed to calculate the image SNR using (3.9)

$$SNR = \frac{S(r)}{\sqrt{2}\sigma} \tag{3.9}$$

where σ is the standard deviation of $S(r)$ in a region of the image away from the phantom which provides the background noise. Fig.3.25 shows the dielectric phantom image with and without HIS. The measured SNR of the dielectric image has been achieved using the two regions approach as shown in Fig. 3.26 which has been described by (3.9). Table 3.4

Fig. 3.24 The proposed system with a 1.5T MRI

Table 3.3 MRI scanner settings

Parameter	Value
Pulse repetition time (ms)	600
Echo time (ms)	20
Bandwidth (kHz)	15.60
Field of view (cm)	30 x 30
Slice thickness (mm)	5
Acquisition matrix (pixels)	256 x 256
Transmission gain TG (dB)	3

shows the measured SNR with and without the HIS at the coil center at (x=20, 25, 50 and 100mm),(y=z=0). The results show that using the HIS as a reflector instead of only PEC the SNR can be improved by up to 6%, and the enhancement is observed for the first 20 mm,then the SNR with using HIS is slightly less than a PEC case. The improvement in measured SNR was lower than the simulated improvement of magnetic field flux density and measured transmission coefficient because of the tolerances fabricated errors.

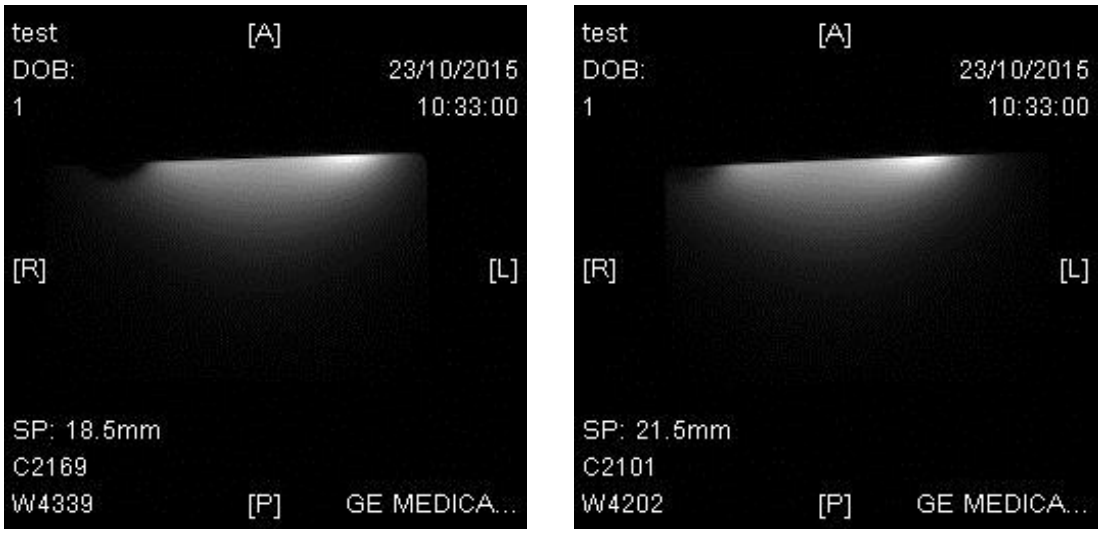

(a) (b)

Fig. 3.25 The Dielectric phantom image (a). No HIS. (b). with HIS

(a) (b)

Fig. 3.26 The measured SNR of Dielectric phantom image at 25mm depth inside the phantom (a). No HIS. (b). with HIS

Table 3.4 Measured signal to noise ratio with and without HIS at the coil center $(x = 0tox = 140mm)(y = z = 0)$

x(mm)	With HIS	Without HIS
20	220	207
25	196	197
50	81.4	84
100	13.7	13.85

3.7 Summary

This chapter presents on the applications of a high impedance surface (HIS) to enhance the performance of 1.5T MRI systems instead of only a PEC shielde. Our work has investigated the 1.5T MRI performance metric, which include (H_1), (B_1), specific absorption rate (SAR), and measured signal to noise ratio (SNR). The proposed structure was based on a miniaturized HIS using an interdigital capacitance approach, where the proposed HIS has unit cell size of $\lambda/94$ at the operation frequency (63.8MHz). The surface utilizes a HIS between the RF transceiver coil and the MRI scanners RF shield which operates at 63.8MHz. Also, this chapter has investigated the normalised magnetic field generated by an RF coil with and without a HIS shielded cross section area of the dielectric phantom and the comparison has been made. This changing of a HIS area shows that the improvement in magnetic field increases with the HIS area. However, HIS area was selected to be $40 \times 40cm$ due to practical limitation of the MRI scanner dimension. The results show using the HIS approach as a reflector instead of only PEC there was maximum improvement of 24%, 34% and 27% in H_1, B_1^+ and $\frac{B_1^-}{\sqrt{P_L}}$ along x-axis respectively. This concept has been demonstrated through the measurements by measuring the transmission S21. The normalised S21 along x-axis, and y-axis was improved by 21%, and 23% on average. The measured results were slightly different of the simulated results, the small difference was due to the tolerances in fabrication of the HIS, for instance the FR4 substrate dielectric constant was assumed to be 4.3 in CST, however, its value in reality is a range between (4 to 5) which has an effects on the capacitive value of the sheet. Nevertheless, the overall trends are almost similar. Table. 3.5 shows the gap which has been demonstrated in this chapter.

Table 3.5 A comparison between using the HIS method against the state-of-art methods from published literature. ((‡- Volume coil †- Surface coil))

Metric	**Approaches**	**1.5T,** $f_0 = 64MHz$	**3T,** $f_0 = 128MHz$	**7T,** $f_0 = 300MHz$
$\lvert B_1^- \rvert$	HIS	**10% †**	-	7% ‡[37] 25%†[72]
	Metasurface	-	-	-
	RF lens	-	-	-
	Dielectric pads	-	50%‡[95]	100%‡[103]
SNR	HIS	**6% †**	-	-
	Metasurface	270%‡[91]	-	-
	RF lens	100% [64]	200% [64]	-
	Dielectric pads	-	20-40%‡[95]	53%‡[98], 200%‡[103]
Penetration depth	HIS	**20mm †**	-	-
	Metasurface	-	-	-
	RF lens	35mm†[64]	40mm†[64]	-
	Dielectric pads	-	-	-
SAR	HIS	**+13.6% †**	-	+48% †[71]
	Metasurface	-	-	-
	RF lens	-	-	-
	Dielectric pads	-	-50% ‡[95]	-33% ‡[98]

Chapter 4

A Reflective Capacitive Impedance Surface for 1.5 Tesla Magnetic Resonance Imaging Applications.

4.1 Introduction

Chapter 3 presents a novel design of a high impedance surface (HIS) to improve the magnetic field strength of a radio frequency (RF) coil at 63.8 MHz, suitable for 1.5 T magnetic resonance imaging systems. The measured SNR results showed that only very limited improvement can be obtained due to fabrication tolerance error. This chapter presents an alternative new approach which is a reflective capacitive impedance surface (RCIS) combined with a radio frequency loop coil to improve 1.5T magnetic resonance imaging performance. The proposed structure is based on a miniaturised frequency selective surface (FSS) using an interdigital capacitance approach. Simulations of the system performance were performed by comparing the performance metrics of the RF coil with and without the proposed method. The performance metrics are; the magnetic field (H_1), magnetic flux density (B_1), electric field (E) and specific absorption rate (SAR). The simulations results were validated by vector network analyser and measured SNR using a 1.5T MRI scanner. This chapter is organized as follows: an idealised surface impedance concept is introduced in section 4.2 in order to find the maximum capacitive value of the sheet. Section 4.3 introduces losses into the RCIS which is determined in the previous section and the impact of this is discussed. The numerical simulation results which represented the 1.5T MRI system performance using CST-MW 2015 time and frequency domains solver are presented in this section. The experimental

measurements results of the proposed system in a RF laboratory are shown in section 4.4. The proposed system is demonstrated within the 1.5T MRI scanner in section 4.5. Finally, section 4.6 concludes the chapter and comparison are made with previous approaches.

4.2 The MRI system concept and CIS design

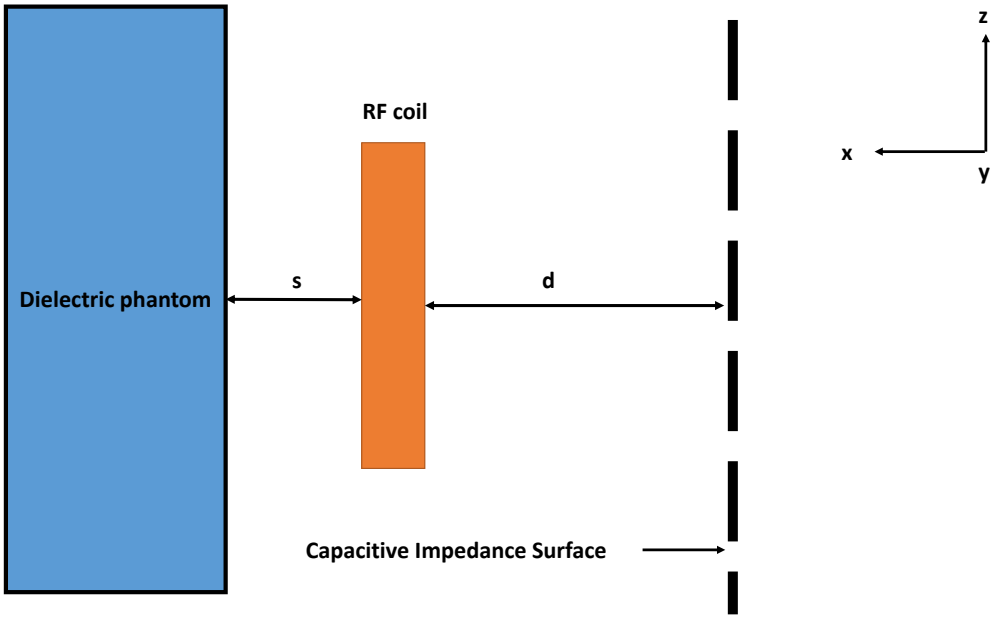

Fig. 4.1 MRI system with surface impedance concept model

4.2.1 System with idealised surface impedance

A cross section of the system of interest is shown in Fig.4.1, which consisted of a reflective capacitance impedance surface (RCIS), where its area was assumed to be 40 cm$\times$40 cm and spaced $d = 20mm$ from the RF coil which operates at 63.8MHz and the dielectric phantom which represented the human body model, was placed a distance $s = 5mm$ away from the RF coil. The RCIS is assumed to have an impedance given by $Z = R - jX_c$ dominated by capacitance. In this section for idealised case, the losses were assumed to be zero (R=0), in order to optimise capacitance value of the RCIS that produces the higher value of the normalised RF magnetic flux density inside the dielectric phantom. During the numerical simulation, performance metrics, which include magnetic field and normalised magnetic flux density, were compared to the case when the RCIS is not included. The RF surface

coil, previously reported in chapter 3, with dimensions of 120 mm width by 150 mm length, was fed by 1A sinusoid current source at 63.8 MHz. A homogeneous dielectric phantom which was used in the previous chapter was used in simulation and experimental work. In this section this simulation was implemented as an ideal surface impedance model as shown in Fig.4.2. The normalised magnitude of the magnetic flux density and magnitude of the RF magnetic field inside the dielectric phantom were monitored through the x-axis. For a

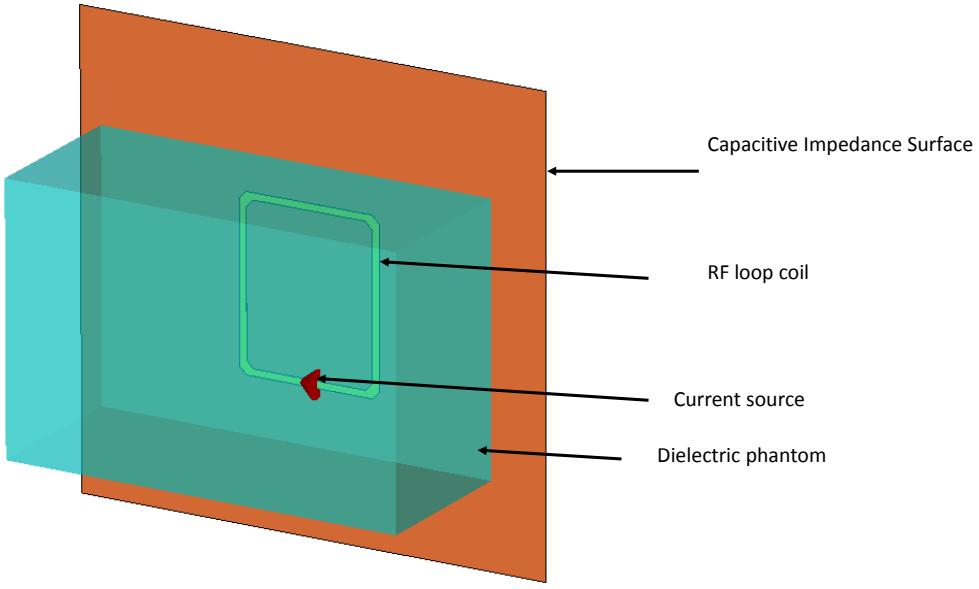

Fig. 4.2 Simulated geometry with ideal CIS

fair comparison the magnetic field H_1, and magnetic flux density B_1^- were normalised to the square root of the system absorbed power $\sqrt{P_L}$. The normalised value of the H_1, and B_1^- are given by 4.1, and 4.2 respectively.

$$H_{1,normalised} = \frac{|H_1|}{\sqrt{P_L}} \tag{4.1}$$

$$B^-_{1,normalised} = \frac{|B_1^-|}{\sqrt{P_L}} \tag{4.2}$$

where P_L is dissipated power through all system components and it can be calculated using 4.3, and 4.4 for the coil only and with the RCIS respectively.

$$P_L = P_{coil} + P_{phantom} \tag{4.3}$$

$$P_L = P_{coil} + P_{phantom} + P_{RCIS} \tag{4.4}$$

The context for these definitions is to establish the important parameters $B_{1,normalised}^{-}$ and $|B_1^+|$ for the designs presented in this thesis. As it mentioned in chapter 1 equation (1.47) and mentioned in chapter 3 that $SNR \approx |sin(\gamma\tau|B_1^+|(B_{1,normalised}^{-})^*|$.

Fig. 4.3 and 4.4 show the $B_{1,normalised}^{-}$ along x-axis of the dielectric phantom when the capacitive sheet changing from 40pF-120pF and from 150pF-250pF, respectively. The results illustrate that the $B_{1,normalised}^{-}$ can be significantly increased with the use of a RCIS and there is maximum improvement at all penetration depths when the sheet capacitive value is $115pF$. Fig. 4.4 illustrates that as the RCIS capacitance value increases further the improvement in $B_{1,normalised}^{-}$ reduces to a point where the impedance is having a detrimental impact. It is observed that there is a limit in the penetration depth inside the phantom that can be accomplished for higher sheet capacitance value, for example there is no enhancement in the normalised magnetic flux density after 60mm when the RCIS capacitance is 150pF, for 220pF there is no improvement beyond 30mm and for 250pF there is a reduction in $B_{1,normalised}^{-}$.

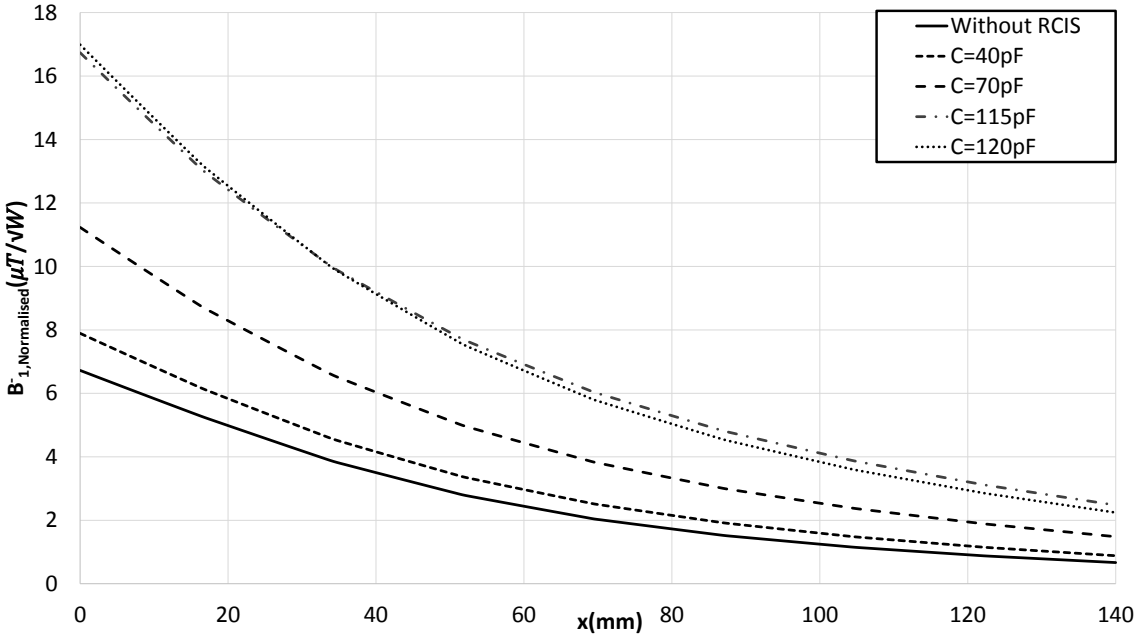

Fig. 4.3 $B_{1,normalised}^{-}$ inside the dielectric phantom along the x-axis for varying capacitance values.

The effect of a variation of the separation distance, d, between the RF coil and the capacitive layer was investigated in Fig.4.5 to provide the largest $B_{1,normalised}^{-}$. The $B_{1,normalised}^{-}$ inside the dielectric phantom was monitored, along the x-axis (x=0, to x=140). The results

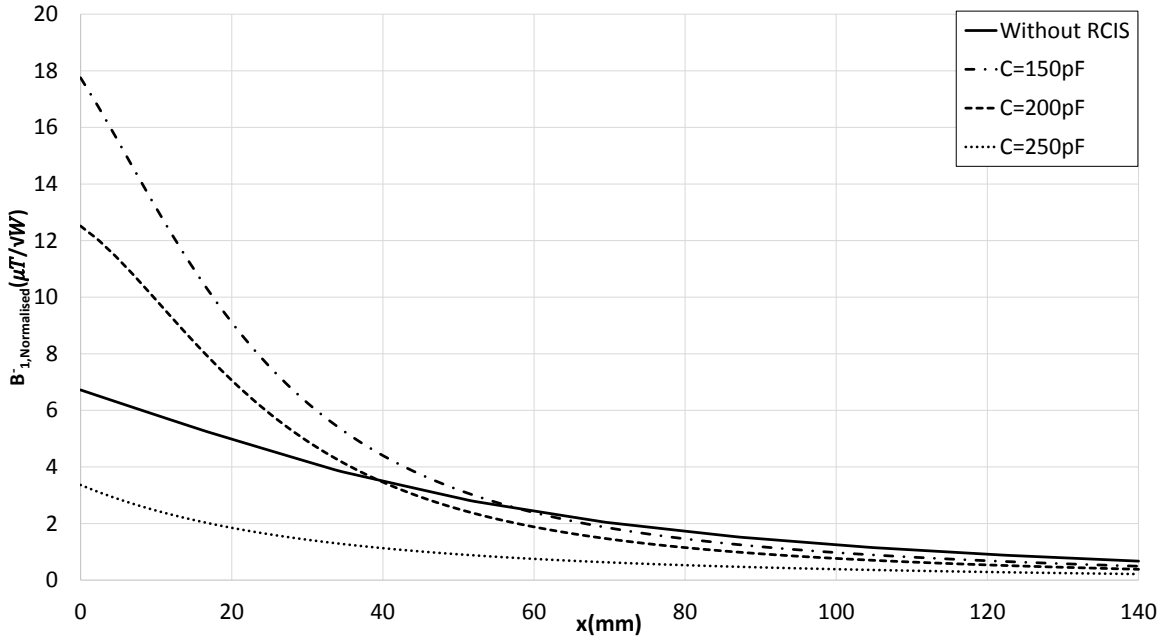

Fig. 4.4 $B^{-}_{1,normalised}$ inside the dielectric phantom along the x-axis for high capacitance values.

show that the largest $B^{-}_{1,normalised}$ can be achieved when $d = 20mm$. However, the $B^{-}_{1,normalised}$ was significantly decreased when the RF coil was close to the (RCIS).

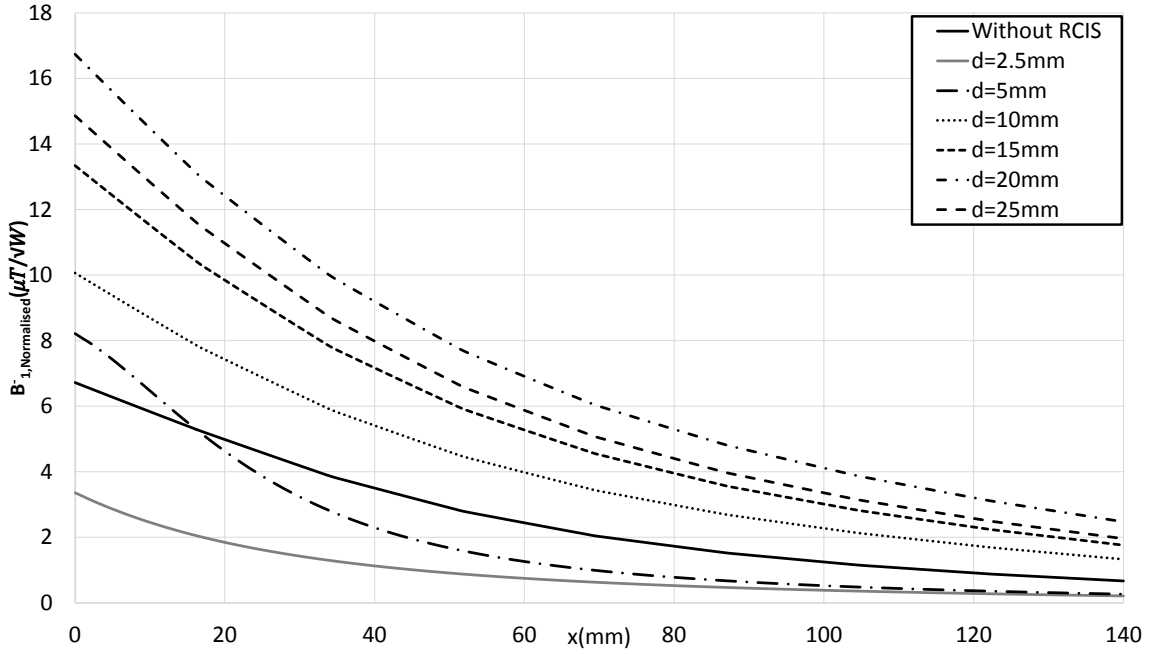

Fig. 4.5 $B^{-}_{1,normalised}$ inside the dielectric phantom along the x-axis for different d values.

Fig.4.6 illustrates the $|B_1^+|$ across the dielectric phantom in the loss less case when the capacitance of the sheet is 115pF. It can be seen that there is a significant improvement in $|B_1^+|$ at all penetration depth of the dielectric phantom.

The fundamental principle behind the magnetic flux density improvement is redistribution of

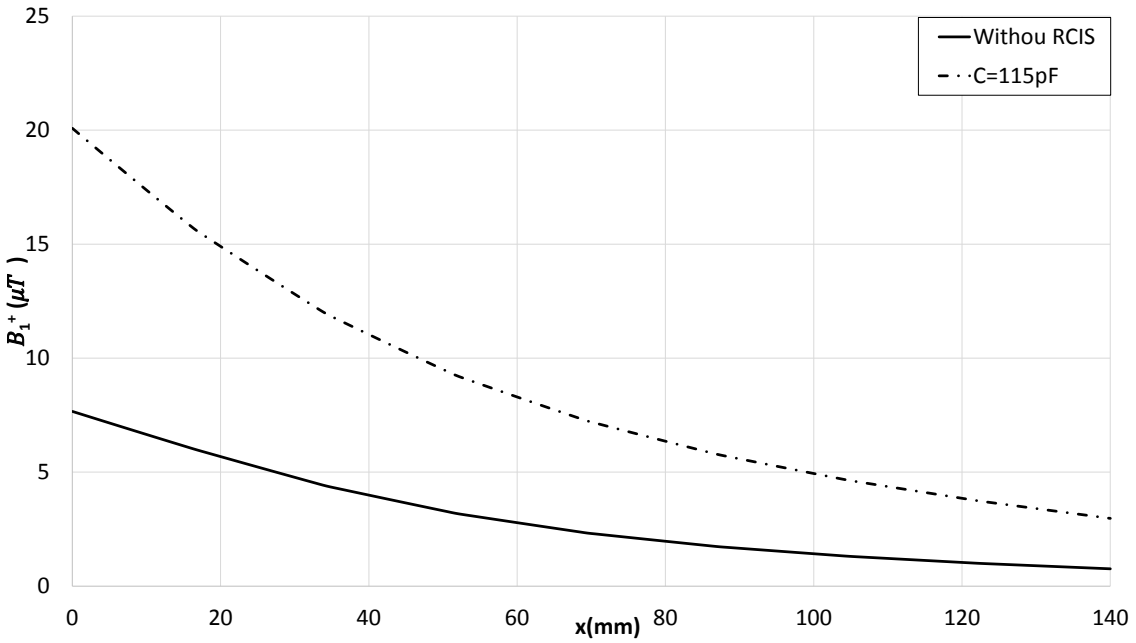

Fig. 4.6 Magnitude of B_1^+ inside the dielectric phantom along the x-axis for 115pF capacitance value

near field properties of the RF coil due to coupling effects with the RCIS. Placing a capactive surface as a reflector can modify the $|B_1|$ pattern of the coil in the region-of-interest ROI inside the dielectric phantom. Fig.4.7 shows the simulated magnitude of $|B_1^+|$ across the xy-plane with and without using the RCIS. Fig.4.7 also shows that the $|B_1|$ increase inside the dielectric phantom due to coupling effects between the RF coil and RCIS. In this way, using RCIS were able to provide higher local efficiency of the RF received magnetic flux density and potentially higher image SNR which will investigate in more detail in the next sections of this chapter.

4.2.2 Realsitic CIS design

After the RCIS was optimised by simulations to produce maximum improvement in magnetic flux density, this section describes a technique for implementing the properties of the ideal reflected CIS for which the basic concept was reported in chapter 3 and is based on a

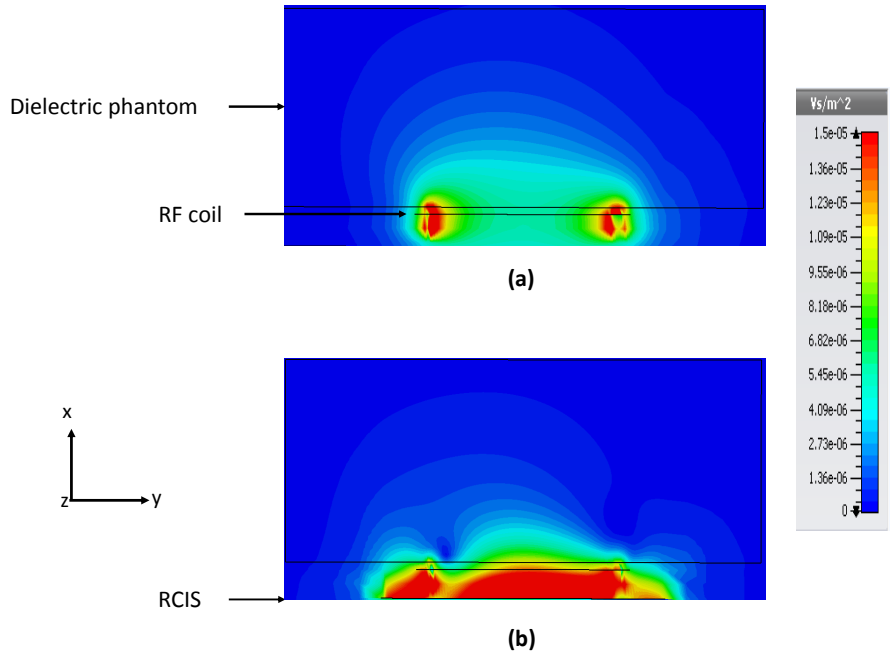

Fig. 4.7 Simulated $|B_1^+|$ across xy plane (z=0), (a) without RCIS, (b) with RCIS

frequency selective surface FSS. Fig.4.8 illustrates the top layer of the proposed FSS unit cell where the back layer is oriented orthogonally. As mentioned in chapter 3 the combination of the top and bottom FSS layers provide a dual polarized unit cell which consists of interdigital metallic elements on a 0.8mm thick FR4 substrate $\varepsilon_r = 4.3, tan\sigma = 0.025)$. This unit cell geometry was chosen as it provides a high capacitance density and hence electrically small unit cells can be produced. The capacitance of the RCIS was estimated using equations (3.1)-(3.3), which were reported in chapter 3, which give the capacitance in pF.
In order to achieve a capacitance of 115pF ($-j22\Omega$ at 63.8MHz) with a square unit cell the dimensions were $D = 50mm, N = 64$, $w_d = 0.5mm$, and $g_d = 0.25mm$. There is a 0.5mm gap between the end of the digits and the metallic horizontal strip and there is a 1mm separation between the FSS unit cells. It was assumed that the metallic elements were $32\mu m$ thick copper.

Full field simulations were carried out on the FSS unit cell using CST microwave studio frequency domain where the unit cell was modeled as an infinite periodic array by employing Floquet mode boundary conditions which provides the reflection and transmission properties of the FSS. From the numerical simulations the equivalent surface impedance of the FSS can be calculated which includes the losses due to the FR4 substrate and copper. Fig.4.9 and Fig. 4.10 show the equivalent resistance and the reactance of the CIS as a function of frequency

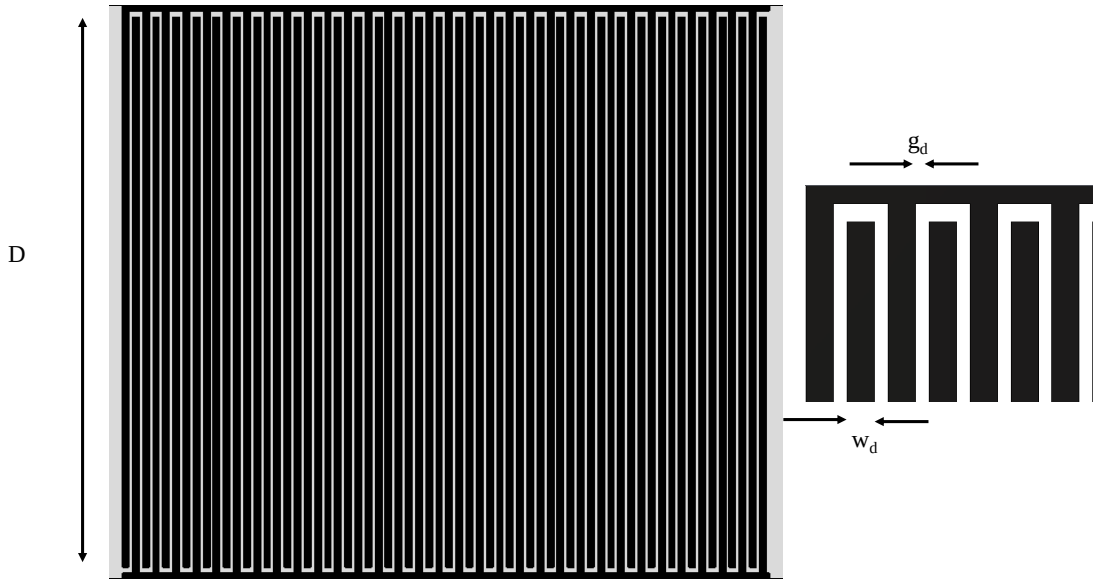

Fig. 4.8 Front layer of FSS unit cell including interdigitation dimensional detail.

from the CST simulations. The results show that the required reactance of $-j22\Omega$ can be realized.

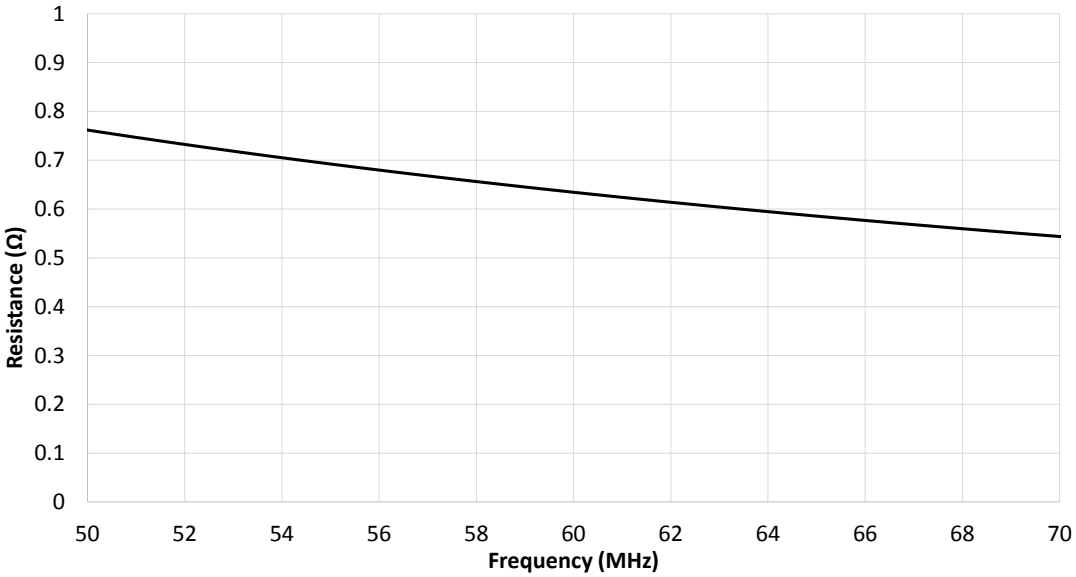

Fig. 4.9 The equivalent resistance of the CIS

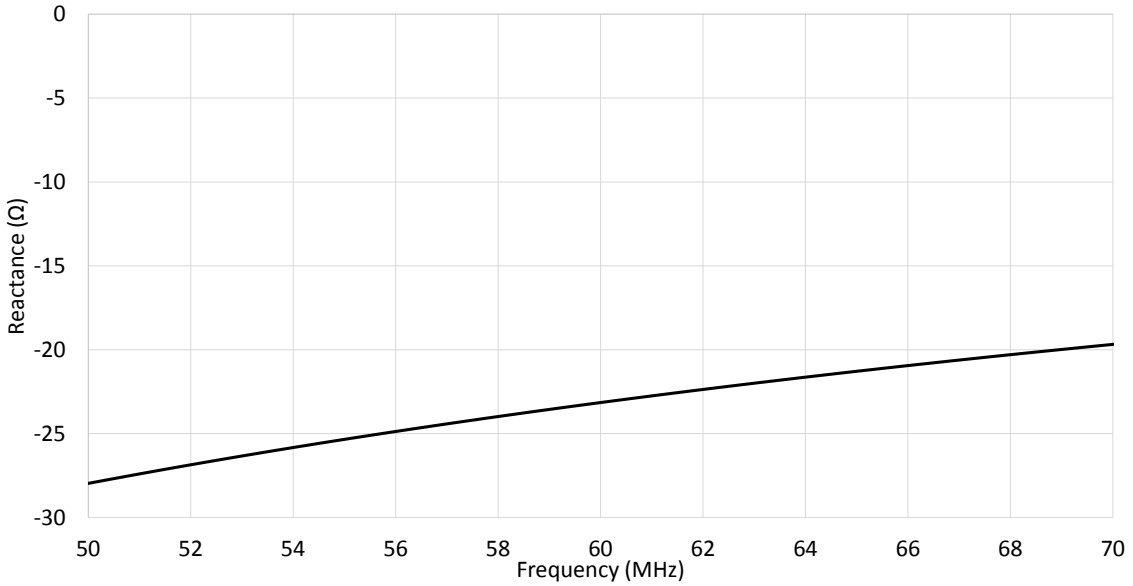

Fig. 4.10 The equivalent reactance of the CIS.

4.3 MRI System with realistic surface impedance

In this section the losses due to the substrate and copper associated with the FSS implementation is assessed in the MRI concept by modeling the frequency dependent complex impedance properties in the CST model of the MRI concept. The RF loop coil used in this chapter was reported in chapter 3 with the same dimensions $120 \times 150mm$. The fixed capacitors $C_1 - C_5$, are $100pF$, and C_m and C_{tune} are variable capacitors(78-168)pF. The power was fed to the coil through a balun circuit that is connected either side of C_m and which was 1W, 50 Ω power source in the simulation process. Fig. 4.11 shows the measured and simulated input matching (S11) when the coil is spaced 20mm away from the RCIS and 5mm away from the dielectric phantom. In the experimental process the fabricated RF loop coil was connected to a RS ZVL Vector Network Analyser and the resonances frequency was tuned to the Larmore frequency of the 1.5T MRI system at 63.86MHz using the variable capactor C_{tune} and it was 91pF, and 156pF for the only coil and with the RCIS respectively. The experimental system was matched in the case when the dielectric phantom and (RCIS) were presented using the variable capacitor C_m which was 100pF, and 168pF for the system without and with the RCIS respectively. Moreover,the S11 is presented when RCIS is removed which has the frequency shifting the measured resonance frequency from 63.8MHz to 75.4MHz. It was tuned back at the 63.8MHz for further measurements. The slight difference between the CST simulation

model and the manufactured model is due to the tolerances in the lumped elements and the coil inductive and material property assumptions.

CST simulation were carried out for the model in Fig. 4.12 where the $H_{1,normalised}$,

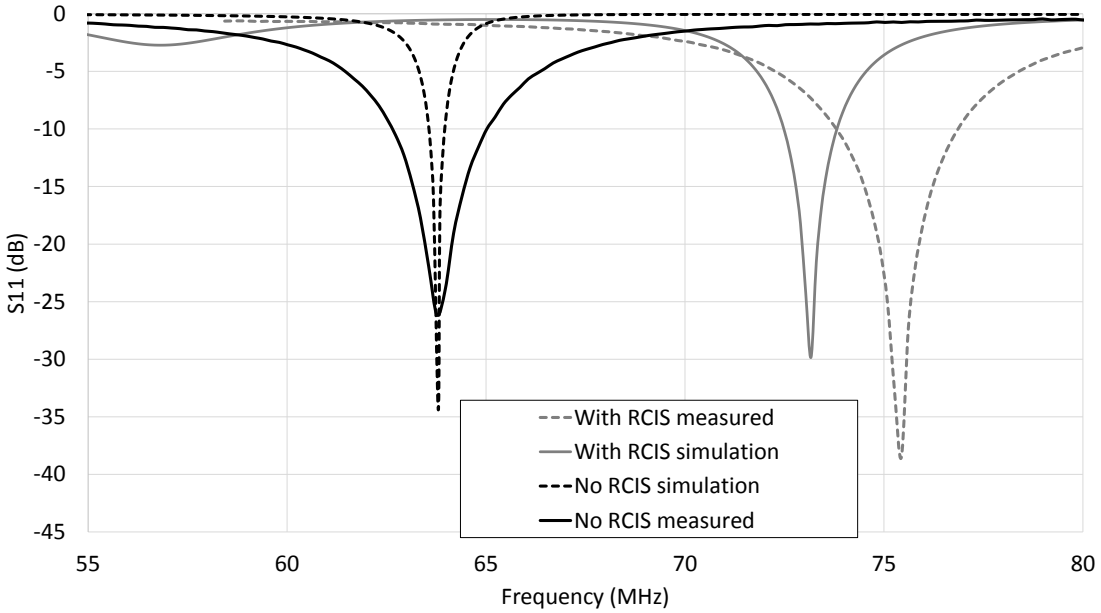

Fig. 4.11 Simulation and measurement of input match of RF coil

$B^{-}_{1,normalised}$ inside the dielectric phantom were monitored along x-axis (y=z=0) assuming the parameters in Fig. 4.1 s=5mm, d=20mm, and the RF loop coil was excited by a 1W, 50Ω source.

4.3.1 Magnetic field simulation result

Fig. 4.13 shows $H_{1,normalised}$ along x-axis throughout the dielectric phantom when the RCIS size was $40cm \times 40cm$ for the RF loop coil only case. It can be seen that there is an enhancement in average magnitude of the magnetic field of approximately 78% at the coil centre (x=0, to x=140,y=0,z=0), compared to coil alone. Further analysis of the magnetic improvement, informing a magnetic flux density is shown in the next section.

4.3.2 Magnetic flux (B_1) density simulation result

Fig. 4.14 shows the $B^{-}_{1,normalised}$ distribution across the dielectric phantom with and without using the RCIS. The results show that the $B^{-}_{1,normalised}$ can be enhanced by approximately 4

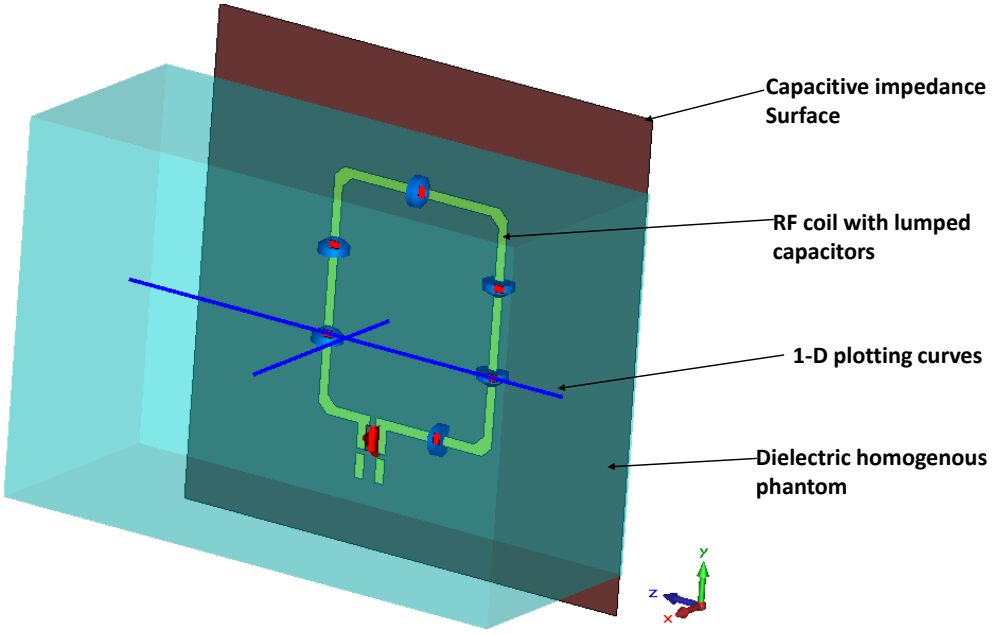

Fig. 4.12 CST simulation realistic geometry

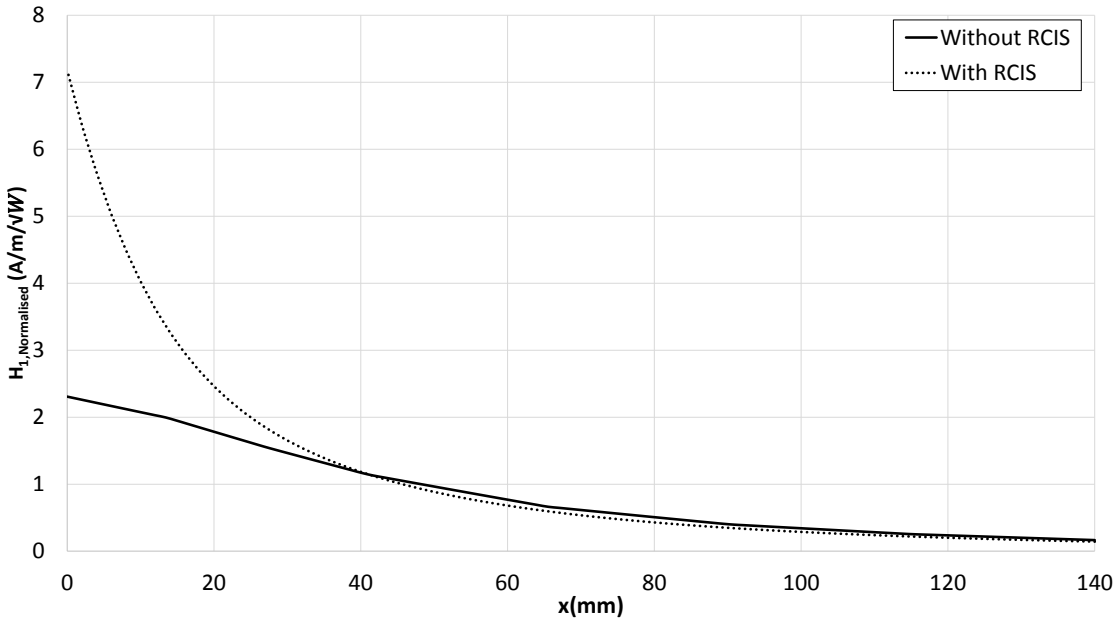

Fig. 4.13 Normalised magnitude of simulated magnetic field

times at the proposal surface of the dielectric phantom and this enhancement is observed for a depth of 30 mm by using RCIS when it compared to only coil case. Fig. 4.15 illustrates the magnitude of positively rotated magnetic flux density $|B_1^+|$ across the dielectric phantom. The result shows that by using the RCIS as a RF coil reflector the magnitude of B_1^+ can be increased up to 4 times at $x = 0$ and it decays to 40mm, then $|B_1^+|$ of both of the coils with and without the RCIS are almost the same. According to equation 1.47, the improvement in $B_{1,normalised}^-$, and $|B_1^+|$ can be directly resulted in signal-to-noise improvement.

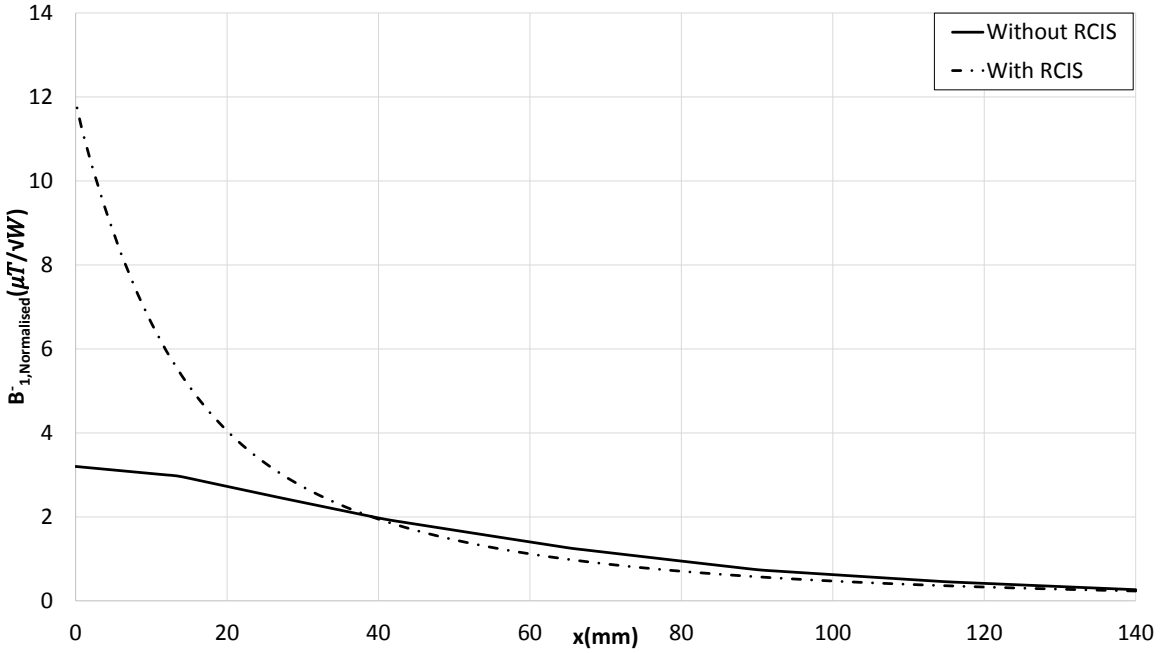

Fig. 4.14 Normalised magnitude of simulated B_1^- through the dielectric phantom B_1^-

4.3.3 E-field

Figs. 4.16, and 4.17 show the magnitude of the electric field at x=10mm, and x=40mm respectively. The Figs illustrate that the magnitude of the electric field is increased when compared to the standard case by approximately 23% at the maximum E-field position (z=-50mm or z=50mm)when the penetration depth (x=10mm). The electric field is decreased by 26% in the case of the reflector CIS to a penetration depth (x=40mm) inside the dielectric phantom compared to the coil only. It is observed from Figs. 4.16, and 4.17 that the minimum electric field is obtained at the centre of the phantom and the maximum values obtained at a position in the phantom corresponding to the distance between the centre of the coil and its arms. Due to this increase in E-field the effect on the SAR was then investigated further.

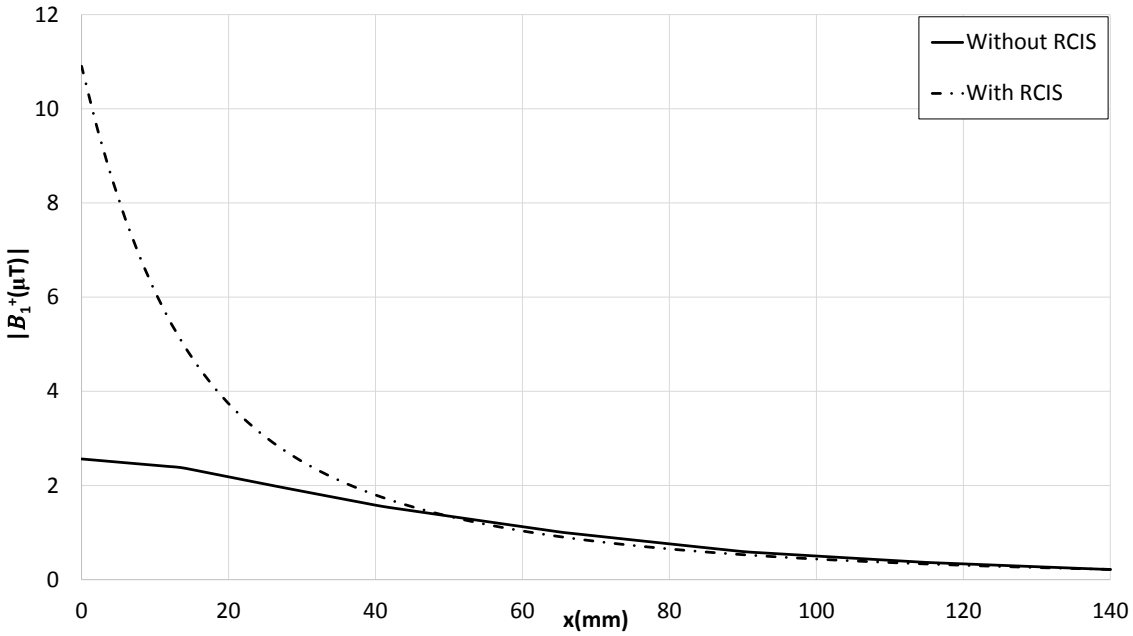

Fig. 4.15 Normalised magnitude of (B_1^+)through the dielectric phantom

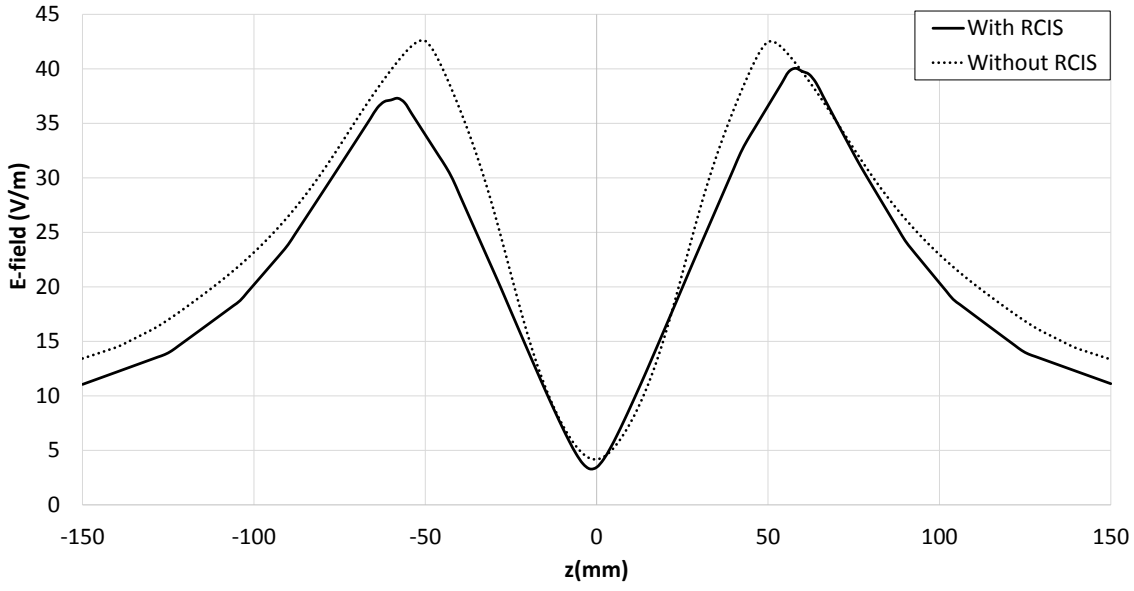

Fig. 4.16 Magnitude of simulated Electric field through the dielectric phantom ($x = 20mm$)

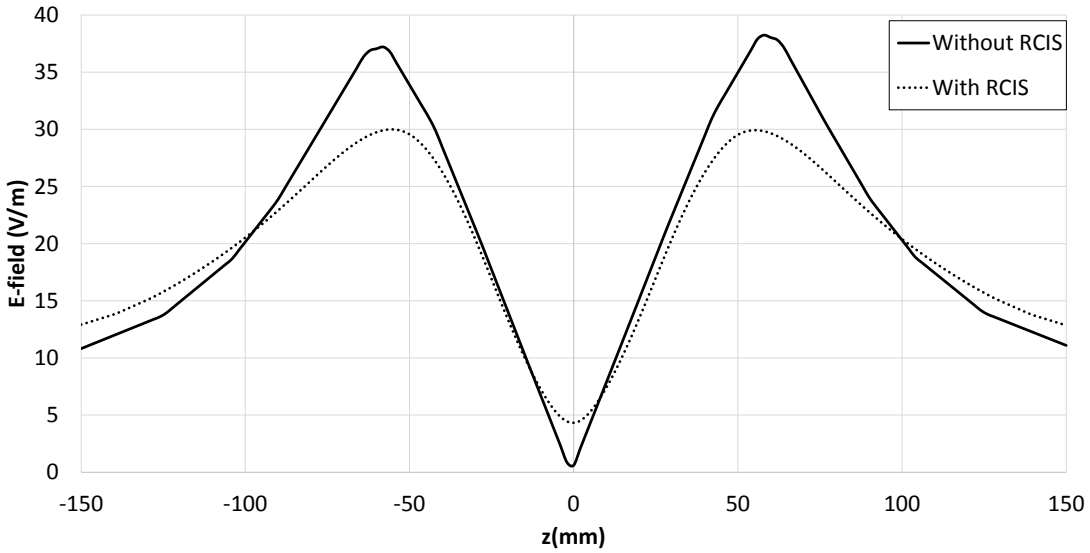

Fig. 4.17 Magnitude of simulated Electric field through the dielectric phantom ($x = 40mm$)

4.3.4 Specific Absorption Rate

The SAR calculated method was described in the previous chapter, the same approach was applied in this section to investigate the SAR level for both cases with and without the RCIS.. The simulated values of SAR for the whole body were 0.08W/kg and 0.11W/kg for with RCIS and without inserting the RCIS respectively. The 10g sample SAR values were 3.75 W/kg and 2.95 W/kg for the RCIS and without using the RCIS respectively. The maximum SAR allowed by IEC standard is 2W/kg and 10W/kg for the whole body and 10g sample respectively [112]. The results illustrated that there was a decrease of SAR value by 39%, however, both SAR values for both cases with and without the RCIS were less than the maximum value allowed by IEC standard.

4.4 Experimental validation method

4.4.1 The measurement of the transmission coefficient S21

To validate the simulation system concepts, the manufactured RF coil and the dielectric phantom which were reported in section 3.4 and 4.3 were used in this section. The RF coil was connected to the Vector Network Analyser (RS ZVL) and the coil was tuned to 63.8MHz with the RCIS as shown in Fig.4.11 using C_{tune} and matching using C_m, then these variable

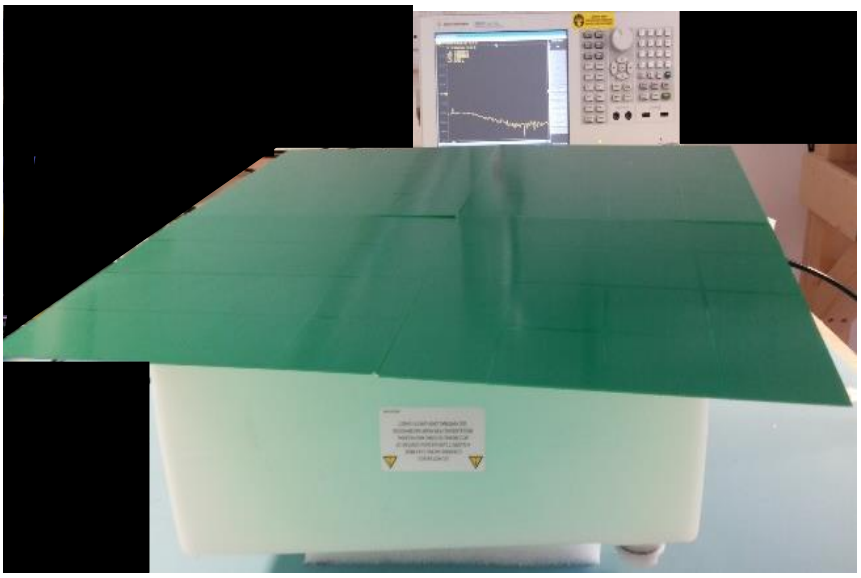

Fig. 4.18 Experimental set-up system

capacitors were replaced by fixed ceramic capacitors with the same values. Fig.4.19 shows the experimental set-up system which include the reflector CIS, RF coil and a probe loop. The coil also incorporates a LC balun with values of $L = 125nH$, and $C = 50pF$. Fig. 4.18 shows the measured set-up of the proposed system configuration. The loop flux probe which was built using semi-rigid coaxial cable was fabricated and the transmission coefficient (S21) between the RF coil and flux probe was measured such that comparative measurements between the models, shown in Fig.4.1, could be carried out. Fig. 4.19 shows the measured S21 along the y-axis (x = z = 0). The S21 was normalised to the maximum of the coil only for case of comparison. The average improvement in magnetic field is 57% at this position.

4.4.2 Measurements of Q-factor

In order to measure the Q-factor of the system with and without the RCIS the same methodology which was described in chapter 3, was followed in this section and the Q-factor loaded, unloaded, and ratio results were illustrated in table 4.1. The results show that the Q-factor of both of the coils with and without the RCIS were more than 3, which indicated that more than 83% of the maximum SNR can be achieved, as explained in appendix B, equation (B.2).

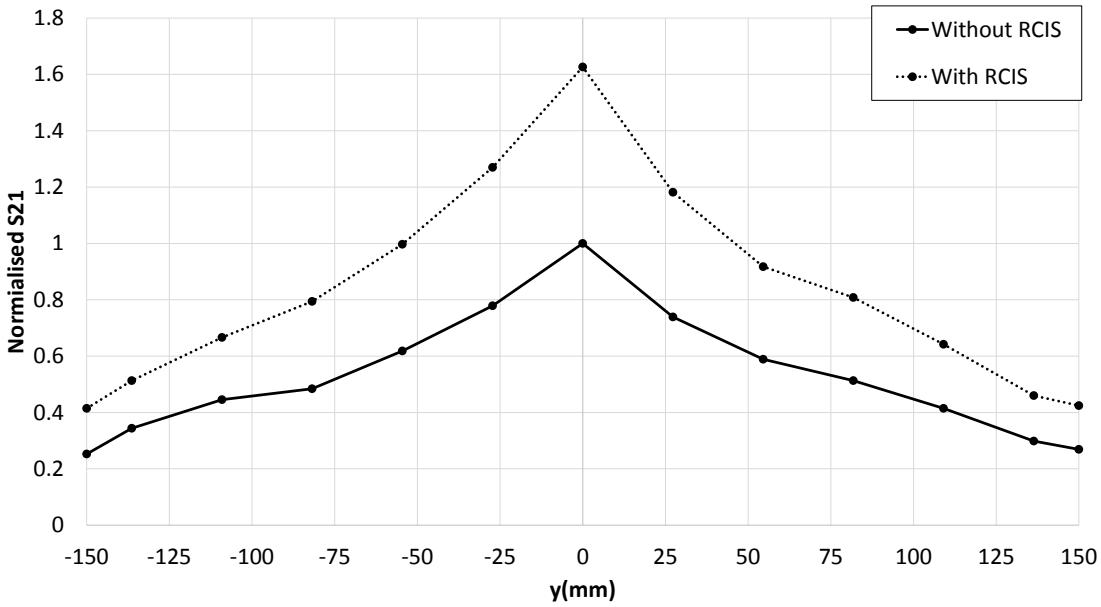

Fig. 4.19 Normalised magnitude of measured S21 along z-axis,(x=y=0)

Table 4.1 The Q-factor measured results with and without the RCIS

	Qunloaded	Qloaded	ratio
coil only	160	47.3	3.38
coil with RCIS	90	28	3.2

4.5 MRI scanner measurements

Fig. 4.20 shows the proposed RF measurements system within the 1.5T whole body MRI scanner. The same approach described in the previous chapter was followed in this section and the measurement parameters are listed in Table 4.2. The images were acquired with identical imaging parameters with and without RCIS placed as shown in Fig.4.20.

Table 4.2 MRI scanner settings

Parameter	Value
Pulse repetition time (ms)	500
Echo time (ms)	50
Bandwidth (kHz)	15.63
Field of view (cm)	36 x 36
Slice thickness (mm)	10
Acquisition matrix (pixels)	256 x 256
Transmission gain (dB)	3

Fig. 4.20 The measurement system at the 1.5T MRI scanner

Fig.4.21 shows the MRI image with and without the RCIS. The result shows that the image intensity with RCIS was higher than without the surface when the regions of interest (ROIs)close to the RCIS surface. Further analysis in terms of SNR was presented in Fig.4.22 where the noise was taken from images with the RF power switched off.

Fig.4.23 illustrates the measured SNR at the coil centre cross the dielectric phantom, where the SNR was calculated using (3.9) as explained in chapter 3. The result shows that using capacitive impedance surface as a loop coil reflector can improve the SNR by 5 times at the phantom surface and improvement is observed for the first 20 mm. These results have been achieved when applied the same TG value which was 3 dB, this improvement is termed as a transceiver improvement

4.6 Summary

In this chapter, numerical simulation and experimental results show that a capacitive impedance surface (CIS) can be used as a RF loop coil reflector for improving a 1.5T MRI system performance. Our work has investigated the MRI performance metric, which include magnetic field (H_1), magnetic flux density (B_1), specific absorption rate (SAR), and measured signal to noise ratio (SNR). Firstly, the surface impedance layer is assumed to be dominated by capacitance and the losses are assumed to be zero ($R = 0$) for the idealised

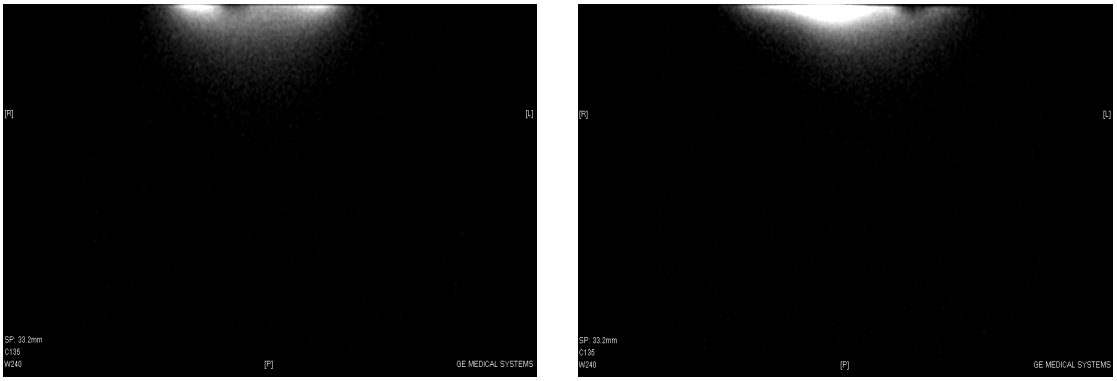

Fig. 4.21 The MRI image.(a). Without RCIS.(b). With RCIS

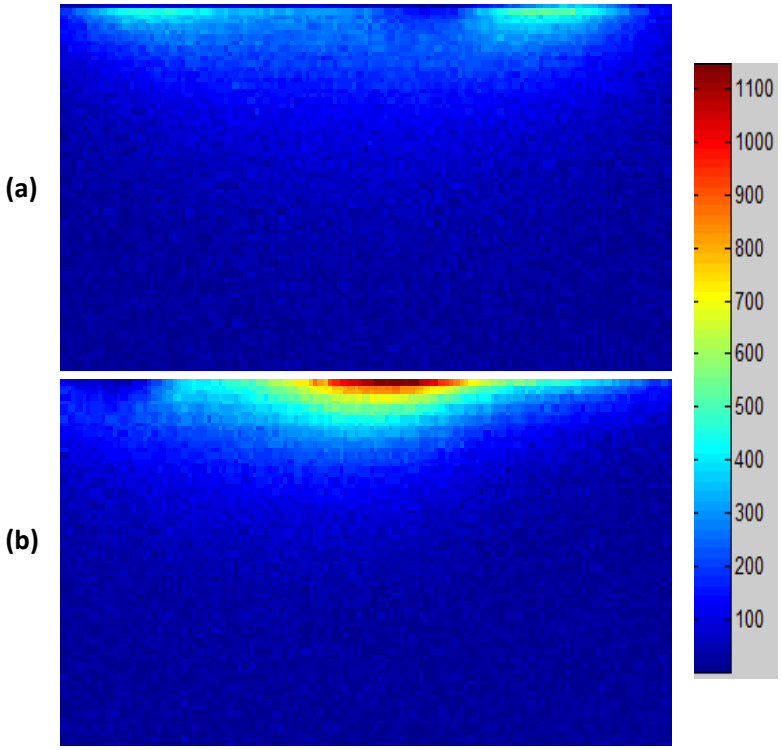

Fig. 4.22 The measured SNR. (a). Without RCIS.(b). With RCIS

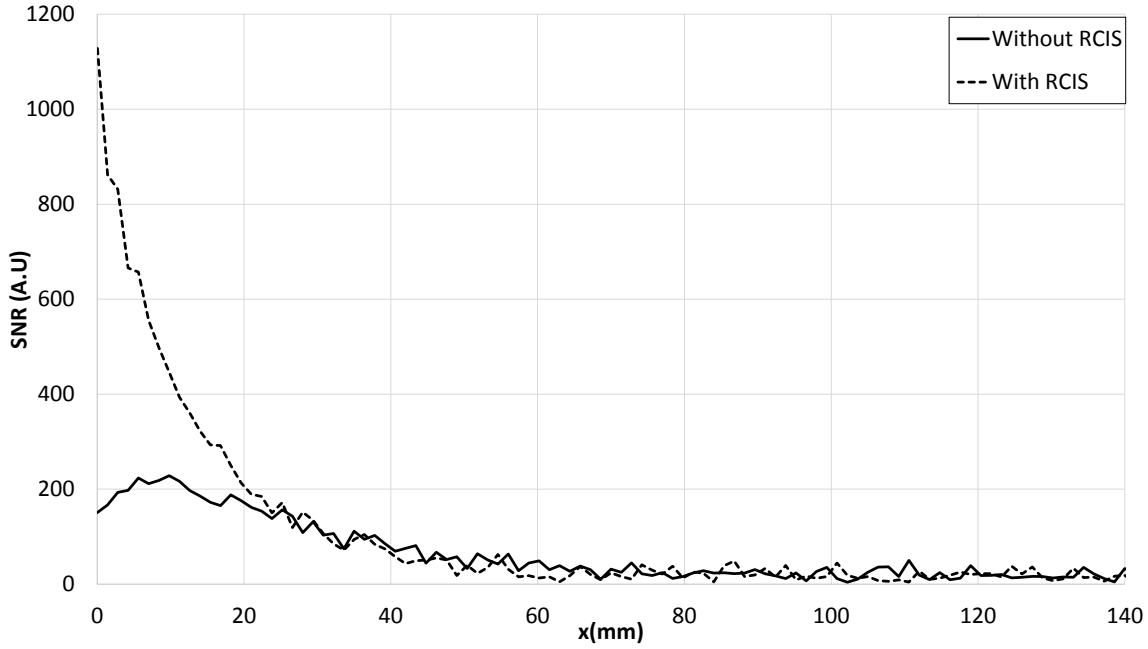

Fig. 4.23 Measured SNR with and without the RCIS, at the coil centre

case. In this case, the results show that the maximum improvement in magnetic field can be achieved when the surface capacitance is $115pF$. The implementation of the capacitive surface is based on a miniaturized frequency selective surface. By applying this surface which include the losses due to the FR4 substrate and copper digits, the normalised magnetic field $H_{1,normalised}$ and normalised negatively rotated magnetic flux density $B^{-}_{1,normalised}$ were improved by 80%, and up to 66%, on average at the coil centre respectively. The results show that both magnetic field and magnetic flux density are reduced when compared to the ideal case. However, there is still improvement when compared to the case without the reflector CIS for initial 25mm inside the dielectric phantom. The advantage of enhancing the $H_{1,normalised}$ which led to improve the $B^{-}_{1,normalised}$ and $|B^{+}_{1}|$, which are important for improving the MRI transverse coil SNR. The result illustrates that the magnitude of the $|B^{+}_{1}|$ can be increased by to 66%.

Also, in this chapter the associated Specific Absorption Rate (SAR) for the surface is simulated and compared to international standards. According to the aforementioned SAR guidelines, the SAR values for both the RF coil and RCIS in this study are below the maximum allowed SAR values. The applying of the CIS concept as a reflector has been demonstrated in the RF lab, whilst the system has been demonstrated within a 1.5T MRI scanner. By using CIS as a reflector the SNR is improved by 5 times at the top of the phantom and the enhancement is observed for the first 20mm inside the phantom. The results show

there is a good comparison between the simulated and measured overall trends of the SNR, however, the penetration depth is lower than the simulations most likely due to tolerances in fabrication and uncertainties in material losses. The comparison of using CIS as a reflector results agrees with the previous studies,however, the applying of the reflector CIS within the MRI was advantageous for a zero thick, simple structures, a comparative small size, and easy to fabricate when compared to the RF lens which has a 15mm thick, and metasurface which is a resonant structure. In general The RCIS locally improves the RF surface coil SNR, however, the improvement depth was limited by 20 mm. For this reason another method used to further increase the MRI system performance metric is investigated in chapter 5, which is based on using the CIS as a transmission instead of reflector of the RF loop coil. Table. 4.3 compared this chapter results with the state-of-art.

Table 4.3 A comparison between using the RCIS method against the state-of-art methods from published literature((‡- Volume coil †- Surface coil))

Metric	**Approaches**	**1.5T,** $f_0 = 64MHz$	**3T,** $f_0 = 128MHz$	**7T,** $f_0 = 300MHz$
$\lvert B_1^- \rvert$	HIS	**10% †**	-	7% ‡[37] 25%†[72]
	Metasurface	-	-	-
	RF lens	-	-	-
	Dielectric pads	-	50%‡[95]	100%‡[103]
	RCIS	**77% †**	-	-
SNR	HIS	**6% †**	-	-
	Metasurface	270%‡[91]	-	-
	RF lens	100% [64]	200% [64]	-
	Dielectric pads	-	20-40%‡[95]	53%‡[98], 200%‡[103]
	RCIS	**450% †**	-	-
Penetration depth	HIS	**20mm †**	-	-
	Metasurface	-	-	-
	RF lens	35mm†[64]	40mm†[64]	-
	Dielectric pads	-	-	-
	RCIS	**22mm†**	-	-
SAR	HIS	**+13.6% †**	-	+48% †[71]
	Metasurface	-	-	-
	RF lens	-	-	-
	Dielectric pads	-	-50% ‡[95]	-33% ‡[98]
	RCIS	**-39% †**	-	-

Chapter 5

A Transmission Capacitive Impedance Surface for 1.5 Tesla Magnetic Resonance Imaging Applications.

5.1 Introduction

Different methods have been used in Chapter 3, and Chapter 4 to enhance the RF magnetic field and SNR of a RF surface coil for a 1.5T MRI system. This chapter investigates the potential benefits of using a capacitance impedance surface (TCIS) as a transceiver flux guide for a surface RF coil. This chapter demonstrates using theoretical design, numerical simulations, vector network analyser measurements, and MRI measurements, that the RF magnetic flux density (B_1) and signal to noise ratio (SNR) can be improved and localised by using the TCIS with even unit cell periodicity as a transceiver placed between RF coil and dielectric phantom. Also, the TCIS size is investigated to find its effects on the $|B_1|$. This chapter is organised as follows: an idealised surface impedance concept is introduced in section 5.2 in order to find the maximum capacitve value of the sheet, which provided a higher enhancement of the $|(B_1)|$. Section 5.3 introduces losses into the CIS which is determined in the previous section and the impact of this is discussed. The numerical simulation results which represent the MRI measurements using CST-MW 2015 time and frequency domains solver are presented in this section. The demonstrated experimental measurements results of the proposed system in the RF laboratory are shown in section 5.4 including the Q-factor and the transmission coefficient (S21) measurements. The proposed system is demonstrated

within the 1.5T MRI scanner shown in section 5.5. Finally, section 5.6 concludes the chapter and draws comparison with previous approaches.

5.2 The MRI system concept and transmission CIS design

5.2.1 The MRI system concept with initial transmission surface

In order to determine the best capactive sheet value, which produced a maximum value of the RF magnetic field inside the dielectric phantom the approach described in Chapter 4 was applied in this section. Fig.5.1 shows a cross section of the system of interest which includes a dielectric phantom, spaced a distance, s=5mm, away from a TCIS. The TCIS, assumed to have an area of X_{TCIS}, is spaced a distance, d, away from a RF loop coil. The impedance of TCIS was characterised by $Z = R - jX$ and it is assumed to be dominated by the reactance value. In this section the(R=0), which represented the losses of the TCIS, is assumed to be zero for idealised case. For a fair comparison the $|B_1^-|$ was normalised to the square root of the dissipated power in the dielectric phantom which was given equation by 4.2, where the P_L was defined as a dissipated power throughout all system components and it was given by (4.3) for only coil and it is calculated by (5.1) of the coil with TCIS.

$$P_L = P_{coil} + P_{phantom} + P_{TCIS} \tag{5.1}$$

During simulations the $B^-_{1,normalised}$ was compared to the case when the surface impedance is not included. In initial simulations the surface impedance was implemented as an ideal surface impedance model as shown in Fig.5.2 in order to investigate the effects of the sheet capacitor value, and a TCIS area, which was denoted by X_{TCIS} on the magnitude of the $B^-_{1,normalised}$. Numerical simulations were performed in two system prototypes. Initially, CST simulations were carried out with and without the transmission sheet where the $B^-_{1,normalised}$ inside the dielectric phantom was monitored along the x-axis when the RF coil was fed by a sinusoidal 1A current source.

The RF coil design was previously reported in chapter 1 and 3 respectively. This RF coil was chosen to be circular for this chapter and designed to trade off depth of field penetration and signal strength for a 140mm thick dielectric phantom, resulted in a coil diameter of 12.3cm, [66], with a coil width of 6mm. The coil model was driven using a numerical simulation with finite integration technique (FIT) with one port of a current source as initial investigation.

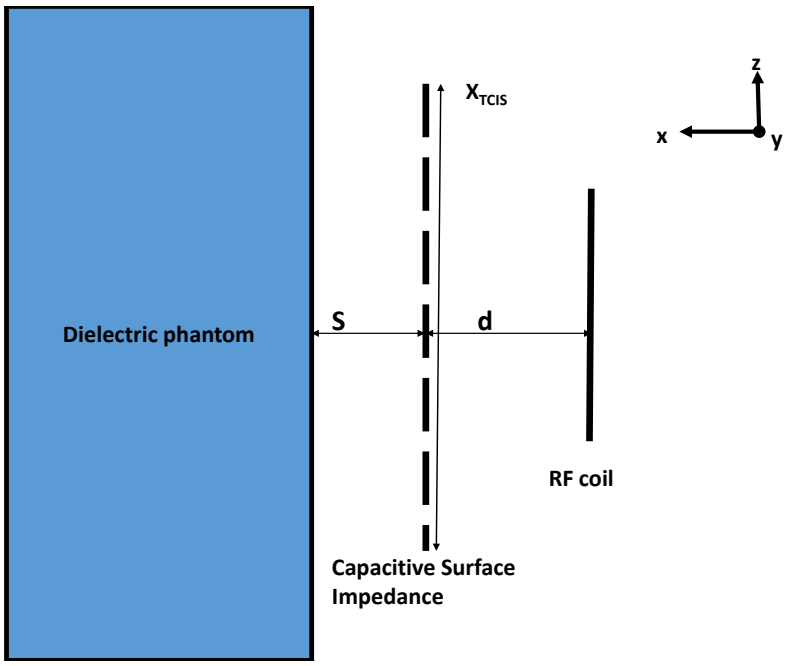

Fig. 5.1 MRI system with surface impedance concept model

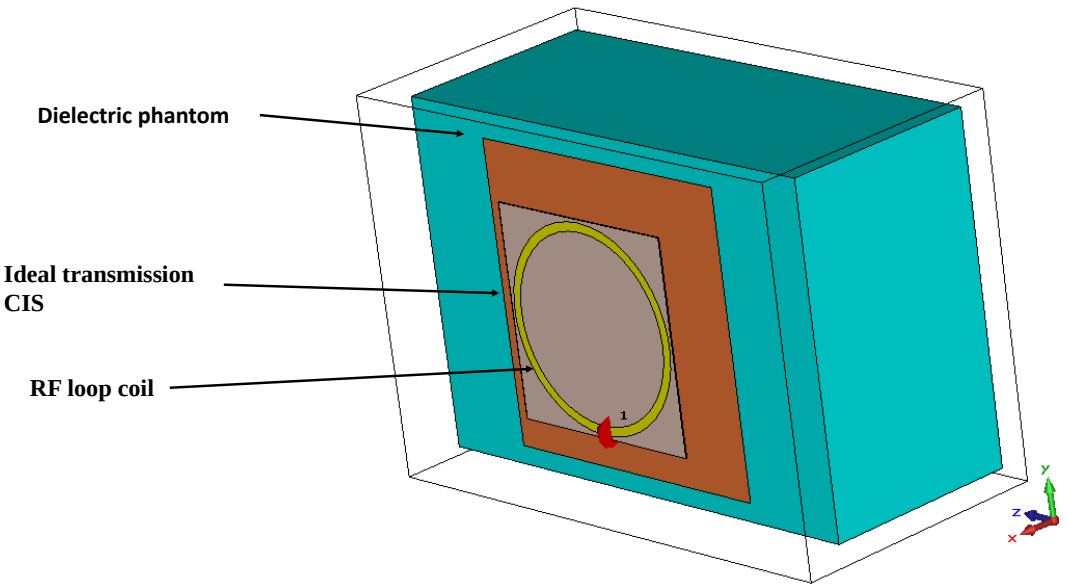

Fig. 5.2 Simulation system with a ideal transmission surface impedance concept model

In initial simulations the sheet area is assumed to be $20 \times 20cm$ in order to determine the sheet capacitive value, which produces a maximum $B^{-}_{1,normalised}$ improvements compared to only coil. Fig. 5.3 illustrates the $B^{-}_{1,normalised}$ at the coil with various value of the capacitive sheet between $200pF - 500pF$. The results show that the $B^{-}_{1,normalised}$ can be significantly increased at the coil centre with the use of a TCIS and as the capacitance value increments, further the improvement in magnetic flux density declines to a point where the TCIS impedance is having a detrimental impact. It is noticed that, for higher values of TCIS capacitance value, there is a limitation in the penetration depth inside the dielectric, for example when the TCIS capacitance value is 400pF there is no enhancement after 50mm and no improvement beyond 30mm when the TCIS capacitance is 500pF. Fig.5.4 shows the SNR $B^{-}_{1,normalised}$ at the coil edge for the same sheet capacitive that was presented in Fig.5.3. The results show that a significant enhancement of the $B^{-}_{1,normalised}$ at the coil edge can be achieved using transmission CIS value of $400pF$ at the ideal cause. Fig. 5.5 illustrates the variation of the transmit $|B^{+}_{1}|$ verses the changing of the sheet capacitance. The result shows that the sheet capacitance of 400pF can maximise the value of $|B^{+}_{1}|$ at the coil centre.

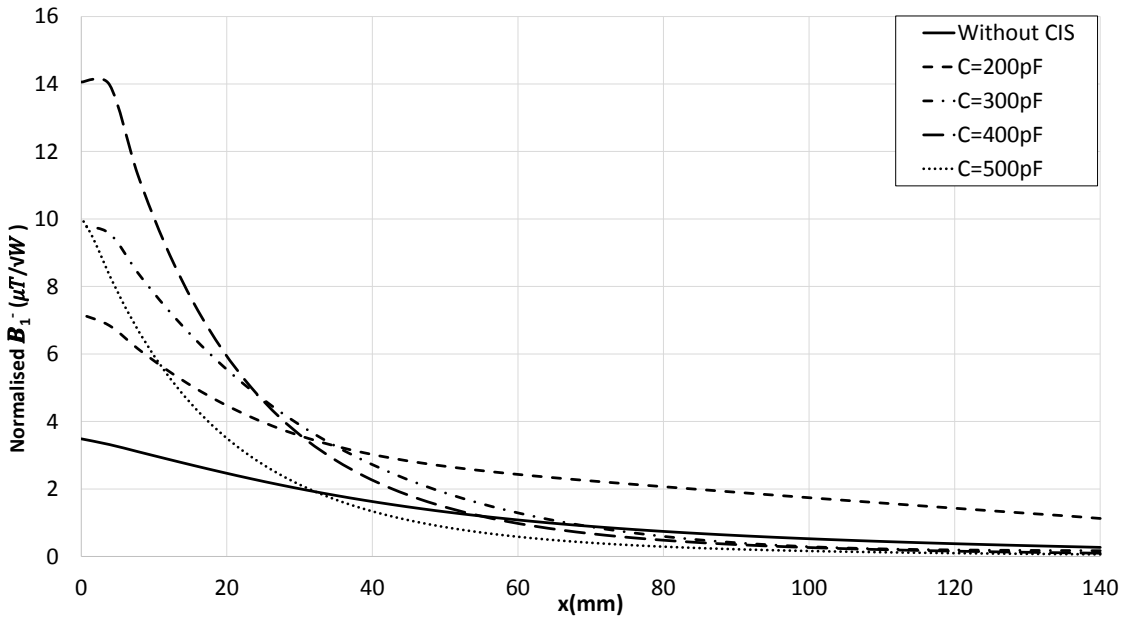

Fig. 5.3 Simulation of $B^{-}_{1,normalised}$ through x-axis at the coil centre.

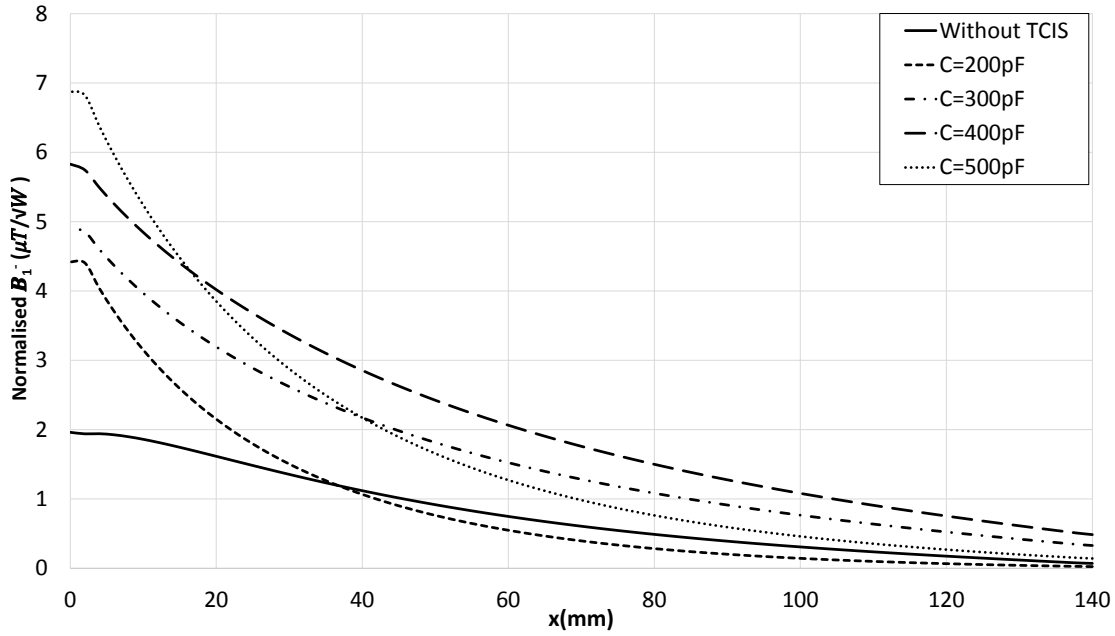

Fig. 5.4 Simulation of $B_{1,normalised}^{-}$ through x-axis at the coil edge.

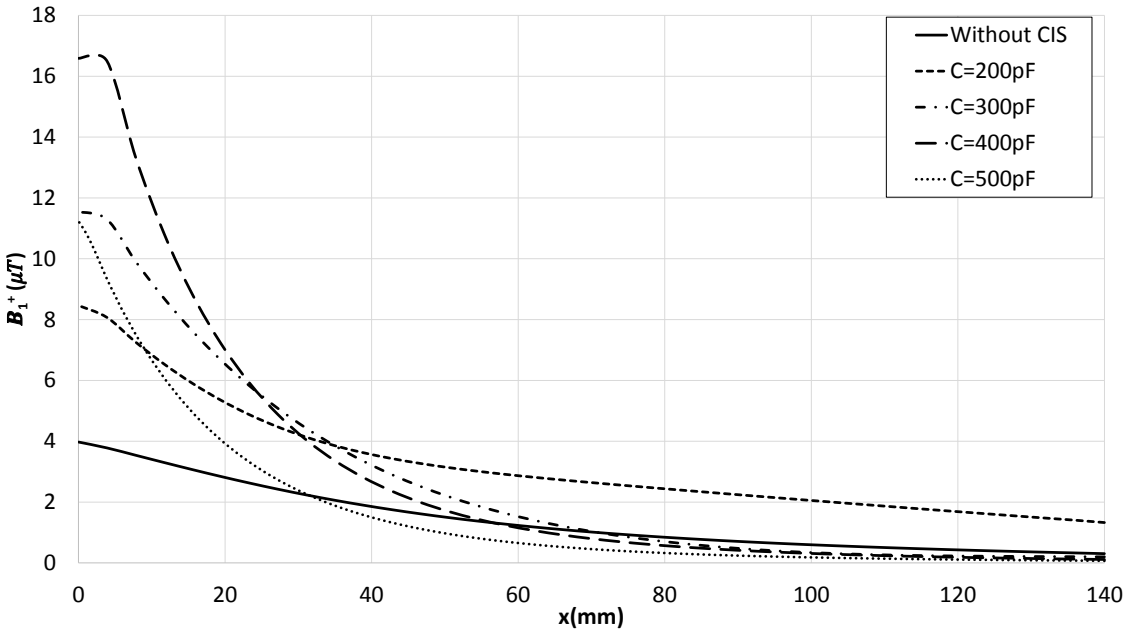

Fig. 5.5 Simulation of $|B_1^+|$ through x-axis at the coil centre.

Fig. 5.6 illustrates the magnitude of the magnetic flux density in xy plane and further illustrates the improvement which can be achieved. The result shows that the maximum improvement of the magnitude of the magnetic flux density can be achieved when the TCIS value equal 400pF.

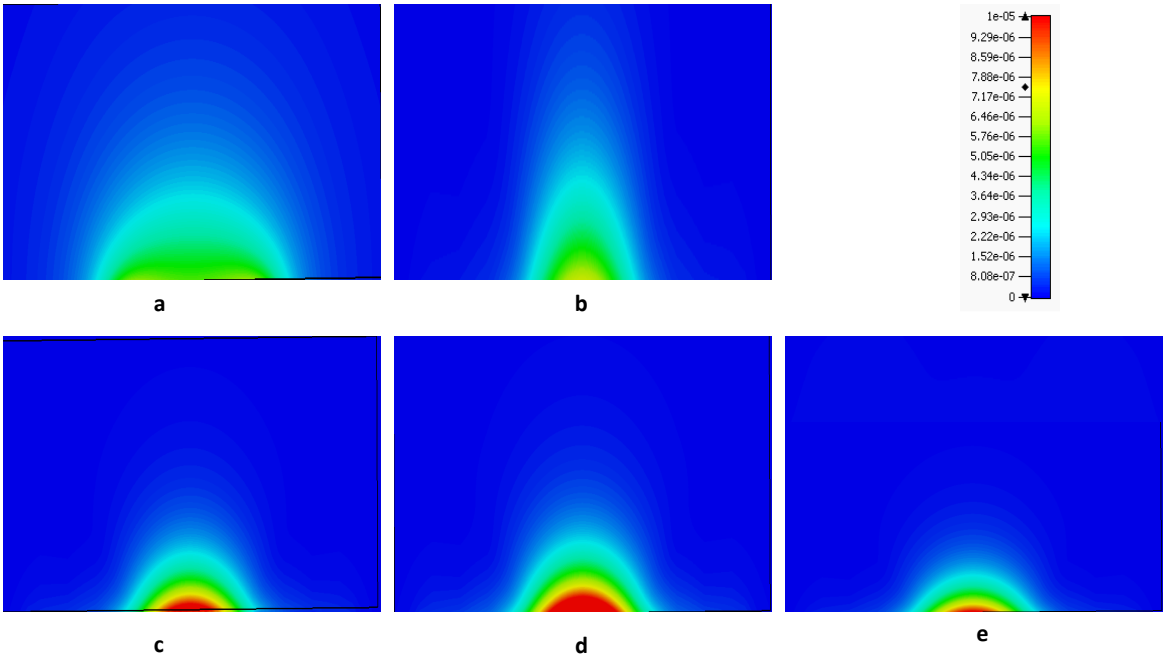

Fig. 5.6 Simulation of $|B_1^+|$ through xy-plane at the coil centre with and without the with ideal CIS of.(a) RF coil alone, (b)CIS=200pF, (c) CIS=300pF, (d) CIS=400pF, (e) CIS=500pF

Effects of X_{TCIS} size, and d on the $B^-_{1,normalised}$

The effect of a cross-sectional area of the sheet X_{TCIS} was investigated based on the normalised magnitude of the received magnetic flux density in Figs.5.7, where the X_{TCIS} vary between $20cm$ to $40cm$. The results show that there is a slight increase of the improvement of the magnitude of $B^-_{1,normalised}$ at the coil centre when the X_{TCIS} increased from 20cm to 40cm, however, the $B^-_{1,normalised}$ remained the same when the cross sectional area changed from 20cm to 30cm. In order to achieve the maximum value of the normalised magnetic field inside the dielectric phantom, the effects of a variation of the gap distance between the RF coil and TCIS was investigated. The RF coil was fed by 1A sinusoidal current source at the frequency of 63.8MHz. Fig. 5.8 illustrates that the highest value $B^-_{1,normalised}$ occurs for $d = 20mm$, whereas increase of decrease , d, higher than or less than 20mm, the normalised magnitude of the magnetic flux density is reduced.

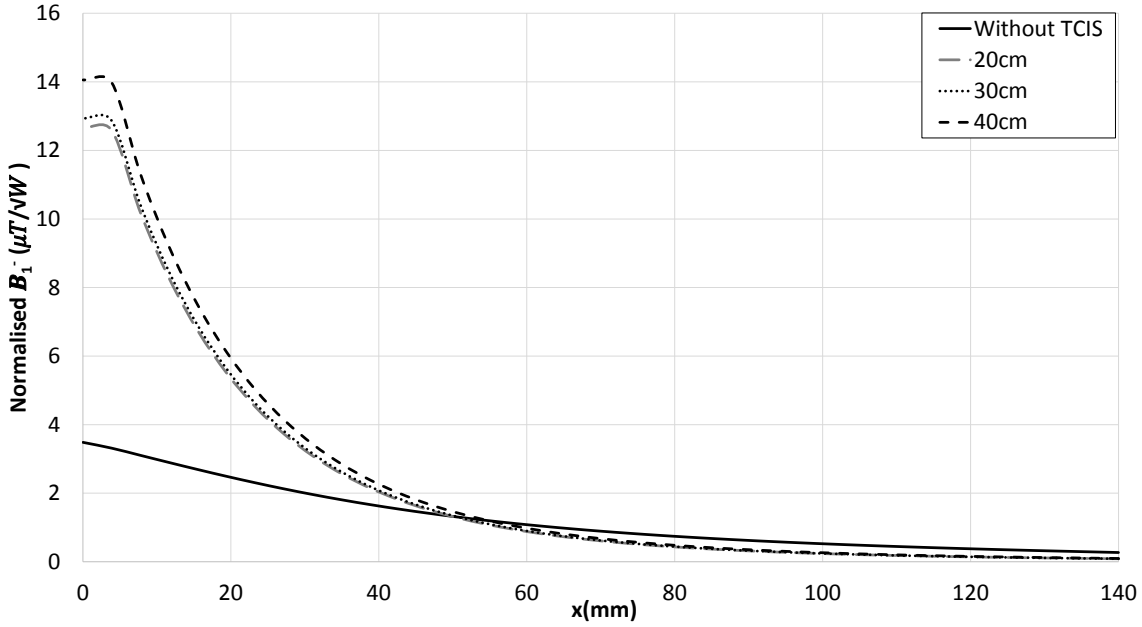

Fig. 5.7 Simulation of $B^{-}_{1,normalised}$ along x-axis for varying TCIS area at the coil centre.

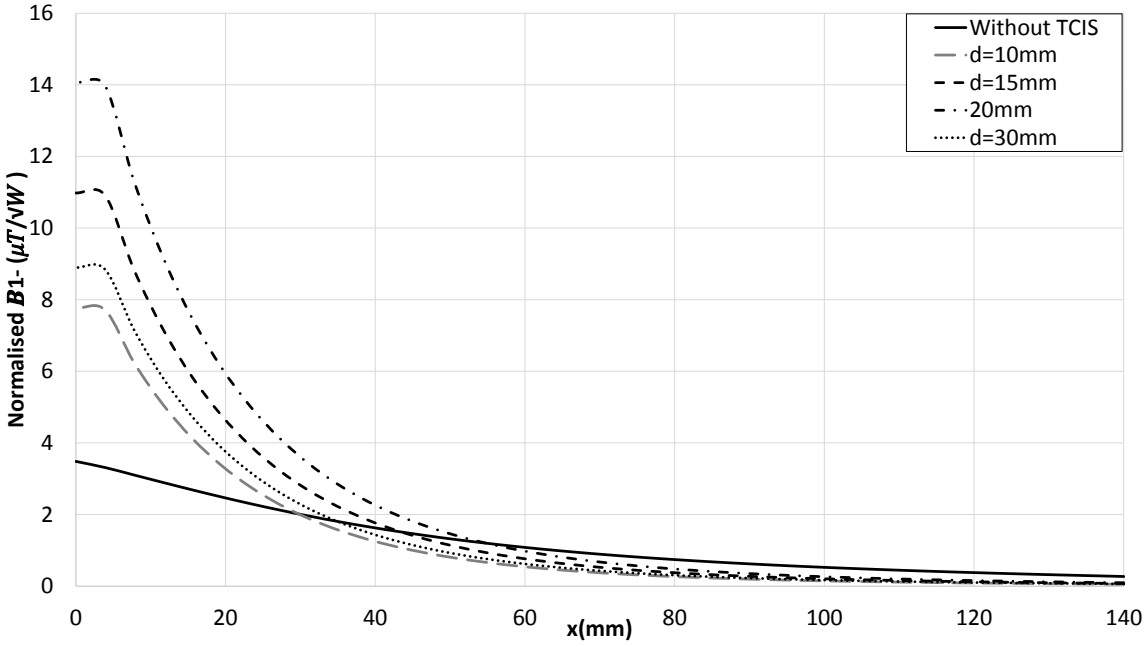

Fig. 5.8 Simulation of $B^{-}_{1,normalised}$ along x-axis for varying space,d, at the coil centre.

As described in section (4.2.1) in chapter 4, the fundamental principle behind the magnetic flux density improvement is redistribution of near field properties of the RF coil due to coupling effects with the TCIS. Fig. 5.9 illustrates the field distribution as a colour map of RF coil only (a) and the case where the capacitance of TCIS metasurface is 400pF with no losses (R=0)(b). Fig. 5.9(b)shows the RF coil performance response with intense field close by the TCIS and this intensity is gradually decaying into phantom. The effects of adding the TCIS metasurface is clear from Fig. 5.9. By adding this layer in between the inductive RF coil and the dielectric phantom, the $|B_1|$ concentrated in the central part of the metasurface which can lead to provide a local enhancement in SNR. It is noticed that, the TCIS works similar to a matched layer, which described by [113]. One of the most remarkable properties of the matched layer is transmitted and focusing the electromagnetic waves without reflections, which leads to increase the magnetic flux density.

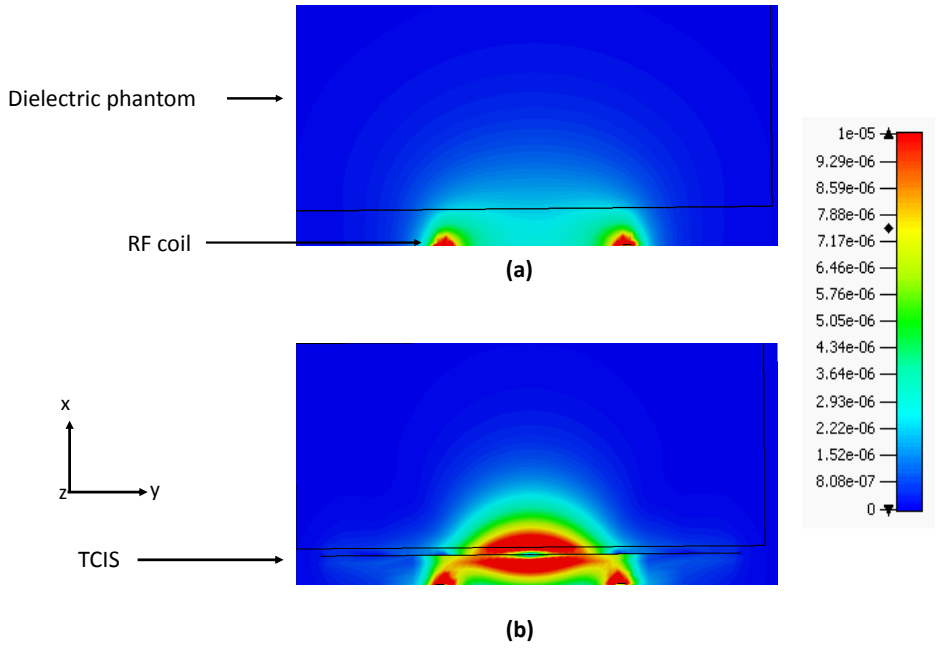

Fig. 5.9 Simulated $|B_1^-|$ across xy plane (z=0), (a) without TCIS, (b) with TCIS

5.2.2 The implementation of the transmission CIS using interdigital approach

To implement the capacitive impedance a frequency selective surface (FSS) approach was adopted which consists of a periodic array of metallic and dielectric elements. There are a range of options for the geometry of the metallic elements of the FSS, including square

patches, Jerusalem crosses, spirals etc. Classic FSS designs tend to have periodic elements which can be a significant fraction of a wavelength which would not be appropriate for MRI applications, as such an interdigital approach was adopted that has been previously reported in chapter 3 and chapter 4, which has a high capacitance density which provides electrically small unit cell designs. Fig. 5.10 shows the unit cell of the upper surface of the CIS which has a 0.8mm FR4 substrate (ε_r=4.3, $\tan\delta$=0.025) and the lower surface consists of an orthogonal copy of the upper surface to ensure dual polarisation performance. The inset of Fig. 5.11 shows the detail of the interdigitation which composes of metallic elements of width w_d, separated by g_d. The capacitance of the CIS can be estimated using (3.1) - (3.3), which gives the capacitance in pF. It was noted that the design equations have uncertainties associated

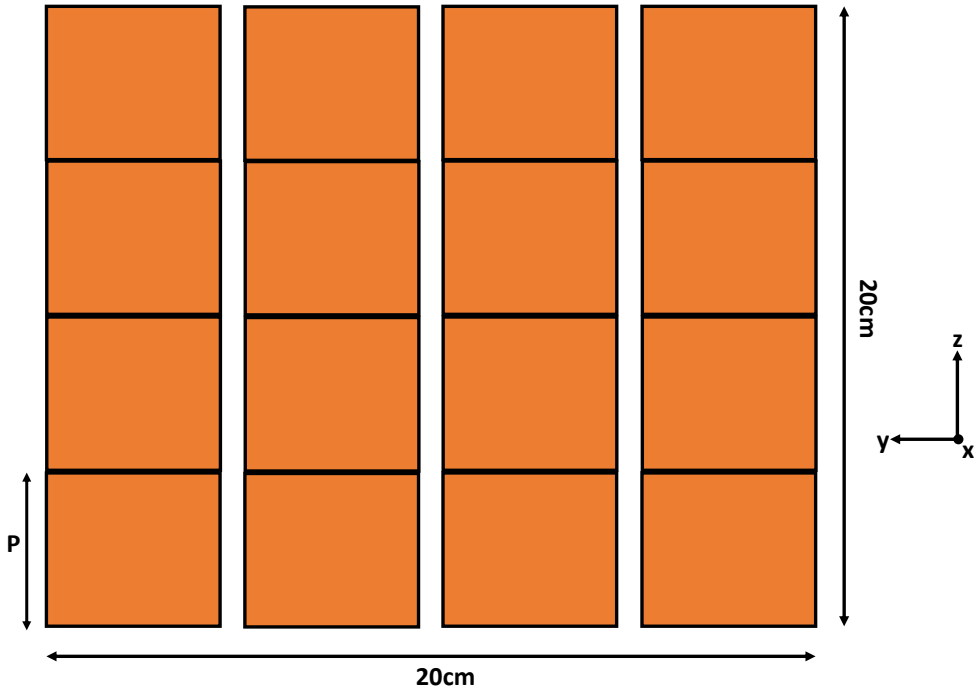

Fig. 5.10 Front layer of a full transmission CIS 4×4 TCIS.

with them, mainly due to the effective permittivity which tends towards $\varepsilon_{eff} = \frac{\varepsilon_r+1}{2}$ for thick substrates. As the substrate is electrically very thin in this work, in order to reduce losses, then the equations are useful as an initial design estimation. To accurately simulate the FSS properties a full field approach was adopted where the unit cell of the FSS was surrounded by periodic, Floquet mode, boundary conditions which effectively provides an infinite structure which is then illuminated with a plane wave and from this the equivalent impedance of the

surface can be easily determined. In designing the FSS a trade off of the number of unit cells for the total surface area ($200mm \times 200mm$) was considered as shown in Fig. 5.10. To

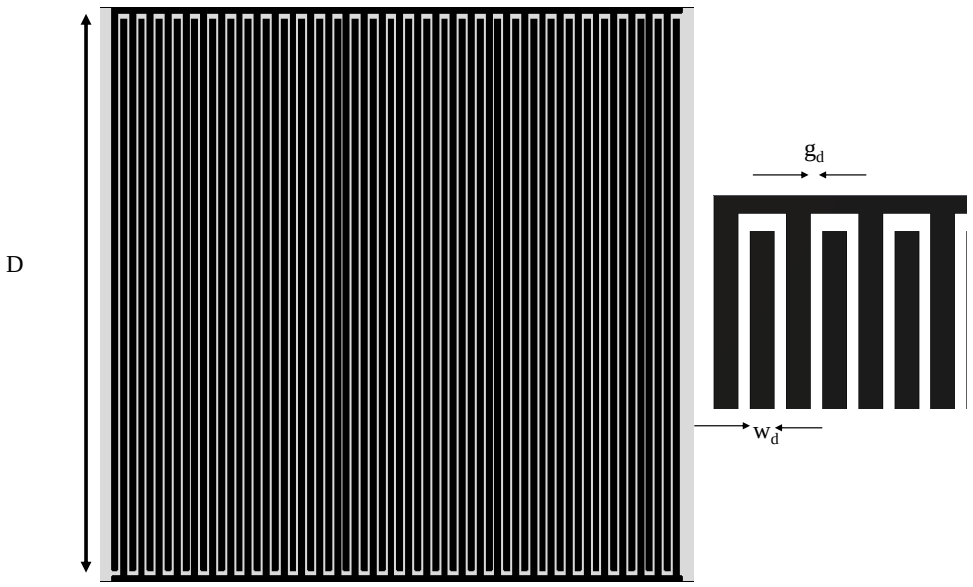

Fig. 5.11 Front layer of a interdigitation unit cell.

demonstrate the highest improvement in magnetic field a capacitance of 400pF was chosen with a unit cell parameters as the following (unit cell periodicity P=50mm, D=49.1mm, N=132,w_d=0.25mm and g_d=0.12mm). There was also a 0.3mm gap between the ends of the digits and the horizontal metallic strip at the top of the unit cell and there is an inter-unit cell separation of 0.58mm. It was assumed that the metallic elements were 32μ m thick copper. The equivalent resistance and reactance of the final FSS design is shown in Fig. 5.12 and Fig. 5.13 respectively and shows that there is a non-zero resistance due to the FR4 substrate. The reactance of the FSS at 63.8MHz is as expected.

5.3 Numerical characterisation of Interdigital implementation

Fig. 5.14shows the full wave field simulated model of the proposal MRI system with the transmission CIS. Numerical simulations were performed using the time domain solver, and GPU server with 4 clusters. Initially, CST simulations were carried out with the TCIS, then the system without the TCIS was performed in order to carry out the comparison. The MRI

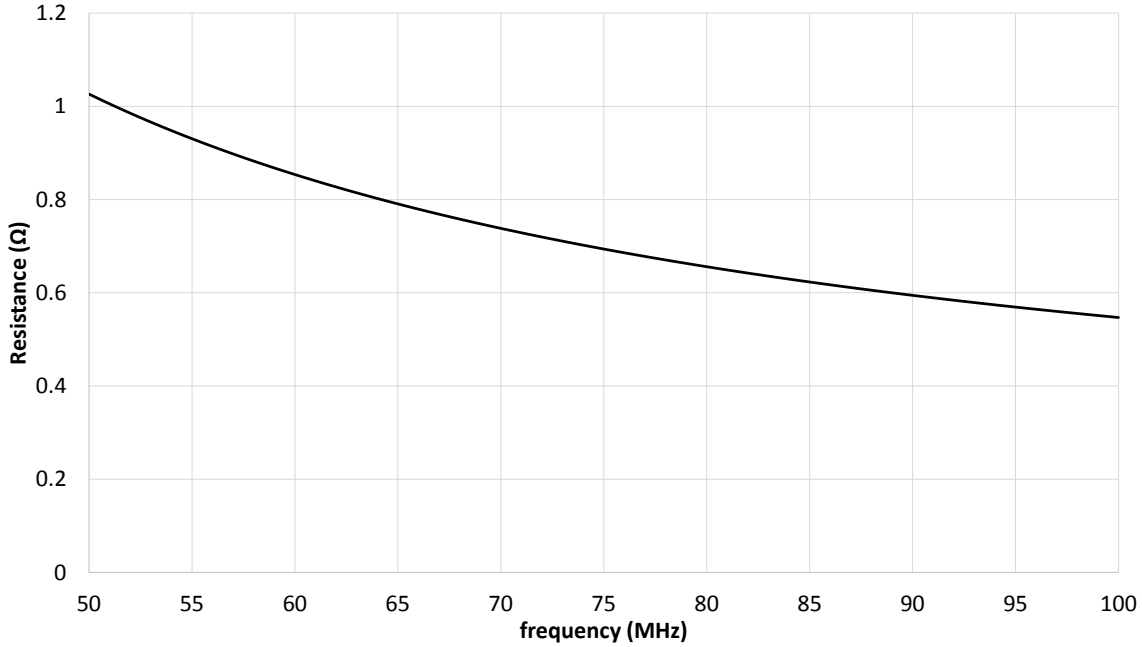

Fig. 5.12 The equivalent resistance of the TCIS.

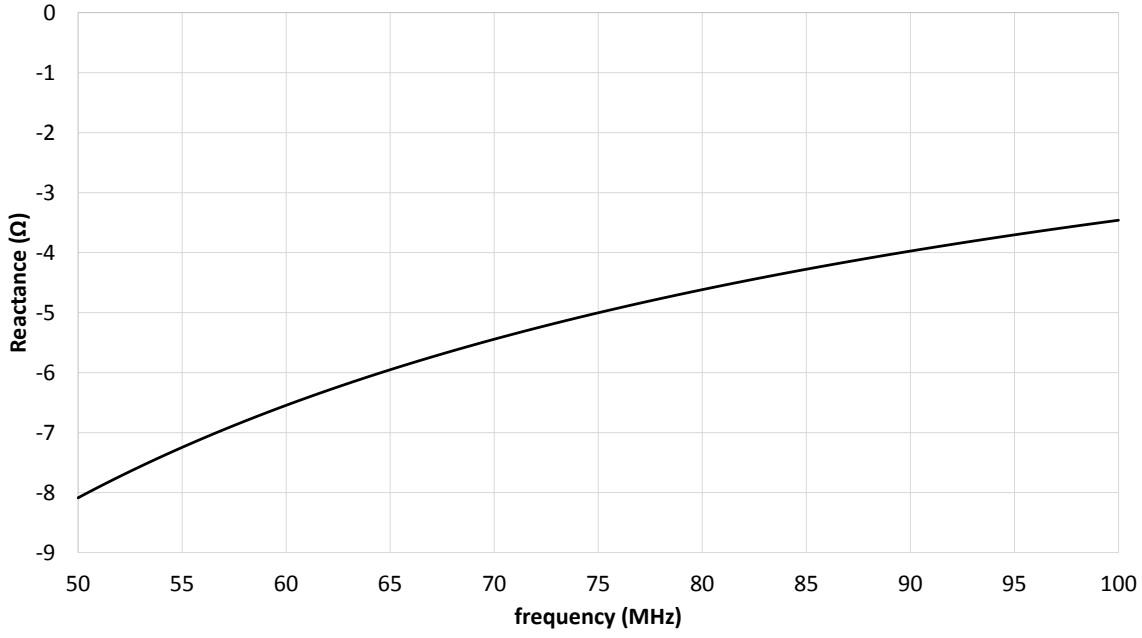

Fig. 5.13 The equivalent reactance of the TCIS.

performance metrics were monitored inside the dielectric phantom along x-axis when the RF coil was fed by a sinusoidal 1A current source.

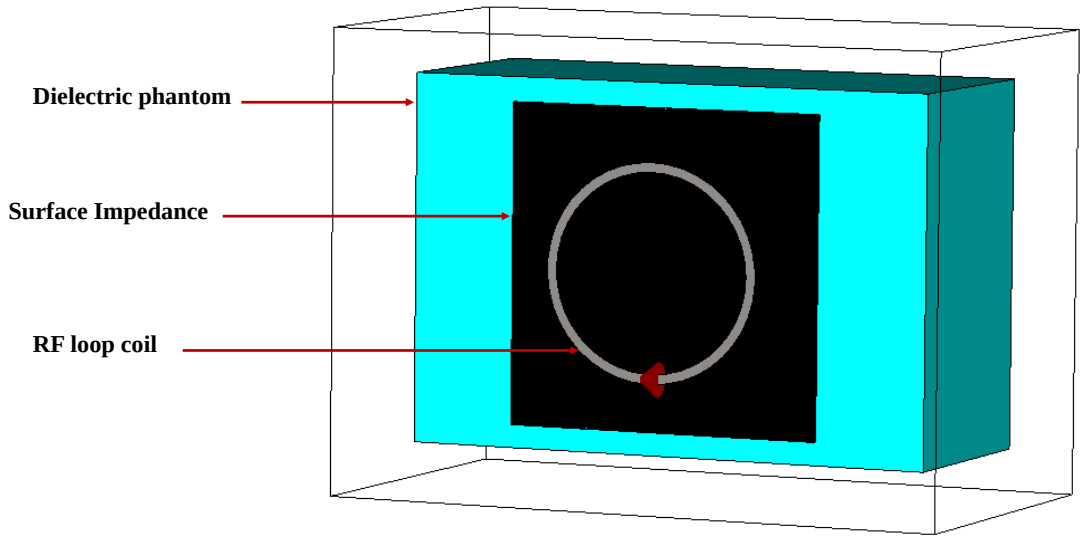

Fig. 5.14 MRI system with the Interdigital TCIS concept using CST-MW

5.3.1 Analysis of the $B^{-}_{1,normalised}$ of using TCIS and without TCIS

This section evaluates the variation of $B^{-}_{1,normalised}$ for different positions across the interdgitial TCIS. This is depicted in Fig. 5.15 which shows the four unit cell of the TCIS including specific regions along yz plane which includes the centre of structure ($z = 0$), intercell region ($z = P/2$), and adjacent cell centre ($z = 3P/2$). Figs. 5.16, 5.17 and 5.18illustrate $B^{-}_{1,normalised}$ along the y-axis at these three yz plane locations when x=5mm inside the dielectric phantom. The results show how the CIS periodicity causes localised $B^{-}_{1,normalised}$ variations and extends the area over which images could be taken with the disadvantage of narrow nulls in the field distribution. This method can be used to refocusing the signal at certain region of the body to improve the SNR of the image at these region of interest, which was at the centre of unit cell. Figs. 5.19, 5.20 and 5.21 show the periodic nature of $|B^{-}_{1}|$ and also present significant improvement away from the coil centre.

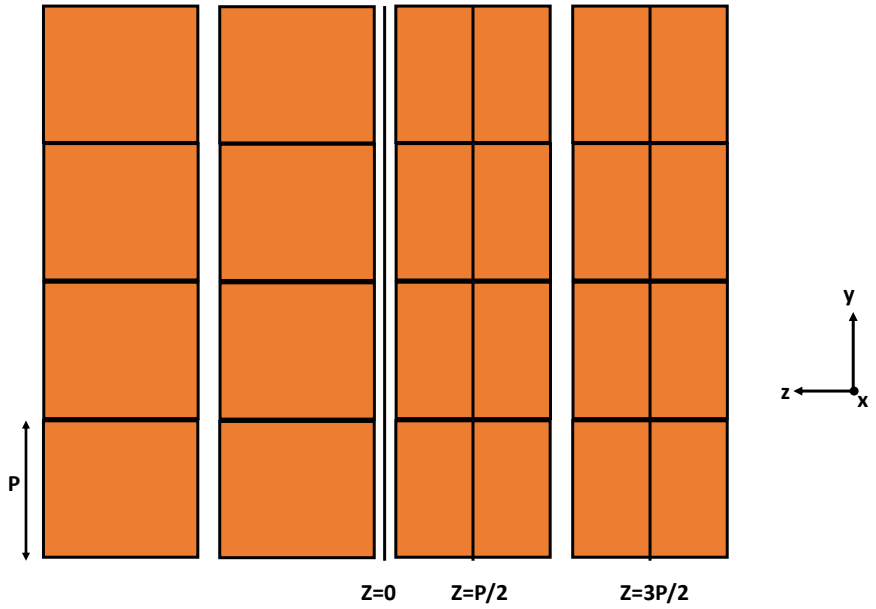

Fig. 5.15 Illustration of TCIS showing yz planes of interest (z=0, z=P/2, z=3P/2)

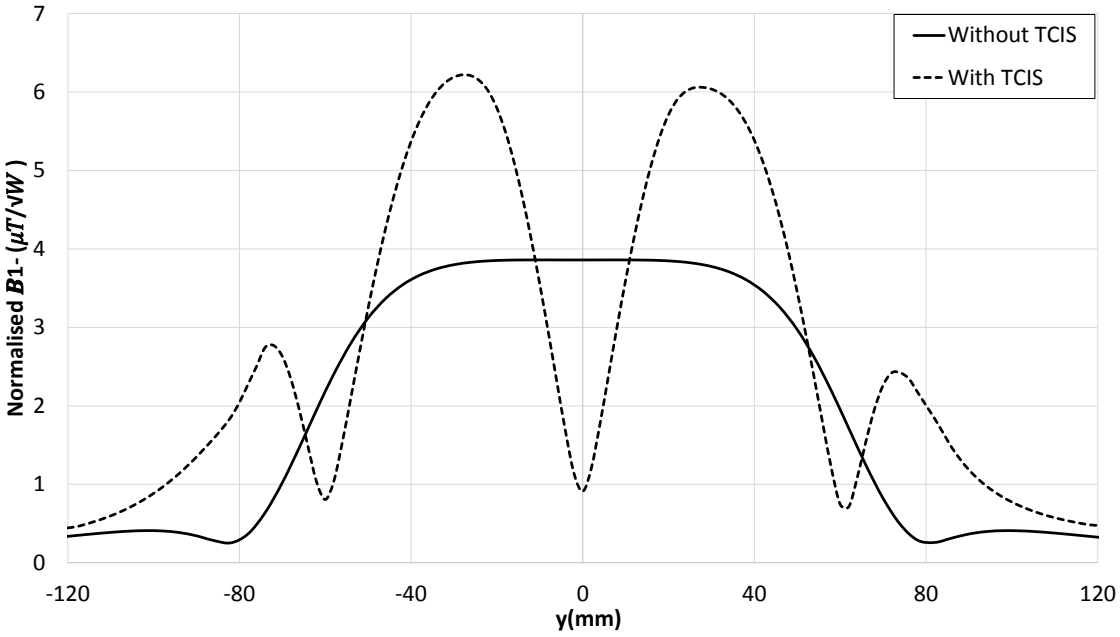

Fig. 5.16 Normalised magnetic flux density B_1^- at $(x = 5, y = -120 or 120mm, z = 0)$ for varying z-axis positions for TCIS, structure centre

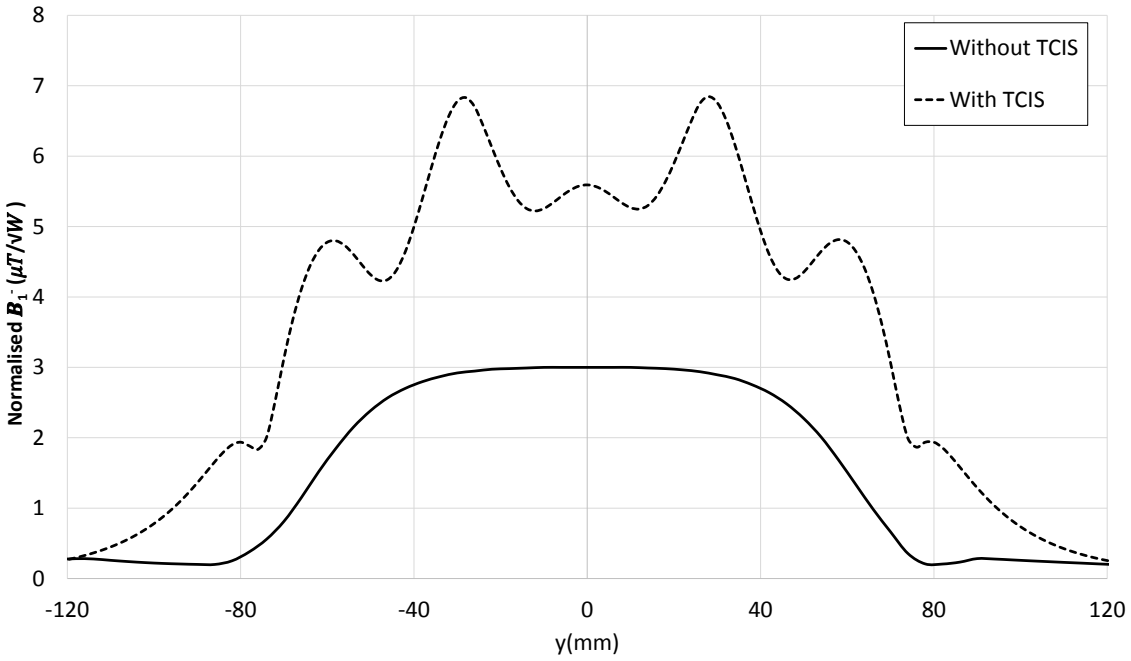

Fig. 5.17 Normalised magnetic flux density B_1^- at $(x = 5, y = -120 or 120 mm, z = P/2)$ for varying z-axis positions for TCIS, intercell region

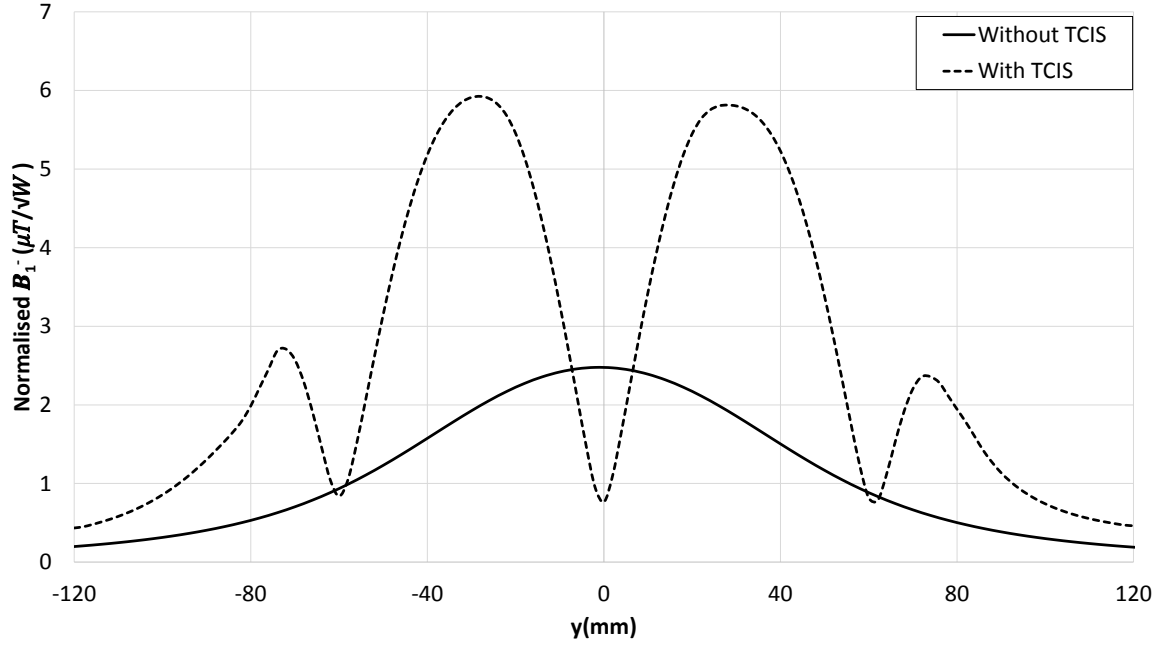

Fig. 5.18 Normalised magnetic flux density B_1^- at $(x = 5, y = -120 or 120 mm, z = 0)$ for varying z-axis positions for TCIS, adjacent cell region

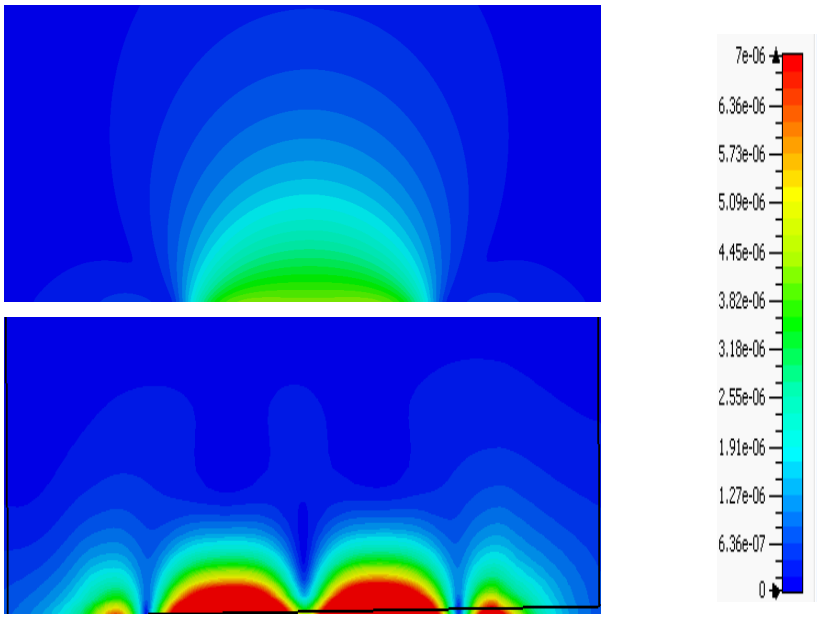

Fig. 5.19 Simulated magnitude of B_1^- a cross xy plane at structure centre

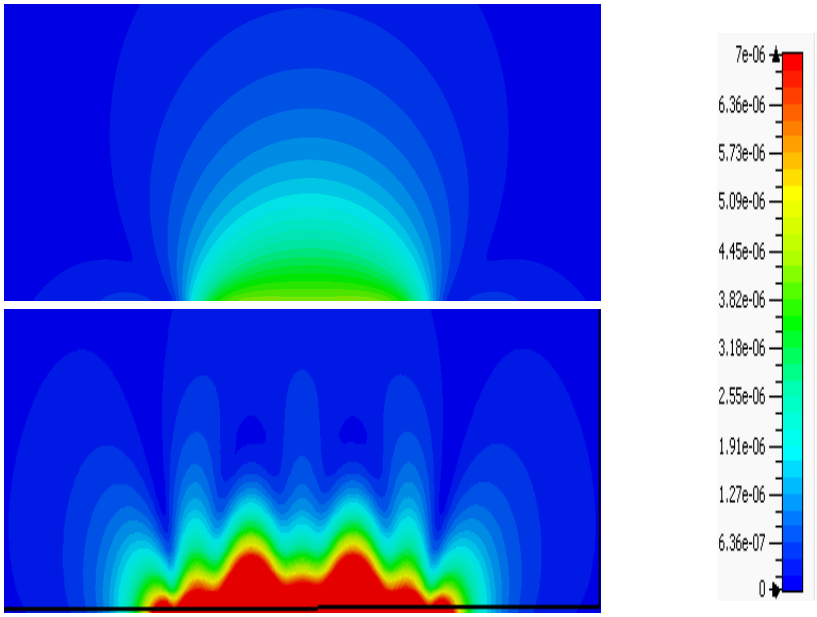

Fig. 5.20 Simulated magnitude of B_1^- a cross xy plane at intercell region

5.3.2 MR slice analysis

One of the key results from the analysis in section (5.3.1)is that the converge area for the TCIS case is greater than of only coil which can be useful for acquiring multiple slices in a

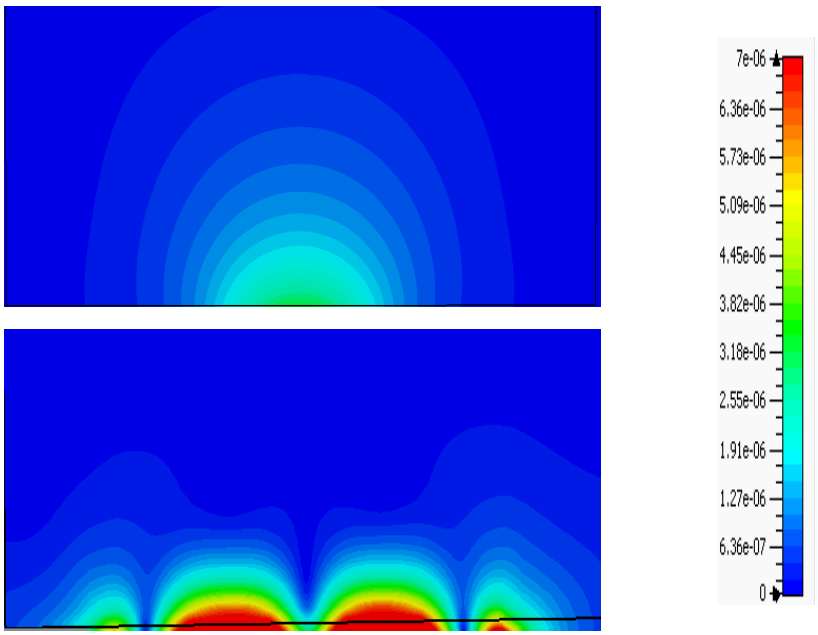

Fig. 5.21 Simulated magnitude of B_1^- a cross xy plane at adjacent cell region

MRI application. This concept is shown in Fig. 5.22 that illustrates a number of MR slices starting at the coil centre and extending towards the end phantom edge. The volume of interest for each slice is defined by $(D_c/\sqrt{(2)} \times D_c \times 10mm)$. The 1cm slice thickness is chosen as this is commensurate with the MRI systems application. Due to RF field symmetry only half of the phantom volume was considered and the mean $B^-_{1,Normalised}$ is shown in Fig. 5.23 Fig.5.23 shows the normalised mean of $B^-_{1,normalised}$, cross the dielectric phantom slices when using the TCIS. The results show that the average mean simulated $B^-_{1,normalised}$ can be improved when the transmission CIS is placed between the RF coil and dielectric phantom. Also, Fig. 5.23 shows that the mean $B^-_{1,normalised}$ can be significantly increased with the use of a TCIS and there is improvement for the off centre slices, however, the influence of nulls which create the localisation in the field distribution is observed at centre of structure and intercell region.

The next evaluation relates to the transmited B_1^+. This is depicted in Fig. 5.24 which shows the B_1^+across the dielectric phantom slices. The result illustrates that by using the transmission CIS the B_1^+ can be enhanced up to 75% for the TCIS at slice 3. This improvement of B_1^+ can reduce the transmission power which is useful for reducing the MRI system amplifier power requirements.

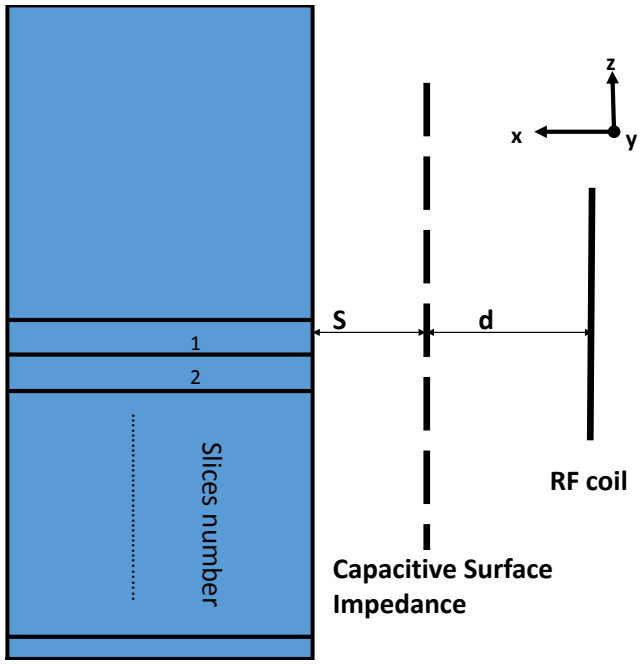

Fig. 5.22 MRI system model with slices numbering

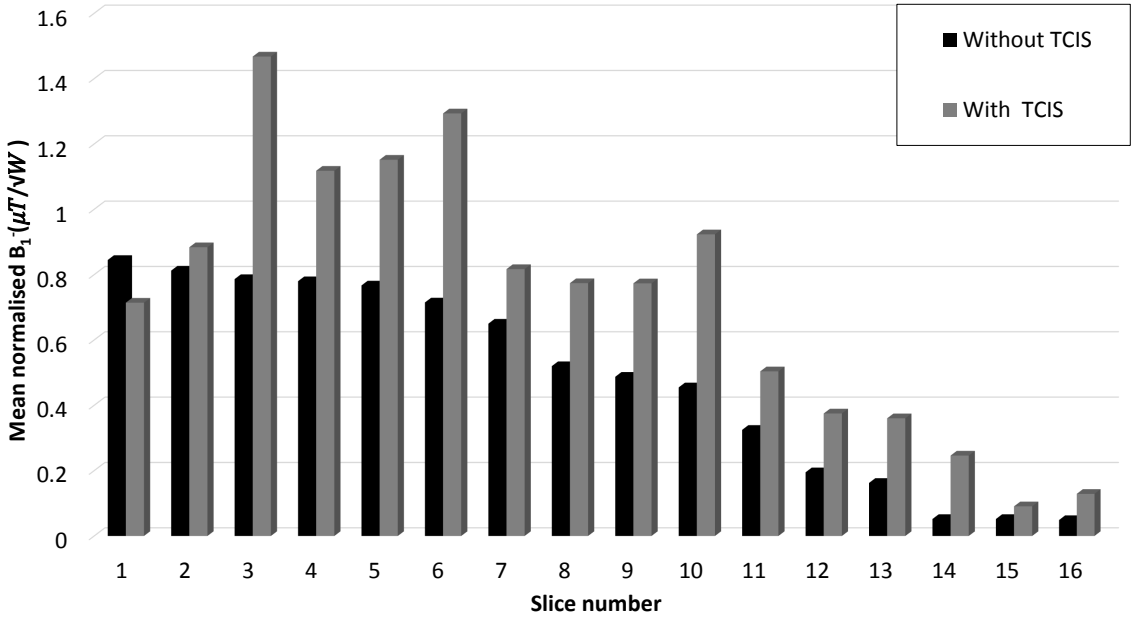

Fig. 5.23 Simulated $B_{1,normalised}^{-}$ cross the dielectric phantom slices

5.3.3 Specific absorption rate (SAR) of the proposed system

In this section SAR levels inside the homogeneous dielectric phantom for the cases of with and without the capacitive layer are investigated and compared. The local SAR within the

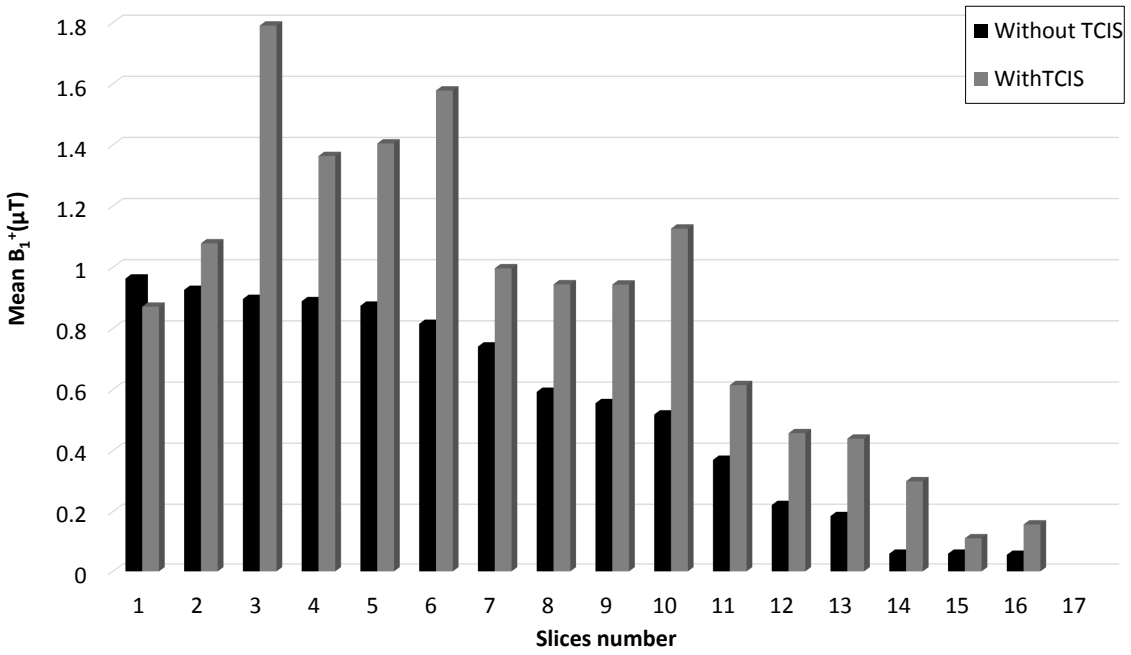

Fig. 5.24 Mean of the magnitude of simulated magnetic flux density B_1^+ cross the dielectric phantom slices with and without of using TCIS

exposed biological tissue can be calculated using Equation 3.11 by using the equivalent surface impedance model. All values of SAR have been normalized to a 1W transmission power. The simulated SAR values for the maximum 10g case were 5.8 W/kg and 2.95 W/kg for the transmission capacitive layer and without the surface respectively. The maximum value allowed by the IEC60604-2-33/2010 standard is 10W/kg. The whole body SAR was 0.068W/kg and 0.11W/kg for the transmission capacitive layer and without the surface respectively which can be compared to the IEC standard of 2W/kg [112]. It can be seen that the whole body SAR is decreased by 60% by using the TCIS, however, the maximum SAR is higher due to increase the electric field at the region nearby the surface.

5.4 Experimental characterisation

This section describes the electromagnetic characterisation of a prototype TCIS based transceiver system as a proof of concept demonstration and a comparison of performance against an RF coil is presented.

5.4.1 Experimental method

The experimental method of RF coil design was reported in (chapter 3, and 4), which requires the coil to be matched to a 50Ω source. When the RF coil is in proximity to the phantom and TCIS the coil impedance is modified which requires different tuning capacitors to achieve resonance. Fig. 5.25 shows the manufactured RF coil which incorporates three tuning capacitors ($C_1 - C_3$) and a matching capacitor C_m. Fig. 5.26 shows the front face of the manufactured TCIS with an inset showing the intedigitation detail which was manufactured using standard PCB methods. The reverse side of the CIS has an orthogonal copy of the front face providing dual polarisation. The experimental method for the near field measurements is shown in Fig. 5.27 which shows the RF coil, and dielectric phantom containing a solution of 5L distilled water and 200g of Sodium Chloride. The RF coil was connected to an Agilent E5071B vector network analyser (VNA) and was initially calibrated for one port measurements. The equivalent inductance of the coil was measured for the with and without CIS cases which produced a required total tuning capacitance of 23.5pF and 41.3pF respectively. The tuning capacitance chosen was $C_1 = 68pF, C_2 = 100pF$ and $C_3 = 56pF$ when the CIS is not included, the matching capacitance, $C_m = 168pF$ and when the CIS was present the tuning capacitance chosen was $C_1 = 221pF, C_2 = 200pF$ and $C_3 = 68pF$ and the matching capacitance, $C_m = 100pF$. It was noted that the tuning capacitors do not need to be equal and are combinations of preferred manufacturers values. Fig. 5.28 shows measured $S11$ of the with and without CIS cases demonstrating resonance at 63.8MHz. The results show the CIS gives a wider bandwidth which is due to the extra loss of the CIS and also due to a low frequency resonance (75MHz) which is an influence of the CIS.

5.4.2 The measured results

Measurements of Q-factor

The same methodology which was presented in chapter 3, section (3.6.2)to measure the Q-factor and used in chapter 4 was followed in this section. The measured Q-factor is shown in table 5.1. The results show that ratio of Q-factor with and without the dielectric phantom (load) and with and without the TCIS are higher than 3, which means both of the coils can achieve $> 82\%$ of the maximum SNR, as explained in appendix B, equation (B.2).

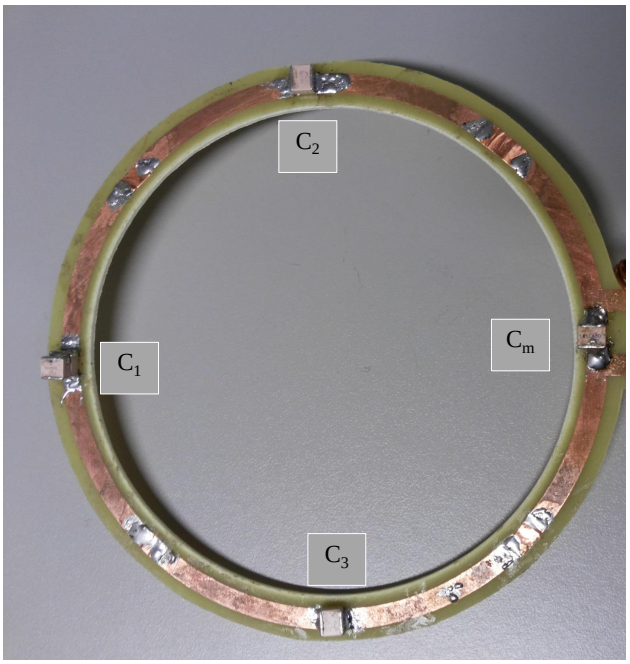

Fig. 5.25 The fabricated RF loop coil

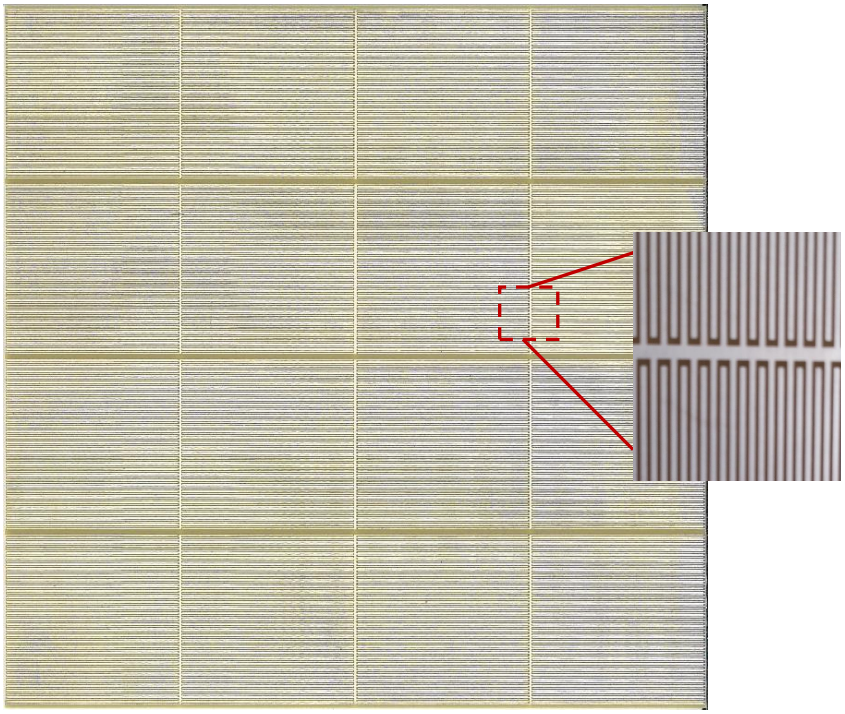

Fig. 5.26 Fornt layer of the 4×4 manufactured dual polarised CIS

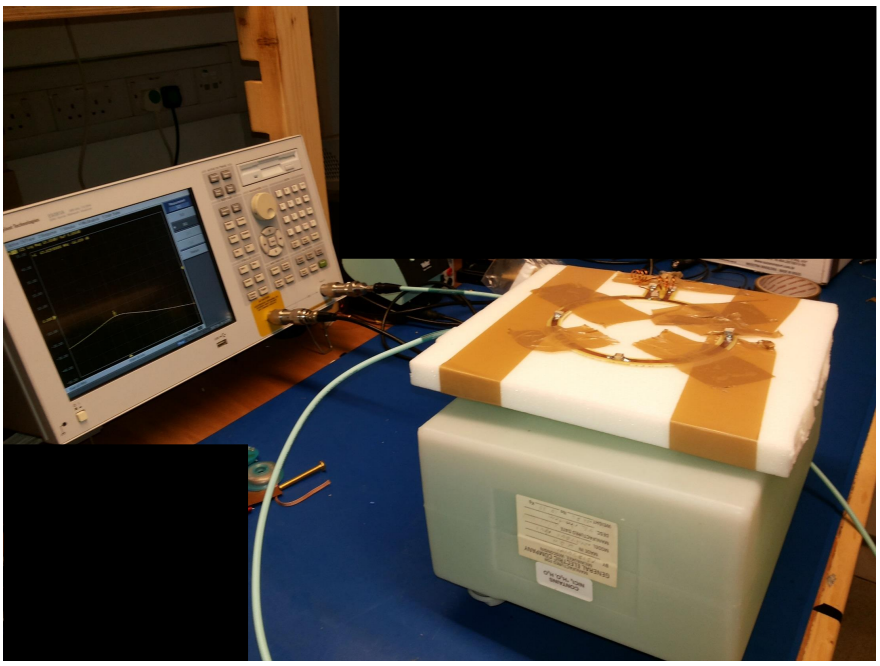

Fig. 5.27 The measured setup for coil only without TCIS

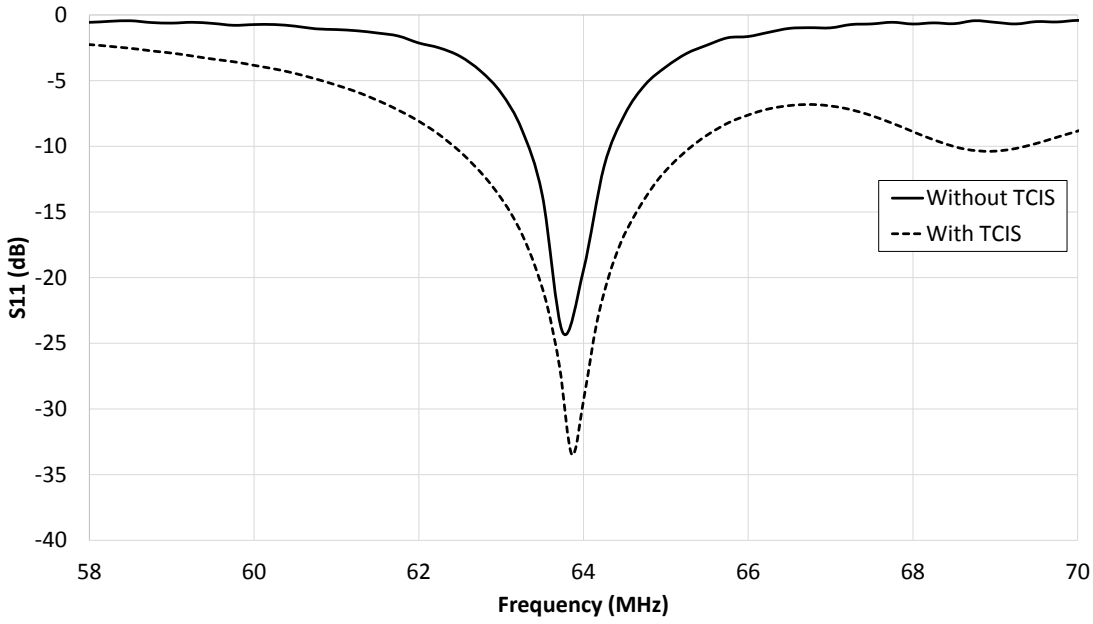

Fig. 5.28 The measured matching input of the RF coil with and without TCIS

Table 5.1 The Q-factor measured results with and without the TCIS

	Qunloaded	Qloaded	ratio
coil only	144	45	3.2
coil with TCIS	92	29	3.19

The measurement of the transmission coefficient S21

To characterise the magnetic field a second coil of diameter 3cm, which is chosen to have minimal influence on the magnetic field, is connected to the port two of the VNA. The self resonant frequency of the coil is 2.2GHz. It is assumed that the measured transmission coefficient (S21) is proportional in the magnetic field. Fig.5.29 shows the measured S21 when the 4×4 was inserted between RF coil and dielectric phantom as a transmission CIS compared to the only coil along y-axis at (x=z=0). The results illustrate that there was an improvement in S21 of all regions of y-axis, however, the improvement at the system centre was not much as other regions due to the even periodicity of the TCIS.

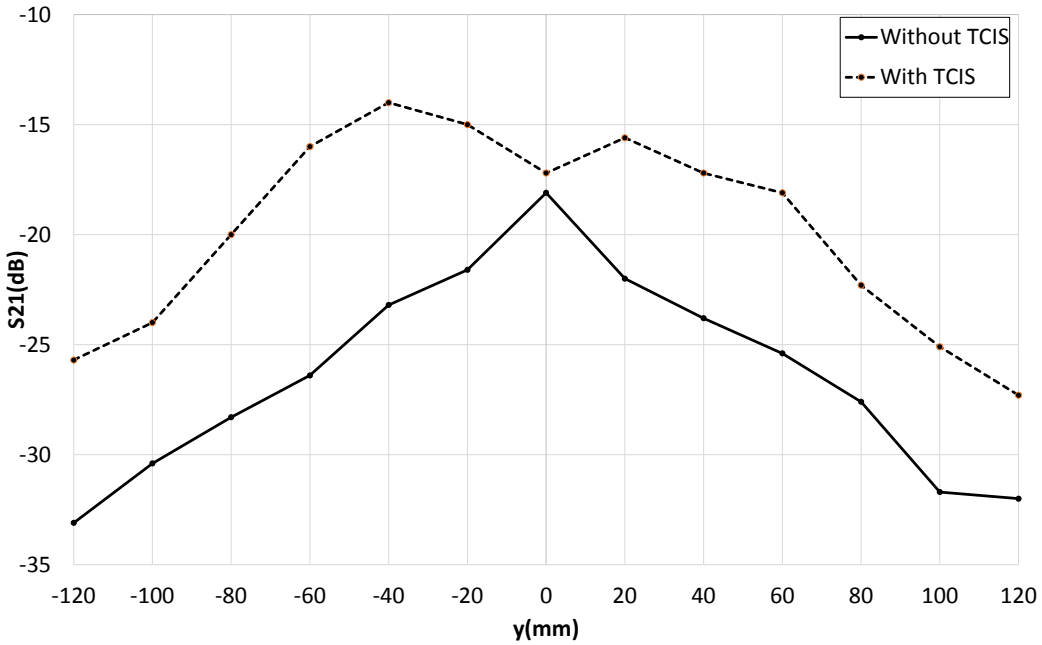

Fig. 5.29 Measured S21 with and without TCIS

5.5 MRI measurements

The same methodology which was used in previous chapters to demonstrate the behavior of the periodic metasurface under the real system is present in this section. Fig. 5.30 and Fig. 5.31 show the process of the proposed system within the 1.5T whole body MRI scanner with the TCIS and without TCIS, respectively. The measurement parameters are listed in Table 5.2.

Table 5.2 MRI image sequence parameters

Parameter	Value
Pulse repetition time (ms)	500
Echo time (ms)	50
Transmission gain (dB)	3
Bandwidth (kHz)	15.63
Field of view (cm)	36 x 36
Slice thickness (mm)	10
Acquisition matrix (pixels)	256 x 256

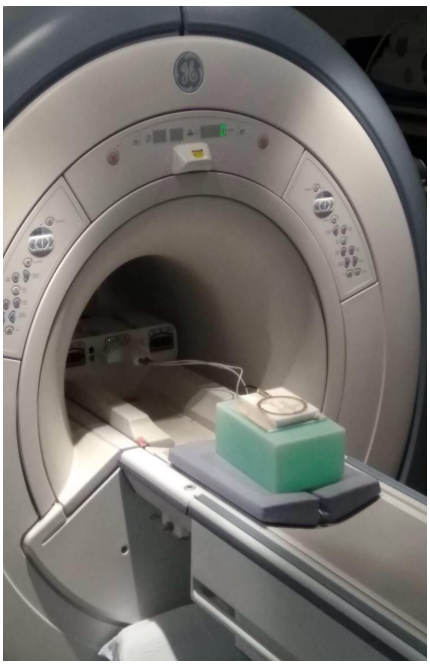

Fig. 5.30 The TCIS system demonstrated within a 1.5T MRI scanner

Fig. 5.31 The coil only measurement system demonstrated within a 1.5T MRI scanner

5.5.1 Analysis of the MRI profile using a TCIS

The RF coil was placed at the centre of the transmission capacitive layer as shown in Fig.5.1. MRI slices were taken as mentioned in section (5.3.1) at $z = 0, z = P/2, z = 3P/2$, spaced 1cm apart as shown in Fig 5.15. Figs. 5.32 and 5.33 show the MRI images of the dielectric phantom with and without 4×4 TCIS at the centre and edge of the RF loop coil with the same image intensity scale. The results illustrate that by using 4×4 TCIS the image intensity was loclaised and significantly improved at the centre of the unit cell at the coil centre and the edge, however, due to a separating gap between the unit cells resulted a small low intensity region resulted in the image at the coil centre. The measured SNR was calculated as described in the chapter 3 using (3.9). More detailed analysis of the MRI image profile Figs.5.34,5.35 and 5.36 show the SNR cross the dielectric phantom at $z = 0, z = P/2, z = 3P/2$ which were named as above centre of structure, intercell region, and adjacent cell region, respectively as shown in Fig.5.15 where the slices of interest is shown. The noise was taken from images with the RF power switched off.

Figs. 5.37, 5.38 and 5.39 illustrate the linear graphs of the images SNR at the same locations of the Figs.5.34,5.35 and 5.36 which describe the SNR comparative in more details with and without the 4×4 TCIS.

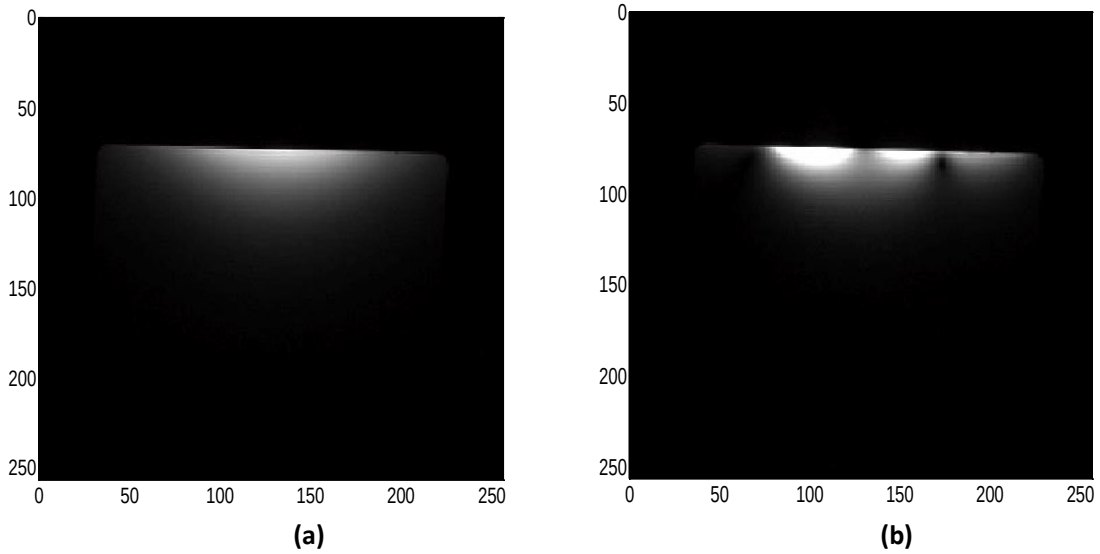

Fig. 5.32 Measured MRI images. (a). The RF coil alone,(b). With the 4×4 TCIS at the coil centre

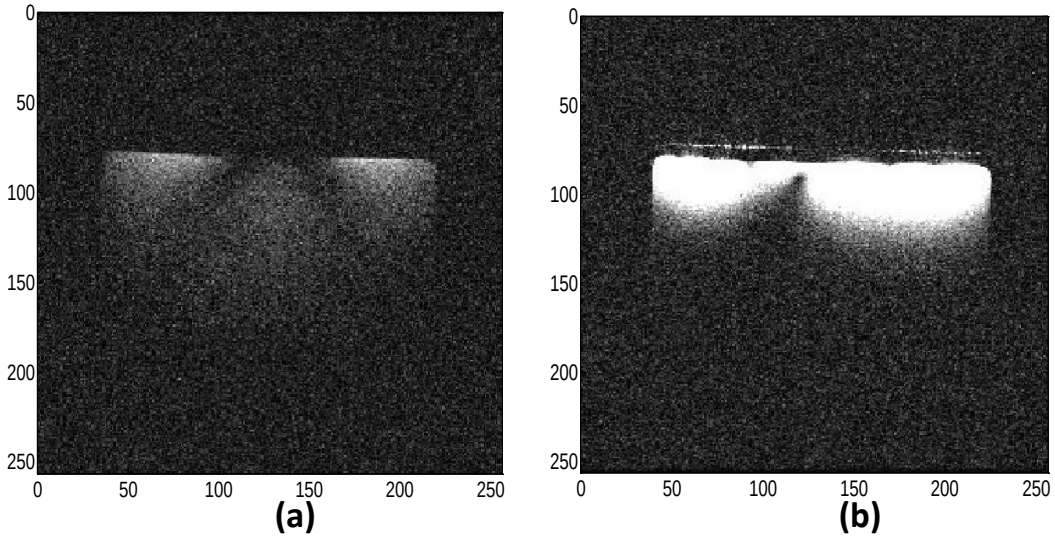

Fig. 5.33 Measured MRI images. (a). The RF coil alone, (b). With the 4×4 TCIS at the coil edge (adjacent cell region)

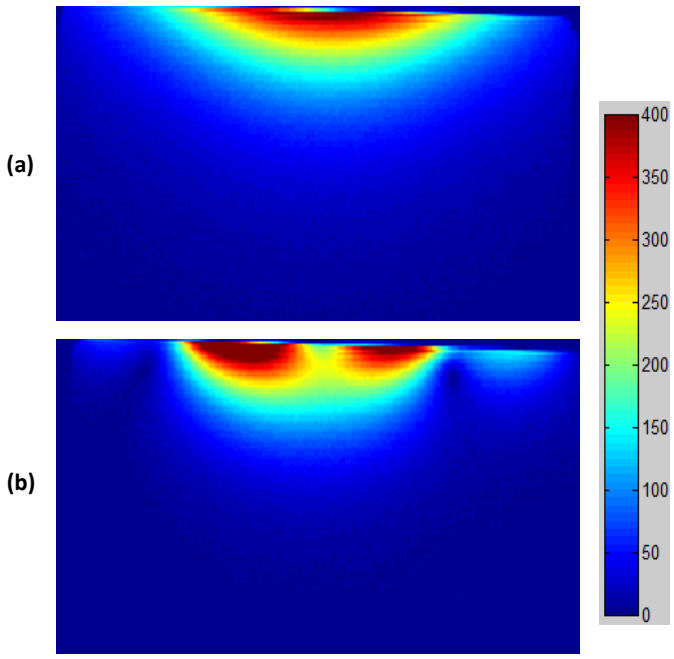

Fig. 5.34 Measured MRI images SNR. (a). Only coil.(b). With the 4×4 TCIS at the coil centre (centre of structure) throughout all the phantom with scale [0 400]

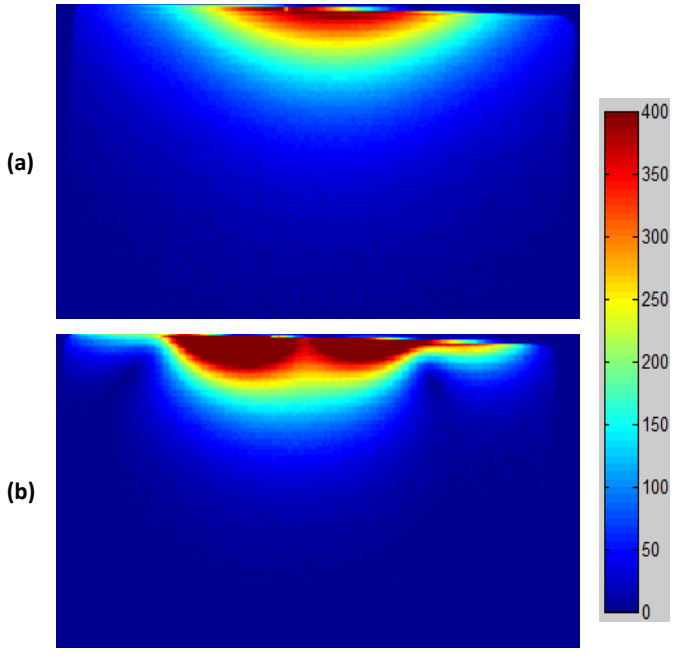

Fig. 5.35 Measured MRI images SNR. (a). The RF coil alone, (b). With the 4×4 TCIS at $z = P/2$ (intercell region) throughout all the phantom with scale [0 400]

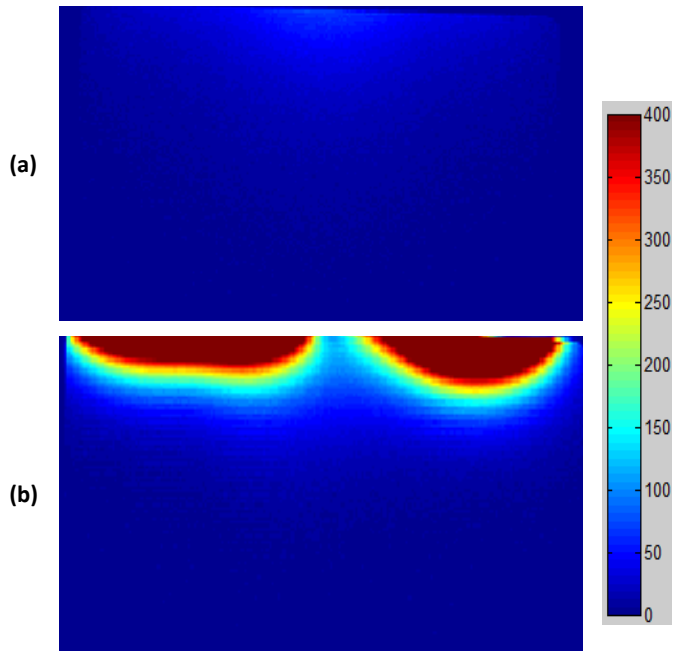

Fig. 5.36 Measured MRI images SNR. (a). The RF coil alone, (b). With the 4×4 TCIS at $z = 3P/2$ (adjacent cell region) throughout all the phantom with scale [0 400]

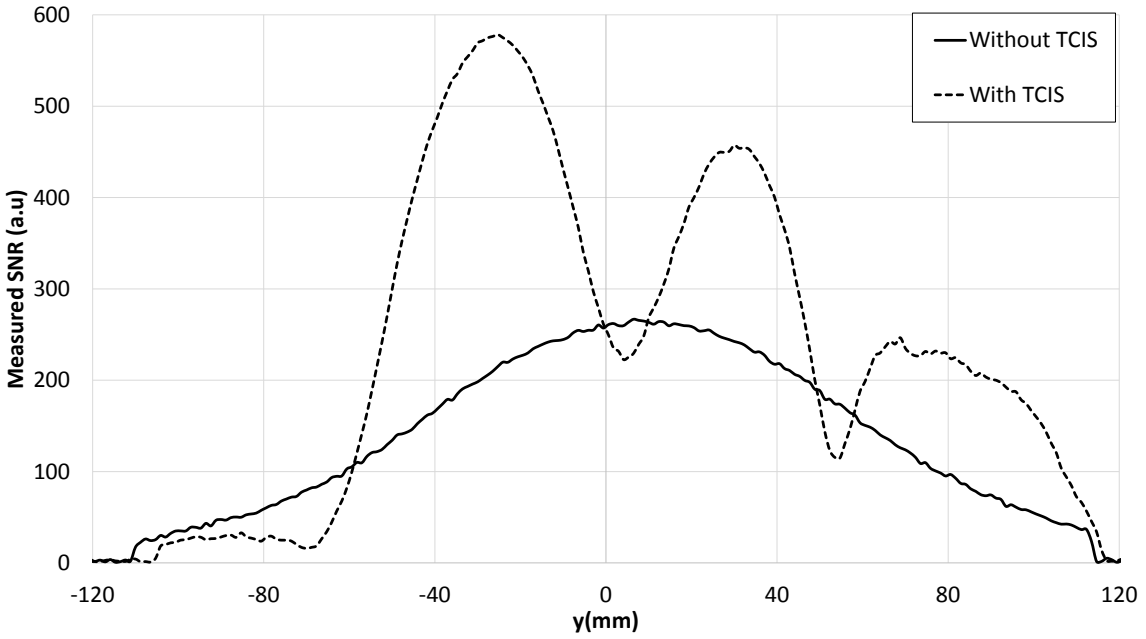

Fig. 5.37 Measured MRI images SNR With and without the 4×4 TCIS at $z = 0$,x=5mm inside the dielectric phantom (centre of structure)

Table. 5.3 shows the maximum SNR and effective coil SNR which is described by the SNR through the cubic voxel with dimensions of $D_c/\sqrt{2} \times D_c$ of the proposed system with

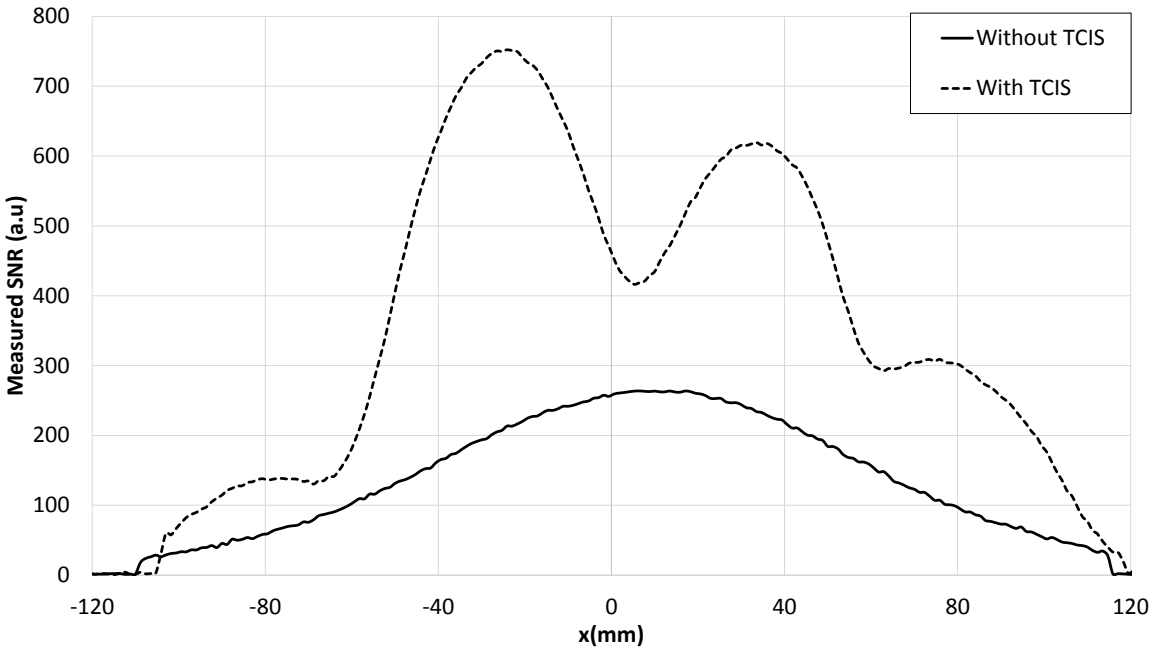

Fig. 5.38 Measured MRI images SNR with and without the 4×4 TCIS at $z = P/2$, x=5mm inside the dielectric phantom (intercell region)

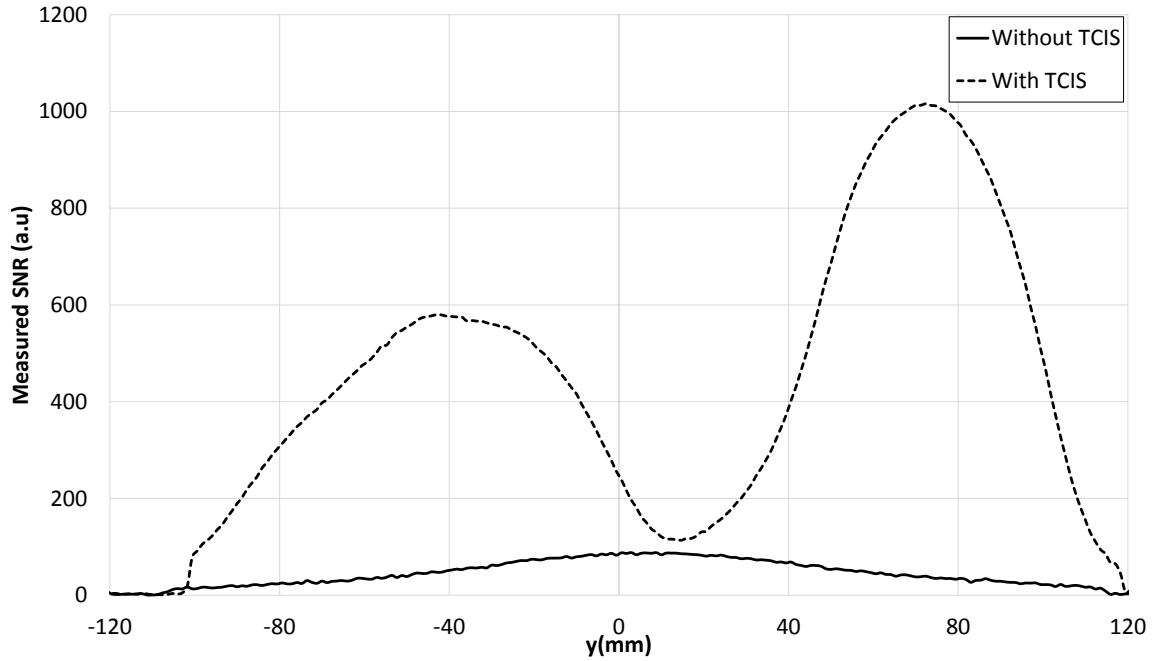

Fig. 5.39 Measured MRI images SNR With and without the 4×4 TCIS at $z = 3P/2$, x=5mm inside the dielectric phantom (adjacent cell region)

and without 4×4 TCIS at slices location centre of structure,intercell region, and adjacent cell region respectively. The results show that there is a transceiver improvement of the

Table 5.3 SNR analysis results with and without TCIS

Slice number	Maximum SNR		Coil SNR	
	With TCIS	Without TCIS	With TCIS	Without TCIS
centre of structure	387	329	58.6	54.3
intercell region	928.6	282	72.2	48.7
adjacent cell region	1286	54.3	38.8	11.43

effective coil SNR of 8% and 49% at centre of structure and intercell region respectively. The effective coil SNR can be significantly enhanced by using the TCIS at the coil edge which was presented at adjacent cell region of 238%. The results demonstrated that by using an even periodicity unit cell of the periodic metasurface the magnetic flux density and SNR can be localised and enhanced at the centre of unit cells throughout the surface.

5.6 Summary

In this chapter, a method for designing a two dimensional periodic capacitive impedance surface for enhancing and localising the $B^{-}_{1,normalised}$ for MRI applications has been demonstrated through numerical and experimental techniques. The method provides values in good agreement with numerical simulation results. The work has been demonstrated by the following next steps: firstly, the surface impedance assumed to be a homogeneous surface and dominated by the capacitance for the ideal case in order to investigate the effects of the capacitance sheet on the $B^{-}_{1,normalised}$. The result shows that the maximum improvement in $B^{-}_{1,normalised}$ and $|B^{+}_{1}|$ at the front surface of the dielectric phantom can be achieved when the value of the sheet capacitance is 400pF and this surface has been implemented using the interdigital technique. Full wave numerical simulations have shown the potential to achieve high improvements in $B^{-}_{1,normalised}$ at the coil edges which was represented by (adjacent cell region) and the improvement at the coil centre was not as high due to the even periodicity of the surface. Experimental results show a 1dB, and 9dB increase at the coil centre and coil edge respectively in received signal when tested within a two port VNA system at the front face of a dielectric phantom, providing confidence in the technique which was the same trend of the simulated results. MRI measurements using a 1.5T scanner have shown similar $B^{-}_{1,normalised}$ trends giving an improvement of high at the coil edges and not that high at the coil centre. The results compare favourably with the simulations albeit as a proof of concept these results are promising. In next the chapter the transmission CIS has been developed in order to achieve the high improvement at the coil centre.

Chapter 6

Enhancing Signal-to-Noise Ratio using a Capacitive Impedance Surface for 1.5 Tesla MRI systems.

Chapter 5 has demonstrated using simulation, network analyser measurements and RF measurements within the MRI scanner that the magnetic flux density and measured SNR can be localised using an even number of unit cells, which was denoted by $N_P = 4$ of the TCIS. Since the maximum SNR that an RF coil can generate is usually focused at the coil centre, improving SNR at the coil centre is required for real MRI applications. In this chapter a two dimensional transmission capacitance impedance surface for enhancing the SNR for the MRI system applications, that take into account the influence of nulls in the field distribution at the RF coil centre has been developed. The difference between a transmission CIS which is presented in this chapter and the transmission CIS which was described in chapter 5 is the number of cells N_P in the structure. In chapter 5 the number of cells were assumed to be an even number $N_P = 4$, and in this chapter the N_P is assumed to be an odd number $N_P = 3$ in order to allow the RF coil to be placed at the centre of the unit cell of the TCIS. This chapter demonstrates that by using theoretical design, numerical simulations, vector network analyser (VNA) measurements, and MRI results, the RF magnetic flux density, (B_1), and SNR can be increased when a capacitive impedance surface (CIS) is placed between a RF loop transceiver coil and homogeneous phantom. Another novel aspect of the chapter is to demonstrate how this approach can locally improve the SNR at the coil centre and also provide SNR improvement away from the centre of the RF coil which would enhance MRI sensitivity. This chapter is organised as follows: Section 6.1 discusses the CIS concept and implementation using an interdigital frequency selective surface. A numerical characterisation of the proposed

system is investigated in section 6.2. Section 6.3 shows the experimental characterisation within a laboratory environment. Section 6.4 details the results from measurements within an MRI scanner to quantify the transverse improvement of SNR. Further detailed analysis is provided in section 6.5 which describes a method of how transmission performance and receiver sensitivity are calculated and improvement results are discussed. Finally, section 6.6 provides a summary of the chapter and compares the chapter results with the state-of-art methods from published literature.

6.1 Capacitive impedance surface concept and implementation

6.1.1 The odd periodicity TCIS implementation

In the previous chapter, section (5.2) the simulated $B^{-}_{1,normalised}$ was observed inside the dielectric phantom, in the case of homogeneous surface impedance with no losses of the various capacitance value of the TCIS model, through the x-axis at the coil centre. To demonstrate the maximum enhancement of $B^{-}_{1,normalised}$ a capacitance of 400pF was selected (which is the same capacitive sheet used in chapter 5) for the remainder of this study which led to the unit cell with the following properties, P=50mm, D=49.1mm, N=132,w_d=0.25mm and g_d=0.12mm. The gap between the ends of the digits and the horizontal metallic strip at the top of the unit cell was 0.3mm and there is an inter-unit cell separation of 0.58mm. It was assumed that the metallic elements were 32μ m thick copper. The main difference between the TCIS which was used in chapter 5 and the TCIS which is used in this chapter is the unit cell periodicity, here the surface with 3×3 unit cell is implemented with a total surface dimensions of 15×15 cm as shown in Fig. 6.1.

6.2 Numerical characterisation of FSS implementation

6.2.1 Analysis of $B^{-}_{1,normalised}$ and $|B^{+}_{1}|$

As it mentioned in chapter 1 equation (1.47) and mentioned in chapter 3 and 4 that $SNR \approx |sin(\gamma\tau|B^{+}_{1}|(B^{-}_{1,normalised})^{*}|$, where transmission performance is a function of $|B^{+}_{1}|$ and receiver performance is a function of $B^{-}_{1,normalised}$. Simulations were carried out with and without the transmission CIS where the magnitude of $B^{-}_{1,normalised}$ and $|B^{+}_{1}|$ inside the dielectric phantom was monitored along the x-axis and y-axis when the RF coil was fed by a

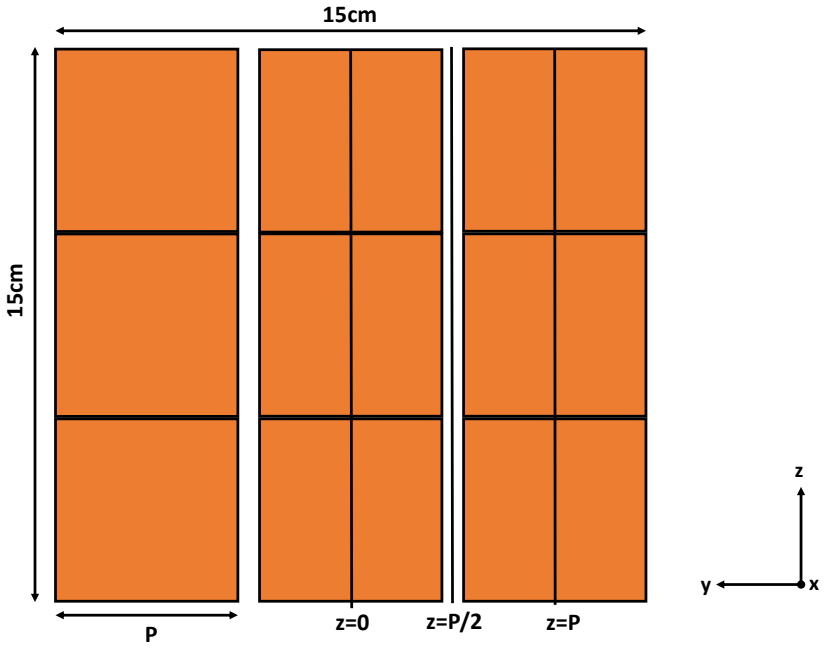

Fig. 6.1 Illustration of CIS showing yz planes of interest (z=0, z=P/2 and z=P)

sinusoidal 1A current source. Fig. 6.2 shows a comparison between the ideal homogeneous CIS and the FSS implementation which includes copper and substrate losses and any effects from the FSS periodicity. Fig. 6.2 and Fig. 6.4 show the $B^{-}_{1,normalised}$ along the x-axis and y-axis respectively. The results show that there is a reduction in $B^{-}_{1,normalised}$ compared to the ideal case, however there is still significant improvement compared to the case without CIS. A $B^{-}_{1,normalised}$ maximum improvement of 160% and 240% is observed for the FSS implementation and ideal case respectively when x=5mm, y=0 and z=0, however, at the centre cell (z=0) the improvement is limited to the first 40mm. Fig. 6.4 illustrates the effect of FSS periodicity giving rise to localised peaks which may be advantageous for image acquisition beyond the edge of the RF coil. Further detail relating to the variation of $B^{-}_{1,normalised}$ for different positions across the FSS is depicted in Fig. 6.1 which shows the three unit cells of the CIS including specific regions along the yz plane which includes the centre of the structure (z=0), intercell region (z=P/2) and adjacent cell centre (z=P). Fig. 6.3 shows the magnitude of the transmission magnetic flux density in ideal case, FSS implementation compared to the $|B^{+}_{1}|$ generated by only RF coil at the centre of the phantom $(y = z = 0)$ along x-axis. The results show that, there is a reduction in $|B^{+}_{1}|$ when compared to the lossless case, however, there is still significant enhancement of 287% and 210% is noticed for the ideal and interdigital implementation respectively and the improvement is observed for the first 40mm inside the phantom.

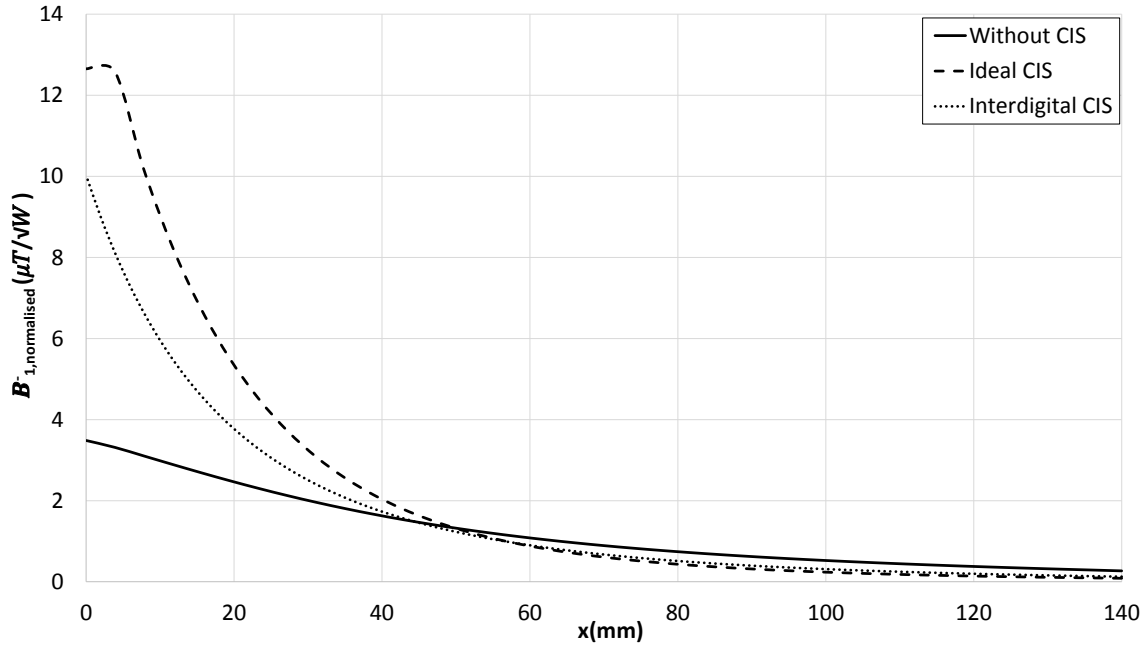

Fig. 6.2 Simulated $B^{-}_{1,normalised}$ along x-axis (y=0, z=0)

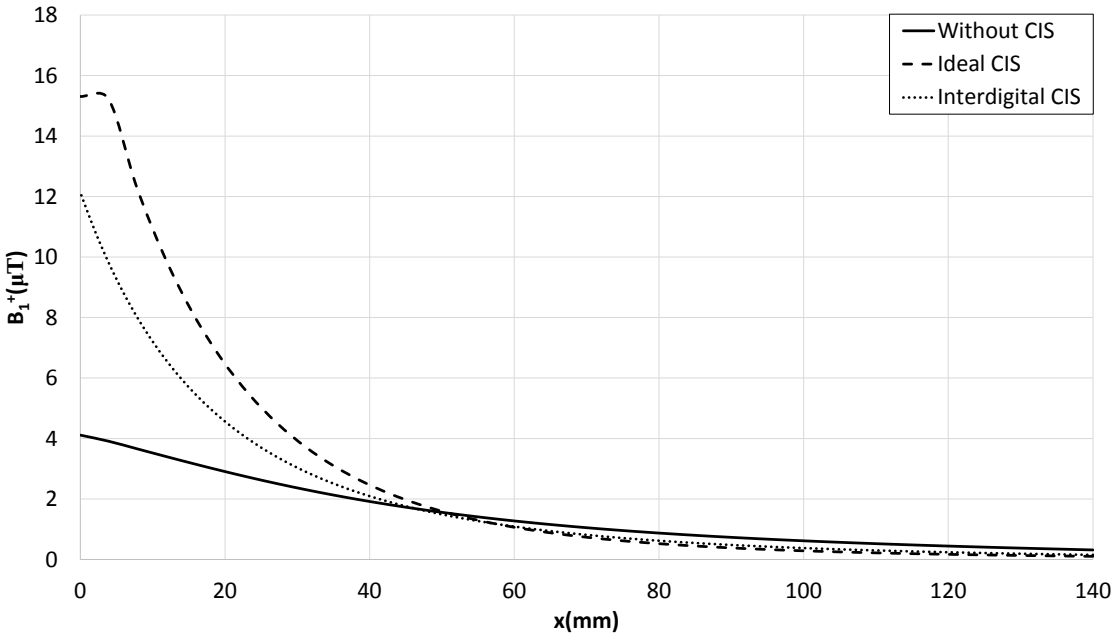

Fig. 6.3 Simulated B_1^+ along x-axis (y=0, z=0)

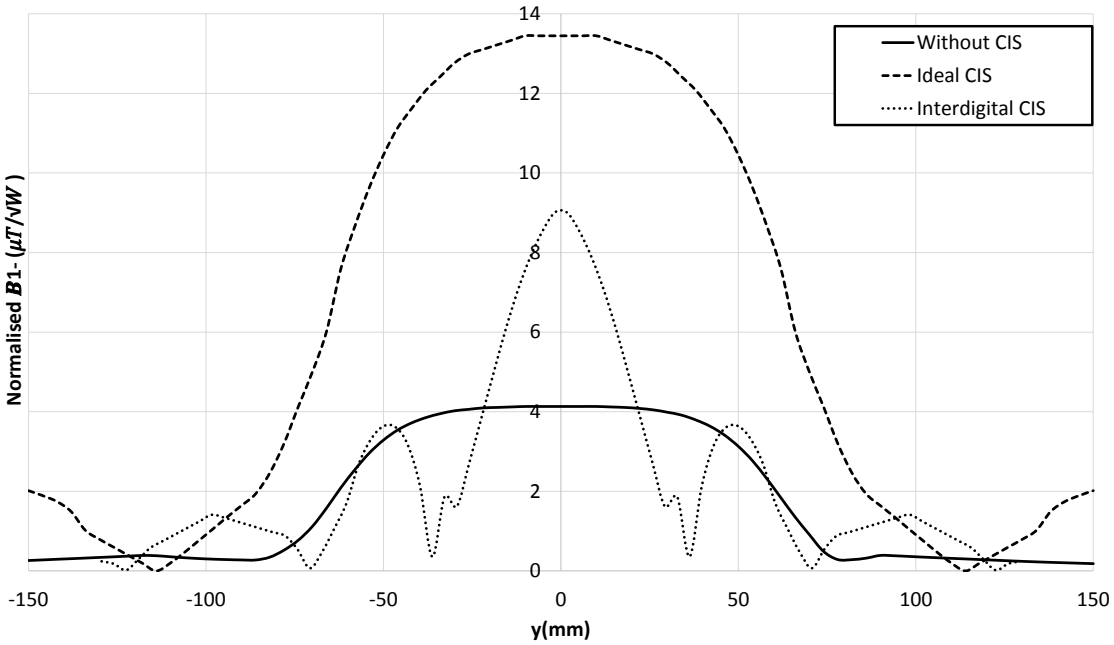

Fig. 6.4 Simulated $B^{-}_{1,normalised}$ along y-axis (x=5, z=0)

Figs. 6.5, 6.6 and 6.7 show $|B^{-}_{1}|$ across the xy-plane at these three locations (z=0, z=P/2 and z=P) planes respectively with and without the CIS providing more detail of the field distribution. The $|B^{-}_{1}|$ has been focused at the coil centre, which leads to enhance the magnetic field at the main beam width approximately equal to the unit cell periodicity. The Figs. 6.5, 6.6 and 6.7 show how the CIS periodicity causes localised $|B^{-}_{1}|$ variations and extends the area over which images could be taken with the disadvantage of narrow nulls in the field distribution.

6.2.2 MR slice analysis

MR slices analysis was investigated in the previous chapter, and the process will follow in this section. Only half of the phantom slices were considered in the simulations, which is described as (region 1) as shown in Fig. 6.8. Because the field distribution is symmetric in both sides of the phantom and the mean $B^{-}_{1,normalised}$ and mean B^{+}_{1} are shown in Figs. 6.9 and 6.10 respectively. The total dissipated powers were 1.30W and 1.46W for with CIS and the coil only cases respectively, for a 1A sinusoidal current source. Figs. 6.9 and 6.10 show that the mean of $B^{-}_{1,normalised}$ and B^{+}_{1} can be significantly increased with the use of a TCIS and there is improvement for all slices.

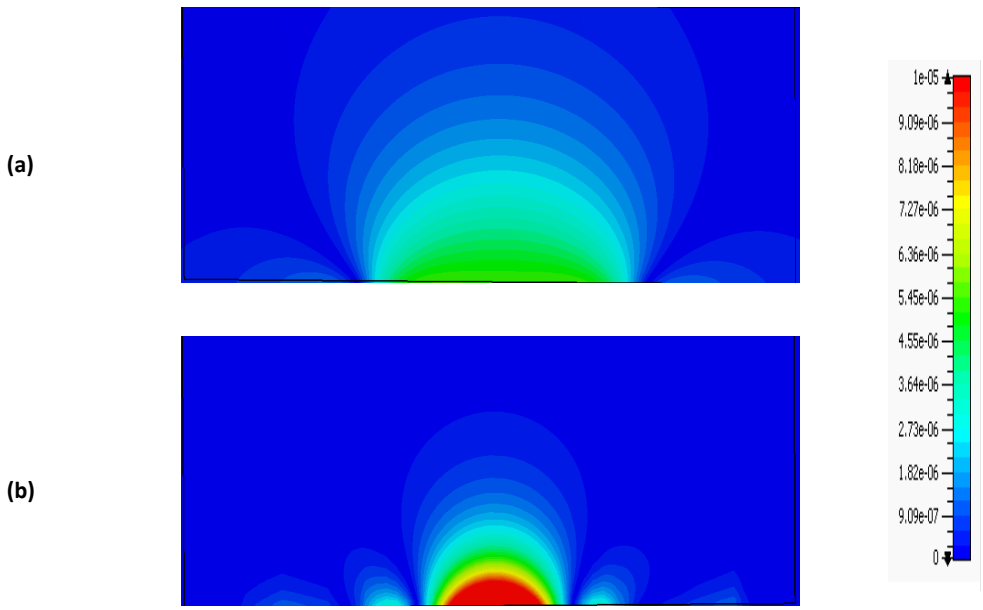

Fig. 6.5 Simulated B_1^- across the xy-plane at (z=0). (a)without TCIS, (b)with TCIS)

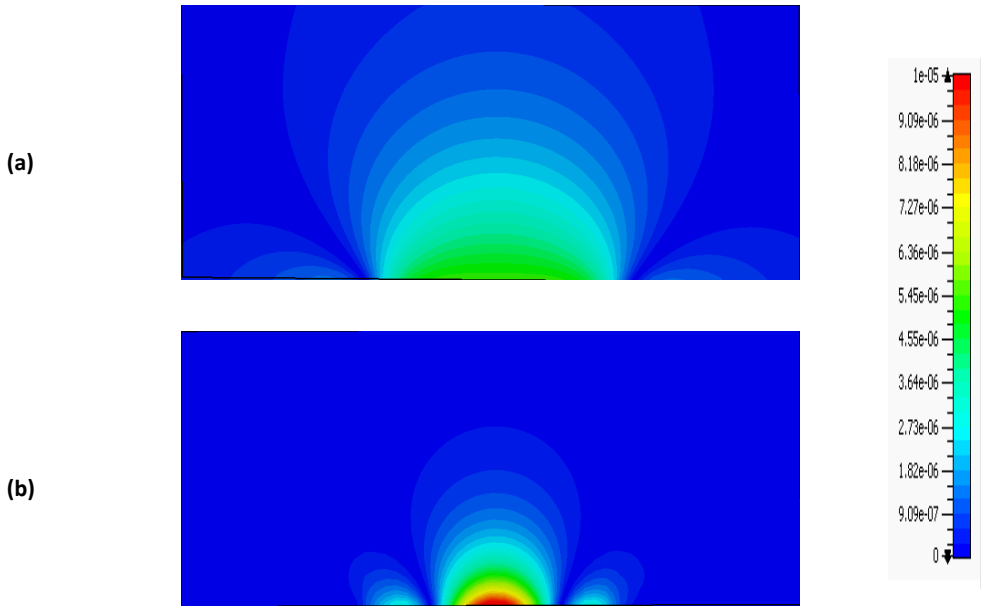

Fig. 6.6 Simulated B_1^- across the xy-plane at (z=25mm).(a)without TCIS, (b)with TCIS)

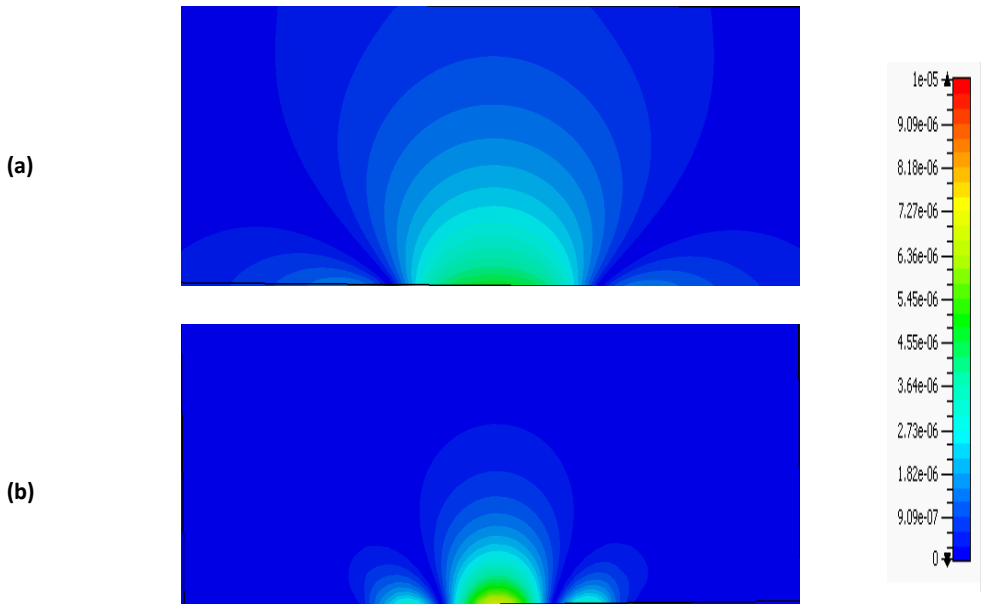

Fig. 6.7 Simulated B_1^- across the xy-plane at (z=50mm)(a)without TCIS, (b)with TCIS)

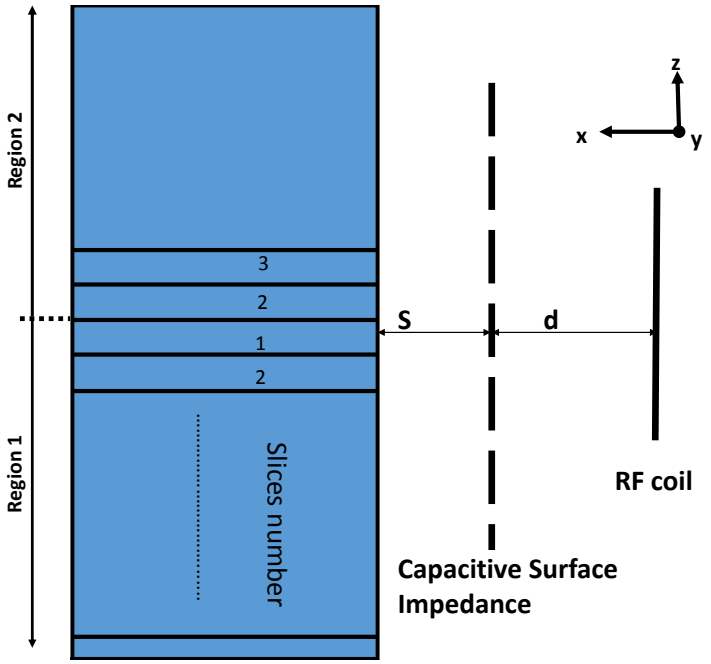

Fig. 6.8 Illustration of system with slice information

6.2.3 E-field

Fig. 6.11 shows a magnitude of E-field inside the dielectric phantom with and without TCIS in xy plane at z=0. Fig.6.12 illustrates across line of the magnitude of the E-field at

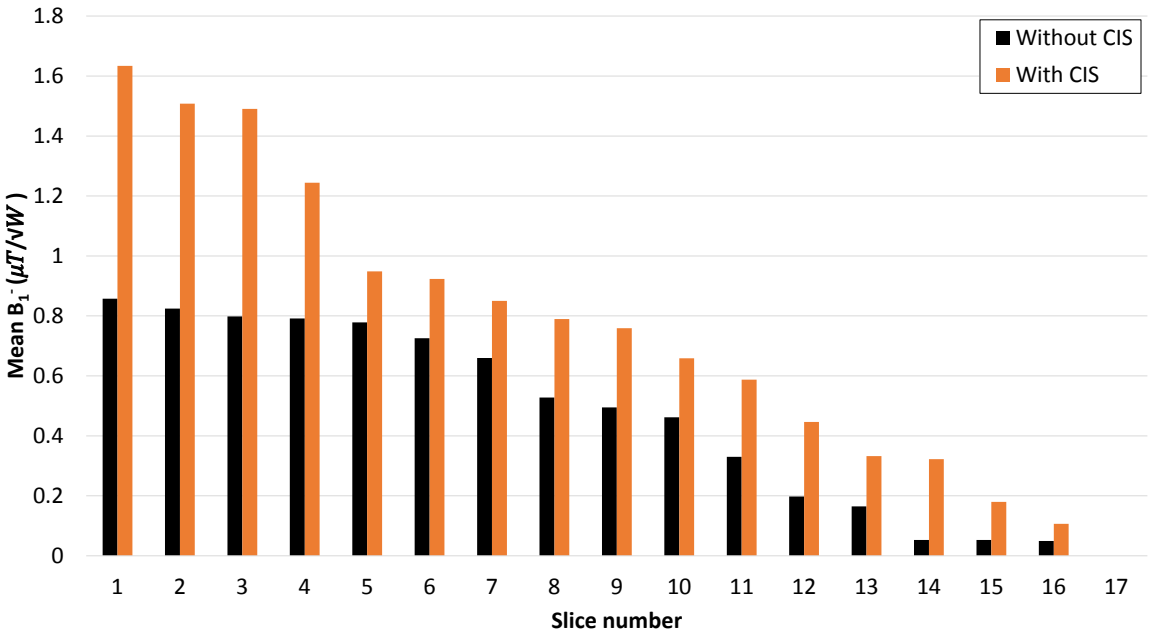

Fig. 6.9 Mean $B^{-}_{1,normalised}$ for varying slices of volume $(D_c/\sqrt{2} \times D_c \times 10mm)$

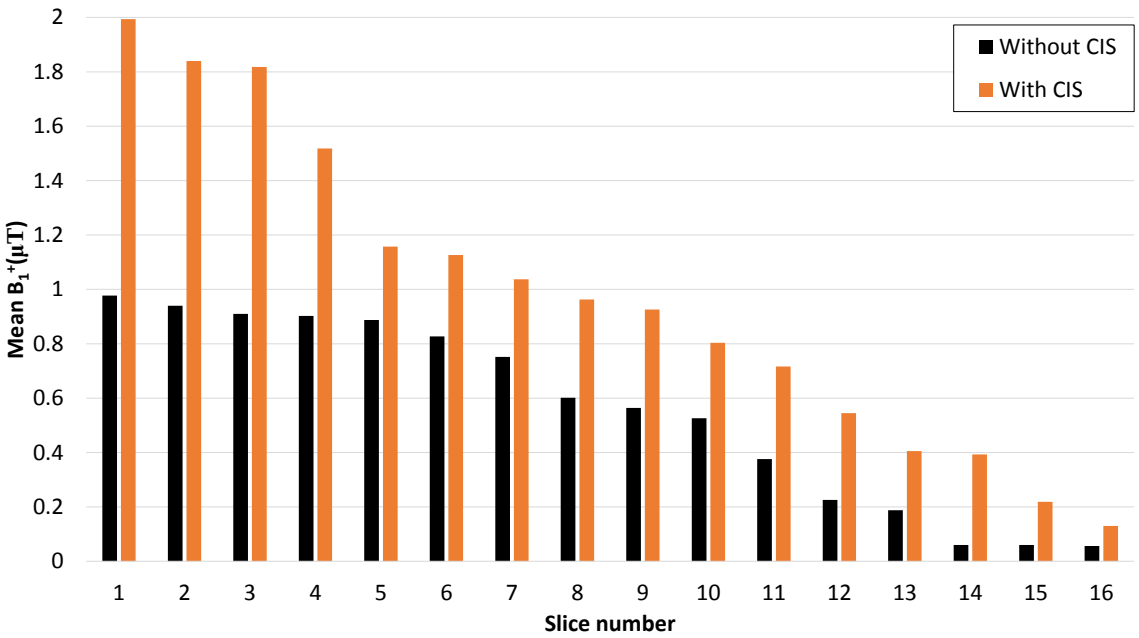

Fig. 6.10 Mean B^{+}_{1} for varying slices of volume $(D_c/\sqrt{2} \times D_c \times 10mm)$

the maximum value regions (R1 and R2) which represented the magnitude of the E-field value with and without TCIS respectively. The regions R1, and R2 are taken at (x=z=0, y=25mm) and (x=z=0, y=30) respectively. The results show that, the magnitude of the e-field is increased by 67% at x=0, then the value decays. It can be seen that there is a decline in the magnitude of E-field after x=45mm.

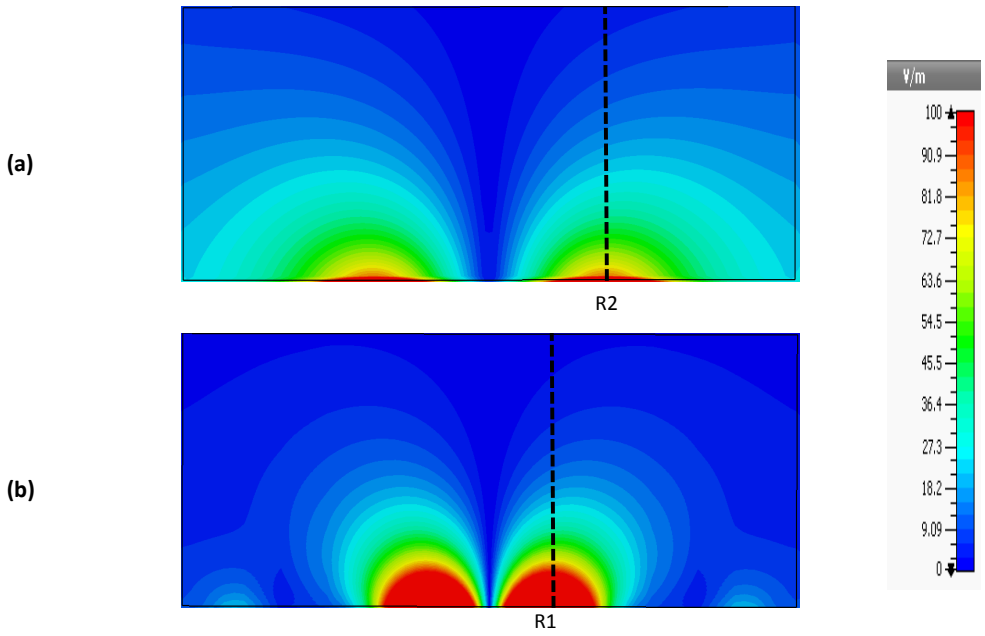

Fig. 6.11 E-field through xy-plane at (z=0), (a)without TCIS, (b) with TCIS

6.2.4 Specific absorption rate (SAR)

The simulated SAR values for the maximum 10g case were 3.47W/kg and 1.18 W/kg for the CIS and coil only cases respectively. The whole body SAR was 0.11W/kg, and 0.135W/kg for the CIS and coil only cases respectively when normalized to a 1W accepted power. The results show that there is an increase of the local SAR value, however, the whole body SAR is decreased by including the TCIS metasurface.The maximum value allowed by the IEC60604-2-33/2010 standard is 10W/kg for 10g and 2W/kg for the whole body [112]. Therefore, both of the local and whole body SAR values of both cases are under the maximum levels.

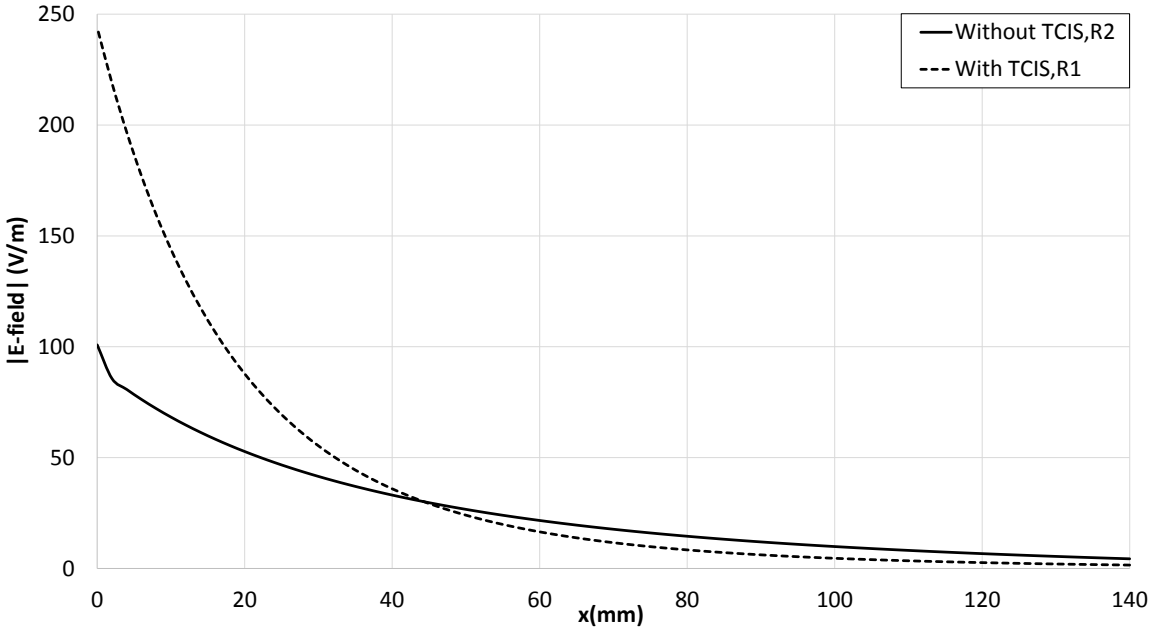

Fig. 6.12 Simulated |E| across the maximum region (R1). and R2 with and without TCIS respectively

6.3 Experimental characterisation

This section describes the electromagnetic characterisation of a prototype CIS based transceiver system as a proof of concept demonstration and comparison of its performance against an RF coil alone is presented.

6.3.1 Experimental method

The RF coil design was previously reported in chapter 5, which used the same value of tuning capacitors ($C_1 - C_3$), however, by modifying the TCIS into 3×3 a matching capacitor C_m when the TCIS included was changed to (148pF). Fig. 6.13 shows the modified front face of the fabricated TCIS with an inset showing the intedigitation detail which was fabricated using standard PCB methods. As described in the previous chapters, the reverse side of the CIS has an orthogonal copy of the front face providing dual polarisation. The experimental method for the near field measurements is shown in Fig. 6.14 which illustrates the RF coil, TCIS, and dielectric phantom. Fig. 6.15 shows measured S11 of the with and without CIS cases demonstrating resonance at 63.8MHz.

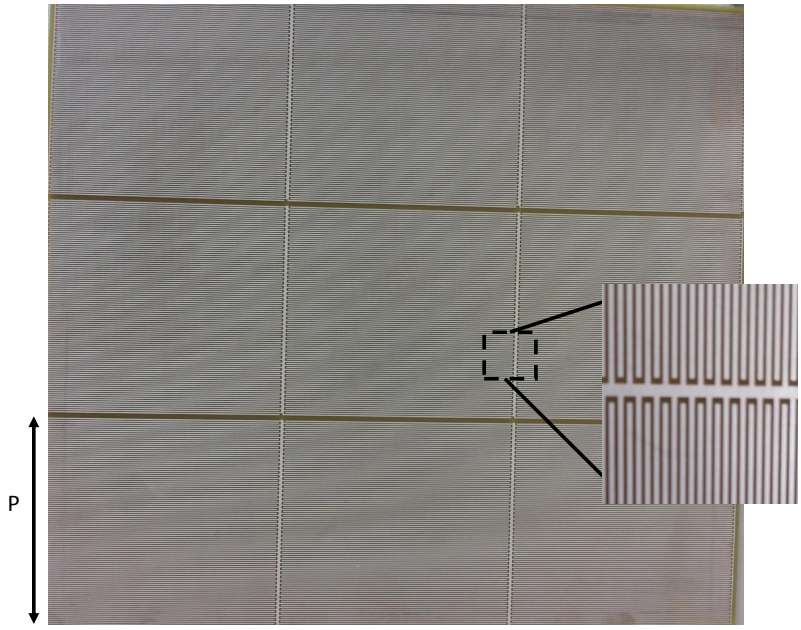

Fig. 6.13 Front layer of the 3×3 manufactured dual polarised CIS

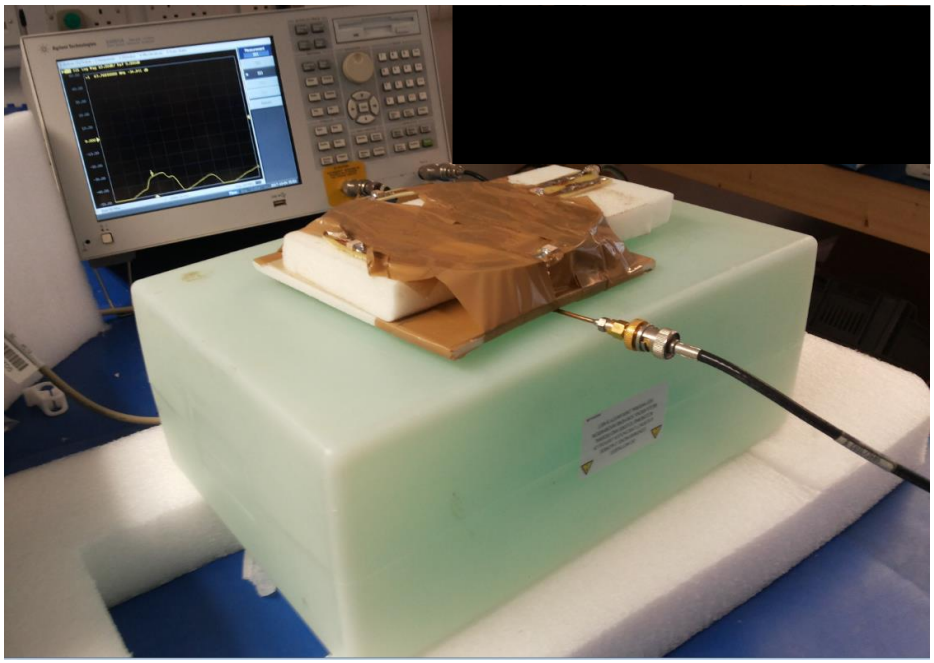

Fig. 6.14 Measurement system

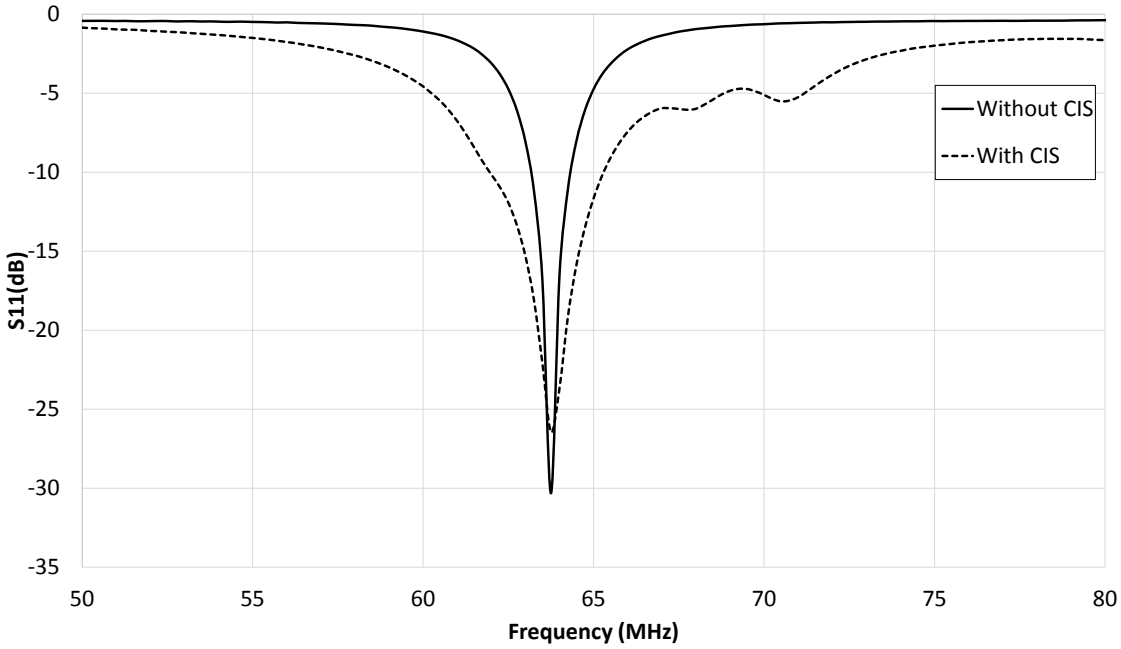

Fig. 6.15 Measured RF coil input match

6.3.2 Measured results

Measurements of Q-factor

The Q-factor measurement method was explained in chapter 3, section (3.6.2) and has been applied in chapter 4 and chapter 5 and it is followed in this section. The table. 6.1 illustrates the measured Q-factor in both cases with and without the TCIS. The results show that both of the coils can achieve more than 81% of the maximum SNR.

Table 6.1 The Q-factor measured results with and without the TCIS

	Qunloaded	Qloaded	ratio
coil only	144	45	3.2
coil with TCIS	95	31	3.06

6.3.3 Measured transmission coefficient S21

Fig. 6.16 shows the measured S21 along the top surface of the phantom. The measurements were taken every 20mm, and the improvement is approximately 5 dB and 7 dB at the centre and edges of the coils respectively.

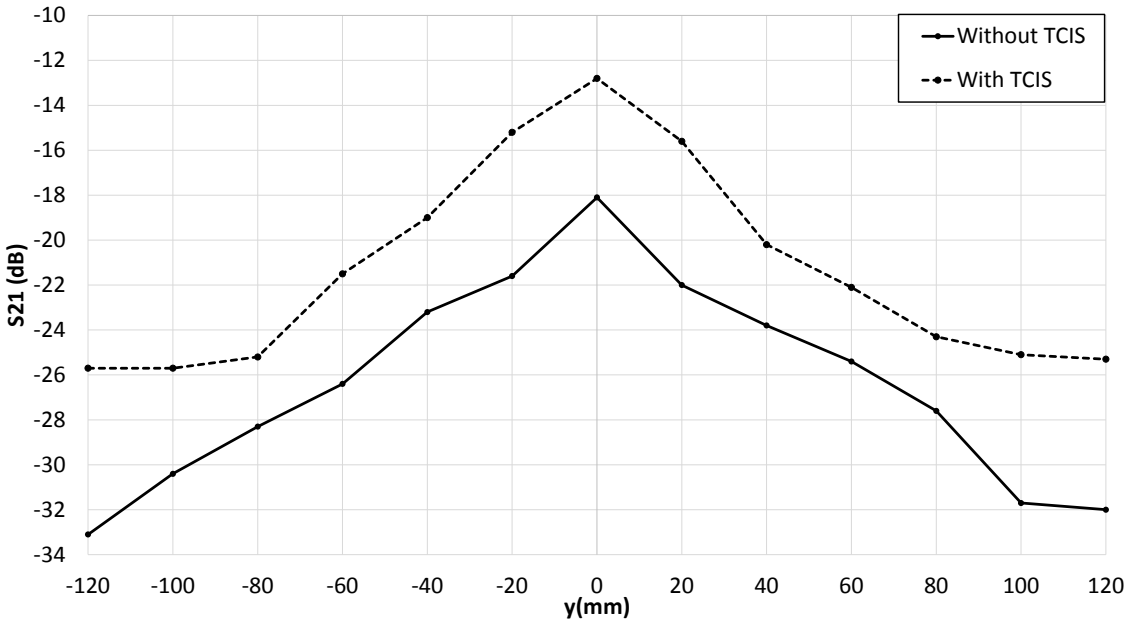

Fig. 6.16 Measured S21 across the top face of the phantom (y-axis), at (x=z=0)

6.4 MRI measurements

6.4.1 The measurement parameters and set-up

Axial MR images of the dielectric phantom used in the previous section were acquired using a 1.5T MRI scanner with gradient eacho pulse sequence. Two sets of image data were taken for the with and without CIS cases. The measurement parameters are listed in Table 6.2. Figs. 6.17, 6.18 and 6.19 show the (a) Image intensity without CIS and (b) with

Table 6.2 MRI measurements sequence parameters

Parameter	Value
Pulse repetition time (ms)	500
Echo time (ms)	50
Transmission gain TG (dB)	3
Bandwidth (kHz)	15.63
Field of view (cm)	36 x 36
Slice thickness (mm)	10
Acquisition matrix (pixels)	128 x 128

CIS respectively for the centre slice at (z=0), inter cell slice (z=P/2=25 mm), and adjacent slice (z=P=50 mm). The results show the image intensity at all these three regions can be

significantly improved at the area which is close to the TCIS surface inside the dielectric phantom, however, the width of the intensity is reduced due to the small size of the unit cell of the TCIS which focuses the RF magnetic field at the structure centre inside the phantom.

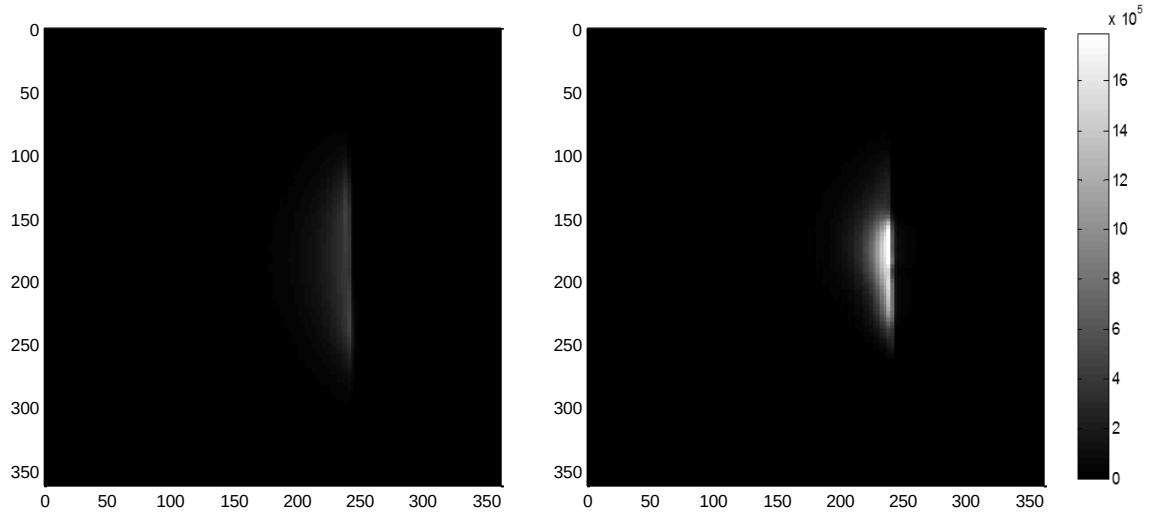

Fig. 6.17 Measured MRI image at the coil centre (z=0), (a) without TCIS and (b) with TCIS

6.4.2 Measured SNR and transceiver enhancement

The SNR calculation method was described in previous chapters which was defined as a ratio between the signal intensity divided by $\sqrt{2}$ times the background noise. The background noise is quantified in this measurement within the region such as shown in Fig. 6.17 at x=20 mm to x=100 mm, y=20 mm to y=300 mm. Figs. 6.20a and Fig. 6.20b show a transceiver SNR without CIS and with CIS respectively for the centre slice at (z=0). The transceiver SNR is the measured SNR at the same applied TG for both coils with and without the TCIS. It is seen that the transceiver SNR can be significantly improved by using the TCIS at the coil centre. Fig. 6.21a and Fig. 6.21b present the transceiver SNR across x-axis and y-axis at central slice respectively. The Fig. 6.21b shows the transceiver SNR can be enhanced by 415% at the coil centre and at the top face of the dielectric phantom $x = y = z = 0$. This improvement is observed for the first 50 mm inside the dielectric phantom, after that the SNR of both cases are almost the same as shown in Fig. 6.21a. Performance across

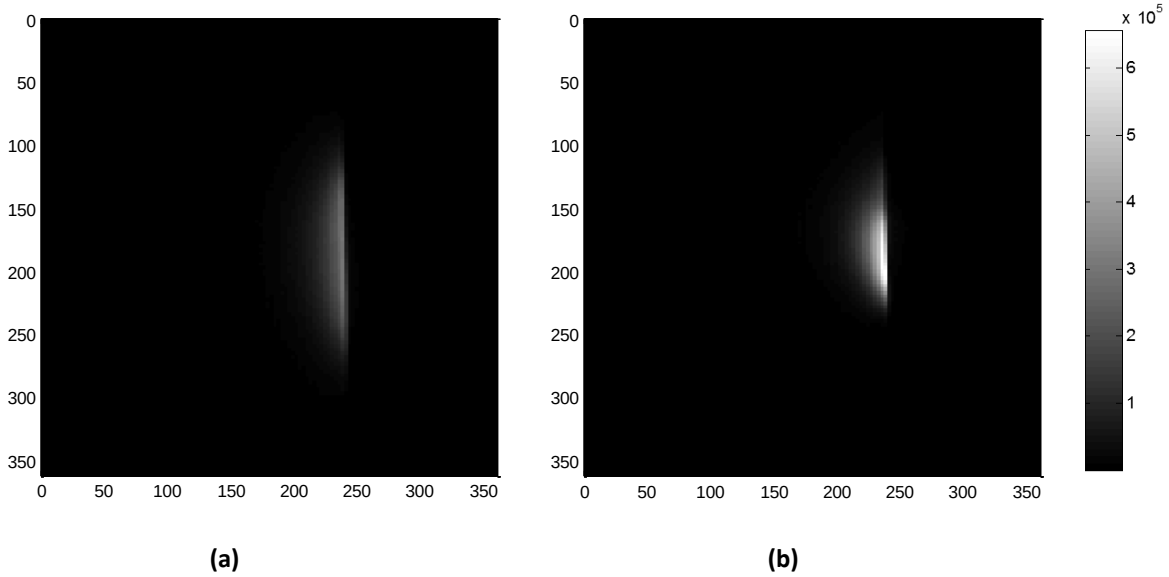

Fig. 6.18 Measured MRI image at an inter cell slice (z=25 mm), (a) without TCIS and (b) with TCIS

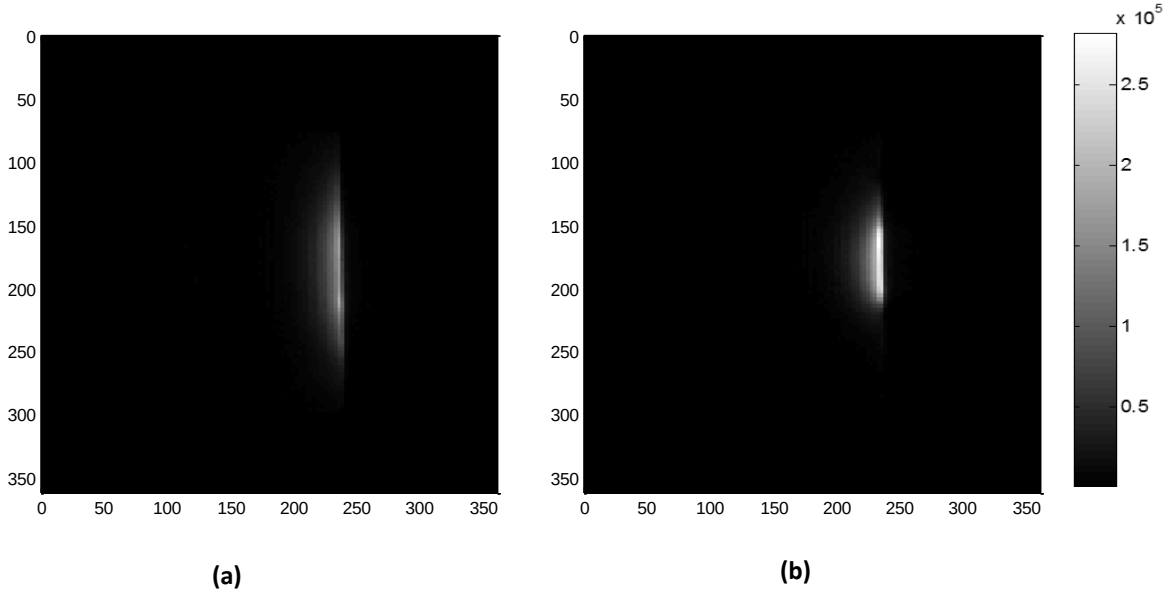

Fig. 6.19 Measured MRI image at adjacent slice (z=50mm), (a) without CIS and (b) with CIS

the phantom (y-axis) is also significant as shown in 6.21b where SNR improvement can be observed over 200 mm width of the phantom. Fig. 6.22(a, b) shows the transceiver

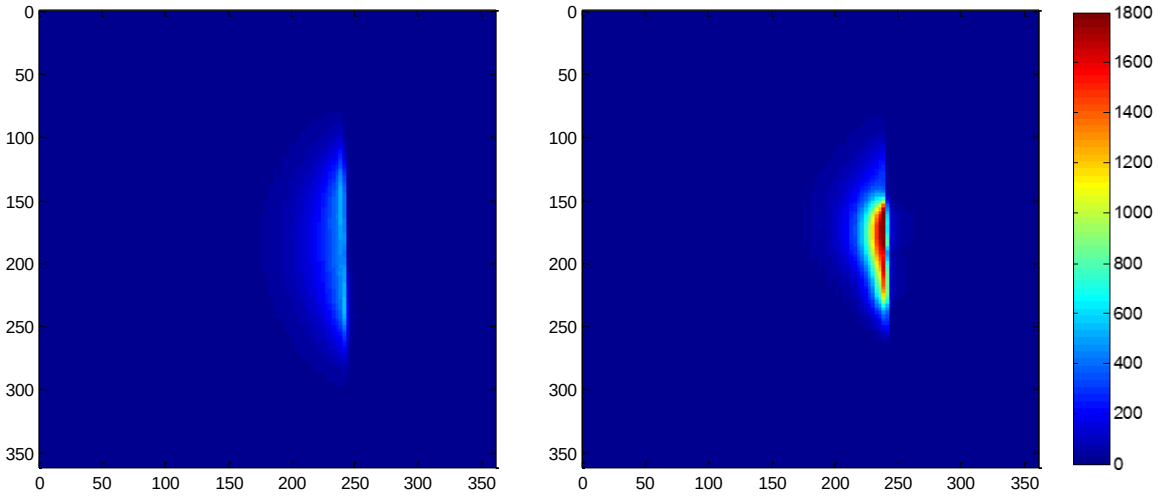

Fig. 6.20 Measured transceiver SNR at the centre(z=0), (a) without CIS and (b) with CIS

SNR at the inter cell slices(z=P/2) of both cases without TCIS and with TCIS respectively. Fig. 6.23(a, b) shows the linear cross-section throughout x-axis and y-axis respectively. The results illustrate that there is significant transceiver SNR improvement, which is about 140% at $x = y = 0, z = 25mm$ and it observed for the first 50mm inside the phantom as suggested by the simulations. To illustrate the transceiver SNR improvement in further surface area details, Fig. 6.24 shows the SNR as a function of penetration depth at the adjacent slice (z=P) and Fig. 6.25 shows the transceiver SNR across the phantom at x-axis and y-axis. The result shows that there is an enhancement of the transceiver SNR about 80% at the top of the phantom at the adjacent slice $x = y = 0, z = 50mm$ and the improvement decay for the first 50mm. Fig. 6.26 and 6.27 show the mean measured SNR throughout the effective coil dimensions of $(D_c/\sqrt{2} \times D_c \times 10mm)$ varies slices number, starting of slice number 1, which is the centre slice and moving toward the end of the slices of both of the regions as shown in Fig. 6.8. The results illustrate significant improvvement for the first two slices in each region of 102% and 80% of region 1, 78% and 25% of region 2. The remaining slices also show improvements through reduced due to field focusing. Also, It can be seen that the SNR of the coils with and without CIS are almost symmetric.

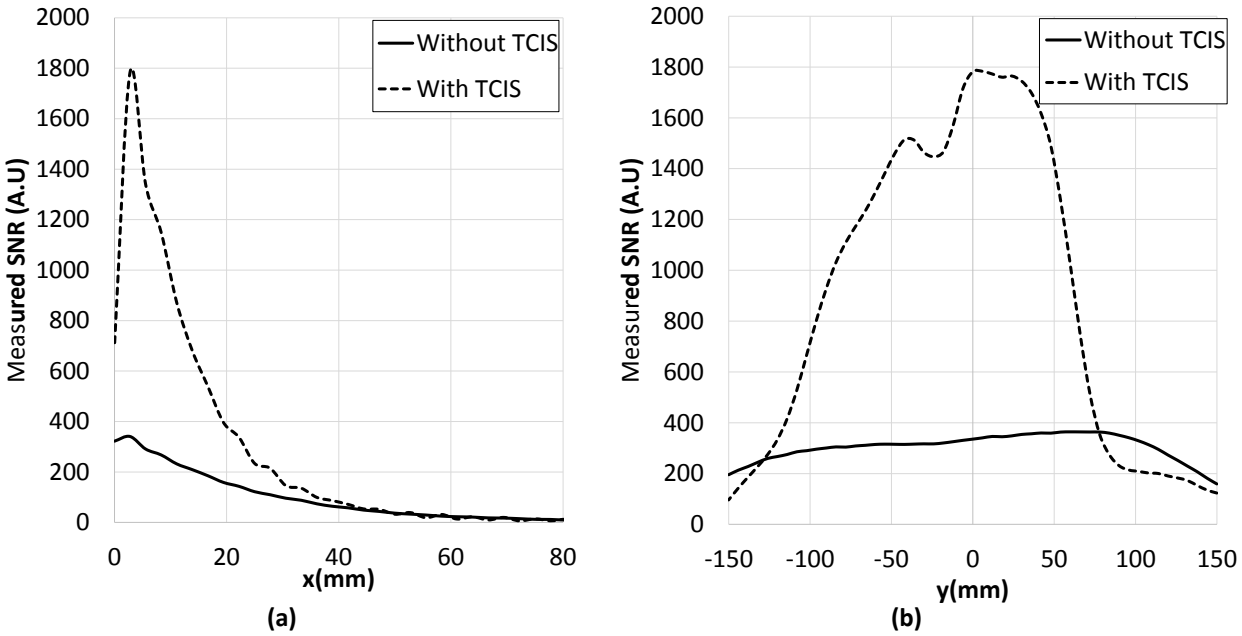

Fig. 6.21 Linear graph of the measured transceiver SNR at the centre(z=0), (a) across x-axis at y=0 (b) across y-axis at x=5mm inside the phantom

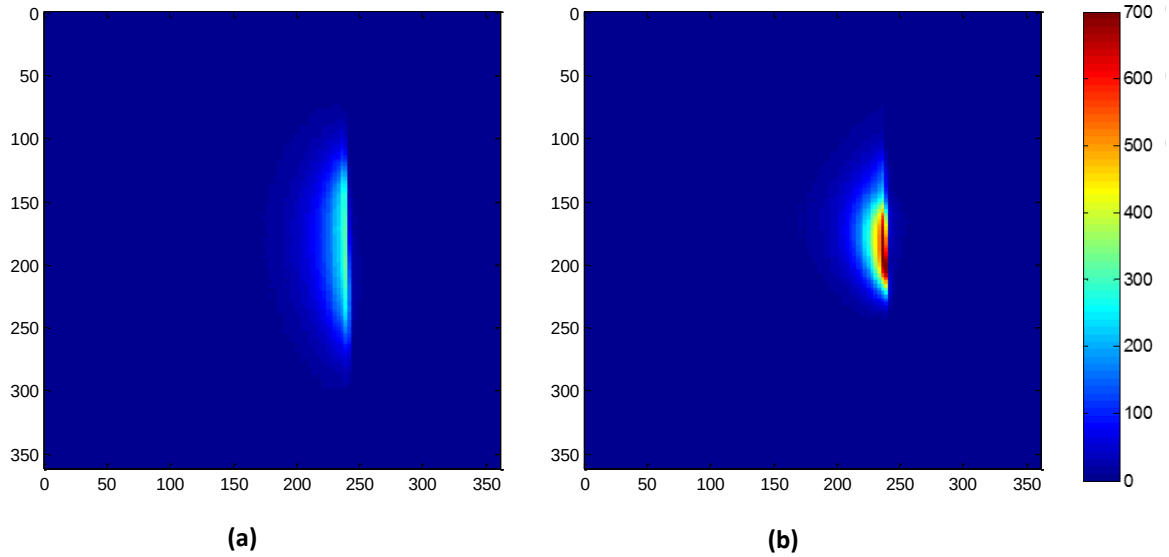

Fig. 6.22 Measured transceiver SNR at inter cell slice (z=25mm), (a) without CIS and (b) with CIS

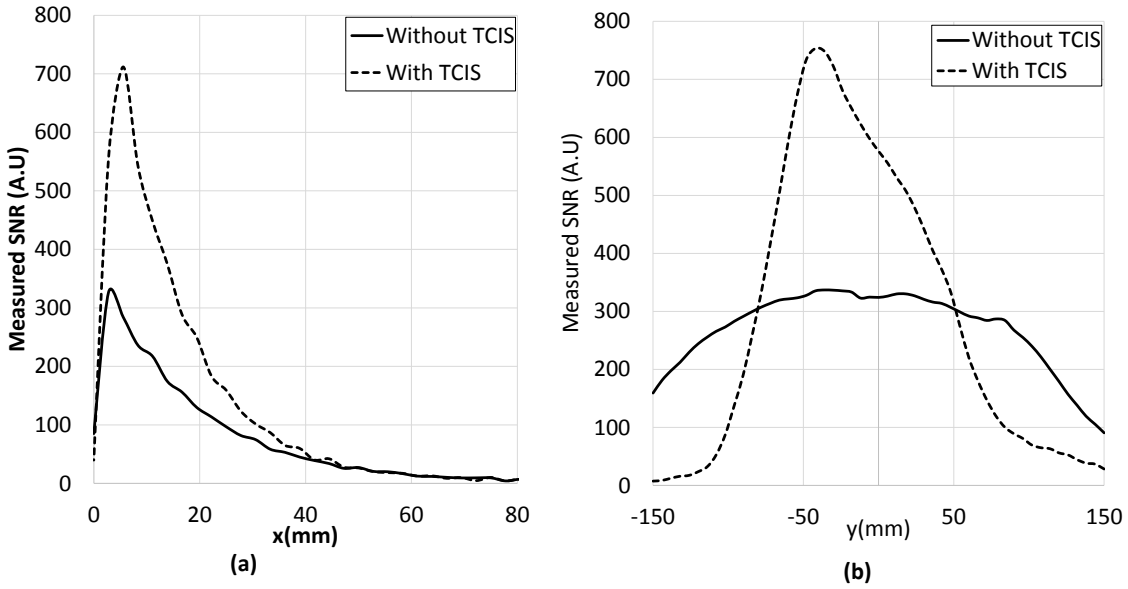

Fig. 6.23 Linear graph of the measured transceiver SNR at the centre(z=25mm), (a) across x-axis at y=0 (b) across y-axis at x=5mm inside the phantom

Section 6.4 has shown proof-of-principle implementation of the odd number of unit cells of a thin metasurface in MRI environments and the initial transceiver SNR improvement is very promising. In more detailed analysis, in order to quantify the transmission efficiency which is proportional to $|B_1^+|$ and the receiver sensitivity which is proportional to $|B_{1,normalised}^-|$, the flip angle will be calculated. These analyses are presented in the next sections.

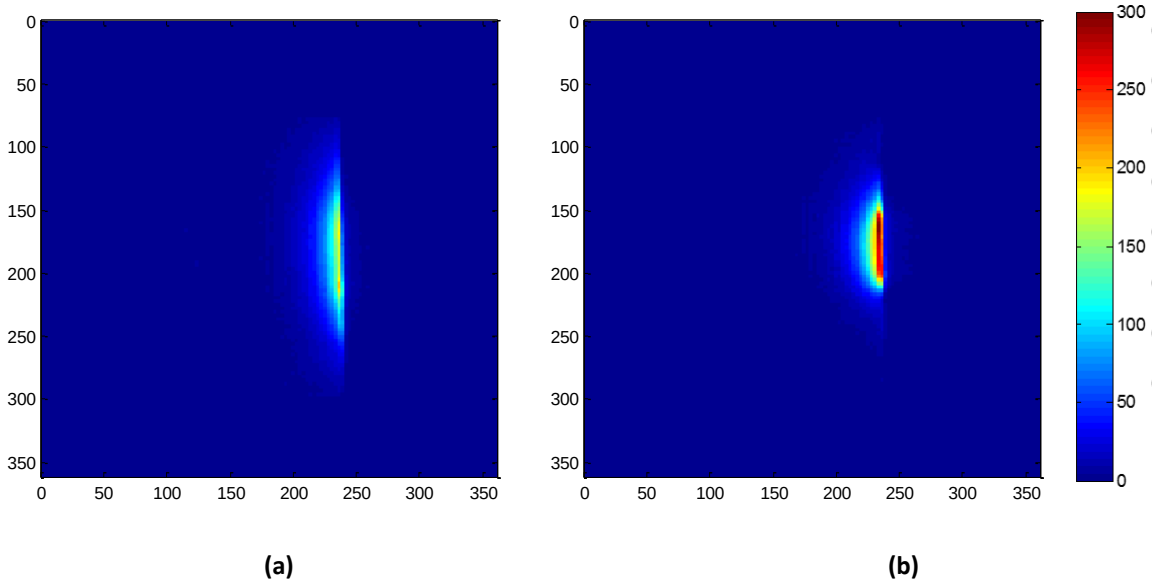

Fig. 6.24 Measured transceiver SNR at adjacent slice(z=P), (a) without CIS and (b) with CIS

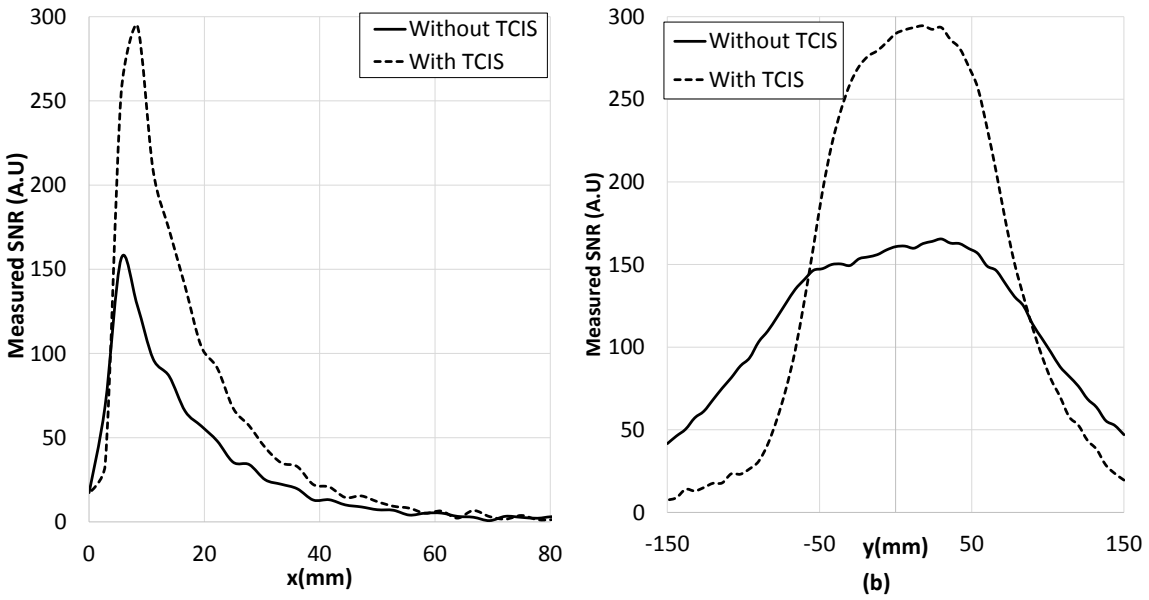

Fig. 6.25 Linear graph of the measured transceiver SNR at the centre(z=50mm), (a) across x-axis at y=0 (b) across y-axis at x=5mm inside the phantom

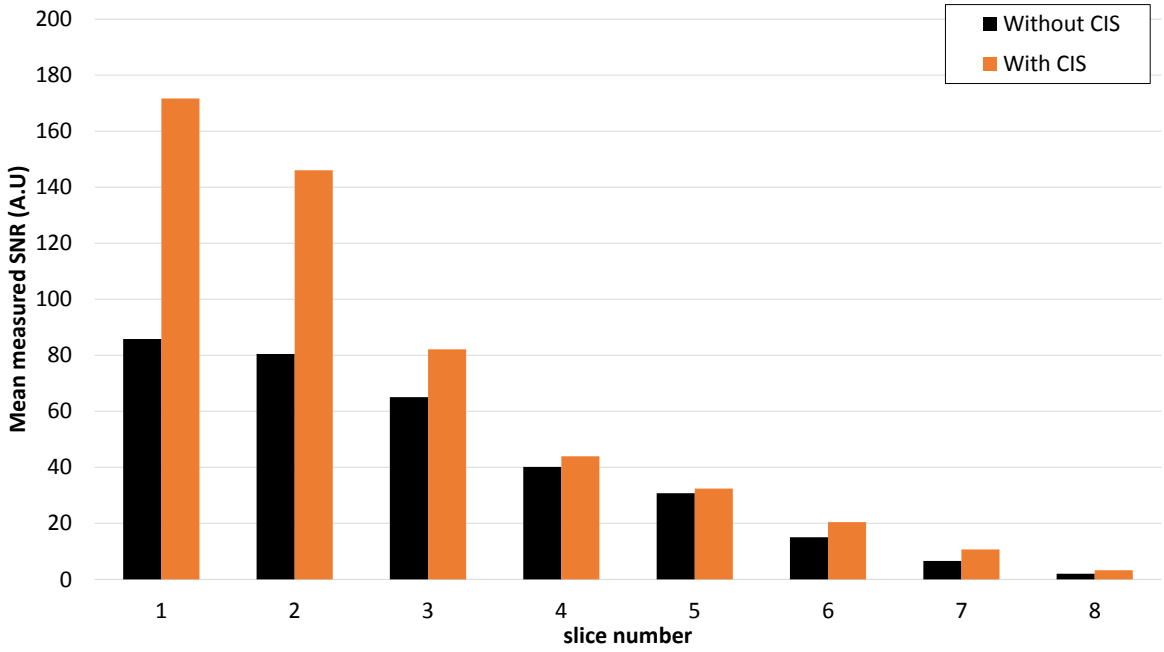

Fig. 6.26 Mean measured SNR for varying slices of volume $(D_c/\sqrt{2} \times D_c \times 10mm)$, region 1.

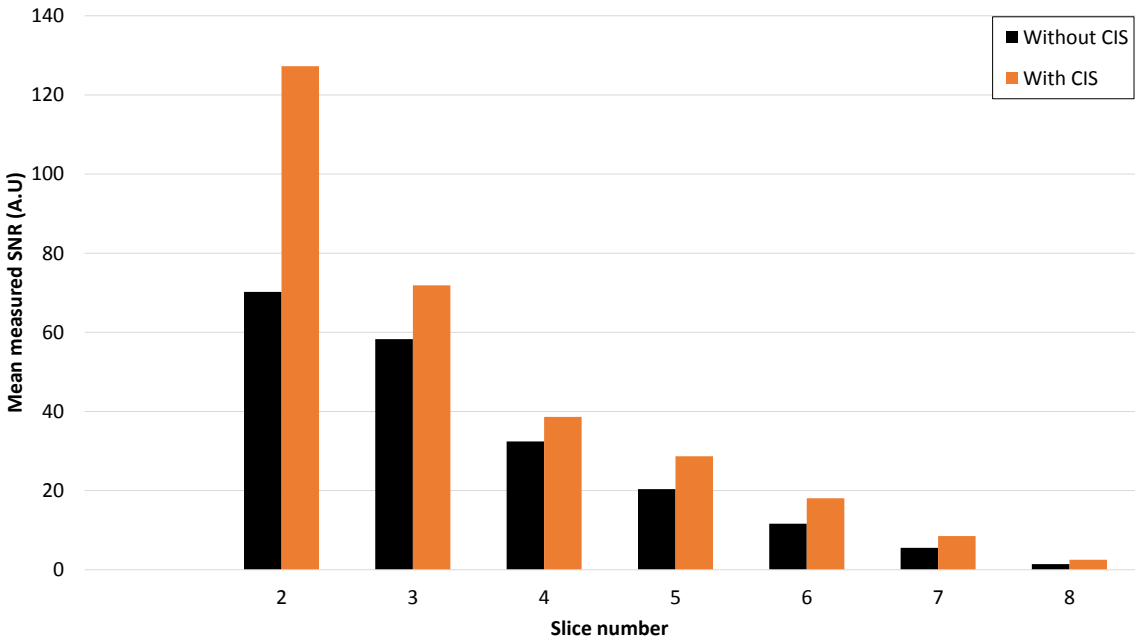

Fig. 6.27 Mean measured SNR for varying slices of volume $(D_c/\sqrt{2} \times D_c \times 10mm)$, region 2.

6.5 Transmission efficiency and receiver sensitivity analysis

6.5.1 Flip angle calculation

A flip angle was explained in chapter 1, which is proportional to the transmit magnetic flux density B_1^+ and in order to calculate this angle, the signals were acquired with various TG values. In this experiment the signals were acquired when TG=0, 30, 60, 90, 120, 150 and 180 with 15 slices and a matrix size was assumed to be 128×128 pixels and the FOV was $36 \times 36cm$ for each TG in both cases without and with TCIS. The first step to calculate the flip angle determines SNR for all pixels within all 15 slices of the phantom image of all TG values. The noise region was taken from the bottom corner of the image in all cases as described in the previous section. The TG value has been converted to the linear scale using equation (6.1), as shown in Table. 6.3 and the linearity of the amplifier has been checked by measuring the changing of the voltage with various TG values using an oscilloscope. The results show that the increase of the voltage is linear with increase of TG. It was assumed that the transmit power delivered to a 50Ω transceiver and that the TG(V) can be calcalted using equation (6.2)as shown in Table. 6.3.

$$TG(W) = P_{max} 10^{\left(\frac{-(200-TG)}{100}\right)} \tag{6.1}$$

where P_{max} is a maximum power and its value is $2kW$ of a head model.

$$TG(V) = \sqrt{TG(W) * R} \tag{6.2}$$

where $R = 50\Omega$ is a transceiver resistor. Figs.6.29 and 6.30 show a measured SNR with

Table 6.3 The power and voltage of transmission gain

TG(dB)	0	3	6	9	12	15	18
TG(W)	20	39.905	79.62	158.87	316.98	632.46	1261.92
TG(V)	31.62	44.67	63.10	89.13	125.89	177.83	251.19

various TG (i.e flip angle) of different pixels location inside the phantom image of the RF coil without and with TCIS respectively. These pixels were selected at the central slice, inter cell slice and adjacent slices which were numbered 1, 2, 3 and 4. These pixels location are given in Fig. 6.28, for both cases with and without TCIS.

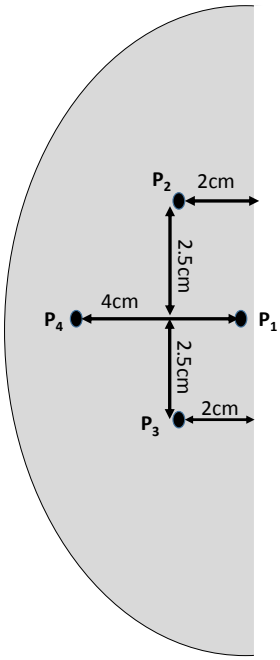

Fig. 6.28 Examples of Pixels location inside the phantom image

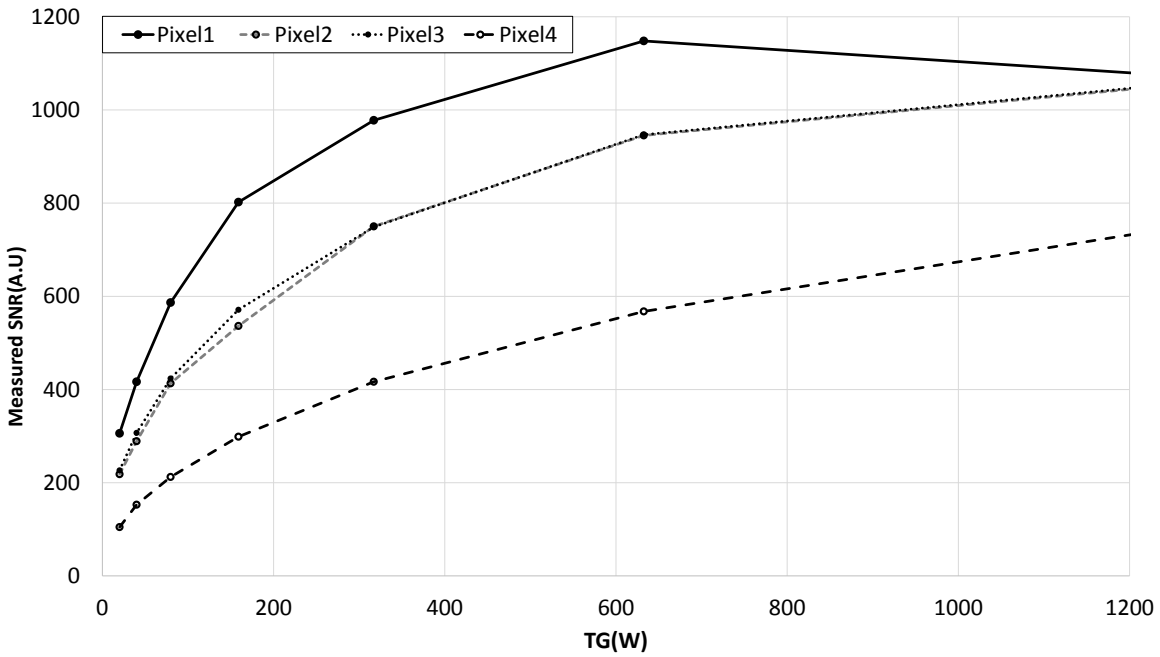

Fig. 6.29 Examples of pixels SNR with various locations inside the dielectric image, in the case of without using TCIS

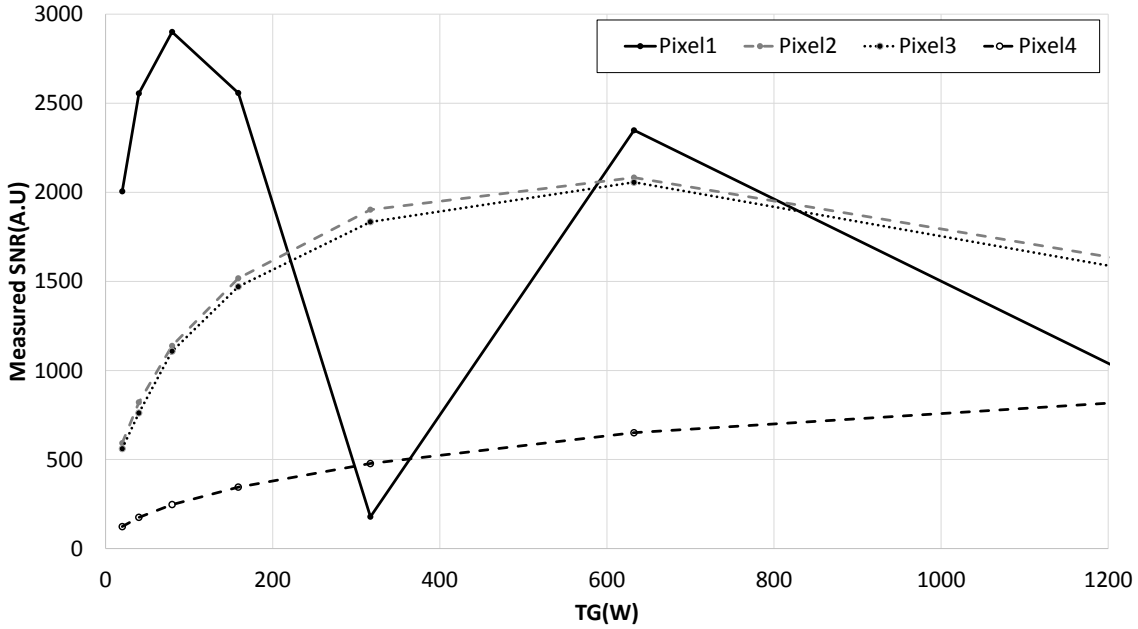

Fig. 6.30 Examples of pixels SNR with various locations inside the dielectric image, in case of with using TCIS

The results illustrate that both of the coils are able to reach a 90^o flip angle by increasing TG power, the SNR is increased until it reaches a certain point, which is a 90^o pulse, then as TG power increases the SNR decrease because there is a direct proportional between SNR and $sin(\alpha)$ as given by equation (1.47). The pixel1 result shows that the coil without TCIS reached a 90^o flip angle when the TG power was about 600W and the coil with TCIS reached at 90^o RF pulse flip angle when the TG value was approximately 80W. Since the flip angle is directly proportional to the transmit magnetic flux density B_1^+, which was characterised by equation(1.16), increasing the flip angle is cause for improving the B_1^+. These analysis results demonstrated that both of the coils followed the equation(1.47) and the value of B_1^+ increased using the TCIS. It was assumed that the transmit power was delivered to a 50Ω transceiver and that the $|B_1^+|$ is proportional to the transmit voltage. As an example of the curve fitting algorithm the SNR against RMS voltage for a pixel close to the surface of the dielectric phantom is shown in Figs. 6.32 and 6.33 of without and with the TCIS respectively. It can be seen that the maximum SNR of the RF coil alone occurs at approximately 200V compared to 66V when the TCIS is present translating to a 3 fold reduction in voltage or a 9 fold reduction in transmit power.

The automatic sinusoidal wave curve fitting is accomplished by using MATLAB program. A full map of the flip angles has been generated by fitting all acquired image pixels to

different amplitude sinusoidal waves, where the maximum amplitudes were at the coils centre at the top face of the phantom. After that, the waves amplitude decayed by increasing the depth inside the phantom. Since the imaged phantom in this section contains 128 by 128 pixels, only the pixels which have a SNR value higher than 10 times of the noise background are considered as described by ($SNR > 10 \times noise$) as shown in Fig. 6.31 to reduce errors in the curve fitting algorithm.

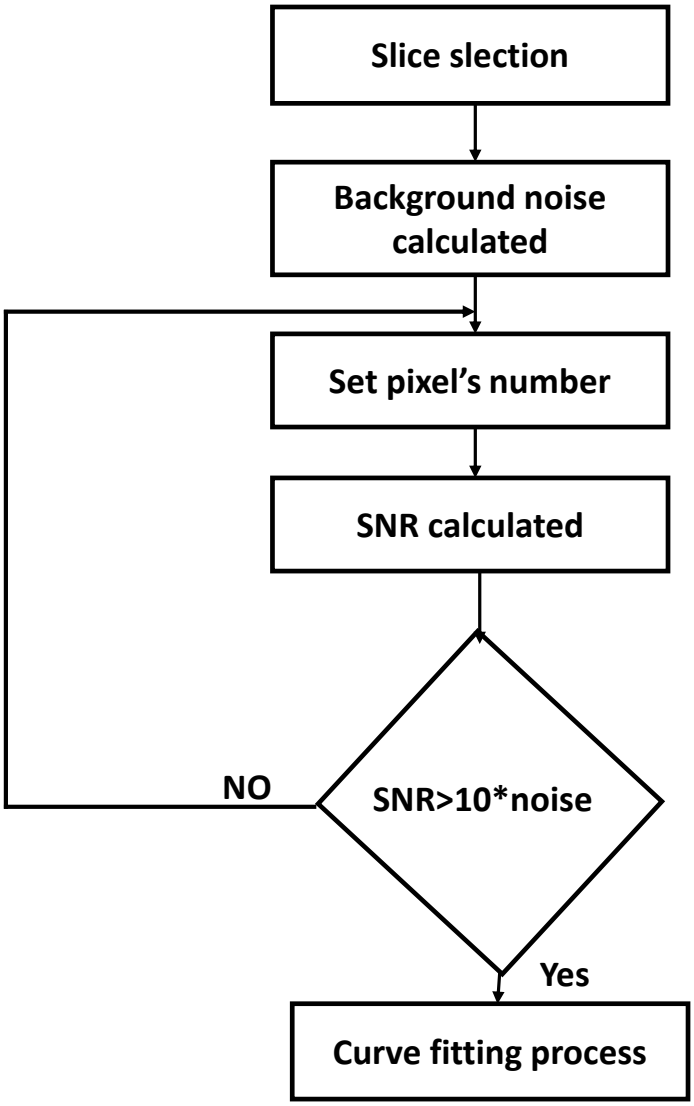

Fig. 6.31 Flip angle calculating process

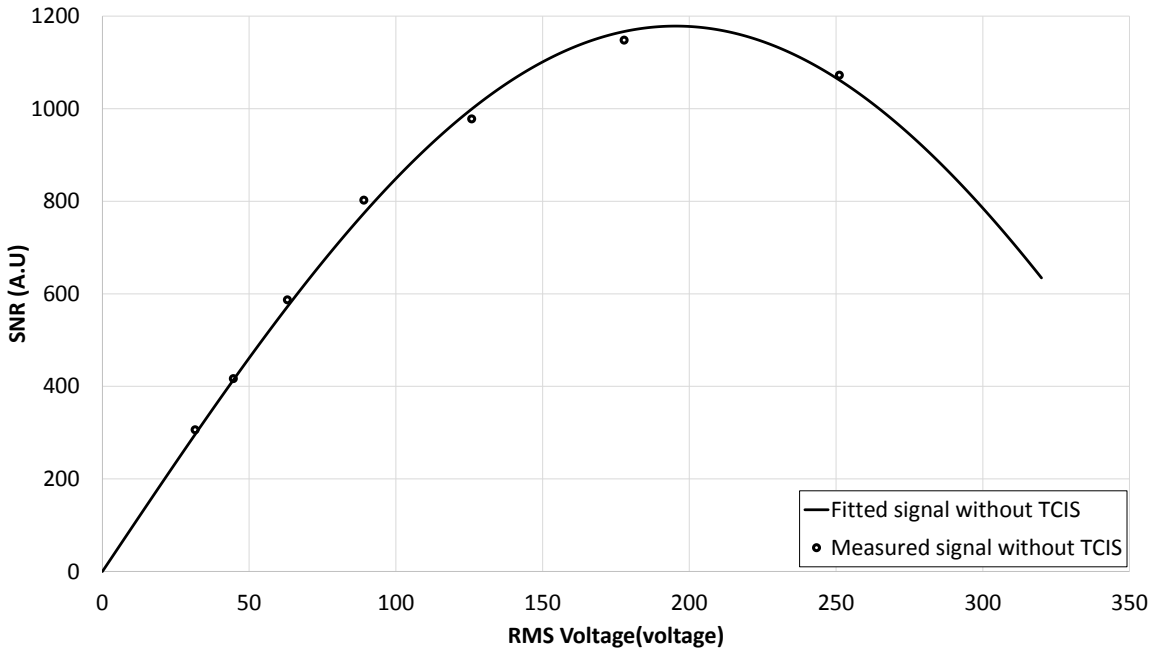

Fig. 6.32 Curve fitting for the P_1 Pixel, TG=60, no TCIS

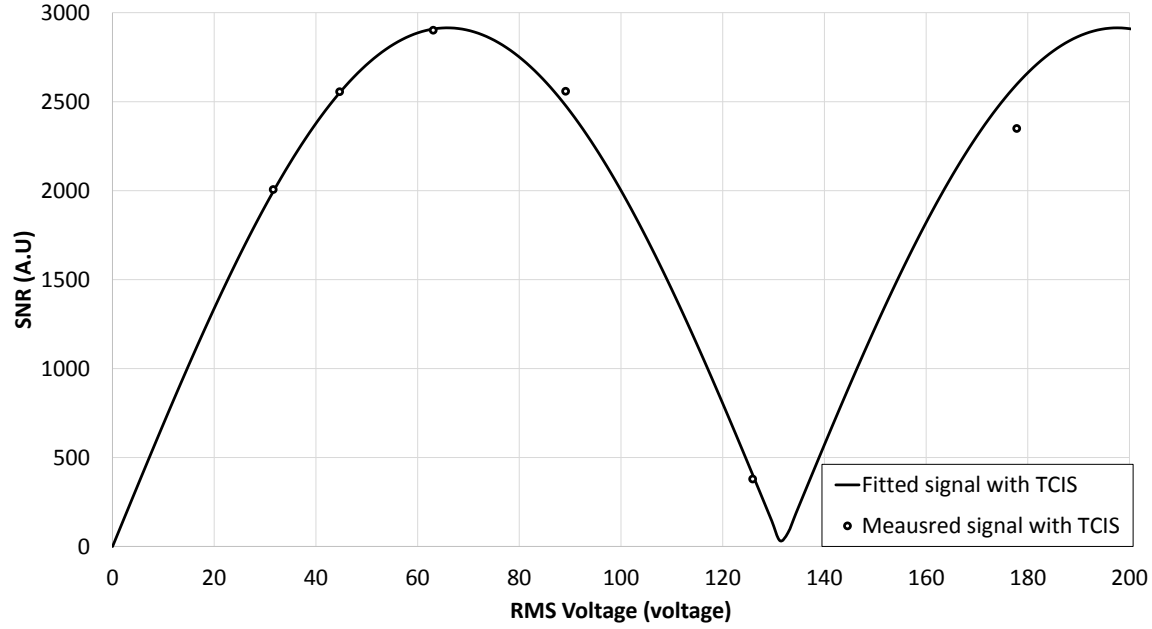

Fig. 6.33 Curve fitting for the P_1 Pixel, TG=60, with TCIS

Figs. 6.34, 6.35 and 6.36 illustrate the full flip angle maps of (a) without TCIS and (b) with using TCIS of the three slices which are centre slice, intercell slice and adjacent slice. It can be seen that, the flip angle decayed inside the depth of the phantom, where the maximum value was at the centre slices close to the TCIS surface.

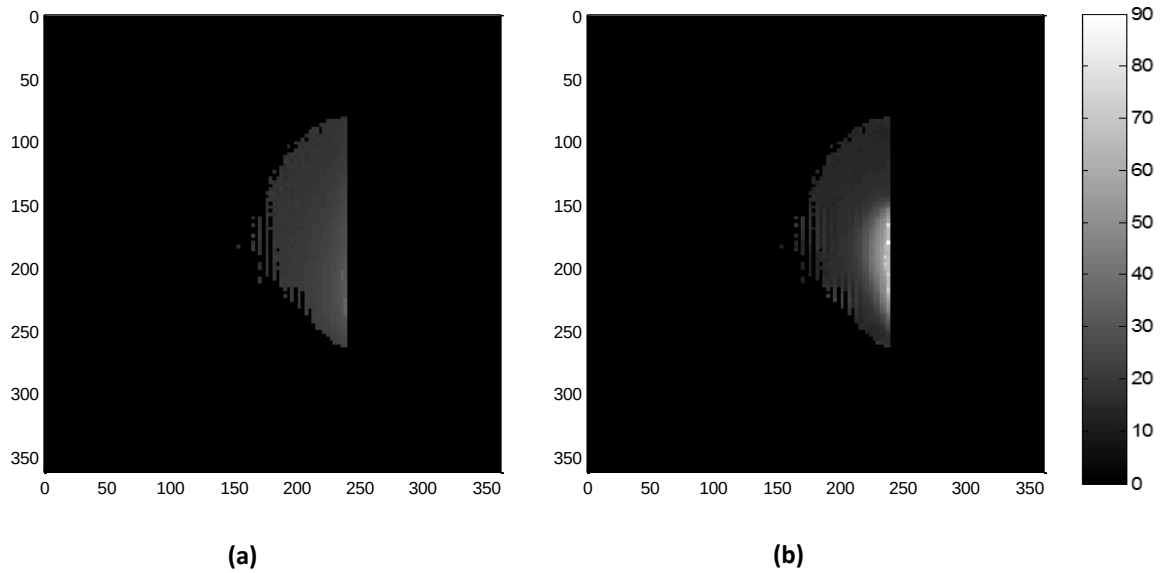

Fig. 6.34 Full map of the flip angle (a)no TCIS, (b) with TCIS, central slice, z=0, TG=60

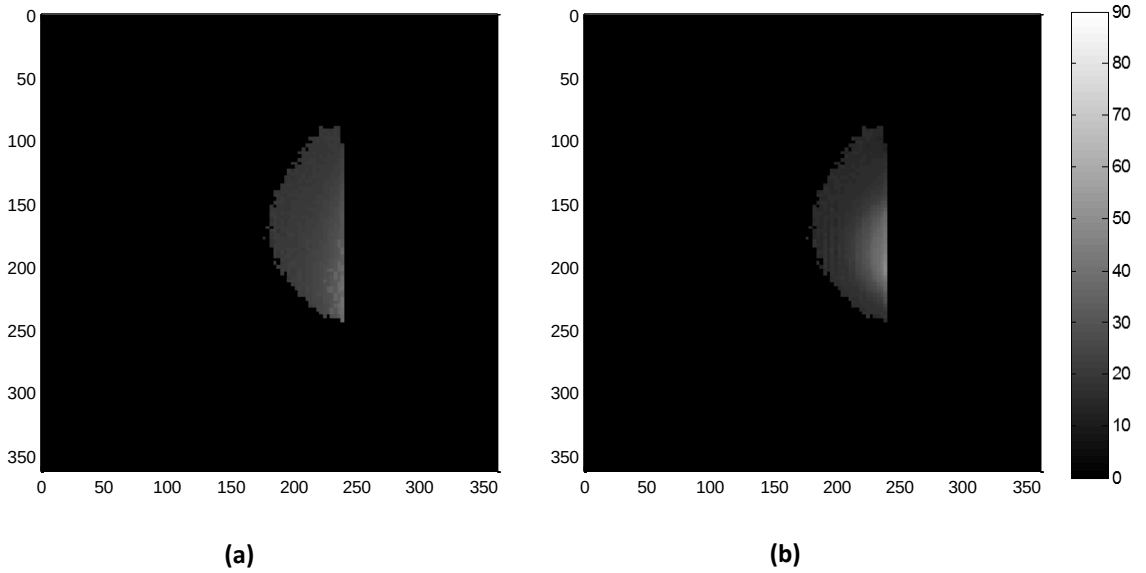

Fig. 6.35 Full map of the flip angle (a)no TCIS, (b) with TCIS, inter cell slice at z=25mm, TG=60

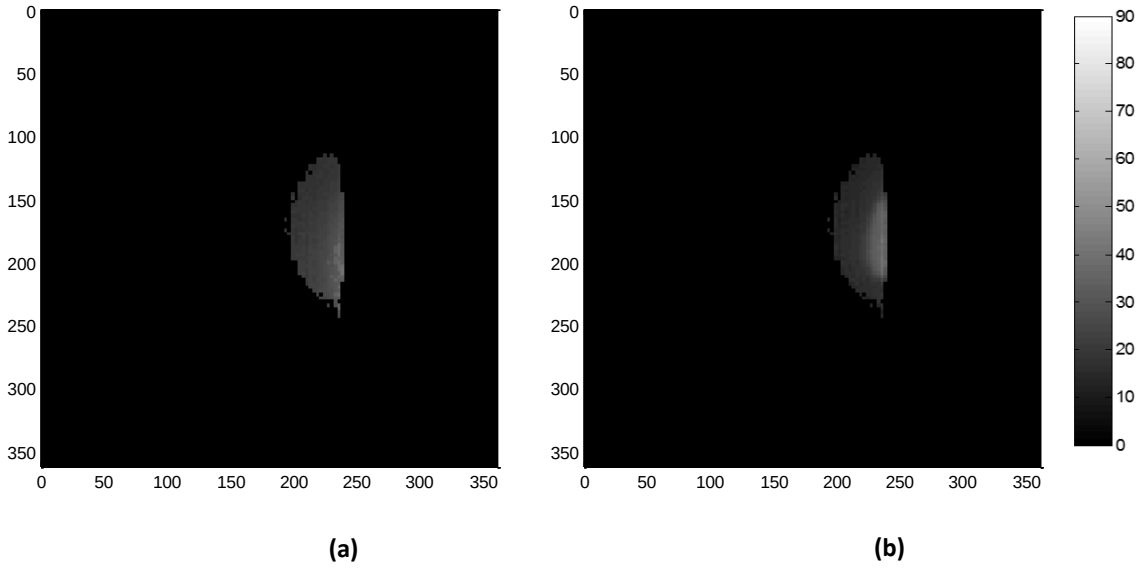

Fig. 6.36 Full map of the flip angle (a)no TCIS, (b) with TCIS, adjacent cell slice at z=50mm, TG=60

6.5.2 Transmission efficiency

Since the flip angle maps, which have been calculated in the previous section, directly proportional to the $|B_1^+|$, the percentage improvement in transmission efficiency, which is termed by η, can be quantified by using equation 6.3. This can be achieved by comparing the pixels flip angle of both the cases with and without TCIS at the same TG value.

$$\eta(i,j) = \frac{\alpha_w(i,j) - \alpha_{wt}(i,j)}{\alpha_{wt}(i,j)} \times 100 \tag{6.3}$$

where α_{wt} is the flip angle of the case without TCIS, α_w is the flip angle of the case with TCIS and i, j are pixels number between 1 to 128. Figs. 6.37, 6.38 and 6.39 show the linear plots of the pixels flip angles as a function of penetration depth at the centre, intercell and adjacent slices.

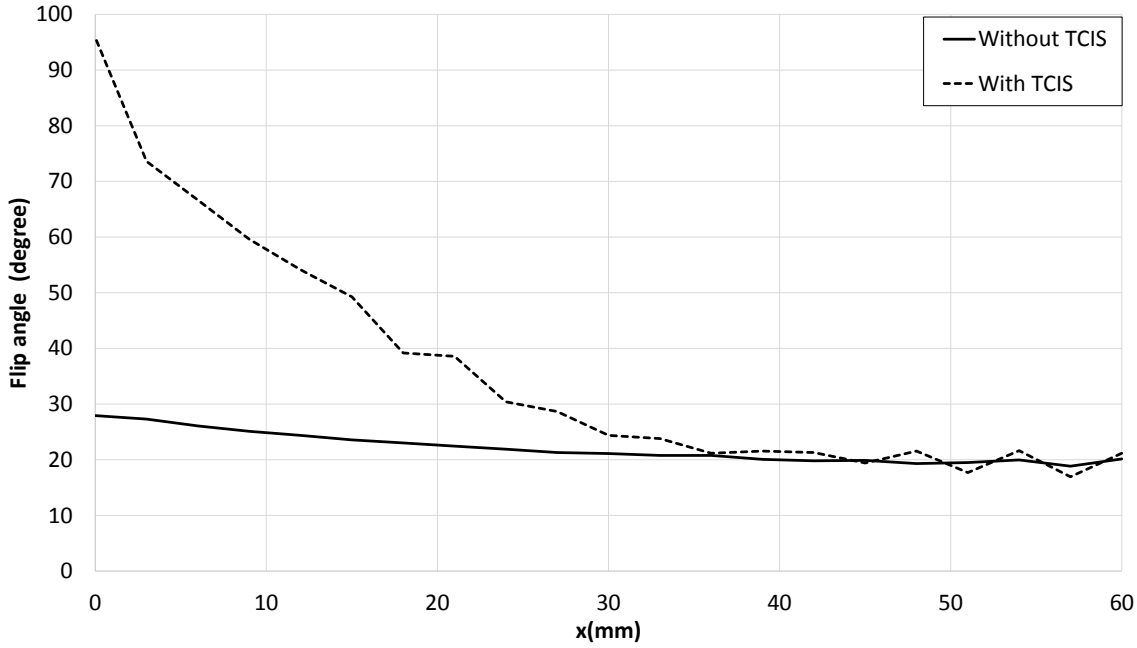

Fig. 6.37 Linear plot of the flip angle of the coil at the centre of the central slice with and without TCIS at z=0 and TG=60

Fig. 6.37 illustrates that there is a maximum of 216% of the $\eta(i,j)$ when using TCIS compared with only coil and it is observed for the first $40mm$. The Fig. 6.38 shows a maximum of $\eta(i,j)$ of 68% at the centre of the intercell slice at $(x = y = 0, z = 25)$ and also the it is noticed for the $40mm$ inside the phantom. The Fig. 6.39 shows there is a maximum $\eta(i,j)$ of 35% at adjacent slice at $(x = y = 0, z = 50mm)$ and this enhancement is shown for the first $25mm$ inside the phantom. To illustrate the transmission performance in further

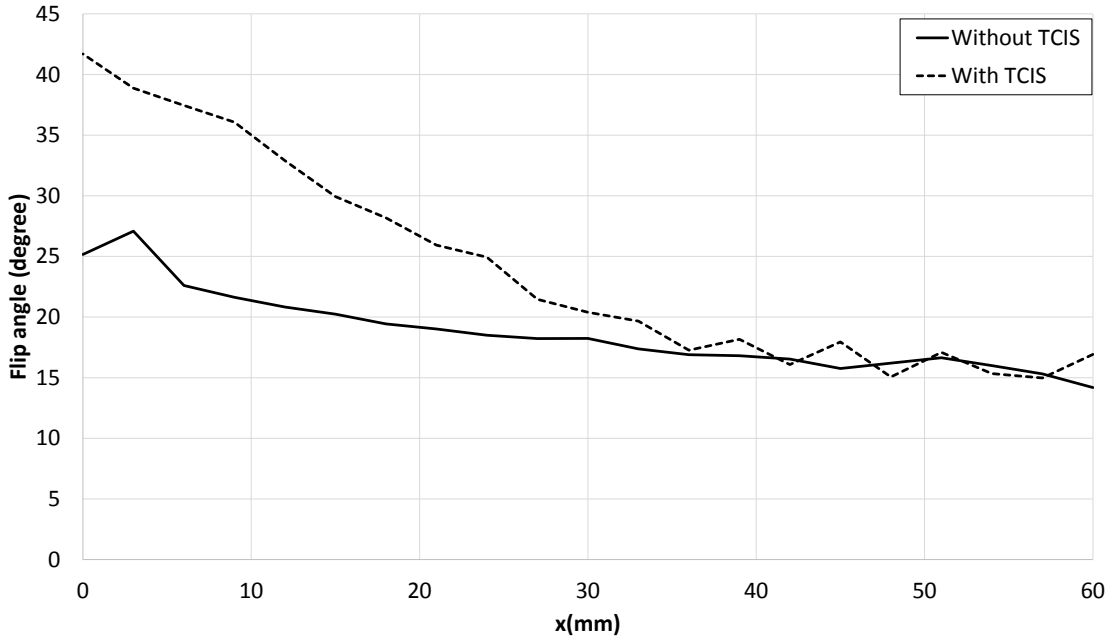

Fig. 6.38 Linear plot of the measured SNR of the coil at the centre of the inter cell slice with and without TCIS at z=P/2 and TG=60

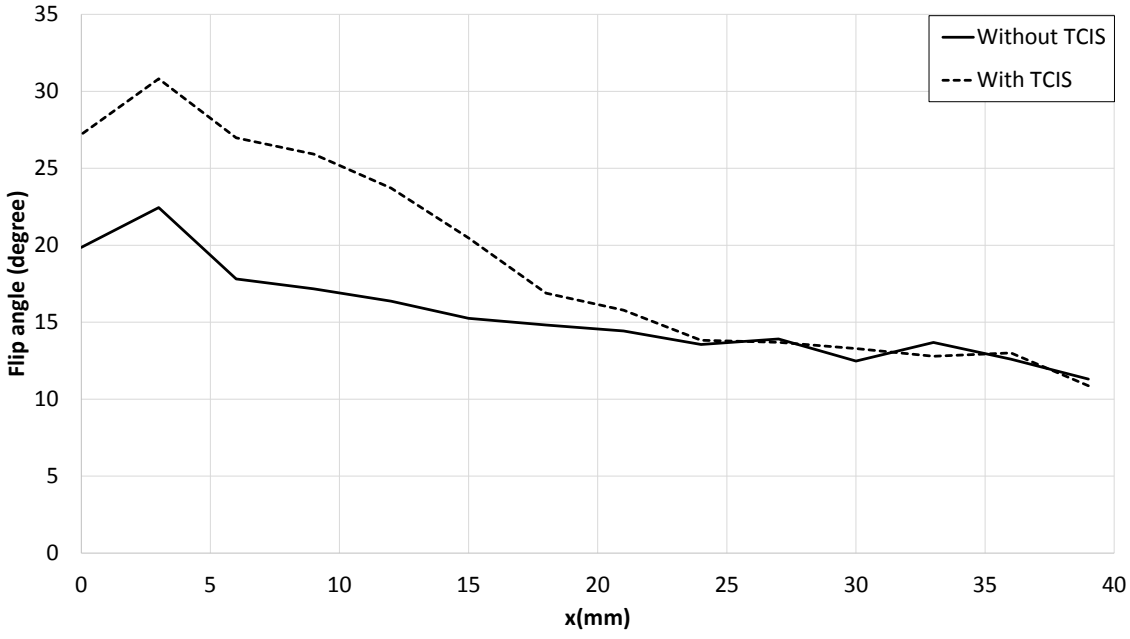

Fig. 6.39 Linear plot of the flip angle of the coil at the centre of the adjacent slice with and without TCIS at z=P and TG=60

detail, an xy-plane of a percentage transmission efficiency improvement, which is termed by,$\eta_I(i,j)$, and transmission efficiency reduction, which is denoted by,$\eta_R(i,j)$, inside the phantom at the centre, intercell and adjacent cell are shown in Figs. 6.40, 6.41 and 6.42. The $\eta_I(i,j)$ and $\eta_R(i,j)$ can be calculated using equations 6.4 and 6.5 respectively.

$$\eta_I(i,j) = \frac{\alpha_w(i,j) - \alpha_{wt}(i,j)}{\alpha_{wt}(i,j)} \times 100 \quad if \quad \alpha_{wt}(i,j) \leq \alpha_w(i,j) \tag{6.4}$$

$$\eta_R(i,j) = \frac{\alpha_{wt}(i,j) - \alpha_w(i,j)}{\alpha_{wt}(i,j)} \times 100 \quad if \quad \alpha_{wt}(i,j) > \alpha_w(i,j) \tag{6.5}$$

Figs 6.40, 6.41 and 6.42 show the transmission efficiency of the RF coil (a) percentage of the reduction regions,$\eta_R(i,j)$, and (b) percentage of the improvement regions,$\eta_I(i,j)$, at different slices positions, such as central slice, inter cell slice and adjacent slice respectively when TG was 60. The results illustrate that the transmission efficiency can be improved using TCIS compared to standard coil image at the centre of the three selected regions, however, there is a reduction in the sides of the slices due to the effects of the unit cell size.

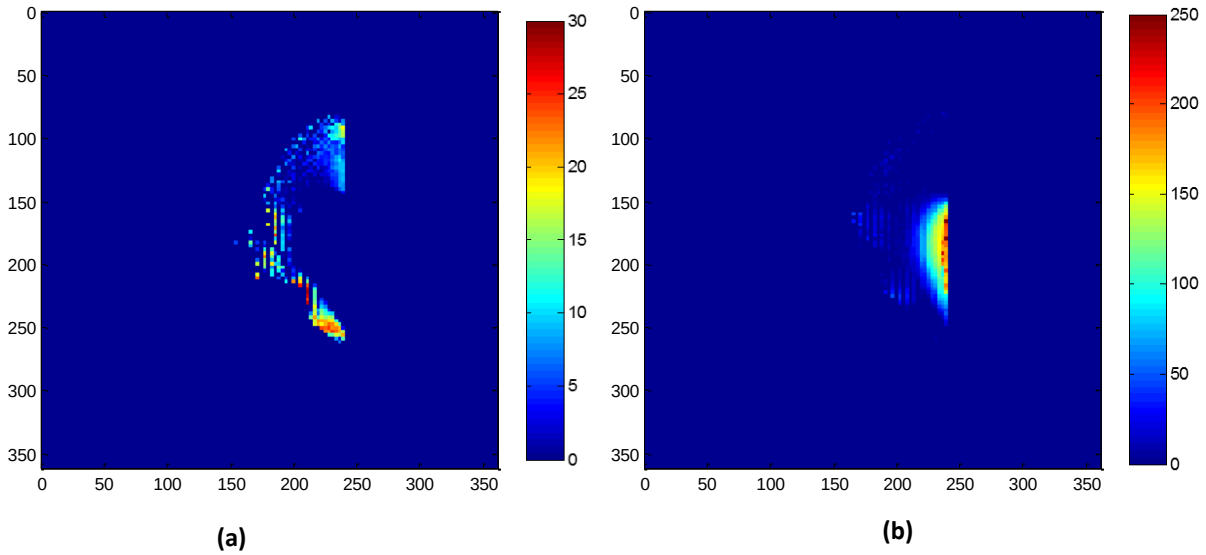

Fig. 6.40 The transmission efficiency of the coil at the central slice (a)reduction regions η_R, (b) improvement regions η_I at z=0 and TG=60

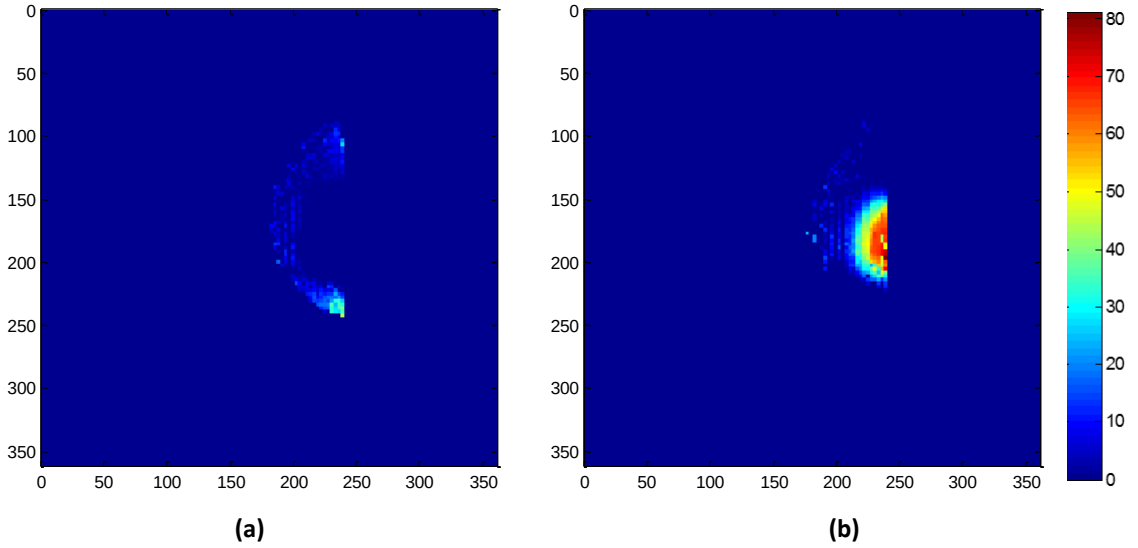

Fig. 6.41 The transmission efficiency of the coil at the intercell slice (a)reduction regions η_R, (b) improvement regions η_I at z=25mm and TG=60

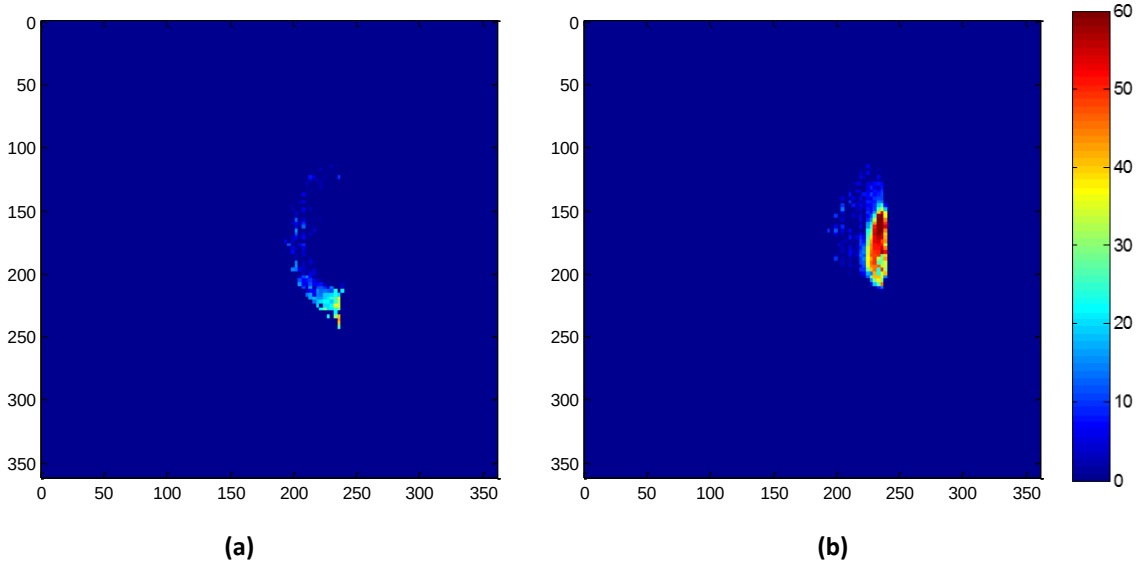

Fig. 6.42 The transmission efficiency of the coil at the adjacent cell slice (a)reduction regions η_R, (b) improvement regions η_I at z=50mm and TG=60

6.5.3 Receiver sensitivity

To make a fair comparison of receiver sensitivity the effect of transmit efficiency needs to be taken into account. A receiver sensitivity, is denoted by Ψ, can be calculated by equation 6.6. The receiver sensitivity of the cases of with and without TCIS are termed Ψ_w and Ψ_{wt} respectively, can be calculated using equations 6.7 and 6.8, respectively. In order to fully explain the improvement in SNR on the receiver side, a mean global flip angle, which is denoted as αg, for each single TG and slice is calculated by taken the mean value of the flip angle map of all pixels within the region-of-interest (ROI). The ROI was defined as a non-zero values region inside the total FOV. Table 6.4 shows examples of the global flip angle with and without using the TCIS various the TG values at the centre, intercell and adjacent slices. The result shows that the global flip angle by using TCIS is higher than the case without using TCIS for all TG values.

$$\Psi(i,j) = \frac{SNR(i,j)}{sin(\alpha(i,j))} \tag{6.6}$$

$$\Psi_w(i,j) = \frac{SNR_w(i,j)}{sin(\alpha_w(i,j))} \tag{6.7}$$

$$\Psi_{wt}(i,j) = \frac{SNR_{wt}(i,j)}{sin(\alpha_{wt}(i,j))} \tag{6.8}$$

where SNR_{wt} and SNR_w are a SNR in the cases without and with using the TCIS, respectively. The $\alpha_{wt}(i,j)$ and $\alpha_w(i,j)$ are the pixels flip angle of the cases without and with using the TCIS, respectively.

Table 6.4 Global flip angle in degree (αg_{wt}) without TCIS and (αg_w) with TCIS

	Centre slice		**Intercell slice**		**Adjacent slice**	
TG	αg_{wt}	αg_w	αg_{wt}	αg_w	αg_{wt}	αg_w
0	8.69	11.24	7.13	8.84	7.02	8.54
30	11.92	15.29	10.17	11.69	9.47	10.28
60	17.16	21.58	16.50	19.45	12.95	16.47
90	24.36	29.33	23.52	26.35	19.57	22.47
120	31.80	34.59	30.35	34.14	25.79	28.41
150	67.57	76.33	50.14	59.10	48.75	53.68
180	75.16	83.45	62.08	71.97	58.94	62.58

In order to calculate the receiver sensitivity at the same global flip angle for the cases of with and without the TCIS, the receiver sensitivity is normalised. This normalisation are

termed as $\Psi_{wt}(i,j)_{normalised}, \Psi_{w}(i,j)_{normalised}$, can be achieved by applying the equations 6.9 and 6.10 for the case of without and with, respectively. It was previously shown that the with/without TCIS global flip angle is not the same for a given transmit power, hence, for a fair comparison $\alpha_{wt}(i,j)$ is modified by the global flip angle ratio of two cases $\frac{\alpha g_w}{\alpha g_{wt}}$.

$$\Psi_{wt}(i,j)_{normalised} = \frac{SNR_{wt}(i,j)}{sin(\alpha_{wt}(i,j) \times \frac{\alpha g_w}{\alpha g_{wt}})} \tag{6.9}$$

$$\Psi_{w}(i,j)_{normalised} = \Psi_{w}(i,j). \tag{6.10}$$

Figs. 6.43, 6.44 and 6.45 illustrate the $\Psi_{wt}(i,j)_{normalised}$ and $\Psi_{w}(i,j)_{normalised}$ respectively at three different slices, at z=0, z=25mm and z=50mm, respectively in the receiver sensitivity side. The results show there is an improvement in $\Psi(i,j)_{normalised}$ compared to the case when TCIS is not included. In order to quantify the SNR enhancement, linear plots through x-axis at the centre of the slices are presented in Figs.6.46, 6.47 and 6.48. The results

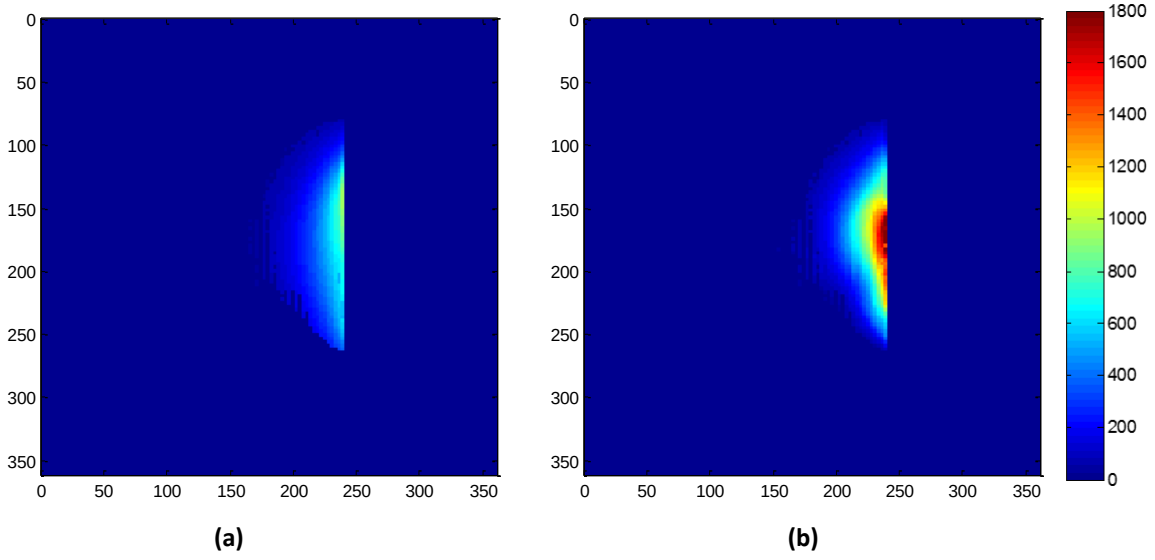

Fig. 6.43 The normalised receiver sensitivity of the coil at the central slice (z=0), TG=60 (a)no TCIS ($\Psi_{wt}(i,j)_{normalised}$), (b) with TCIS ($\Psi_{w}(i,j)_{normalised}$)

illustrate that there is a maximum enhancement of 113% at $x = 3mm, y = z = 0$ and the improvement is observed for 55 mm inside the dielectric phantom. With more in-depth

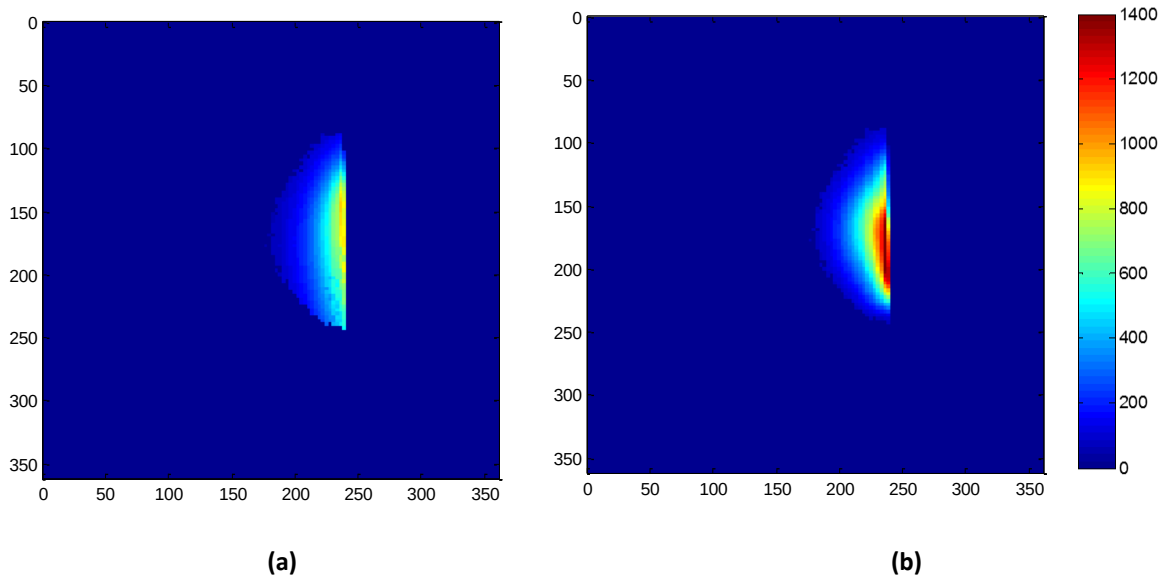

Fig. 6.44 The normalised receiver sensitivity of the coil at the intercell slice (z=25mm), TG=60 (a)no TCIS ($\Psi_{wt}(i,j)_{normalised}$), (b) with TCIS ($\Psi_{w}(i,j)_{normalised}$)

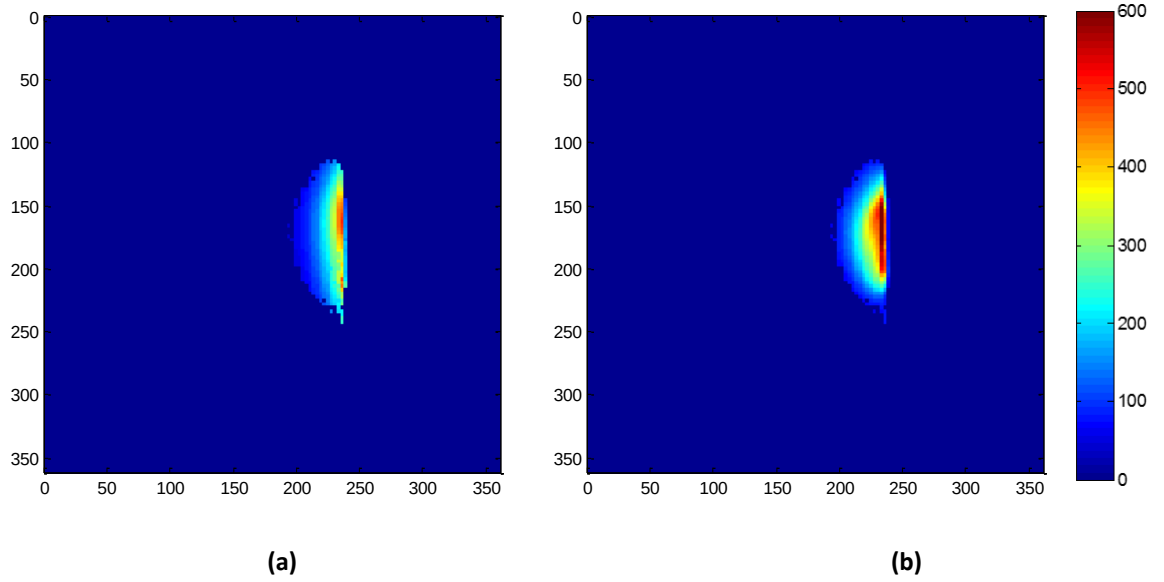

Fig. 6.45 The normalised receiver sensitivity of the coil at the adjacent slice (z=50mm), TG=60 (a)no TCIS ($\Psi_{wt}(i,j)_{normalised}$), (b) with TCIS ($\Psi_{w}(i,j)_{normalised}$)

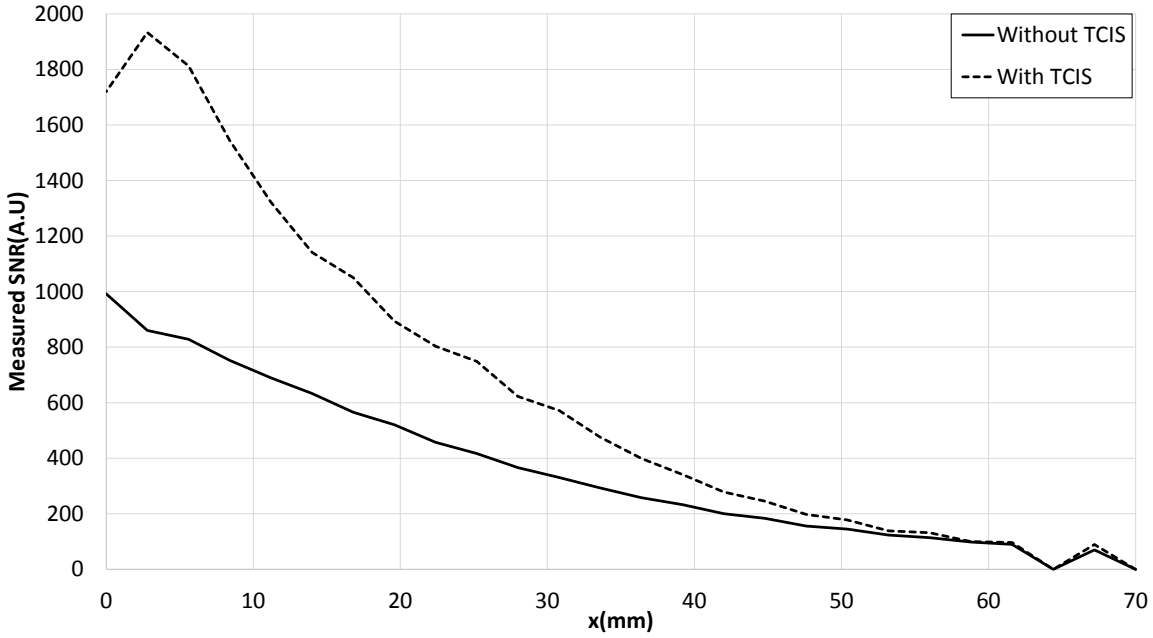

Fig. 6.46 Linear plot of the normalised receiver sensitivity of the RF coil at the centre of the central slice with and without TCIS, TG=60

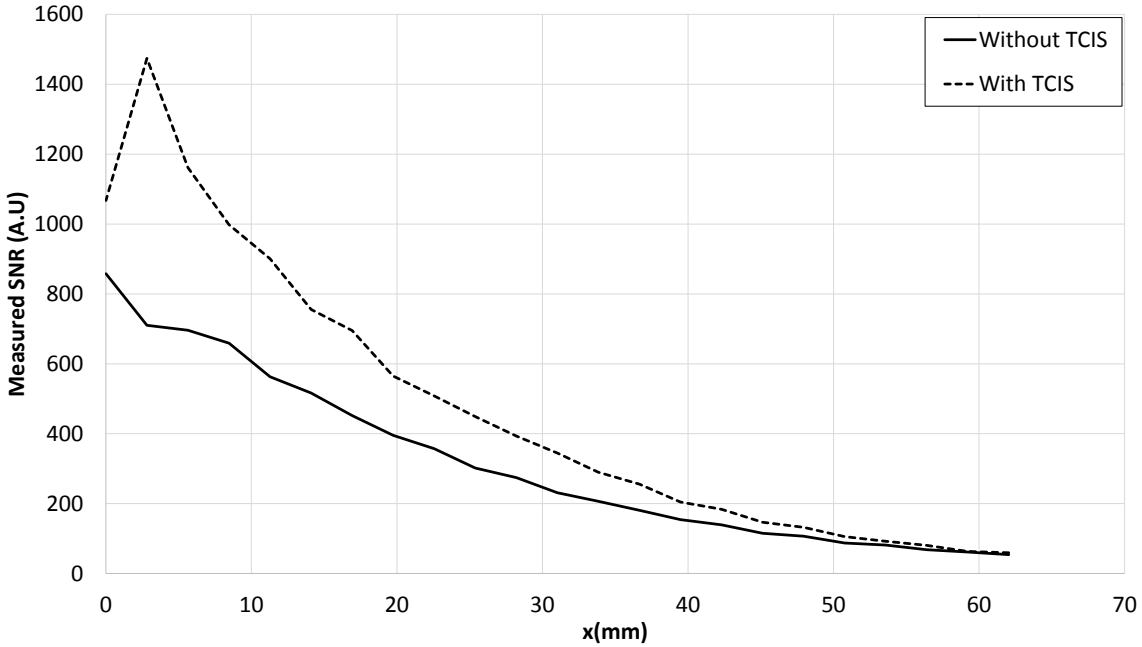

Fig. 6.47 Linear plot of the normalised receiver sensitivity of the RF coil at the centre of the inter cell slice with and without TCIS, TG=60

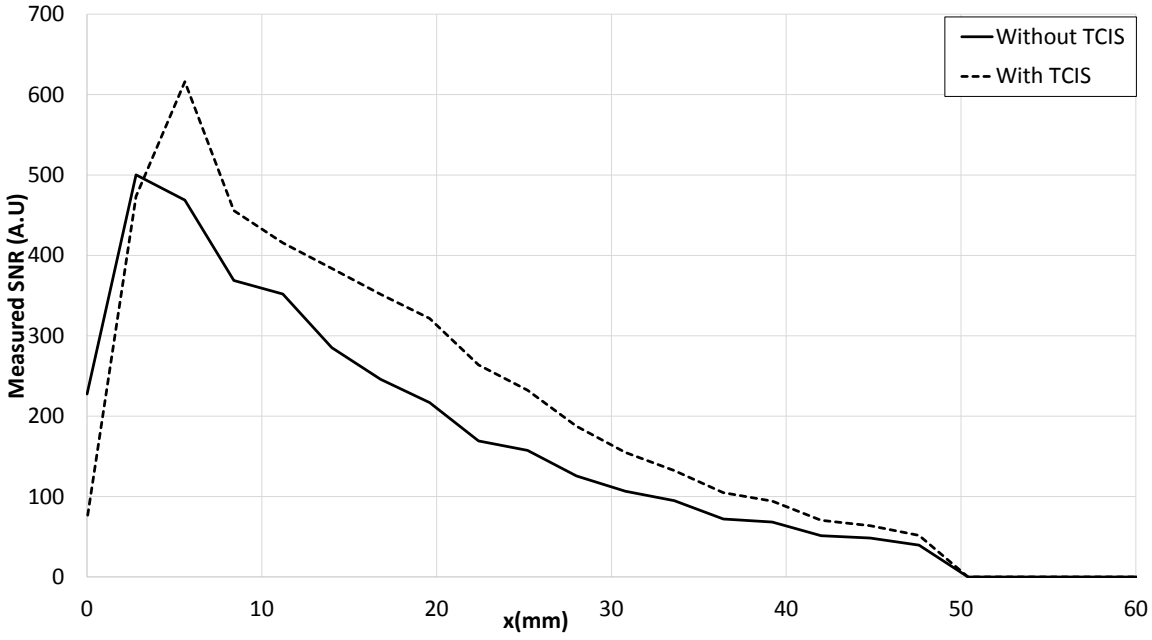

Fig. 6.48 Linear plot of the normalised receiver sensitivity of the RF coil at the centre of the adjacent slice with and without TCIS, TG=60

analysis at the inter cell and adjacent cell, the SNR can be improved by 87% and 38% at $x = 3mm, y = 0, z = 25mm$ or $50mm$ respectively. For more detailed analysis of the receiver sensitivity point of view, an xy-plane of the percentage of improvement of the normalised receiver sensitivity and reduction regions inside the phantom at the centre, inter cell and adjacent cell are shown in Figs.6.49, 6.50 and 6.51, which present (a) percentage of the improvement regions, which is termed by $\eth_I$ and (b) the percentage of the no improvement regions, which is denoted by $\eth_R$ respectively. The $\eth_I$ and $\eth_R$ can be calculated using equations 6.11 and 6.12 respectively.

$$\eth_I(i,j) = \frac{\Psi_w(i,j)_{normalised} - \Psi_{wt}(i,j)_{normalised}}{\Psi_{wt}(i,j)_{normalised}} \times 100 \quad if \quad \Psi_{wt}(i,j)_{normalised} \leq \Psi_w(i,j)_{normalised} \tag{6.11}$$

$$\eth_R(i,j) = \frac{\Psi_{wt}(i,j)_{normalised} - \Psi_w(i,j)_{normalised}}{\Psi_{wt}(i,j)_{normalised}} \times 100 \quad if \quad \Psi_{wt}(i,j)_{normalised} > \Psi_w(i,j)_{normalised} \tag{6.12}$$

The results demonstrate that the normalised receiver sensitivity can be improved at the phantom centre using the 3×3 TCIS and a maximum improvement of 120%, 100% and 60% for the first 60mm can be achieved at the centre slice, inter cell and adjacent slices compared

to the only coil case. However, there is a reduction in SNR at the main beam sides due to the size of the unit cell of the TCIS. This problem could be solved by using a bigger unit cell.

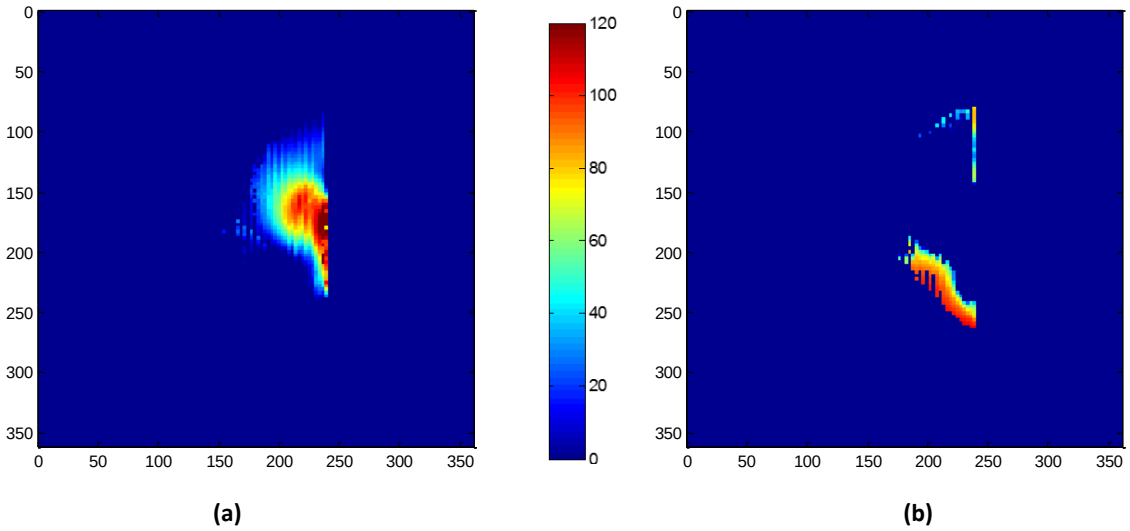

Fig. 6.49 The percentage of the normalised receiver sensitivity of the coil with TCIS at the central slice (z=0) , TG=60(a) percentage of improvement regions ($\eth_I(i,j)$), (b) the percentage of reduction regions ($\eth_R(i,j)$)

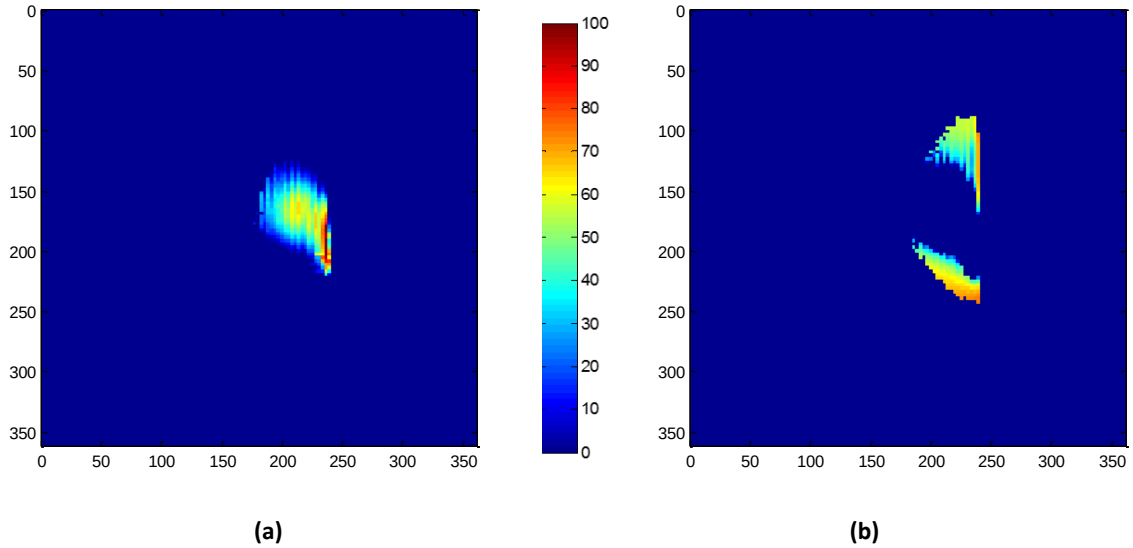

Fig. 6.50 The percentage of the normalised receiver sensitivity of the coil with TCIS at the intercell slice (z=25mm) , TG=60(a) percentage of improvement regions ($\eth_I(i,j)$), (b) the percentage of reduction regions ($\eth_R(i,j)$)

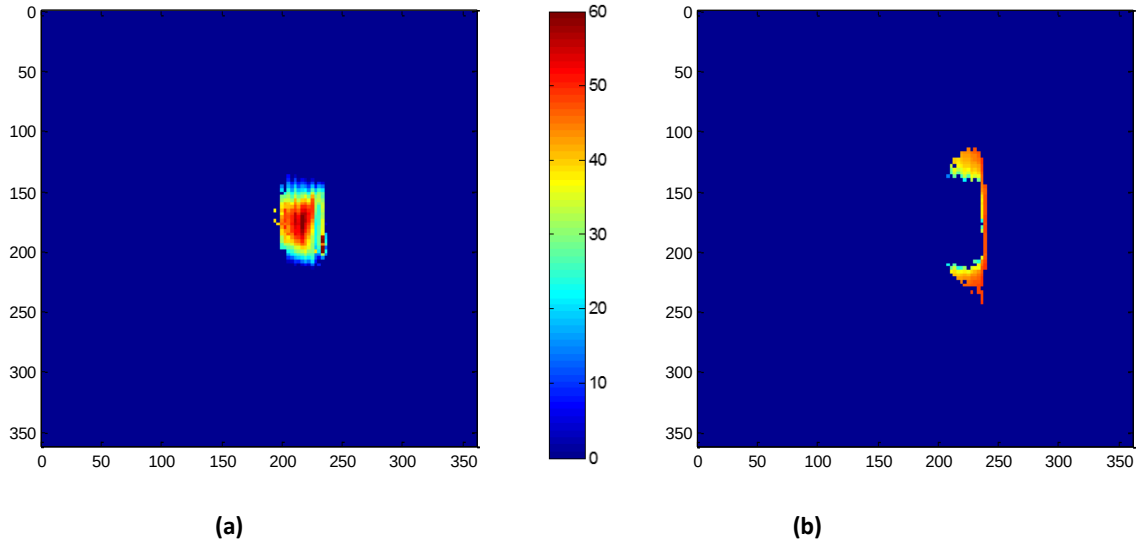

Fig. 6.51 The percentage of the normalised receiver sensitivity of the coil with TCIS at the adjacent cell slice (z=50mm) , TG=60(a) percentage of improvement regions ($\eth_I(i,j)$), (b) the percentage of reduction regions ($\eth_R(i,j)$)

6.6 Summary

In this chapter a two dimensional capacitive impedance surface for enhancing the SNR for MRI applications has been demonstrated through numerical and experimental techniques. Numerical simulations have shown the potential to achieve $B_{1,normalised}^{-}$ maximum improvements of 240% and 160% and $|B_1^+|$ maximum improvements of 287% and 210% at the centre in ideal surface impedance and an FSS implementation model of the RF coil respectively. Experimental results show up to 5dB increase in received signal when tested within a two port VNA system at the centre front face of a dielectric phantom, providing confidence in the technique. MRI measurements using a 1.5T scanner have shown similar SNR trends giving a transceiver improvement of 415% and 80% for the centre and edges of the RF coil respectively for the first 50 mm inside the phantom. The results are proof of concept and are promising in using such a small and thin metasurface in MRI applications for local SNR improvement. In context with the state-of-the-art we are demonstrating a thin two dimensional structure as compared to thicker metamaterials employing lumped components [64], which provided local enhancement for the first 3cm inside the phantom or resonant structures [40] which can enhance the transceiver SNR by 270%. Further analysis of the SNR improvement throughout the volume of the dielectric phantom, in the form a transmission efficiency and a receiver sensitivity have been accomplished by calculating the full map pixels flip angles and global flip angle of both cases with and without TCIS. The enhancement of SNR has been summarised as shown in Table. 6.5. Table 6.6 compares the results carried out in this chapter against the state-of-art methods from publish literature review.

Table 6.5 Maximum SNR improvement (%)

	Transceiver improvement	Transmission efficiency	Receiver sensitivity
Centre slice	415	216	133
Intercell slice	140	68	87
Adjacent slice	80	35	38

Table 6.6 A comparison between using the TCIS method against the state-of-art methods from published literature ((‡- Volume coil †- Surface coil))

Metric	**Approaches**	**1.5T,** $f_0 = 64MHz$	**3T,** $f_0 = 128MHz$	**7T,** $f_0 = 300MHz$
$\|B_1^-\|$	**HIS**	**10% †**	-	7% ‡[37] 25%†[72]
	Metasurface	-	-	-
	RF lens	-	-	-
	Dielectric pads	-	50%‡[95]	100%‡[103]
	RCIS	**77% †**	-	-
	TCIS	**100% †**	-	-
SNR	**HIS**	**6% †**	-	-
	Metasurface	270%‡[91]	-	-
	RF lens	100% [64]	200% [64]	-
	Dielectric pads	-	20-40%‡[95]	53%‡[98], 200%‡[103]
	RCIS	**450% †**	-	-
	TCIS	**415% †**	-	-
Penetration depth	**HIS**	**20mm †**	-	-
	Metasurface	-	-	-
	RF lens	35mm†[64]	40mm†[64]	-
	Dielectric pads	-	-	-
	RCIS	**22mm†**	-	-
	TCIS	**50mm †**	-	-
SAR	**HIS**	**+13.6% †**	-	+48% †[71]
	Metasurface	-	-	-
	RF lens	-	-	-
	Dielectric pads	-	-50% ‡[95]	-33% ‡[98]
	RCIS	**-39% †**	-	-
	TCIS	**-22.7% †**	-	-

Chapter 7

Conclusion and Future work.

7.1 Conclusion

The work carried out in this thesis was focused on enhancing the RF magnetic field and SNR for 1.5T MRI system applications using a metasurface methods. Chapter 1 provides an introduction to the thesis aim, objectives and lists the thesis novelty and contributions. A background of an MRI which include introduction of a magnetic spins system, radiofrequency pluses, spin lattice and spin relaxation times were presented. Also, slice selection, phase encoding, frequency encoding, K-space and RF surface coils design and characterisation were discussed. The parameters for improving the image quality were also covered, including spatial resolution, image contrast and SNR, followed by highlighting the importance of the issue of signal to noise ratio in MRI system applications. Chapter 2 points out the need of a thin and small metasurface for improving a magnetic field and SNR of MRI systems. A literature review of existing approaches used to enhance the SNR of the MRI system applications were divided into three categories: metamaterial, which include RF magnetic lenses, flux guide, wire medium and high impedance surface. The second method was metasurfaces and the third approach was high constant dielectric pads. These methods were presented in order to identify any limitation in the existing approaches and defined the research gaps. The simulation comparison performance metrics used in this thesis are RF magnetic field, magnetic flux density, SAR values for a local sample and whole body mode. These parameters are validated by measurements performance metrics including the S11, S21 and measured SNR within the MRI scanner. The process of applying the High impedance surface to improve the magnetic field and SNR of the MRI system has been described in detail in chapter 3. Since the physical size of applying such material in this system is a challenge, a novel miniaturisation design approach was proposed. The unit cell size of the

proposed HIS is $\lambda/94$ of the operation frequency. The simulated results have shown that there was maximum improvement of 34% and 27% of the $|B_1^+|$ and $\frac{|B_1^-|}{\sqrt{P_L}}$ respectively. The measured SNR validated the concept,however, it illustrated limited improvement due to the fabricated tolerances.

In chapter 4 a new method to improve the SNR has been proposed, based on a combination between RF coil loaded by a reflector capacitive impedance surface. An new results were presented when the sheet capacitance value was 115pF and these results illustrated that the normalised magnetic flux density can be improved by 244% at the top face of the phantom for the first 3.5 cm inside the phantom and there was an enhancement of 450% in measured transceiver SNR and the improvement was observed for the first 2cm inside the phantom. The differences between the simulation and measurement results were because of the manufacturing tolerances.

An new approach for localising magnetic field and SNR was investigated in chapter 5. This approach uses a capacities impedance surface between RF coil and dielectric phantom, named transmission surface impedance. In order to demonstrate the magnetic field localisation, the simulation and measured SNR analysis has been investigated through the phantom slices and three slices were selected including centre, intercell and adjacent slices. The simulation results have shown that normalised magnetic flux density can be localised using an even number of the unit cells of the TCIS, which was assumed to be 4 unit cells of 20×20 cm dimensions. The measurements of SNR through the slices have validated the concept of the magnetic field localisation with 238% improvement of the transceiver measured SNR compared to only coil case. However, the improvement at the coil centre was not as high due to redistribution of the magnetic field throughout the sheet unit cells.

To solve this problem, a modified version of the TCIS was studied and it included an odd numbers of unit cell, which was assumed to be a three by three unit cells of 15×15 cm dimensions. The same evaluation framework of chapter 5 is adopted to quantify the normalised received magnetic flux density, transmit magnetic flux density, electric field, SAR and measured SNR through 15 slices of the phantom. A new results have been demonstrated by numerical simulation and validated by VNA measurements and within a real MRI environment. The achieved normalised magnetic flux density simulated improvement was 100% at the centre of the phantom and it can be observed for 5cm inside the phantom. The simulated E-field locally increased by using the TCIS compared to no TCIS case for the first 5cm inside the phantom, this led to an increase of the local SAR value. However, the whole body SAR of using TCIS was less than with no TCIS case. The measured transceiver

SNR through the phantom slices have shown 415%, 140% and 80% for the centre, intercell and adjacent cell slices respectively.

In this context with the literature review this thesis demonstrated a thin and small metasurface as compared to thicker metamaterials structure or resonance metasurface with a big physical size. More in-depth analysis in terms of the transmission efficiency and receiver sensitivity were also investigated by calculating the local and global flip angles. The results have shown that the achieved transmission efficiency improvements at the top face of the phantom were 216%, 68% and 35% for centre, intercell and adjacent cell slices respectively. Also, the improvements in receiver sensitivity were 133%, 87% and 38% for centre, intercell and adjacent cell slices respectively. Throughout the thesis work, it has been noticed that the fabricated tolerances can lead to the differences between simulation and measurements because the capacitive value of the surface is very sensitive for any small variety in a surface design. To solve this problem the configurable capacitive impedance was proposed in(Appendix A) to be a promising candidate because the capacitive value of the surface can be tuned after the surface is manufactured and it is recommended to demonstrate this surface using VNA and within a real MRI environment.

7.2 Future work

This section outlines some new areas of research for future work based on our finding in this thesis.

1. Development of metasurface approaches to improve SNR of the MRI system is ongoing. This thesis has aimed to enhance the SNR of the surface coil operating at 63.84MHz, which applied for 1.5T MRI system using different types of a periodic metasurface. The analysis in this thesis has been validated by realistic MRI measurements and these results are promising. Another project is seeking to find out more about ways to apply these approaches in a volume coil, for instance a birdcage coil and for a 1.5T or 3T MRI system.

2. The investigation process of this thesis has observed that by utilizing the transmission metasurface between the RF coil and dielectric phantom, dual resonance frequency can be obtained. Fig. 7.1 shows the simulations and measurement of $S21$ varied the CIS impedance value, where it can be clearly seen that the second resonance frequency can be achieved. Since the dual nuclear system is very complex to be achieved by standard RF coils, this approach is recommended to be studied in more in-depth detail.

3. The metasurface structures have been fabricated by printing the metallic digits on FR4 substrate. In reality, the prematurity of this substrate vars between 4.2 to 5.1, however, in

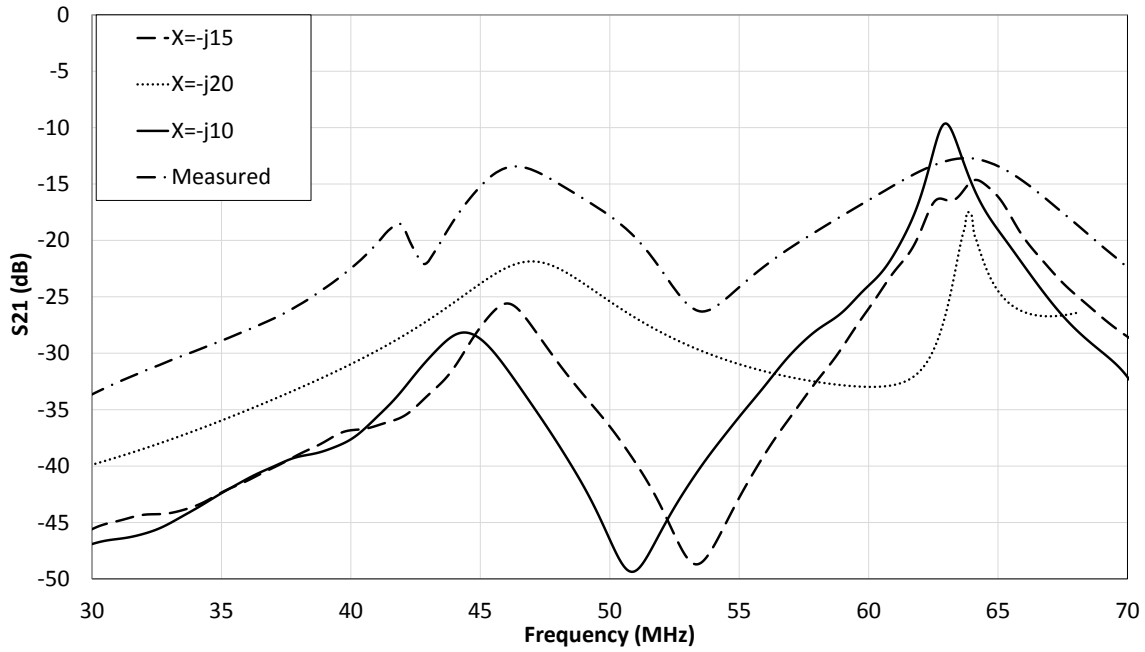

Fig. 7.1 Simulated and measured *S*21 of dual band system using a transmission CIS

simulation it has been assumed to be 4.3. Since the metasurface capacitance is function of the substrate prematívity, variety of substrate may increase the tolerance errors in the results. The next investigation could be achieved by printing the metasurface on high accrue substrate prematívty, a Roger is a good candidate recommended. investigate.

4.In this work a homogeneous dielectric phantom was considered for all the methods and results, with further exploration and development, use of capacitance impedance surface may provide a relatively low-cost and simple approach for enhancing quality and safety of MRI in a variety of vivo applications, which refers to experimentation using a whole, living organism.

References

[1] J. Vaughan and J. Griffiths, *RF Coils for MRI*. Wiley, 2012.

[2] M. Brown and R. Semelka, *MRI: Basic Principles and Applications*. Wiley, 2003.

[3] A. Webb, *Introduction to biomedical imaging*. Wiley-Interscience, 2003.

[4] K. Ugurbil, "Magnetic resonance imaging at ultrahigh fields," *IEEE Transactions on Biomedical Engineering*, vol. 61, no. 5, pp. 1364–1379, 2014.

[5] F. Bloch, "Nuclear induction," *Physical review*, vol. 70, no. 7-8, p. 460, 1946.

[6] E. M. Purcell, H. Torrey, and R. V. Pound, "Resonance absorption by nuclear magnetic moments in a solid," *Physical review*, vol. 69, no. 1-2, p. 37, 1946.

[7] M. H. Levitt, *Spin dynamics: basics of nuclear magnetic resonance*. John Wiley & Sons, 2001.

[8] W. Siemens-Aktiengesellschaft Berlin and A. Hendrix, *Magnets, spins, and resonances: an introduction to the basics of magnetic resonance*. Siemens AG, 2003.

[9] Z.-P. . Liang and P. C. Lauterbur, *Principles of magnetic resonance imaging: a signal processing perspective*. "The" Institute of Electrical and Electronics Engineers Press, 2000.

[10] J. Malmivuo and R. Plonsey, *Bioelectromagnetism: principles and applications of bioelectric and biomagnetic fields*. Oxford University Press, USA, 1995.

[11] M. T. Vlaardingerbroek and J. A. Boer, *Magnetic resonance imaging: theory and practice*. Springer Science & Business Media, 2013.

[12] D. W. McRobbie, E. A. Moore, and M. J. Graves, *MRI from Picture to Proton*. Cambridge university press, 2007.

[13] J. M. Jin, "Electromagnetic in magnetic resonance image," *IEEE Antennas and Propagation Magazine*, vol. 40, no. 6, pp. 7–22, 1998.

[14] B. O. Zhu, E. X. Wu, P. P. Gao, P. Cao, and L. J. Jiang, "The serial resonant antenna for the large field of view magnetic resonance imaging," *Progress In Electromagnetics Research*, vol. 136, pp. 635–646, 2013.

[15] Q. X. Yang, J. Wang, X. Zhang, C. M. Collins, M. B. Smith, H. Liu, X.-H. Zhu, J. T. Vaughan, K. Ugurbil, and W. Chen, "Analysis of wave behavior in lossy dielectric samples at high field," *Magnetic resonance in medicine*, vol. 47, no. 5, pp. 982–989, 2002.

[16] M. Tincher, C. R. Meyer, R. Gupta, and D. M. Williams, "Polynomial modeling and reduction of rf body coil spatial inhomogeneity in mri," *IEEE transactions on medical imaging*, vol. 12, no. 2, pp. 361–365, 1993.

[17] R. Rojas and A. O. Rodriguez, "Numerical study of the optimal geometry of mri surface coils," in *Engineering in Medicine and Biology Society, 2007. EMBS 2007. 29th Annual International Conference of the IEEE*, pp. 3890–3893, IEEE, 2007.

[18] C.-N. Chen, D. Hoult, and V. Sank, "Quadrature detection coils a further $\sqrt{2}$ improvement in sensitivity," *Journal of Magnetic Resonance (1969)*, vol. 54, no. 2, pp. 324–327, 1983.

[19] F. E. Terman, *Radio engineers' handbook*. New York; London: McGraw-Hill Book Co., 1943.

[20] X. Zhang, K. Ugurbil, and W. Chen, "Microstrip rf surface coil design for extremely high-field mri and spectroscopy," *Magnetic resonance in medicine*, vol. 46, no. 3, pp. 443–450, 2001.

[21] J. Fang, M. S. Chow, K. C. Chan, K. K. Wong, G. X. Shen, E. Gao, E. S. Yang, and Q. Y. Ma, "Design of superconducting mri surface coil by using method of moment," *IEEE Transactions on Applied Superconductivity*, vol. 12, pp. 1823–1827, Jun 2002.

[22] G. Mayer, "Resolution enhancement in magnetic resonance imaging by frequency extrapolation," 2008.

[23] E. Carmi, S. Liu, N. Alon, A. Fiat, and D. Fiat, "Resolution enhancement in mri," *Magnetic resonance imaging*, vol. 24, no. 2, pp. 133–154, 2006.

[24] C.-n. Chen and D. I. Hoult, *Biomedical magnetic resonance technology*, vol. 100. Adam Hilger Bristol, 1989.

[25] C. M. Collins and M. B. Smith, "Calculations of b1 distribution, snr, and sar for a surface coil adjacent to an anatomically-accurate human body model," *Magnetic resonance in medicine*, vol. 45, no. 4, pp. 692–699, 2001.

[26] K. Ocegueda and A. Rodriguez, "A simple method to calculate the signal-to-noise ratio of a circular-shaped coil for mri," *Concepts in Magnetic Resonance Part A*, vol. 28, no. 6, pp. 422–429, 2006.

[27] D. Hoult and P. C. Lauterbur, "The sensitivity of the zeugmatographic experiment involving human samples," *Journal of Magnetic Resonance (1969)*, vol. 34, no. 2, pp. 425–433, 1979.

[28] D. Hoult, "The principle of reciprocity in signal strength calculations—a mathematical guide," *Concepts in Magnetic Resonance Part A*, vol. 12, no. 4, pp. 173–187, 2000.

[29] M. E. Kowalski, J.-M. Jin, and J. Chen, "Computation of the signal-to-noise ratio of high-frequency magnetic resonance imagers," *IEEE Transactions on Biomedical Engineering*, vol. 47, pp. 1525–1533, Nov 2000.

[30] P. Kellman and E. R. McVeigh, "Image reconstruction in snr units: a general method for snr measurement," *Magnetic resonance in medicine*, vol. 54, no. 6, pp. 1439–1447, 2005.

[31] Z. Chen, K. Solbach, D. Erni, and A. Rennings, "Improving b_1 efficiency and signal-to-noise-ratio of a surface coil by a high-impedance-surface rf shield for 7-t magnetic resonance imaging," *IEEE Transactions on Microwave Theory and Techniques*, vol. 65, pp. 988–997, March 2017.

[32] L. Kaufman, D. M. Kramer, L. E. Crooks, and D. A. Ortendahl, "Measuring signal-to-noise ratios in mr imaging.," *Radiology*, vol. 173, no. 1, pp. 265–267, 1989.

[33] O. Dietrich, J. G. Raya, S. B. Reeder, M. F. Reiser, and S. O. Schoenberg, "Measurement of signal-to-noise ratios in mr images: Influence of multichannel coils, parallel imaging, and reconstruction filters," *Journal of Magnetic Resonance Imaging*, vol. 26, no. 2, pp. 375–385, 2007.

[34] J. Algarin, M. Lopez, M. Freire, and R. Marques, "Signal to noise ratio evaluation in resonant ring metamaterial lenses for mri applications," *New Journal of Physics*, vol. 13, no. 11, 2011.

[35] J. B. Pendry, A. J. Holden, D. J. Robbins, and W. J. Stewart, "Magnetism from conductors and enhanced nonlinear phenomena," *IEEE Transactions on Microwave Theory and Techniques*, vol. 47, pp. 2075–2084, Nov 1999.

[36] X. Radu, A. Lapeyronnie, and C. Craeye, "Numerical and experimental analysis of a wire medium collimator for magnetic resonance imaging," *Electromagnetics*, vol. 28, no. 7, p. 531–543. dummy note.

[37] Z. Chen, K. Solbach, D. Erni, and A. Rennings, "Electromagnetic field analysis of a dipole coil element with surface impedance characterized shielding plate for 7-t mri," *IEEE Transactions on Microwave Theory and Techniques*, vol. 64, pp. 972–981, March 2016.

[38] V. G. Veselago, "The electrodynamics of substances with simultaneously negative values of and μ," *Soviet physics uspekhi*, vol. 10, no. 4, p. 509, 1968.

[39] J. B. Pendry, "Negative refraction makes a perfect lens," *Physical review letters*, vol. 85, no. 18, p. 3966, 2000.

[40] S. B. Glybovski, S. A. Tretyakov, P. A. Belov, Y. S. Kivshar, and C. R. Simovski, "Metasurfaces: From microwaves to visible," *Physics Reports*, vol. 634, pp. 1–72, 2016.

[41] B. Munk, *Frequency Selective Surface*. Wiley, 2000.

[42] S. Tretyakov, *Analytical modeling in applied electromagnetics*. Artech House, 2003.

[43] F. Costa, A. Monorchio, and G. Manara, "An overview of equivalent circuit modeling techniques of frequency selective surfaces and metasurfaces," *Appl. Comput. Electromagn. Soc. J.*, vol. 29, no. 12, pp. 960–976, 2014.

[44] G. I. Kiani, K. L. Ford, L. G. Olsson, K. P. Esselle, and C. J. Panagamuwa, "Switchable frequency selective surface for reconfigurable electromagnetic architecture of buildings," *IEEE Transactions on Antennas and Propagation*, vol. 58, pp. 581–584, Feb 2010.

[45] K. L. Ford, J. Roberts, S. Zhou, G. Fong, and J. Rigelsford, "Reconfigurable frequency selective surface for use in secure electromagnetic buildings," *Electronics Letters*, vol. 49, pp. 861–863, July 2013.

[46] G. I. Kiani, K. P. Esselle, K. L. Ford, A. R. Weily, and C. Panagamuwa, "Angle and polarization-independent bandstop frequency selective surface for indoor wireless systems," *Microwave and Optical Technology Letters*, vol. 50, no. 9, pp. 2315–2317, 2008.

[47] A. O. AlAmoudi, S. Almari, S. Zhu, and R. J. Langley, "Improved performance of 2.45 ghz implanted antenna for wireless communication," in *2012 IEEE Asia-Pacific Conference on Applied Electromagnetics (APACE)*, pp. 308–312, Dec 2012.

[48] S. Zhu, S. Almari, A. O. AlAmoudi, and R. J. Langley, "Implanted antenna efficiency improvement," in *2013 7th European Conference on Antennas and Propagation (EuCAP)*, pp. 3247–3248, April 2013.

[49] M. Wiltshire, J. Pendry, I. Young, D. Larkman, D. Gilderdale, and J. Hajnal, "Microstructured magnetic materials for rf flux guides in magnetic resonance imaging," *Science*, vol. 291, no. 5505, pp. 849–851, 2001.

[50] J. B. Pendry, A. J. Holden, D. Robbins, and W. Stewart, "Magnetism from conductors and enhanced nonlinear phenomena," *IEEE transactions on microwave theory and techniques*, vol. 47, no. 11, pp. 2075–2084, 1999.

[51] M. Wiltshire, J. Pendry, and J. Hajnal, "Sub-wavelength imaging at radio frequency," *Journal of Physics: Condensed Matter*, vol. 18, no. 22, 2006.

[52] M. Wiltshire, J. Pendry, D. Larkman, D. Gilderdale, D. Herlihy, I. Young, and J. Hajnal, "Geometry preserving flux ducting by magnetic metamaterials," in *Proc. Int. Soc. Mag. Reson. Med*, vol. 11, pp. 713–713, 2003.

[53] O. Zhuromskyy, E. Shamonina, and L. Solymar, "2d metamaterials with hexagonal structure: spatial resonances and near field imaging," *Opt. Express*, vol. 13, pp. 9299–9309, Nov 2005.

[54] W. Rotman, "Plasma simulation by artificial dielectrics and parallel-plate media," *IRE Transactions on Antennas and Propagation*, vol. 10, no. 1, pp. 82–95, 1962.

[55] P. Belov, R. Marques, S. Maslovski, I. Nefedov, M. Silveirinha, C. Simovski, and S. Tretyakov, "Strong spatial dispersion in wire media in the very large wavelength limit," *Physical Review B*, vol. 67, no. 11, p. 113103, 2003.

[56] P. A. Belov, Y. Hao, and S. Sudhakaran, "Subwavelength microwave imaging using an array of parallel conducting wires as a lens," *Physical Review B*, vol. 73, no. 3, p. 033108, 2006.

[57] A. P. Slobozhanyuk, I. V. Melchakova, A. V. Kozachenko, D. S. Filonov, C. R. Simovski, and P. A. Belov, "An endoscope based on extremely anisotropic metamaterials for applications in magnetic resonance imaging," *Journal of Communications Technology and Electronics*, vol. 59, no. 6, pp. 562–570, 2014.

[58] M. J. Freire and R. Marques, "Planar magnetoinductive lens for three-dimensional subwavelength imaging," *Applied Physics Letters*, vol. 86, no. 18, 2005.

[59] M. J. Freire, L. Jelinek, R. Marques, and M. Lapine, "On the applications of metamaterial lenses for magnetic resonance imaging," *Journal of Magnetic Resonance*, vol. 203, no. 1, pp. 81 – 90, 2010.

[60] J. D. Baena, L. Jelinek, R. Marqués, and M. Silveirinha, "Unified homogenization theory for magnetoinductive and electromagnetic waves in split-ring metamaterials," *Phys. Rev. A*, vol. 78, p. 013842, Jul 2008.

[61] D. M. Pozar, "Microwave engineering 3rd ed., ma john wiley & sons," 2005.

[62] M. Lapine, L. Jelinek, M. Freire, and R. Marques, "Realistic metamaterial lenses: Limitations imposed by discrete structure," *Physical Review B*, vol. 82, no. 16, pp. 165–172, 2010.

[63] M. J. Freire and R. Marques, "Near-field imaging in the megahertz range by strongly coupled magnetoinductive surfaces: Experiment and ab initio analysis," *Journal of applied physics*, vol. 100, no. 6, 2006.

[64] J. M. Algarin, M. Freire, and F. Breuer, "Metamaterial magnetoinductive lens performance as a function of field strength," *Journal of Magnetic Resonance*, vol. 247, pp. 9–14, 2014.

[65] R. A. Shelby, D. R. Smith, and S. Schultz, "Experimental verification of a negative index of refraction," *Science*, vol. 292, no. 5514, pp. 77–79, 2001.

[66] V. G. Veselago, "The electrodynamics of substances with simultaneously negative values of μ, and ε," *Soviet Physics Uspekhi*, vol. 10, no. 4, p. 509, 1968.

[67] J. Joannopoulos, D. Robert, and N. W. Joshua, *Photonic crystals : molding the flow of light*. Princeton, N.J. : Princeton University Press,, 1995.

[68] V. Kumar, B. Suthar, J. Malik, A. Kumar, K. S. Singh, T. Singh, and A. Bhargva, "Defect mode properties and origin in one dimensional photonic crystal," *Photonics and Optoelectronics*, 2013.

[69] D. Sievenpiper, Z. Lijun, R. F. J. Broas, N. G. Alexopolous, and E. Yablonovitch, "High-impedance electromagnetic surfaces with a forbidden frequency band," *IEEE Transactions on Microwave Theory and Techniques*, vol. 47, no. 11, pp. 2059–2074, 1999.

[70] R. Marqués, F. Martín, and M. Sorolla, *Metamaterials with Negative Parameters: Theory, Design and Microwave Applications*. Wiley, 2011.

[71] G. Saleh, K. Solbach, and A. Rennings, "Ebg structure to improve the b_1 efficiency of stripline coil for 7 tesla mri," in *6th European Conference on Antennas and Propagation (EUCAP)*, pp. 1399–1401, 2012.

[72] Z. Chen, K. Solbach, D. Erni, and A. Rennings, "Improved b1 distribution of an mri rf coil element using a high-impedance-surface shield," in *2015 German Microwave Conference*, pp. 111–114, March 2015.

[73] F. Bayatpur and K. Sarabandi, "Single-layer high-order miniaturized-element frequency-selective surfaces," *IEEE Transactions on Microwave Theory and Techniques*, vol. 56, pp. 774–781, April 2008.

[74] S. R. Best, "A comparison of the performance properties of the hilbert curve fractal and meander line monopole antennas," *Microwave and Optical technology letters*, vol. 35, no. 4, pp. 258–262, 2002.

[75] J. McVay, N. Engheta, and A. Hoorfar, "High impedance metamaterial surfaces using hilbert-curve inclusions," *IEEE Microwave and Wireless Components Letters*, vol. 14, pp. 130–132, March 2004.

[76] H. Sagan, *Peano's Space-Filling Curve*, pp. 31–47. New York, NY: Springer New York, 1994.

[77] J. Zhu, A. Hoorfar, and N. Engheta, "Peano antennas," *IEEE Antennas and Wireless Propagation Letters*, vol. 3, pp. 71–74, Dec 2004.

[78] K. Sarabandi and N. Behdad, "A frequency selective surface with miniaturized elements," *IEEE Transactions on Antennas and Propagation*, vol. 55, pp. 1239–1245, May 2007.

[79] H. Liu, K. L. Ford, and R. J. Langley, "Miniaturised bandpass frequency selective surface with lumped components," *Electronics Letters*, vol. 44, no. 18, pp. 1054–1055, 2008.

[80] H. Liu, K. L. Ford, and R. J. Langley, "Miniaturised artificial magnetic conductor design using lumped reactive components," *Electronics Letters*, vol. 45, no. 6, pp. 294–295, 2009.

[81] R. Kuse, T. Hori, M. Fujimoto, T. Seki, K. Sato, and I. Oshima, "Equivalent circuit analysis for amc with double layer patch type fss," in *2013 IEEE Antennas and Propagation Society International Symposium (APSURSI)*, pp. 1360–1361, July 2013.

[82] R. Kuse, T. Hori, M. Fujimoto, T. Seki, K. Sato, and I. Oshima, "Equivalent circuit analysis for double layer patch type amc in consideration of mutual coupling between layers," in *2013 Asia-Pacific Microwave Conference Proceedings (APMC)*, pp. 591–593, Nov 2013.

[83] G. D. Alley, "Interdigital capacitors and their application to lumped-element microwave integrated circuits," *IEEE Transactions on Microwave Theory and Techniques*, vol. 18, pp. 1028–1033, Dec 1970.

[84] R. C. Hadarig, M. E. de Cos, and F. Las-Heras, "Novel miniaturized artificial magnetic conductor," *IEEE Antennas and Wireless Propagation Letters*, vol. 12, pp. 174–177, 2013.

[85] R. Saad and K. L. Ford, "Miniaturised dual-band artificial magnetic conductor with reduced mutual coupling," *Electronics Letters*, vol. 48, no. 8, pp. 425–426, 2012.

[86] R. Saad and K. L. Ford, "A miniaturised dual band artificial magnetic conductor using interdigital capacitance," in *Antennas and Propagation (EuCAP), 2014 8th European Conference on*, pp. 25–26, 2014.

[87] C. L. Holloway, E. F. Kuester, J. A. Gordon, J. O'Hara, J. Booth, and D. R. Smith, "An overview of the theory and applications of metasurfaces: The two-dimensional equivalents of metamaterials," *IEEE Antennas and Propagation Magazine*, vol. 54, pp. 10–35, April 2012.

[88] R. E. Munson, H. A. Haddad, and J. W. Hanlen, "Microstrip reflectarray for satellite communication and radar cross-section enhancement or reduction," Aug. 4 1987. US Patent 4,684,952.

[89] A. Yu, F. Yang, A. Elsherbeni, and J. Huang, "Experimental demonstration of a single layer tri-band circularly polarized reflectarray," in *Antennas and Propagation Society International Symposium (APSURSI), 2010 IEEE*, pp. 1–4, IEEE, 2010.

[90] D. McGrath, "Planar three-dimensional constrained lenses," *IEEE Transactions on Antennas and Propagation*, vol. 34, no. 1, pp. 46–50, 1986.

[91] A. P. Slobozhanyuk, A. N. Poddubny, A. J. Raaijmakers, C. A. van den Berg, A. V. Kozachenko, I. A. Dubrovina, I. V. Melchakova, Y. S. Kivshar, and P. A. Belov, "Enhancement of magnetic resonance imaging with metasurfaces," *Advanced Materials*, 2016.

[92] W. Teeuwisse, W. Brink, K. Haines, and A. Webb, "Simulations of high permittivity materials for 7 t neuroimaging and evaluation of a new barium titanate-based dielectric," *Magnetic resonance in medicine*, vol. 67, no. 4, pp. 912–918, 2012.

[93] J. Snaar, W. Teeuwisse, M. Versluis, M. van Buchem, H. Kan, N. Smith, and A. Webb, "Improvements in high-field localized mrs of the medial temporal lobe in humans using new deformable high-dielectric materials," *NMR in Biomedicine*, vol. 24, no. 7, pp. 873–879, 2011.

[94] W. M. Brink, J. S. van den Brink, and A. G. Webb, "The effect of high-permittivity pads on specific absorption rate in radiofrequency-shimmed dual-transmit cardiovascular magnetic resonance at 3t," *Journal of Cardiovascular Magnetic Resonance*, vol. 17, no. 1, p. 82, 2015.

[95] Q. X. Yang, J. Wang, J. Wang, C. M. Collins, C. Wang, and M. B. Smith, "Reducing sar and enhancing cerebral signal-to-noise ratio with high permittivity padding at 3 t," *Magnetic resonance in medicine*, vol. 65, no. 2, pp. 358–362, 2011.

[96] W. M. Brink and A. G. Webb, "High permittivity pads reduce specific absorption rate, improve b1 homogeneity, and increase contrast-to-noise ratio for functional cardiac mri at 3t," *Magnetic resonance in medicine*, vol. 71, no. 4, pp. 1632–1640, 2014.

[97] B. S. Park, S. S. Rajan, J. W. Guag, and L. M. Angelone, "A novel method to decrease electric field and sar using an external high dielectric sleeve at 3 t head mri: Numerical and experimental results," *IEEE Transactions on Biomedical Engineering*, vol. 62, pp. 1063–1069, April 2015.

[98] Q. X. Yang, W. Mao, J. Wang, M. B. Smith, H. Lei, X. Zhang, K. Ugurbil, and W. Chen, "Manipulation of image intensity distribution at 7.0 t: passive rf shimming and focusing with dielectric materials," *Journal of magnetic resonance imaging*, vol. 24, no. 1, pp. 197–202, 2006.

[99] R. Schmidt and A. Webb, "Improvements in rf shimming in high field mri using high permittivity materials with low order pre-fractal geometries," *IEEE Transactions on Medical Imaging*, vol. 35, pp. 1837–1844, Aug 2016.

[100] W. M. Brink, R. F. Remis, and A. G. Webb, "A theoretical approach based on electromagnetic scattering for analysing dielectric shimming in high-field mri," *Magnetic resonance in medicine*, 2015.

[101] L. W. X.Qing, M.Yang and Christopher, "Rf field enhancement with high dielectric constant (hdc) pads in a receive arry coil at 3t," *Journal of magnetic resonance imaging JMRI*, 2013.

[102] B. Park, T. Neuberger, A. G. Webb, D. C. Bigler, and C. M. Collins, "Faraday shields within a solenoidal coil to reduce sample heating: Numerical comparison of designs and experimental verification," *Journal of Magnetic Resonance*, vol. 202, no. 1, pp. 72–77, 2010.

[103] B. Y. Lee, X. H. Zhu, S. Rupprecht, M. T. Lanagan, Q. X. Yang, and W. Chen, "Large improvement of rf transmission efficiency and reception sensitivity for human in vivo mrs imaging using ultrahigh dielectric constant materials at 7 t," *Magnetic resonance imaging*, vol. 42, no. 18, pp. 158–163, 2017.

[104] A. Shchelokova, R. Schmidt, A. Slobozhanyuk, T. Kallos, A. Webb, and P. Belov, "Enhancement of magnetic resonance imaging with metasurfaces: From concept to human trials," in *Engineered Materials Platforms for Novel Wave Phenomena (Metamaterials), 2017 11th International Congress on*, pp. 31–33, IEEE, 2017.

[105] R. Schmidt, A. Slobozhanyuk, P. Belov, and A. Webb, "Flexible and compact hybrid metasurfaces for enhanced ultra high field in vivo magnetic resonance imaging," *Scientific reports*, vol. 7, no. 1, p. 1678, 2017.

[106] F. Lemoult, G. Lerosey, J. de Rosny, and M. Fink, "Resonant metalenses for breaking the diffraction barrier," *Physical review letters*, vol. 104, no. 20, p. 203901, 2010.

[107] K. Foster and H. Schwan, "Dielectric properties of tissues and biological material," *Critical Reviews in Biomedical Engineering*, vol. 17, pp. 25–104, 1989.

[108] M. Stuchly and S. Stuchly, "Dielectric properties of biological substances-tabulated," *Journal of Microwave Power*, vol. 15, pp. 19–26, 1980.

[109] N. E. Farber, J. McNeely, and D. Rosner, "Skin burn associated with pulse oximetry during perioperative photodynamic therapy," *The Journal of the American Society of Anesthesiologists*, vol. 84, no. 4, pp. 983–985, 1996.

[110] I. Bahl, *Lumped Elements for RF and Microwave Circuits*. Artech House, 2003.

[111] M. J. Freire, R. Marques, and L. Jelinek, "Experimental demonstration of a μ=- 1 metamaterial lens for magnetic resonance imaging," *Applied Physics Letters*, vol. 93, no. 23, 2008.

[112] "Iec 60601-2-33: Particular requirements for the basic safety and essential performance of magnetic resonance equipment for medical diagnosis," 2010.

[113] J.-P. Berenger, "A perfectly matched layer for the absorption of electromagnetic waves," *Journal of computational physics*, vol. 114, no. 2, pp. 185–200, 1994.

[114] J. M. Algarin, M. J. Freire, M. A. Lopez, M. Lapine, P. M. Jakob, V. C. Behr, and R. Marqués, "Analysis of the resolution of split-ring metamaterial lenses with application in parallel magnetic resonance imaging," *Applied Physics Letters*, vol. 98, no. 1, p. 014105, 2011.

[115] S. Jarrix, T. Dubois, R. Adam, P. Nouvel, B. Azais, and D. Gasquet, "Probe characterization for electromagnetic near-field studies," *IEEE Transactions on Instrumentation and Measurement*, vol. 59, pp. 292–300, Feb 2010.

[116] X. Yang, T. Zheng, and H. Fujita, "T/r switches, baluns, and detuning elements in mri rf coils," in *ISMRM Fourteenth Scienti^c Meeting Weekend Syllabus*, 2006.

[117] B. C. Wadell, *Transmission line design handbook*. Artech House, 1991.

Appendix A

Reconfigurable Capacitive Impedance Surface for 1.5T Magnetic Resonance Imaging Applications.

A.1 Introduction

The appendix A presents a reconfigurable capacitive impedance surface (CIS) combined with a radio frequency loop coil to improve the radio frequency (RF) magnetic flux density, B_1, for magnetic resonance imaging applications. The proposed technique offers advantages of being able to tune performance in-situ as compared to passive solutions which may suffer from issues associated with manufacturing tolerances. The proposed structure is based on a periodic array of metallic patches loaded by variable capacitors. Full field simulations employing a surface with a dielectric phantom, represented the human body, show the tuneable capacitive property of the surface can be used to maximise B_1^+, which is advantageous for reducing transmitted power, and B_1^- which is important for receiver sensitivity.

A.2 Reconfigurable Capacitive Impedance Surface Concept

Fig.A.1a shows a cross section of the concept of interest which includes a dielectric phantom, mimicking a biological sample, spaced a distance, s=5mm, away from a surface impedance layer. Fig.A.1b illustrates the proposed technique for achieving reconfigurability using a periodic array of metallic patches which include variable capacitors. A homogeneous dielec-

tric phantom with dimensions length=335mm, width=230mm, height=140mm was assumed. The dielectric properties of the phantom were $\varepsilon_r = 65, \sigma = 0.4S/m, \rho = 1000kg/m^3$.

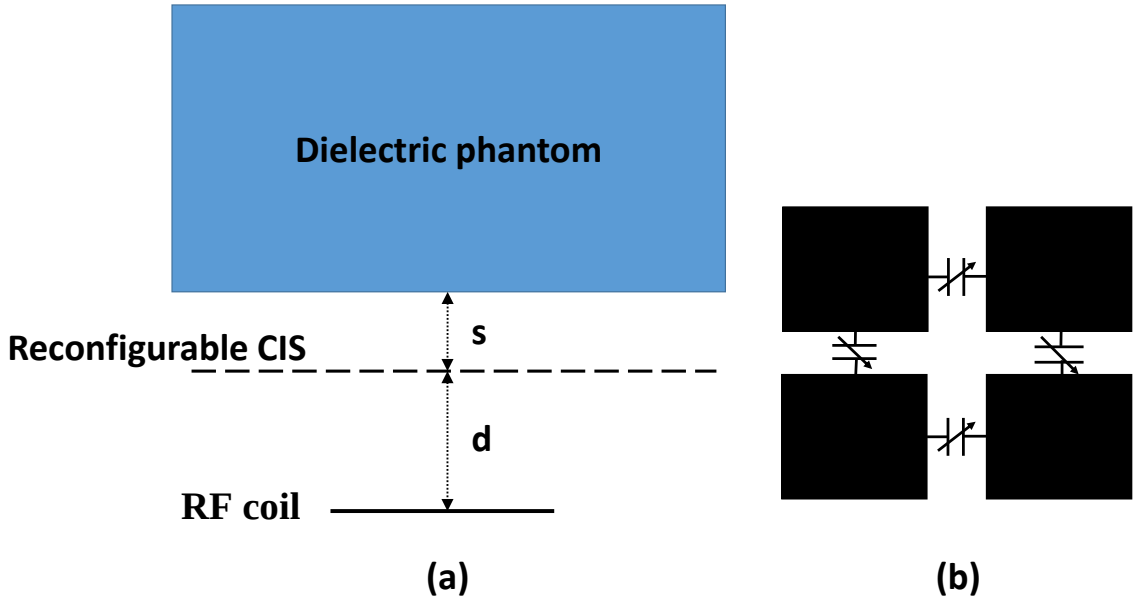

Fig. A.1 (a)Cross-section of reconfigurable transceiver system (b) Illustration of reconfigurable surface

A.2.1 Reconfigurable Capacitive Impedance Surface Design

The reconfigurable CIS comprises of an array of metallic patches which are spacing a distance, g, apart and the periodicity is, P. These periodic patches are on a 0.8 mm thick FR4 substrate (ε_r=4.3, tan δ=0.025) and include variable capacitors across the gaps between the patches. The unit cell geometry is assumed to be square with dimensions of P=40mm, g=10mm, and total surface dimension size are 200mm by 160mm. The proposed surface is spaced a distance, d=20mm, away from a circular RF loop coil. The surface impedance is assumed to be dominated by variable capacitance and in this section the losses associated with the tuning components are assumed to be zero (R=0) for the idealised case.

The RF coil design was previously reported in previous chapters, and in this study a circular RF surface coil with a diameter of $D = 12.3cm$ was assumed. The coil size was designed in order to optimise the magnetic flux density for 140mm penetration depth. The coil model was fed using a $50\Omega, 1W$ source. The coil has three capacitors, C_1, C_2, C_3, which have equal values, $100pF$, which are used to tune the resonant frequency. Fig. A.2

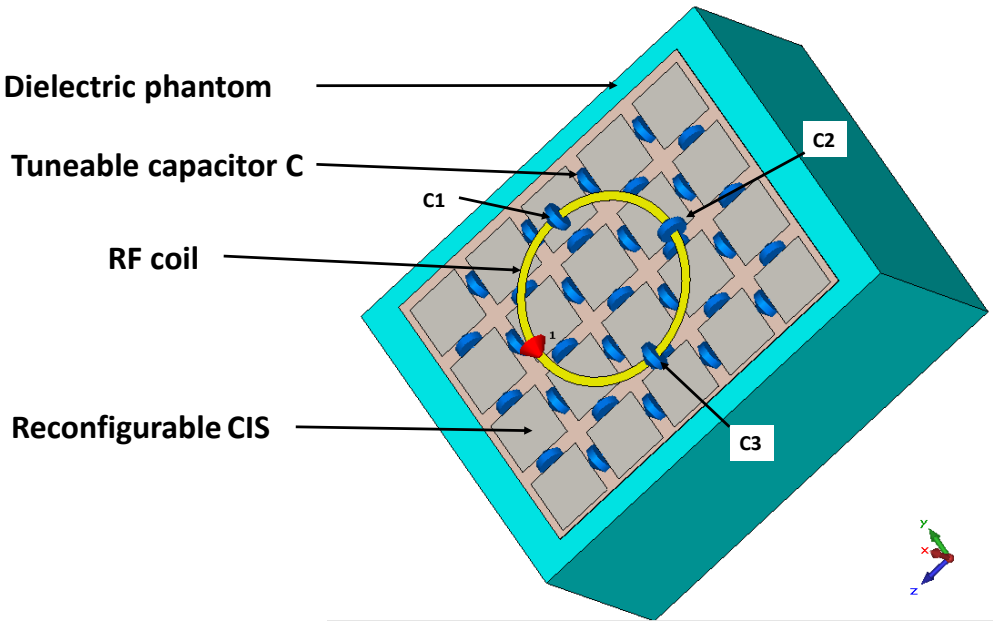

Fig. A.2 CST simulation geometry

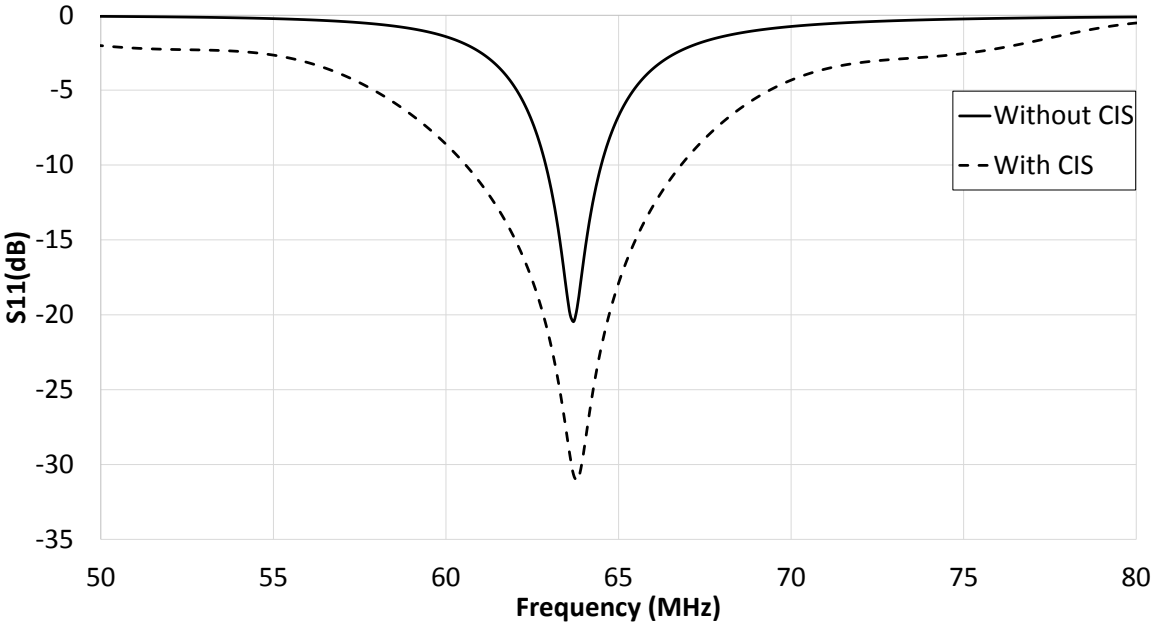

Fig. A.3 Simulation of the input matching RF coil

shows the simulation geometry. The simulations were performed using the time domain solver within CST Microwave Studio 2015. The coil was tuned and matched using a co-simulation technique at the Larmor frequency of 63.8MHz. Fig. A.3 shows the simulated $S11$ when $s = 5mm, d = 20mm$, both with and without the CIS. It should be noted that different matching circuits are needed for the two cases as the CIS loads the RF coil resulting in a shift in resonant frequency. The results show an increase in bandwidth when the CIS is present which is due to the losses in the FR4 substrate.

A.2.2 Results of ideal reconfigurable surface

Fig. A.4 shows the simulated B_1^- in the dielectric phantom through the coil centre, which has been normalised to the square root of the absorbed power, ($\sqrt{P_{abs}}$), in the system, for a range of variable capacitance values. It can be seen that as the capacitance is varied between $150pF$ to $250pF$ the B_1^- also increases, however, for higher capacitance there is a reduction in performance. Fig.A.5 shows the B_1^- at the coil edge for the same change in capacitance. The results show the potential to provide significant performance improvements which can be controlled to take account of practical tolerances.

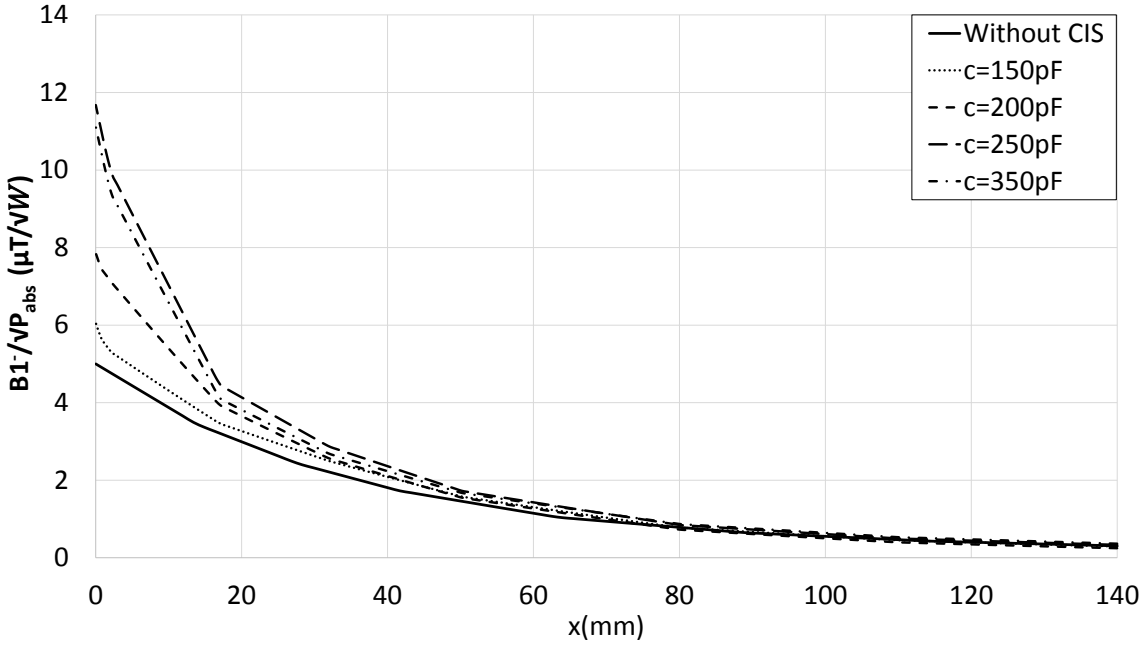

Fig. A.4 Simulated $\frac{B_1^-}{\sqrt{P_{abs}}}$ at the RF coil center for lossless variable capacitance

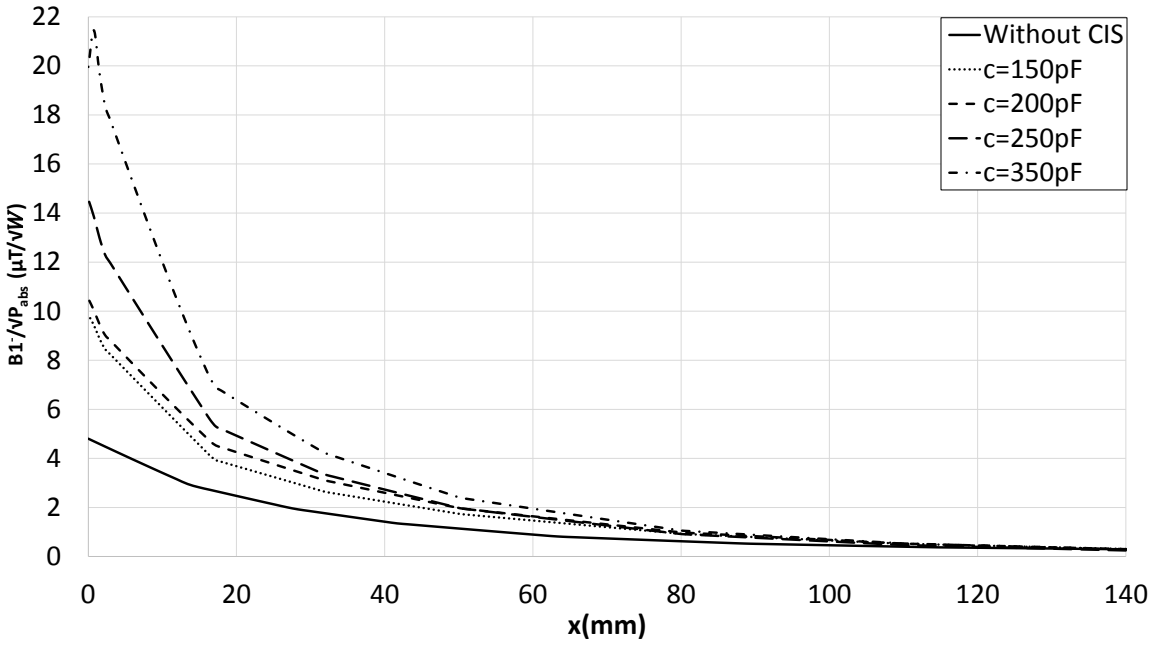

Fig. A.5 Simulated $\frac{B_1^-}{\sqrt{P_{abs}}}$ at the RF coil edge for lossless variable capacitance

A.3 Reconfigurable capacitive impedance surface incorporating device losses

In this section the losses due to the resistance of a realistic variable capacitance is assessed for the MRI concept. The variable capacitors have been modelled as series RC lumped elements with values of $R = 1.5\Omega, C = 100pF - 350pF$ which are typical for possible tunable elements such as a varactor diode. Fig. A.6 and Fig. A.7 show the B_1^- through the coil centre and coil edge respectively where the B_1^- has been normalised to $\sqrt{P_{abs}}$. The results show that the B_1^- is reduced compared to the ideal case, however, there is still improvement when compared to the case without the CIS for the initial 20mm inside the phantom. At the coil edge there is improvement for all penetration depths as compared to the RF coil only. A more detailed analysis, Fig. A.8 and Fig. A.9 shows the magnitude of transmitted magnetic flux density, B_1^+ and the magnitude of received magnetic flux density $\frac{B_1^-}{\sqrt{P_{abs}}}$ respectively for a range of 1cm thick slices where increasing slice number indicates moving away from the centre of the coil. The values presented are the mean over an area of $(D/\sqrt{2} \times D \times 10mm)$, where D is the diameter of the RF coil and for these results the capacitance is fixed at $250pF$. The slice thickness is commensurate with the practical dimensions that might be found in MRI systems. The results show that the potential improvement could be significant over a large volume

of the phantom, however, the losses associated with realistic variable capacitors reduces the improvement from 88% to 12% for B_1^+ and 201% to 68% for $\frac{B_1^-}{\sqrt{P_{abs}}}$.

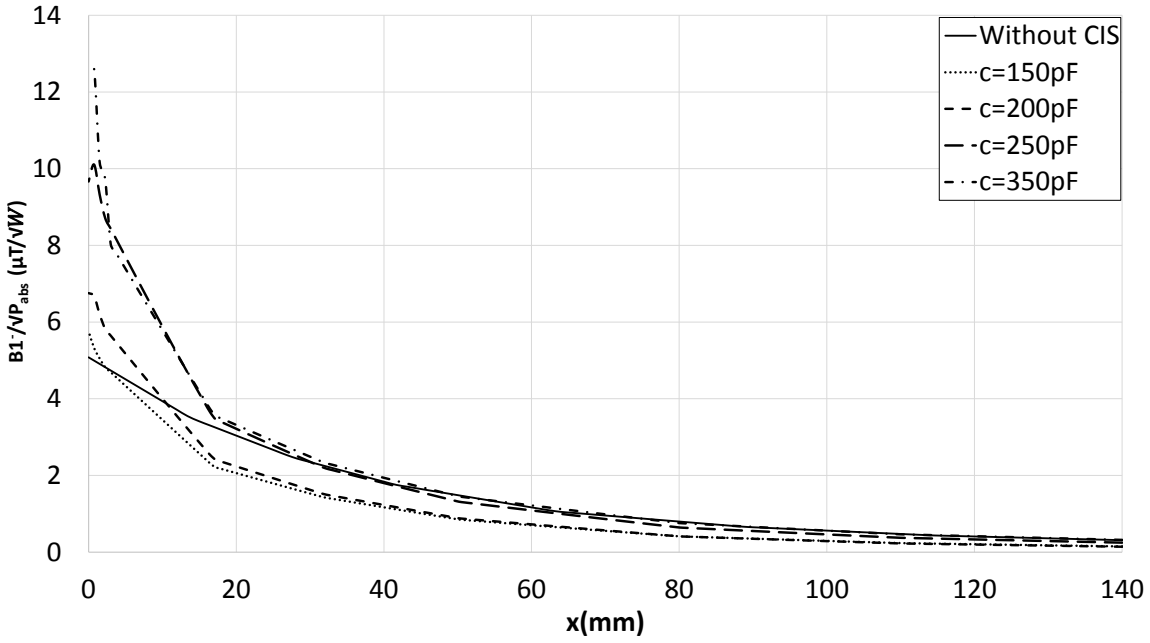

Fig. A.6 Simulated $\frac{B_1^-}{\sqrt{P_{abs}}}$ at the RF coil centre for lossy variable capacitance, $R = 1.5\Omega$

A.3.1 Summary

In this section, numerical simulation results show that a reconfigurable CIS can be used for optimising the received and transmitted magnetic flux density inside a dielectric phantom. The reconfigurability can be used to control the magnetic field in-situ to mitigate against the impact of manufacturing and other tolerances. The results show that there is an 88.5% improvement in the magnitude of B_1^+ for an ideal design, however, 12% on average can be achieved when reconfigurable component losses are taken into account. An average improvement in received $\frac{|B_1^-|}{\sqrt{P_{abs}}}$ over 200% for the ideal case is shown which reduces to 68% when component losses are included. The results also show that the improvements can be maintained towards the edge of the RF coil where classic approaches lose signal intensity.

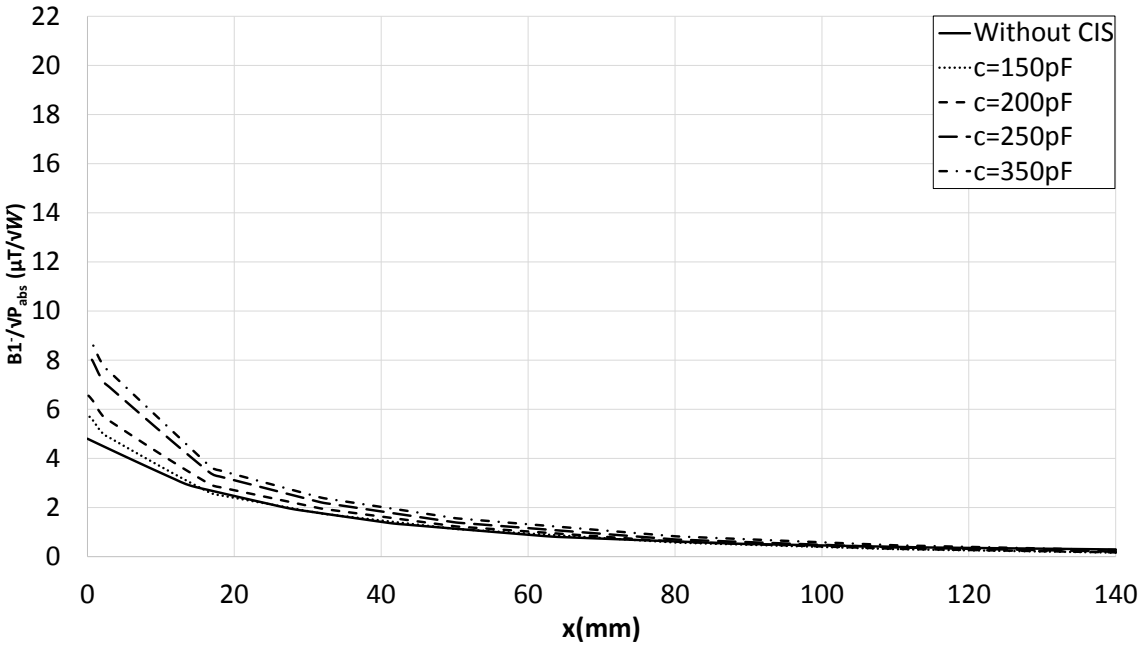

Fig. A.7 Simulated $\frac{B_1^-}{\sqrt{P_{abs}}}$ at the RF coil edge for lossy variable capacitance, $R = 1.5\Omega$

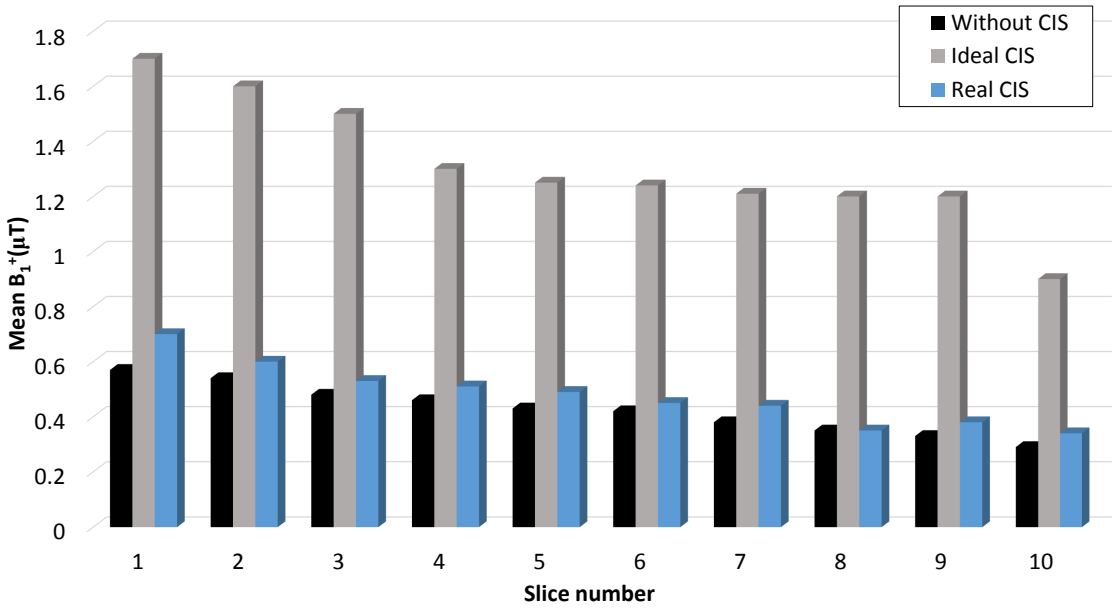

Fig. A.8 Simulated B_1^+ for 1cm thick slices, $C = 250pF$.

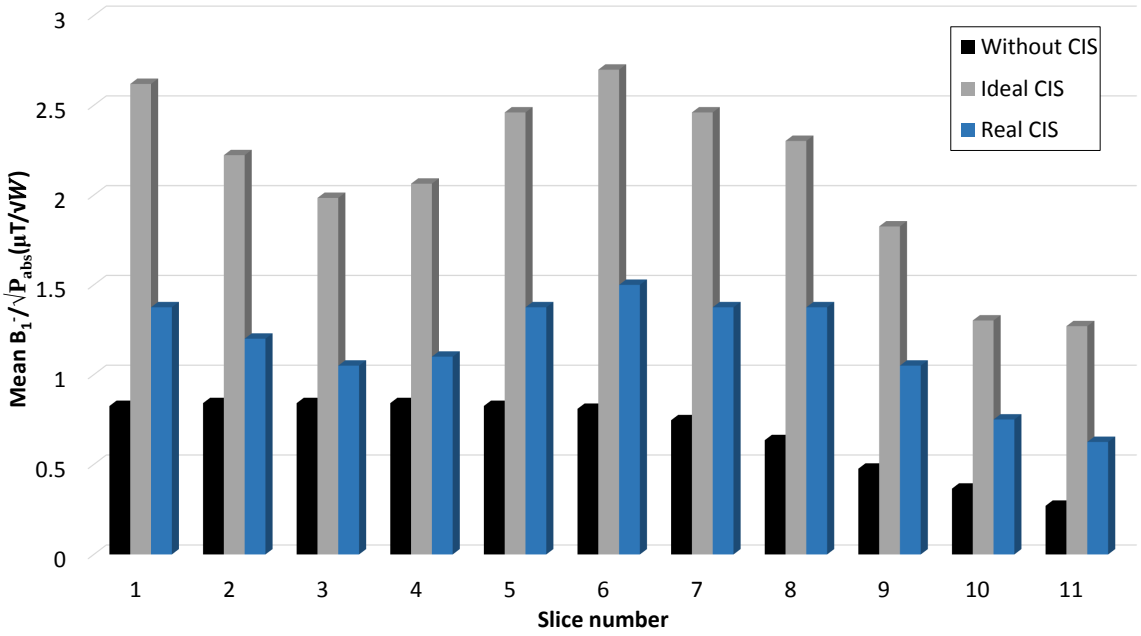

Fig. A.9 Simulated $\frac{B_1^-}{\sqrt{P_{abs}}}$ for 1cm thick slices, $C = 250pF$.

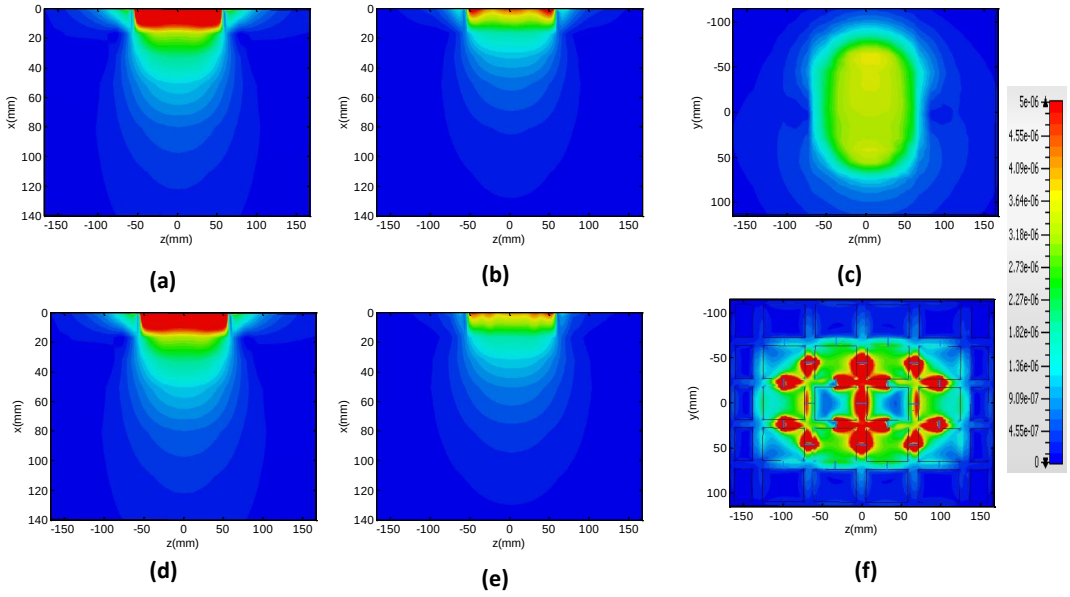

Fig. A.10 The 2D magnitude of B_1^- in xy-plan

Appendix B

Tools and materials

This section presents the simulation and experimental tools that are used to evaluate the 63.8MHz RF system. These tools are key to refining an objective basis for the the systems with and without metasurfaces comparing arrays.

B.0.1 Shielded Loop probes

Single probe shielded loops, as illustrated in , are used to induce a magnetic field (B-flux) based on Faraday's law [115]. When two of these probes are placed together they can be evaluated a resonance circuits, they behave as transmit /receive system.

In transmission probe, a resonant circuit is coupled to the H-field transmitted, if it is at resonant frequency (Larmor frequency), this probe will focus the magnetic field so that the receiver probe can detect it. In this research, these shielded probes were manufactured using semi-rigid coaxial cable 50 ohm, and connecting at the end of the loop probe inner conductor to the cable probe shielded and soldered with each other. The double loop probes are used with the vector network analyser (VNA) in transmission mode ($S21$), with the loops connected to port 1 and port 2. Further details about the shielded loop probes, self resonance frequency of the probes using in this thesis.

B.0.2 Liquid dielectric phantom human body model

A human body phantom was developed to be used to have the same human body loading conduction. Fig. B.2 (a) illustrates Aplastic container with dimensions (mm) $(335 length \times 230 with \times 140 high$, and 5L in volume) was used to hold the phantom in the bench measurements. This bottle was filled with distilled water and then was placed above the RF coil, after that NaCI was added to the bottle in small quantity until the S11 trace matching the

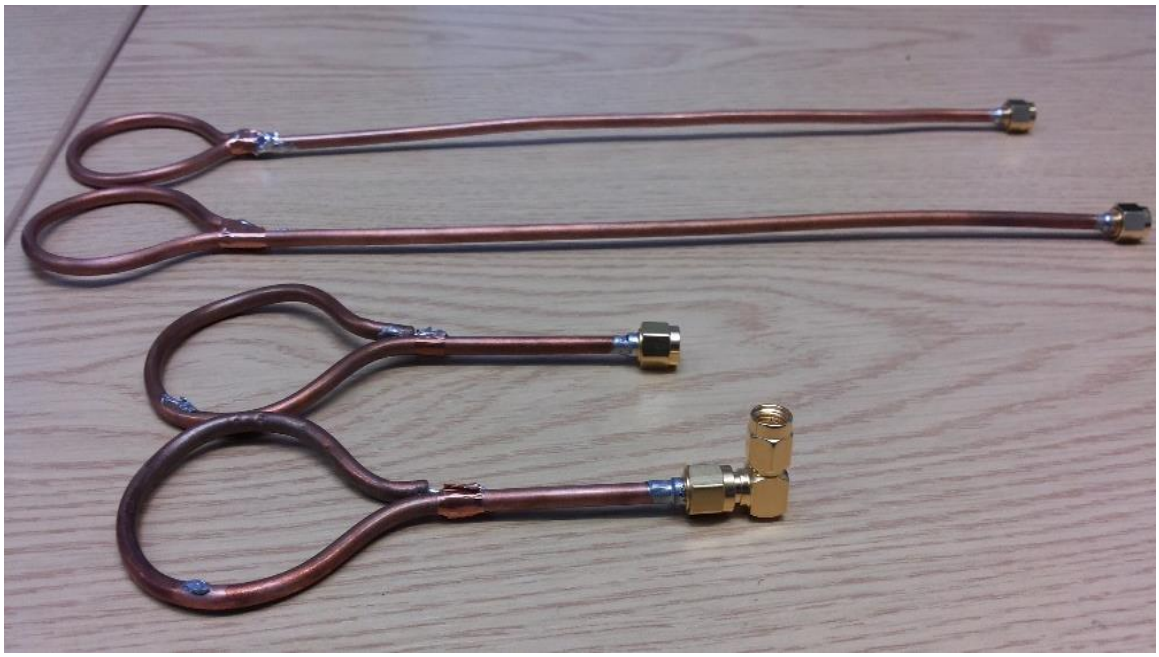

Fig. B.1 The RF shielded loop probes

S11 of the real human body. The S11 was observed using network analyser and the RF coil was tuned to the Larmor frequency at 1.5 Tesla. In the CST simulation the human body phantom can be developed by the cube shape with the same dimensions that was used in experimental work with permittivity $\varepsilon_r = 65$ and conductivity $\sigma = 0.4 S/m$ [62, 63]as shown in B.2a, experimental phantom and B.2b, CST-MW simulated phantom. In MRI scanner measurements, a standard dielectric phantom was used, which was provided by the Radiology department at Hallamshair hospital.

B.1 RF coil engineering

The Q-factor concept of the RF coil

A coil is characterized by the ability to store energy versus the energy that is dissipated by the coil in well coil constructed, if the coil is not loaded means without the sample to be tested it should have a high Q-factor value, and when the coil is loaded by a dielectric sample the Q-factor is expected to decrease which can lead to an overall increase in resonator losses. The Q-factor is given by Equation B.1 which represent the ratio between the storage and dissipated power.

$$Q = \frac{Storage power}{Dissipated power} = \frac{\omega L}{R} = \frac{f_0}{\Delta f} \tag{B.1}$$

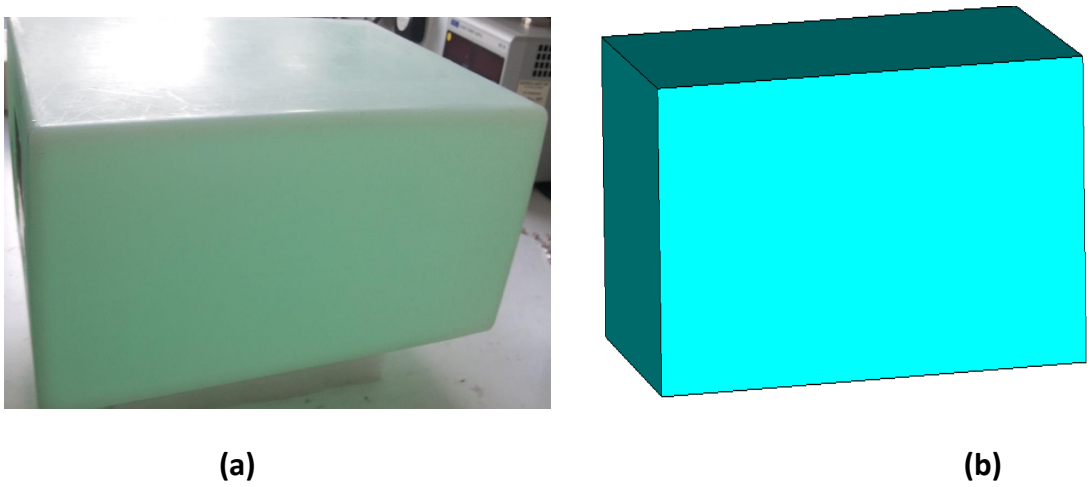

Fig. B.2 The dielectric phantom.(a). Experimental phantom.(b). Simulated phantom

where $\omega = 2\pi f_0$, f_0 resonance frequency. Δf is a -3dB bandwidth of the RF coil.
The Q-factor is an alternative approach to estimate the percentage of the SNR, which can be achieved by the coil as given by B.2. The term loaded means the coil with dielectric sample 'load' ,which denoted by Q_{loaded} and unloaded means the coil without the dielectric sample and termed $Q_{unloaded}$. $Q_{unladed}$ coil is combination the effects associated with lumped elements, conductors, and radiation losses. The $Q_{unloaded}$ coil is responsible for all losses except the losses of the sample. The Q_{ratio} can be determined by B.3 [1].

$$\frac{SNR}{SNR_{max}} = \sqrt{1 - \frac{1}{Q_{ratio}}} \tag{B.2}$$

$$Q_{ratio} = \frac{Q_{unloaded}}{Q_{loaded}} \tag{B.3}$$

where the SNR_{max} is a maximum SNR at the ideal case (losses=0).

Balance to unbalance (BALUN) circuit

Ideally RF signals are transmitted through the cables in different mode, and due to imperfection as a results there can be exist common mode currents. In MRI applications common mode current signals are problematic because they represent a loss in the RF coil efficiency, also, the common mode current produce unnecessary RF coupling and heating of both the

cables and RF coils. This can lead to reduce the received signal intensity and if large common mode currents are induced they can cause a RF patient burns if the patient is close to the cables [24]. In order to overcome this problem the researchers such as [116] suggested to use a Balance to unbalance devices (BALUN). The Balun is the common mode choke in the radio frequency coils and it presents high impedance to the signal current which is in common mode, and low impedance in signal current in differential mode and DC coupling is allowed. There are several types of Balun used in RF coils, the main two common are solenoid and transformer like Baluns. The solenoid balun is has a strong blocking impedance, however, the capacitor has to be connected directly to the cables which may lead to be an unstable. Fig. B.3.a shows the equivalent circuit of solenoid balun. The second main type of Balun is a transformer like balun some studies called it 'Lattice balun' and its equivalent circuit is shown in figure B.3.b. Due to the disadvantages of the solenoid balun, in this thesis the 1:1 lattice balun has been used in all models. For design 1:1 Lattice balun the value of C, and L are calculated by equation B.4 and B.5 [117].

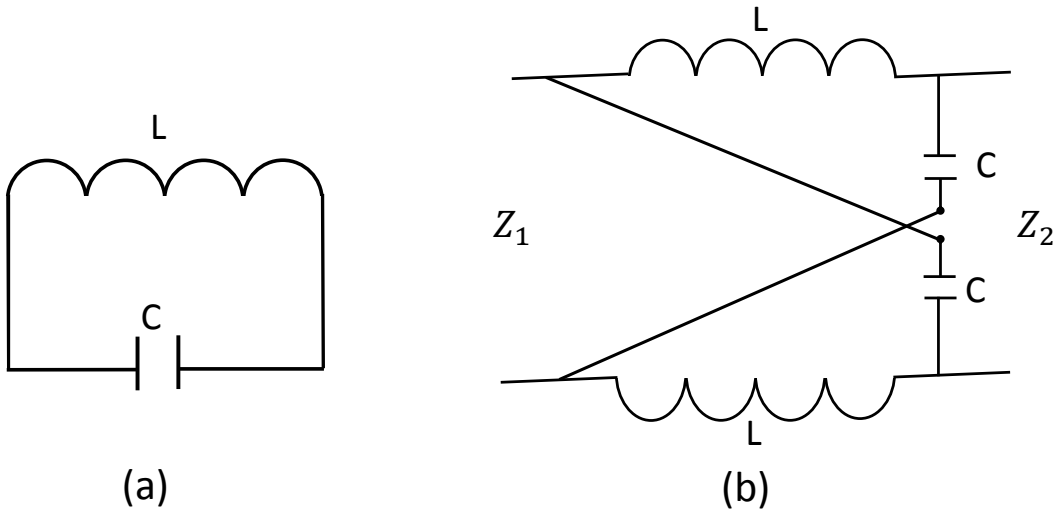

Fig. B.3 Block diagram of the RF coil Balun: (a). solenoid (b). Lattice

$$L = \frac{\sqrt{Z_1 Z_2}}{\omega} \tag{B.4}$$

$$C = \frac{1}{\sqrt{Z_1 Z_2}\omega} \tag{B.5}$$